

CHARACTERIZATION OF
COLLECTIVE SPIN STATES IN ATOMIC ENSEMBLES
TRAPPED AROUND TAPERED NANOFIBERS

KILIAN W. KLUGE

Master Thesis

October 2015 – Version 1.0

Kilian W. Kluge: *Characterization of Collective Spin States in Atomic Ensembles Trapped Around Tapered Nanofibers*, Master Thesis, October 2015

This thesis is the result of experimental work conducted at [QUANTOP](#), Niels Bohr Institute, University of Copenhagen from October 2014 to October 2015. The author was supported by a Deutschlandstipendium funded jointly by the Bundesministerium für Bildung und Forschung and GE Germany, and an ERASMUS+ grant by the European Union. Travel funding by [QUANTOP](#) is thankfully acknowledged.

PRINCIPAL SUPERVISOR AT TU BERLIN:

Prof. Dr. Stephan Reitzenstein

PRINCIPAL SUPERVISOR AT NBI:

Assoc. Prof. Dr. Jörg-Helge Müller

ADDITIONAL SUPERVISORS AT NBI:

Assoc. Prof. Dr. Jürgen Appel

Prof. Dr. Eugene S. Polzik

*And all at once
a step outside
into the wind and rain.*

– Villagers

PUBLICATIONS

A paper on the experiment described in part III of this thesis has been prepared for submission:

1. H. L. Sørensen, J.-B. S. Béguin, **K. W. Kluge**, I. Iakoupov, A. S. Sørensen, J.-H. Müller, E. S. Polzik, J. Appel: *Coherent back-scattering off one-dimensional atomic strings*. (2015)

A publication on the experiment described in part IV is planned.

PRESENTATIONS & POSTERS

1. K. W. Kluge et al.: *Coherent Bragg-reflections from a one-dimensional atomic crystal*. Optical Nanofiber Applications: From Quantum to Bio Technologies, Okinawa, Japan (May 2015) – Contributed poster
2. K. W. Kluge et al.: *Coherent Bragg scattering from a one-dimensional atomic crystal*. QUANTOP Fuglsang Workshop, Fuglsang, Denmark (July 2015) – Invited talk
3. K. W. Kluge et al.: *Coherent Bragg-reflections from a one-dimensional atomic crystal*. Vienna Summer School on Complex Quantum Systems, Vienna, Austria (September 2015) – Contributed poster

ABSTRACT

Ultracold atomic ensembles trapped in the evanescent field of tapered nanofibers have emerged as a novel and efficient light-matter interface with promising applications for quantum information science and metrology. With a strong single atom coupling to the fundamental guided mode of the fiber, this interface allows for high optical depths for ensembles of only a few thousand atoms. Paired with the complex optical properties of the fiber modes, this makes nanofiber trapped atoms a prime candidate for the realization of a high-fidelity quantum memory.

During the first experimental steps towards this goal, we develop and explore a novel optical pumping method to imprint a superstructure on the nanofiber trapped atomic ensemble. By investigating Bragg scattering from the resonantly structured atoms, we realize the first atomic Bragg mirror in this system, observing as much as $(11.6 \pm 1.1)\%$ intensity reflection off only about 800 atoms. We also further study the atom's dynamics, thereby investigating the suitability of the scheme for applications in quantum state preparation.

In the main line of experiments, we work towards the creation and tomography of a single excitation state stored in an atomic ensemble. The preparation and characterization of such a non-Gaussian, genuinely quantum state is an important step towards the realization of quantum memories and quantum communication networks. Employing a hybrid discrete-continuous approach, the preparation of the state is heralded by the detection of a single photon. Subsequently, a tomography is performed using a [QND](#) two-color heterodyne scheme.

In this thesis, a main focus is the preparation of the initial state. To this end, we adapt a proposal by [\(Christensen et al., 2013\)](#) to the case of nanofiber trapped atoms, most notably incorporating the directionality of spontaneous emission. We further implement and characterize state manipulation through optical and microwave interactions, thereby observing Rabi oscillations and estimating the relevant coherence properties.

Additionally, we design, implement, and characterize the optical filtering setup necessary for the detection of the heralding photon.

ZUSAMMENFASSUNG

Im evaneszenten Feld einer optischen Nanofaser gefangene ultrakalte Atome sind ein exzellentes System zur Untersuchung der Wechselwirkung von Licht und Materie. Durch die starke Kopplung zwischen den Atomen und der Grundmode werden schon für wenige tausend Atome hohe optische Dichten erreicht. In Verbindung mit den komplexen optischen Eigenschaften der Faser macht dies nanofaserbasierte Atomfallen zu aussichtsreichen Kandidaten für die Realisierung eines Quantenspeichers hoher Güte und Anwendungen in der Metrologie und Quanteninformationsverarbeitung.

In einer ersten Reihe von Experimenten erzeugen wir durch optisches Pumpen erstmals ein Übergitter in den im optischen Gitter um die Nanofaser gefangenen Atomen. Wir untersuchen Bragg-Reflektionen von diesen Strukturen und optimieren auf diese Weise unsere Präparationsmethode. Dabei beobachten wir bis zu $(11.6 \pm 1.1)\%$ Reflektion von einer Struktur, die aus nur ungefähr 800 Atomen besteht. Um festzustellen, ob sich die von uns entwickelte Methode zum Einsatz bei der Erzeugung von Quantenzuständen eignet, untersuchen wir zudem die Dynamik der Atome.

Das zentrale Experiment dieser Arbeit widmet sich der Erzeugung und Tomographie eines single excitation state. Die Präparation und Charakterisierung eines solchen nicht-Gauß'schen, unzweifelhaft quantenmechanischen Zustands ist ein wichtiger Schritt auf dem Weg zu einem Quantenspeicher sowie der Entwicklung von Quantenkommunikationsnetzwerken. Grundlage unseres Experiments ist ein diskret-kontinuierlicher Hybridansatz: Während die erfolgreiche Erzeugung eines single excitation state durch die Detektion eines Einzelphotons angezeigt wird, verwenden wir zur Tomographie eine spezielle Variante der heterodynen Detektion, mit der QND-Messungen möglich sind.

Der Schwerpunkt dieser Arbeit liegt auf der Erzeugung des Ausgangszustands. Hierzu übertragen wir den von (Christensen et al., 2013) ausgearbeiteten Vorschlag auf nanofaserbasierte Atomfallen, dabei berücksichtigen wir insbesondere, dass die spontane Emission von Atomen in die Nanofaser gerichtet ist. Zudem implementieren und charakterisieren wir die Manipulation atomarer Zustände durch Wechselwirkung mit optischem Licht und Mikrowellen. So beobachten wir unter anderem Rabi-Oszillationen und schätzen die relevanten Kohärenzzeiten ab.

Schließlich entwerfen wir das optische Filtersystem für die Detektion des Einzelphotons, das wir umsetzen und auf seine Eigenschaften überprüfen.

CONTENTS

PREFACE	1
INTRODUCTION	3
I FOUNDATIONS	9
1 LIGHT	11
1.1 Photons	11
1.2 Quadrature Operators and Phase Space	12
1.3 Quantum States	12
1.4 Quasi-Probability Distributions	15
1.5 Non-Classicality	18
2 ATOMS	21
2.1 Multi-Level Atoms	21
2.2 Two-Level Atoms	23
2.3 Collective Spin States	26
2.4 Atom Trapping and Cooling	28
3 MEASUREMENT	35
3.1 Introduction	35
3.2 Homodyne Detection	36
3.3 Quantum Noise and Quantum Limits	38
3.4 Heterodyne Detection	41
II NANOFIBER TRAPPED ATOMS	47
4 OPTICAL NANOFIBERS	49
4.1 Fabrication	50
4.2 Light Propagation	50
4.3 Interaction of Guided Modes with Atoms	55
4.4 Further Applications	61
5 DUAL-COLOR DIPOLE TRAP	63
5.1 Nanofiber Trapped Atoms as a Light-Matter Interface	63
5.2 Trap Configuration and Potential	65
5.3 Optical Setup	67
5.4 Trap Operation	69
5.5 Some Properties	70
5.6 Polarization Control and Alignment	72
5.7 Counting the Trapped Atoms	74
III AN ATOMIC MIRROR	77
6 BRAGG SCATTERING OFF A ONE-DIMENSIONAL ATOMIC CRYSTAL	79
6.1 Coherent Enhancement of Atomic Emission	80
6.2 Bragg Scattering in Optical Lattices	82
6.3 Bragg Scattering Off Nanofiber Trapped Atoms	84

6.4	Engineering a Bragg Superstructure	85
7	EXPLORING THE BRAGG SUPERSTRUCTURE	91
7.1	Towards High Reflection	91
7.2	Dynamics	97
7.3	Applications and Outlook	104
IV	TOWARDS THE SINGLE EXCITATION FOCK STATE	109
8	PRELIMINARY	111
8.1	Creating a Single Excitation State	111
8.2	Choice of Level Set	112
8.3	A Single Excitation in a Nanofiber Trapped Atomic Ensemble	114
8.4	Setup Requirements and Overview	121
9	PREPARATION	123
9.1	Optical Pumping	123
9.2	Microwave	127
9.3	Raman	137
9.4	Final Preparation Sequence	145
10	DETECTION	147
10.1	Filter Cavity	147
10.2	Volume Bragg Grating	153
10.3	Single Photon Detection	154
10.4	Expected State Purity	155
	CONCLUSION	161
11	OUTLOOK	163
11.1	Quantum State Preparation	163
11.2	Future Directions for Nanofiber Trapped Atoms	166
	Appendix	171
A	SUPPLEMENTAL MATERIAL ATOMIC MIRROR	173
A.1	Structuring Pulse Duration	173
A.2	Structuring Pulse Power	173
A.3	Effect of Probe Light Detuning on Dynamics	175
A.4	Transmission Signal Repeated Preparation	177
A.5	Atoms Do Not Heat Without Structuring	177
A.6	Detecting a Bragg reflection in a Few Shots	179
B	MODE MATCHING	181
C	SIMULATING THE VOLUME BRAGG GRATING	183
D	EXTERNAL CAVITY DIODE LASERS	185
D.1	Design	185
D.2	Frequency Stabilization	186
D.3	Test Setup	186
E	ELECTRONICS	189
E.1	SPCM Control Circuit	189

E.2 Lock Circuit	204
BIBLIOGRAPHY	205
LIST OF FIGURES	223
LIST OF TABLES	225
LISTINGS	225
LIST OF ACRONYMS	225
ACKNOWLEDGMENTS	229

PREFACE

When I first encountered optical nanofibers in the summer of 2008, the field was still in its infancy. Their fabrication had been mastered and first experiments with ultracold atoms had been performed, but the work towards a nanofiber trap for atoms was just beginning. I still remember how peculiar I thought a fiber “smaller than the wavelength of light” was – and frankly I felt it was a bit absurd that a group of grown adults would spend several years to fabricate such a thing, just to “put atoms on the outside”. Nevertheless, this short visit in the Rauschenbeutel group at the University of Mainz strengthened once more my decision to study Physics. Surely though, I thought to myself, I would spend my time with experiments more exciting and meaningful.

Little did I know.

Six years and many coincidences later I found myself in the basement of the Niels Bohr Institute in Copenhagen, staring at precisely one of these fibers, which had even been made in the very lab I had visited as a high school student. And contrary to then, I now began to understand that this little glass wire was full of exciting possibilities.

As my Master thesis project, I set out to create a single excitation state in a nanofiber trapped ensemble of ultracold cesium atoms. Such a truly quantum state had been observed for a little more than 40 atoms ([Haas et al., 2014](#)), and the goal now was to bring all of the about 2000 atoms in the nanofiber trap into this state. Shortly after I started, we learned that [McConnell et al. \(2015\)](#) had been successful in entangling almost 3000 Rubidium atoms in a more traditional cavity QED setup, which made us at best the runner-up, but also held the chance for us to demonstrate that nanofiber trapped atoms were at the very least a serious alternative – if not, perhaps, the superior platform.

At [QUANTOP](#), for more than a decade there had been a long-lasting effort to create “exotic” quantum states in a free space dipole trap (cf. [Oblak, 2010](#)). Together with the last student on this experiment, Stefan Lund Christensen, I began to port his PhD project – the experimental verification of the non-Gaussianity of a prepared single excitation state ([Christensen, 2014](#), [Christensen et al., 2014](#)) – to the new nanofiber platform, which had been in development at [QUANTOP](#) for about four years when I arrived (cf. [Béguin, 2015](#), [Sørensen, 2015](#)). After Stefan defended and left the group, I continued along these lines, working on the optical filtering system and detection electronics.

As it is often the case in experimental physics, surprising discoveries and technical difficulties had slowed down the work on the predecessor “Atomic Mirror” experiment occupying the nanofiber setup. Therefore I joined the at the time only remaining PhD student Heidi Lundgaard Sørensen in this

investigation of Bragg scattering from nanofiber trapped atoms, which resulted in [Sørensen et al. \(2015a\)](#) and became part of my thesis work. Over the course of this endeavour, we resolved many of the small issues with the nanofiber setup and worked towards more reliability and consistency.

With Jean-Baptiste Béguin back in the lab after his PhD defense, we finally set out to prepare the single excitation state. After fast progress on implementing a microwave source and optical pumping schemes, my time in Copenhagen slowly but surely came to an end.

So while the non-Gaussian nature of the single excitation state continues to remain hidden in the basement at Blegdamsvej, there is – as I hope to convey to the reader on the following pages – much reason to hope that its true colors will show within the next months.

INTRODUCTION

As is often the case for a thesis, “Characterization of Collective Spin States in Atomic Ensembles Trapped Around Tapered Nanofibers” is an accurate, but equally generic title which does not reveal much about the content. Before we jump in and for the next 150-or-so pages cover many experimental details, we would therefore like to give a broad overview of the things to come.

NANOFIBER TRAPPED ATOMS

An optical fiber with a diameter smaller than the wavelength of light it guides exhibits a large evanescent field, through which emitters like atoms can be coupled to the fiber’s guided mode. By sending two beams of far-detuned light with the right polarization configuration down the fiber, atoms can be trapped in the fiber’s vicinity (Le Kien et al., 2004, Vetsch et al., 2010). Since the evanescent field and the atoms’ position within it can be tailored precisely, the absorption per single atom can be maximized and high optical depths (ODs), i. e. an optically thick ensemble, can be achieved with only a few thousand atoms. Since the OD is the figure of merit e. g. for an atomic quantum memory (Hammerer et al., 2010), in the past years nanofiber trapped atoms have attracted significant interest. In addition to the low number of atoms necessary, the main advantage of a nanofiber trap compared to free-space dipole traps is that it is not limited by the Rayleigh length and that the coupling strength of the atoms to the light field is homogenous throughout the trap to a much better degree.

At QUANTOP, a nanofiber trap for cesium atoms was implemented starting in 2010 (Béguin, 2011, Béguin et al., 2014a, Béguin, 2015). In short, the nanofiber is placed in a vacuum chamber, where the trap created around it can be loaded from a cloud of ultracold atoms. The atoms can be interrogated by sending light through the fiber, either by performing spectroscopy or by detecting the phaseshift the atoms imprint on the light when it passes through. As we will show, the latter method is a very sensitive probe which allows for quantum non-demolition measurements.

With a nanofiber trap in place, there is a wide variety of experiments one can undertake. The two experiments covered in this thesis, which are quite different in nature, reflect this: The “atomic mirror” builds on the well-known phenomenon of Bragg reflections, which can readily be understood through classical physics, and our task is mainly to understand how such a structure can be created in the atoms around a nanofiber. The preparation and tomography of a single excitation state on the other hand is a well-defined goal and requires e. g. advanced methods of atomic state control and the ability to measure said state at the projection noise quantum limit. However, ultimately both experiments are steps towards the realization of a high-

fidelity quantum memory capable of storing and releasing arbitrary numbers of excitations.

ATOMIC MIRROR

At first sight a rather simple idea, resonantly structured atoms near photonic waveguides lead to interesting effects, such as superradiance (Goban et al., 2015) or, as we present here, coherent enhancement of emission in the counterpropagating direction to a weak probe beam, a special case of Bragg reflections. Furthermore, there is by now a wealth of proposals for applications of such systems, ranging from the preparation of atomic mirror resonators suitable for cavity QED experiments (Chang et al., 2012) over the deterministic creation of arbitrary photonic number states (González-Tudela et al., 2015) to quantum simulation of many-body systems (Douglas et al., 2015).

While Bragg scattering is an effect well-studied in optical lattices (cf. Weidemüller et al., 1995, Birkl et al., 1995, Slama et al., 2005a, Schilke et al., 2011, and references therein), in the case of atoms in a caterpillar-type nanofiber trap, the main challenge to overcome is that the spacing d of atoms in the lattice is unsuitable for Bragg reflections, which requires $2d = n \cdot \lambda$, where λ is the probe wavelength (necessarily coinciding with an atomic resonance) and n an integer. Therefore, up until the work conducted as part of this thesis, only reflection from unstructured ensembles had been observed (Goban et al., 2012, Reitz et al., 2014). To overcome the unsuitable spacing of nanofiber trap sites, one needs to find a way to imprint a superstructure on the atoms, i. e. to create a Bragg lattice by selecting correctly placed atoms within the trap lattice. To this end, we use a standing wave light pulse to optically pump atoms into dark and bright states according to their position along the nanofiber.

With this preparation method implemented, we then investigate how the numerous accessible parameters have to be tuned to achieve maximum reflection. This constitutes the results awaiting publication as Sørensen et al. (2015a). For the prepared Bragg resonant superstructure to be suitable for the applications mentioned in the first paragraph of this section, it needs to prevail for a sufficient amount of time. We therefore extensively study the dynamics and investigate whether and how the superstructure's lifetime can be enhanced.

SINGLE EXCITATION STATE

While nanofiber trapped atoms are a prime candidate to serve as a quantum memory in a future quantum network,¹ so far only classical states have been stored in such a system (Sayrin et al., 2015, Gouraud et al., 2015). In general, the verification of the storage of a non-Gaussian state – a state which loosely speaking is “so very much quantum” that its quantum phase space probability density given by the Wigner function becomes negative – in an ensemble

¹ We will make some remarks regarding this commonly made claim in section 11.2.4.

of more than a few ten atoms (Haas et al., 2014) was achieved only recently (McConnell et al., 2015).

The quest for a single excitation state (SES) – a state where all but one atom are in the state $|\downarrow\rangle$ while the remaining one is in $|\uparrow\rangle$, which is the analogue to a photonic Fock state (number state) – builds on a long history at QUANTOP, where over the years a number of quantum states was prepared in a cloud of 10^5 atoms in a free-space dipole trap and ultimately spin-squeezing and measurement at the projection noise limit was demonstrated (Petrov, 2006, Windpassinger, 2008, Oblak, 2010, Christensen, 2014). However, due to excess noise and inherent detection inefficiencies (Christensen, 2014, sec. 8.4) the achievable state purity of the SES was not high enough to verify its non-Gaussianity.

As we highlighted above, the nanofiber trap offers the same optical depth with only a few thousand atoms, which pushes down classical noise. Furthermore, the complex polarization properties of the nanofiber’s evanescent field lead to a directionality of spontaneous emission, which greatly enhances the attainable state purity. In this thesis, building on Christensen et al. (2013), Christensen (2014), we work out a quite detailed proposal for the preparation, detection, and tomography of an SES in a nanofiber trapped ensemble of atoms.

Using the protocol by Duan et al. (2001a), we store a single excitation by sending light through the atomic ensemble and detecting a single photon which heralds that the SES has been created. Subsequently, the tomography is performed by interfering the two states using a microwave rotation and measuring the population difference between $|\uparrow\rangle$ and $|\downarrow\rangle$ using a two-color heterodyne detection scheme pioneered at QUANTOP (Saffman et al., 2009, Louchet-Chauvet et al., 2010, Béguin et al., 2014a). This reveals the SES’s non-Gaussian signature and allows for the reconstruction of the state’s Wigner function.

We emphasize that this is a hybrid approach, combining discrete photon counting for state preparation and continuous heterodyne detection for its tomography. If successful, the experiment we work towards in this thesis will be the first demonstration of an unambiguously non-classical state in a nanofiber trapped ensemble – or, for that matter, in any atomic ensemble coupled to a photonic waveguide.

OUTLINE

This thesis spans a wide range of physics, from fundamental quantum mechanics over semi-classical models of Nature to technical applications. At the same time, the space available is limited, so a selection had to be made. In all parts where the covered topics are treated elsewhere in much greater detail, a self-contained summary geared towards experiment is given. Everywhere else, the focus is placed on genuinely new experimental results and the documentation of the setup and methods used to obtain them.

- The first part of the thesis reviews the foundations of the experiments, the quantum theory of light and atoms. We introduce the quantum phase space, show how quasi-probability distributions are a signature of non-classicality and how all this relates to collective spin states in atomic ensembles. Furthermore, we cover the trapping and cooling of atoms. We also give a short introduction to quantum measurement and introduce the heterodyne detection scheme employed throughout this thesis.
- The second part is devoted entirely to our experimental platform, the tapered optical nanofiber. We describe its fabrication, optical properties, and the trapping of atomic ensembles in its vicinity. A focus is placed on spontaneous emission into the guided mode, where we derive the chirality of this process.
- In the third part, we present the first of the two big experiments performed for this thesis: the preparation of Bragg superstructures in the trapped atomic ensemble and the investigation of coherent reflections off these “atomic mirrors”. We place an emphasis on the investigation into the dynamics and limited lifetime of the observed reflections and share some ideas for future directions and applications.
- The fourth part finally concerns itself with the experiment at the heart of this thesis: the experimental realization of an “atomic Fock state” by means of detecting a heralding photon and the measurement of its Wigner function to prove its non-Gaussian nature. Here, we incorporate the optical properties of the nanofiber into the existing proposal. Then we extensively discuss the preparation of the initial state and the development and properties of the heralding photon detection setup.
- We conclude this thesis with an outlook on the next steps in the quest for the single excitation state and possible goals beyond. We also briefly discuss future paths to take on the nanofiber platform.
- The appendices contain supplemental material, mainly technical descriptions, additional figures, and calculations which are not relevant to the main text, but might serve as a reference in the future.

NOTE TO THE READER

While certainly its main and formal purpose, this thesis was not only written as one of the requirements necessary for the author to graduate with a Master’s degree. I therefore want to make a few remarks on the structure and provide suggestions for readers who are not members of the examination committee.

Since the two experiments described in this thesis have almost nothing but the nanofiber platform in common, the overall structure of the thesis is built around the single excitation state (SES) experiment, which also reflects its complexity and amount of hours spent on its development. After this decision was finalized, there were many discussions on where to place the atomic mirror experiment within this framework, but no entirely satisfactory solution could be found. It now appears at the point in the thesis where all concepts and tools necessary to understand it have been introduced. Since the first part covers many concepts only relevant to the SES experiment, a reader only interested in the atomic mirror is suggested to start with chapter 4 and to refer back to specific sections of part I as it becomes necessary for them. Vice versa, a reader only interested in the SES can skip part III entirely.

While the very basic idea of nanofiber trapped atoms can be understood within a few minutes, the experiments carried out at QUANTOP combine a wealth of theoretical concepts and experimental techniques. While each of these can be grasped with the knowledge obtained from coursework and entry-level literature is available for most of them, the true barrier to overcome is the combination and interplay which seems to be oh so easy to navigate for the more senior people on the experiment. While there is now a monumental PhD thesis (Béguin, 2015) detailing every step in the development of the nanofiber experiment at QUANTOP and at the time of writing a second one was underway shedding much more light on the atomic mirror than was possible in this work (Sørensen, 2015), there is still a lack of introductory material which is accessible to a Master student beginning research for their thesis. I therefore tried to make this thesis the guidebook I would have liked to read when I started. This mainly means that I made an effort to rather spell out an argument explicitly than assuming the reader would see it between the lines, while at the same time not meandering down every possible sidetrack. Wherever possible, I point to material I found especially useful when first encountering a topic.

It will be for my successors on this wonderful experiment to decide whether I succeeded.

Part I

FOUNDATIONS

We set the stage with a review of the underlying physical models, concepts, and experimental tools. To this end, we begin with an overview of the quantum mechanical description of the electromagnetic field. In doing so, we introduce fundamental quantum states, review the phase space formulation of quantum optics, and present a criterium for non-Gaussianity. We then turn to the structure of atoms and their interaction with light, subsequently giving an overview of our setup for atom trapping and cooling. Finally, we cover quantum measurement and noise, thereby introducing our two-color heterodyne detection scheme.

*Was ist nun aber dieses Etwas, das sich in dem leeren Weltenraum oder in der atmosphärischen Luft mit der ungeheuren Geschwindigkeit von 300 000 km in der Sekunde nach allen Seiten ausbreitet?*¹

— *Max Planck: Das Wesen des Lichts*

The nature of light has concerned, puzzled and excited scientists over many millennia. Especially the 20th century has seen many leaps and revolutions in the understanding of its nature, starting with Planck's explanation of blackbody radiation and Einstein's revival of the previously dismissed idea that light is a particle.

Although a highly interesting subject in its own right, in the experiments described in this thesis light is mostly used as a tool. Be it to cool and trap atoms, be it to prepare and probe atomic states. Perhaps most importantly, light will appear again and again as carrier of (quantum) information.

This chapter is no different: In presenting a short summary of a quantum theory of light, we introduce quantum states and the phase space formulation of quantum mechanics. In later chapters we will transfer the developed concepts to atomic systems – to then describe ways to extract the information contained in these systems by sending light through them. A much more complete and thorough treatment of the quantum theory of light can be found e. g. in the textbooks by [Gerry and Knight \(2005\)](#) and [Walls and Milburn \(2007\)](#).

1.1 PHOTONS

We will adopt the constructive approach of [Leonhardt \(1997\)](#) and start by filling the Universe with spatio-temporal modes

$$u(x, t) = \epsilon e^{i(kx - \omega t)}, \quad (1.1)$$

where ϵ is the polarization vector, $k = \omega/c$ with c the speed of light is the wave vector, and ω the angular frequency. Each of these modes can be excited, and the degree of excitation is given by its amplitude \hat{a} . Classically, this amplitude is a complex number α , with $|\alpha|$ the magnitude and $\arg(\alpha)$ the phase of the oscillation. Singling out a mode, we can then postulate that

$$\hat{E} = u^*(x, t)\hat{a} + u(x, t)\hat{a}^\dagger \quad (1.2)$$

¹ But what is this Something which spreads into all directions in the empty space or the atmospheric air with the monstrous velocity of 300 000 kilometers per second?

is the strength of the electric field of the light field in this mode, and that \hat{a} is the bosonic annihilation operator, i. e.

$$[\hat{a}, \hat{a}^\dagger] = 1, \quad (1.3)$$

where $[a, b] = [a, b]_- \equiv ab - ba$ is the commutator. Then the number operator

$$\hat{n} = \hat{a}^\dagger \hat{a} \quad (1.4)$$

gives the number of excitations – *photons* – in the mode, the quantum analogue to the light intensity $I = |\alpha|^2$.

1.2 QUADRATURE OPERATORS AND PHASE SPACE

What we have presented so far is a representation of light in a single mode as excitations of a quantum mechanical harmonic oscillator. Thus, we can define the two quadrature operators

$$\hat{q} = \frac{1}{\sqrt{2}}(\hat{a} + \hat{a}^\dagger) \text{ and } \hat{p} = \frac{i}{\sqrt{2}}(\hat{a} - \hat{a}^\dagger). \quad (1.5)$$

\hat{q} (\hat{p}) is the real (complex) part of \hat{a} , i. e.

$$\hat{a} = \frac{1}{\sqrt{2}}(\hat{q} + i\hat{p}) \text{ and } \hat{a}^\dagger = \frac{1}{\sqrt{2}}(\hat{q} - i\hat{p}). \quad (1.6)$$

Although it can be instructive to think of \hat{q} and \hat{p} in terms of position and momentum of a harmonic oscillator ($[\hat{q}, \hat{p}] = i\hbar$), they are not properties of the photons, but the mode. From the experimenter's point of view, \hat{q} (\hat{p}) is the in-phase (out-of-phase) component of the electric oscillation, relative to an arbitrary reference phase φ_{ref} .

Again in analogy to classical mechanics, the total energy of the mode is

$$\hat{H} = \frac{\hat{q}^2 + \hat{p}^2}{2} = \hbar\omega(\hat{n} + \frac{1}{2}), \quad (1.7)$$

where $1/2\hbar\omega = \hat{H}_{\text{vac}}$ is the vacuum energy, i. e. the mode's energy when no photon is present.

1.3 QUANTUM STATES

A quantum state $|\Psi\rangle$ describes a system completely. Its time evolution is governed by Schrödinger's equation:

$$i\hbar\partial_t |\Psi\rangle = \hat{H} |\Psi\rangle. \quad (1.8)$$

We are free to choose a basis $|\Psi_j\rangle$, such that each

$$|\Psi\rangle = \sum_{j=0}^{\infty} c_j |\Psi_j\rangle, \quad (1.9)$$

with c_j a complex number. We only require that the states $|\Psi_j\rangle$ form a complete and orthonormal basis, i. e.

$$\sum_{j=0}^{\infty} |\Psi_j\rangle \langle \Psi_j| = 1 \text{ and } \langle \Psi_j | \Psi_k \rangle = \delta_{jk}. \quad (1.10)$$

1.3.1 Fock States

One fairly obvious and natural choice to describe a mode is to count the photons it contains. These quantum states of light are called Fock states (or, alternatively, number states) and are the eigenstates of the number operator \hat{n} :

$$\hat{n} |n\rangle = n |n\rangle. \quad (1.11)$$

It comes to no surprise that if $|n\rangle$ is an eigenstate of \hat{n} , that

$$\hat{a} |n\rangle = \sqrt{n} |n-1\rangle \text{ and} \quad (1.12)$$

$$\hat{a}^\dagger |n\rangle = \sqrt{n+1} |n+1\rangle \quad (1.13)$$

are eigenstates as well. Further, it is conceptually clear that one has to require

$$\hat{a} |0\rangle = 0, \quad (1.14)$$

i. e. no less than 0 photons can occupy a mode at a given time. As [Leonhardt \(1997\)](#) demonstrates, this is necessary for the Fock states to form a complete and orthonormal basis.

Although straightforward to construct, Fock states are said to be “truly quantum” (cf. sec. 1.5): Their energy spectrum is given directly by (1.7), and the energy difference between two states $|n\rangle$ and $|m\rangle$ is $\Delta E_{nm} = \hbar\omega$, the energy of a single photon.

1.3.2 Coherent States

A very different class of states are coherent states, which are the eigenstates of the annihilation operator:

$$\hat{a} |\alpha\rangle = \alpha |\alpha\rangle. \quad (1.15)$$

Since \hat{a} is clearly not Hermitian, α is a complex number and can be directly identified with the classical field amplitude. Relating this back to section 1.2, we find that we can decompose each α as $\alpha = \sqrt{2}(q + ip)$ ([Leonhardt, 1997](#)).

Coherent states are minimum uncertainty states. To see this, we calculate the variances of the phase space operators and find that – independent of α –

$$(\Delta\hat{q})^2 = \langle \alpha | \hat{q}^2 | \alpha \rangle - \langle \alpha | \hat{q} | \alpha \rangle^2 = \frac{1}{2} = (\Delta\hat{p})^2, \quad (1.16)$$

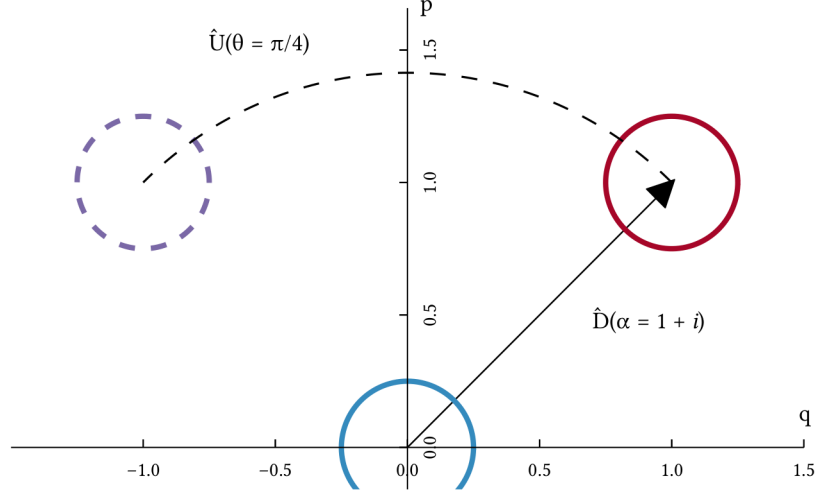


Figure 1.1: Phase space representation of coherent states, which closely resembles that of a harmonic oscillator in classical phase space.

As discussed in the main text, the quadrature uncertainty of a coherent state (red) is identical to that of the vacuum state (blue), and coherent states are created by applying the displacement operator $\hat{D}(\alpha) \equiv \exp(\alpha \hat{a}^\dagger - \alpha^* \hat{a})$ to the vacuum (Walls and Milburn, 2007, sec. 2.3).

We also illustrate the action of the phase shifting operator $\hat{U}(\theta) \equiv \exp(-i\theta \hat{n})$ (Leonhardt, 1997, sec. 2.1).

which exactly fulfil Heisenberg's uncertainty relation

$$(\Delta \hat{q})^2 \cdot (\Delta \hat{p})^2 \geq \frac{1}{4}. \quad (1.17)$$

This is a feature coherent states share with the vacuum state $|0\rangle$ (cf. eq. (1.7); in fact, since $\hat{a}|0\rangle = 0$, $|0\rangle$ is itself a coherent state), and indeed one can construct coherent states by “displacing” the vacuum (fig. 1.1).

Coherent states can be represented in the Fock basis as

$$|\alpha\rangle = e^{-\frac{1}{2}|\alpha|^2} \sum_{n=0}^{\infty} \frac{\alpha^n}{\sqrt{n!}} |n\rangle, \quad (1.18)$$

from which it is straightforward to find that the probability to find n photons in the mode is

$$P(n) = |\langle n|\alpha\rangle|^2 = \frac{|\alpha|^{2n}}{n!} e^{-|\alpha|^2}. \quad (1.19)$$

This is a Poissonian distribution ($\langle P(n) \rangle = \text{var}(P(n)) = |\alpha|^2$). If one measures the intensity of a coherent state on a detector, at any instant in time one draws a sample of $P(n)$, i. e. there are fluctuations Δn – the so-called *shot noise* – around the mean photon number $\bar{n} = \langle \alpha | \hat{n} | \alpha \rangle$. We see that for large α as one typically encounters in the laboratory, \bar{n} is very large and $\Delta n / \bar{n} = 1 / \sqrt{\bar{n}} \approx 0$. E.g. a laser emitting at $\lambda = 852$ nm with a power of

1 mW has a mean photon flux $\bar{n} \approx 4$ PHz, leading to relative number fluctuation on the order of 10^{-8} . Therefore, for strong coherent light we can treat α as a classical quantity. In that sense, coherent states are “the most classical” states (cf. sec. 1.5).

The conjugate to the uncertainty in photon number is the phase uncertainty $(\Delta\theta)^2$. Without proof (cf. Clerk et al. (2010b, app. G) or Fox (2006, sec. 7.6) for derivations) we state that for a coherent state

$$(\Delta\theta)^2 = \frac{1}{4\bar{n}}, \quad (1.20)$$

so the fundamental quantum uncertainty relation

$$\Delta n \Delta\theta \geq \frac{1}{2} \quad (1.21)$$

is fulfilled exactly. This is the first example of a quantum limit, which cannot be surpassed and has severe consequences for (interferometric) quantum measurements (cf. sec. 3.3).

1.4 QUASI-PROBABILITY DISTRIBUTIONS

Often, one is not interested in the precise state of a system, but merely the expectation values of a given operator. Thus it is only natural to wonder whether one can find a probability distribution which contains (at least) enough information about a quantum state to serve this purpose.

Similar to Gerry and Knight (2005), we start with the definition of the density operator

$$\hat{\rho} = \sum_j p_j |\Psi_j\rangle \langle \Psi_j|, \text{ with } \text{Tr}(\hat{\rho}) = 1. \quad (1.22)$$

As above, $|\Psi_j\rangle$ form a complete basis. Then,

$$\langle \hat{O} \rangle = \text{Tr}(\hat{O}\hat{\rho}) = \sum_j p_j \langle \Psi_j | \hat{O} | \Psi_j \rangle \quad (1.23)$$

is the expectation value of an operator \hat{O} . We can express every density operator defined by (1.22) in the Fock basis:

$$\hat{\rho} = \sum_n \sum_m |m\rangle \langle m | \hat{\rho} | n \rangle \langle n| = \sum_n \sum_m \rho_{mn} |m\rangle \langle n|. \quad (1.24)$$

Thus, all ρ_{mn} together contain complete information on the state. While this is a useful representation when only a few $\rho_{mn} \neq 0$, especially for large systems one would prefer a continuous function.

Then, in light of the discussion regarding coherent states above, it suggests itself to find $P(\alpha)$ such that

$$\hat{\rho} = \int P(\alpha) |\alpha\rangle \langle \alpha| d^2\alpha, \quad (1.25)$$

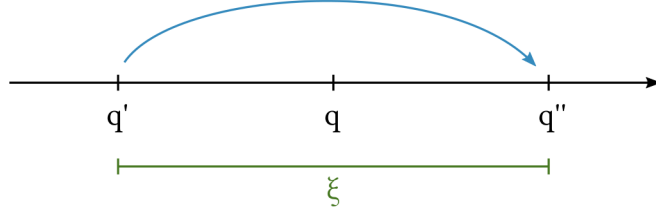


Figure 1.2: Illustration of the “jump start” given by [Schleich \(2001\)](#).

where like a probability distribution $P(\alpha)$, known as the Glauber-Sudarshan P -function, attributes a weight to each $|\alpha\rangle$. Indeed, it is straightforward to use (1.22) and show that

$$\text{Tr}(\hat{\rho}) = \int P(\alpha) d^2\alpha = 1. \quad (1.26)$$

If we remind ourselves that we can decompose each α as $\alpha = 1/\sqrt{2}(q + ip)$, we see that $P(\alpha)$ lives on the quantum phase space and is the first example of a so-called quasi-probability distribution (QPD). This term stems from the fact that $P(\alpha)$ is not a classical probability distribution for all states, e. g. it can become more singular than a δ -function. In general $P(\alpha)$ cannot even be expressed as a function. While this can be seen as a consequence of the fact that the coherent states are overcomplete (i. e. the second part of equation (1.10) is not fulfilled), from a more fundamental point of view it comes as no surprise that it is impossible to express quantum states in terms of classical amplitudes ([Leonhardt, 1997](#), [Gerry and Knight, 2005](#)).

1.4.1 Wigner Function

First introduced by [Wigner \(1932\)](#), the Wigner function $W(q, p)$ is a QPD similar to the Glauber-Sudarshan P -function we just encountered. Unlike $P(\alpha)$, the Wigner function as such is well-behaved and can be reconstructed from experimental data ([Gerry and Knight, 2005](#), [Leonhardt, 1997](#), [Kiesel, 2011](#)).

We introduce the Wigner function using the approach given by [Schleich \(2001\)](#), which sheds some light on its physical interpretation. Imagine a particle whose state is described by the density operator $\hat{\rho}$. Then we can (at least in principle) calculate

$$\langle q'' | \hat{\rho} | q' \rangle, \quad (1.27)$$

the probability for the particle to “jump” from a position q' to q'' (fig. 1.2). With $\xi = q'' - q'$

$$\left\langle q + \frac{1}{2}\xi \left| \hat{\rho} \right| q - \frac{1}{2}\xi \right\rangle \quad (1.28)$$

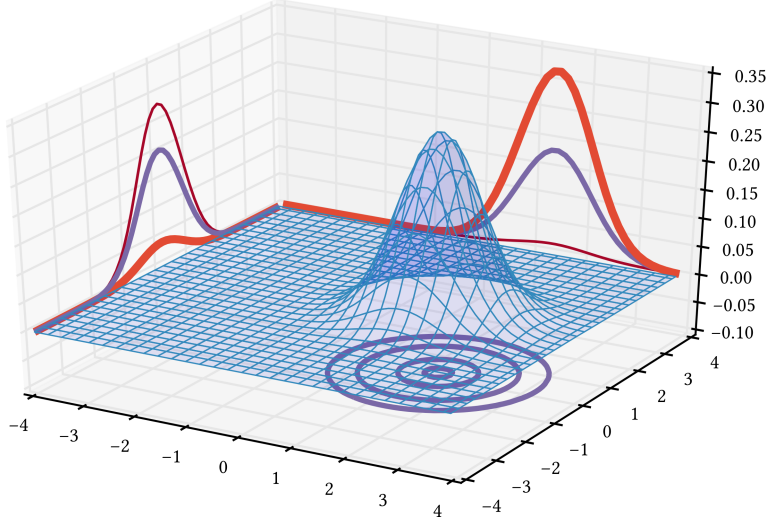


Figure 1.3: Plot of the Wigner function of $|\alpha = 1\rangle$, which resembles a Gaussian displaced from the origin (cf. fig. 1.1).

where q is the center of the jump. To introduce momentum p , we perform a Fourier transform² with respect to the jump length ξ and obtain the Wigner function

$$W(q, p) = \frac{1}{2\pi\hbar} \int_{-\infty}^{+\infty} d\xi \exp\left(-\frac{i}{\hbar} p\xi\right) \left\langle q + \frac{1}{2}\xi \left| \hat{\rho} \right| q - \frac{1}{2}\xi \right\rangle, \quad (1.29)$$

where the normalization factor was chosen such that

$$\int_{-\infty}^{+\infty} dq \int_{-\infty}^{+\infty} dp W(q, p) = 1. \quad (1.30)$$

It is straightforward to calculate that the integral over one variable gives a probability distribution for the conjugate:

$$\int_{-\infty}^{+\infty} dq W(q, p) = \langle p | \hat{\rho} | p \rangle \quad (1.31)$$

$$\int_{-\infty}^{+\infty} dp W(q, p) = \langle q | \hat{\rho} | q \rangle. \quad (1.32)$$

Further, just as we expect for a probability distribution,

$$\langle \hat{A} \rangle = \text{Tr}(\hat{\rho}\hat{A}) = \int_{-\infty}^{+\infty} dq \int_{-\infty}^{+\infty} dp W(q, p) A(q, p) \quad (1.33)$$

gives the expectation value for an operator \hat{A} given the density operator $\hat{\rho}$ (\hat{A} has to be Weyl-Wigner ordered, for details see [Schleich \(2001, sec. 3.7\)](#)).

While the Wigner function for a coherent state $|\alpha = 1\rangle$ (fig. 1.3) is, as one would expect, of Gaussian shape and displaced from the origin (cf. fig. 1.1),

² It is well known that position and momentum wavefunctions are connected through $\Psi(x) = (2\pi\hbar)^{-1/2} \int_{-\infty}^{+\infty} dp \Psi(p) \exp(ixp/\hbar)$.

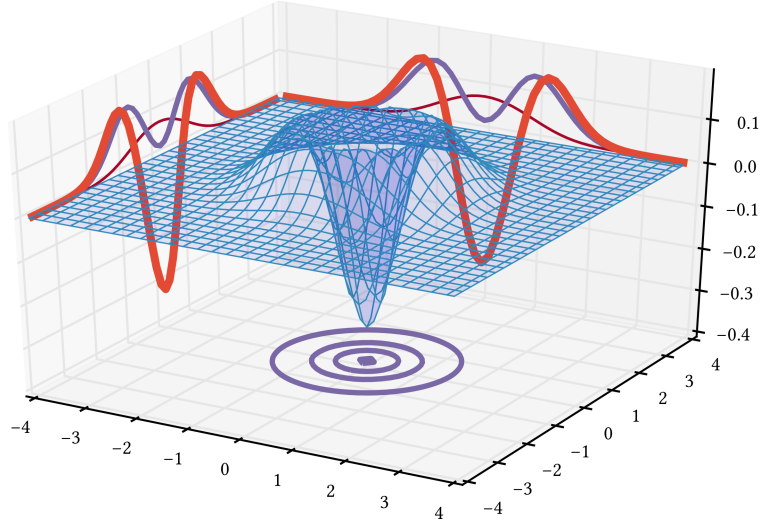


Figure 1.4: Plot of the Wigner function of $|n = 1\rangle$, which takes on negative values around $(q = 0, p = 0)$.

We emphasize a practical implication of the rotational symmetry around the origin: One can recover the full Wigner function if one knows its value along a straight line through phase space which contains the origin.

the Wigner function of the first Fock state shown in figure 1.4 displays a peculiar feature: For much of its footprint, its value is below zero.

To understand when a negative value appears, we state without proof that (Schleich, 2001)

$$\text{Tr}(\hat{\rho}_1 \hat{\rho}_2) = 2\pi\hbar \int_{-\infty}^{+\infty} dq \int_{-\infty}^{+\infty} dp W_{\hat{\rho}_1}(q, p) W_{\hat{\rho}_2}(q, p) \quad (1.34)$$

where $W_{\hat{\rho}_i}(q, p)$ is the Wigner function for the density operator $\hat{\rho}_i$. If $\text{Tr}(\hat{\rho}_1 \hat{\rho}_2) = 0$, which is the case e. g. for the density operators of two different Fock states, the integral is zero and hence at least one of the Wigner functions has to take on a negative value somewhere on (q, p) . In the next section, we show how this can be generalized to find a measure for the “quantumness” of a state.

1.5 NON-CLASSICALITY

Above, we have called Fock states “truly quantum” and coherent states “the most classical” without giving a formal definition. In the previous sections, we have seen that the quasi-probability distributions (QPDs) which describe quantum states in phase space differ remarkably from classical probability distributions. We will now show how their features can be used to distinguish between classical and quantum states.

In figure 1.4 we have seen that the Wigner function of a Fock state – which is certainly not a classical state – is negative for some points (q, p) , which is not compatible with a classical probability distribution. However, it is positive everywhere for a coherent state. Thus, while it is a sufficient criterion,

negativity of the Wigner function cannot be a necessary condition for a non-classical state.

According to the theorem by Hudson (1974), Soto and Claverie (1983), for the Wigner function of a pure state to be non-negative everywhere, it is both necessary and sufficient that the wavefunction is of the form

$$|\Psi(q)\rangle = \exp\left(-\frac{1}{2}(aq^2 + 2bq + c)\right), \quad (1.35)$$

i. e. the state is Gaussian. We note that it automatically follows that

$$P(q) = |\langle\Psi(q) | \Psi(q)\rangle|^2 = \exp(-\operatorname{Re}(a)q^2 + 2\operatorname{Re}(b)q + \operatorname{Re}(c)) \quad (1.36)$$

is Gaussian as well and the same is true for the Wigner function (Soto and Claverie, 1983). The example we already encountered is that of a coherent state.³ We can therefore formalize our notion of “truly quantum” and “classical-like” states by dividing quantum states into Gaussian and non-Gaussian ones.

As we have seen, a negative Wigner function is an unambiguous signature of non-Gaussianity. Thus, if one can experimentally demonstrate that the Wigner function for the quantum state of an atomic ensemble is negative for at least one single point of phase space, this is proof that the ensemble is in a non-Gaussian state. To build and carry out such an experiment is precisely the objective of the experiment described in this thesis.

³ Position and momentum wavefunctions for coherent states are e. g. given in Gerry and Knight (2005, p. 50).

With light and quantum states introduced, we now turn to the system we study in this thesis: ensembles of ultracold atoms.

We start this chapter by introducing the electronic structure of the D line of cesium. Then we simplify our discussion to two level systems, study their radiative interaction with light, and demonstrate how we can view them as spin-1/2 systems. Afterwards, we combine large numbers of these systems to form a single collective spin state. In the last section we take a first step towards experiment and describe how by exploiting its level structure cesium can be cooled and trapped using light and magnetic fields, thereby introducing a first part of our experimental apparatus.

2.1 MULTI-LEVEL ATOMS

In this section we briefly describe the structure of the so-called D line of cesium as depicted in figure 2.1. In doing so, we establish our notation and provide the basis for a treatment of atomic transitions. A complete summary of all relevant quantities can be found in [Steck \(2010\)](#).

2.1.1 Structure of Cesium

As an alkali atom, cesium has only one electron in its valence shell, which in the groundstate occupies the orbital $6^2S_{1/2}$.¹ The D line consists of the two transitions $6^2S_{1/2} \rightarrow 6^2P_{1/2}$ (D1) and $6^2S_{1/2} \rightarrow 6^2P_{3/2}$ (D2).

Due to spin-orbit-coupling – in simple terms, the magnetic field induced by the charged nucleus orbiting the electron in the latter’s reference frame – the 6^2P state’s degeneracy is lifted, resulting in the fine structure splitting. For the D line of cesium, this splitting amounts to 42 nm, which can easily be resolved optically. For the remainder of the thesis, we only consider the D2 line as the D1 line does not possess a closed transition, rendering it unsuitable for laser cooling (cf. sec. 2.4.2) and probing (cf. sec. 3.4).

Taking into account the interaction of the magnetic field induced by the electron with the nuclear spin $I = 7/2$, we obtain the hyperfine structure labeled by $F = |\mathbf{J} + \mathbf{I}|$. While the groundstate splits into $F = 3$ and $F = 4$, the excited state splits into $F = 2, 3, 4, 5$. Due to the vectorial nature of \mathbf{J} and \mathbf{I} , each hyperfine level contains $2F + 1$ magnetic sublevels labeled $m_F = -F, \dots, -1, 0, 1, \dots, F$. Their degeneracy can be lifted by an external

¹ In the commonly used notation $n^{2S+1}X_J$, n is the main quantum number, the superscript denotes the multiplicity $2S + 1$ with $S = 1/2$ the electron’s spin (i. e. there are a maximum of 2 fine structure states), $X = S, P, D, \dots$ denotes the orbital with angular momentum $L = 0, 1, 2, \dots$ and $J = |\mathbf{S} + \mathbf{L}|$ is the total angular momentum.

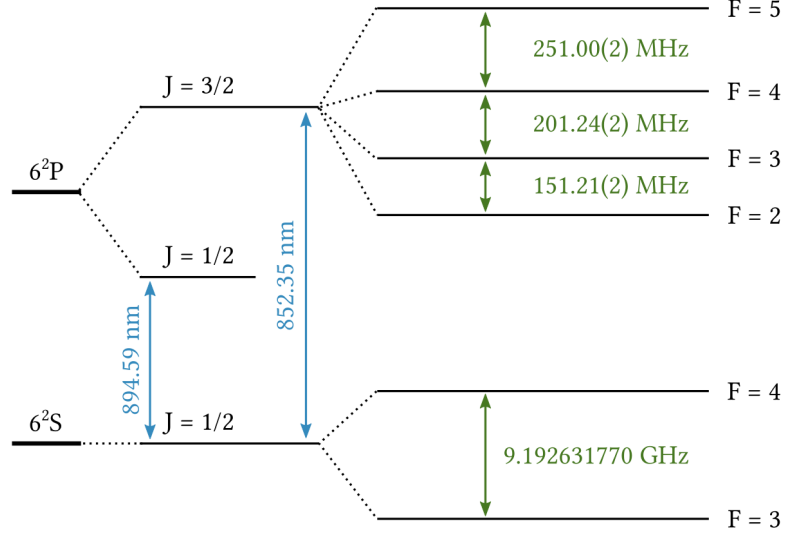


Figure 2.1: Structure of the D line of cesium as discussed in the main text. The hyperfine structure of $6^2S_{1/2}$ and $6^2S_{1/2} \rightarrow 6^2P_{3/2}$ (D2 line) are shown in full. Data from Steck (2010).

magnetic bias field which is commonly known as the Zeeman effect lending the name “Zeeman levels” (cf. sec. 9.2.3).

2.1.2 Interaction with Radiation

In the context of this thesis we are interested in the interaction of cesium atoms with a radius $r_{\text{atom}} \approx 2.7 \text{ \AA}$ (Steck, 2010) with light in the microwave and optical domain. Since $\lambda \gg r_{\text{atom}}$, the field will be uniform at the position of the atom, which we can therefore treat as a dipole (Gerry and Knight, 2005).

Adopting the dipole approximation and denoting the levels (sublevels) of $6^2P_{3/2}$ as $F' (m'_F)$, we have (Wigner-Eckart Theorem)

$$\langle F m_F | d_q | F' m'_F \rangle = \langle F || \mathbf{d} || F' \rangle (-1)^{F'-1+m_F} \sqrt{2F+1} \begin{pmatrix} F' & 1 & F \\ m'_F & q & -m_F \end{pmatrix}, \quad (2.1)$$

where $q = 0, \pm 1$ labels the component of \mathbf{d} in the spherical basis

$$\mathbf{e}_{\pm 1} = \frac{\mp (\mathbf{e}_x \pm i \mathbf{e}_y)}{\sqrt{2}}, \quad \mathbf{e}_0 = \mathbf{e}_z, \quad \mathbf{e}_q \cdot \mathbf{e}_{q'} = \delta_{qq'} \quad (2.2)$$

and the braced part is a Wigner $3j$ -symbol. We note that only if $m'_F = m_F + q$ the dipole matrix element is non-vanishing and a transition exists. We will term transitions where $m_F = m'_F$ π -transitions driven by linearly polarized light, i. e. light not carrying spin angular momentum, and those where $m'_F = m_F \pm 1$ as σ_{\pm} -transitions driven by circularly polarized light.

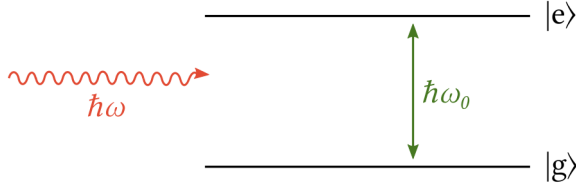


Figure 2.2: A two-level system comprised of a ground state $|g\rangle$ and an excited state $|e\rangle$ is the simplest model of an atom.

We note that

$$\sum_{q, F'} |\langle F(m'_F + q) | d_q | F'm'_F \rangle|^2 = \frac{2J+1}{2J'+1} |\langle J || \mathbf{d} || J' \rangle| \quad (2.3)$$

is independent of the choice of m'_F , therefore all excited state sublevels decay with the same rate $\Gamma = 2\pi \cdot 5.22 \text{ MHz}$ (Steck, 2010) and in the absence of a Zeeman sublevel resolving magnetic bias field we can treat $|F\rangle \rightarrow |F'\rangle$ as a transition between two levels. From

$$\langle F || \mathbf{d} || F' \rangle = \langle J || \mathbf{d} || J' \rangle (-1)^{F'+J+1+I} \sqrt{(2F'+1)(2J+1)} \begin{Bmatrix} J & J' & 1 \\ F' & F & I \end{Bmatrix}, \quad (2.4)$$

where the braced part is a Wigner $6j$ -symbol, we see that $\langle J || \mathbf{d} || J' \rangle$ is a common factor of all matrix elements on a given line, i. e.

$$\langle F m_F | d_q | F' m'_F \rangle = \langle J || \mathbf{d} || J' \rangle \cdot K \quad (2.5)$$

where K is a constant obtained from evaluating equations (2.1) and (2.4). The values for K can be found in Steck (2010, p. 18–19).

As a consequence of (2.3) and (2.5) we can – as long as coherences between sublevels are negligible – treat decays of excited state sublevels in a simple rate equation picture, where the decay rate is given by Γ and the branching ratio into different groundstate sublevels can be calculated from the K value of the respective transition.

2.2 TWO-LEVEL ATOMS

For a full description of the cesium D2 line, we need to take into account the population in 48 sublevels as well as the coherences between each pair of them. In virtually all situations we encounter in the context of this thesis where we need to perform calculations, however, we find that only two sublevels exhibit an appreciable population probability. If both the population probability of all other sublevels vanishes and significant coherences only appear between the two sublevels in question, we can approximate them as an atom with only two (non-degenerate) levels.

The Hamiltonian of such a system is

$$\hat{H}_a = E_g |g\rangle \langle g| + E_e |e\rangle \langle e|, \quad (2.6)$$

where $|g\rangle$ ($|e\rangle$) is the ground (excited) state and $E_e - E_g = \hbar\omega_0$ with ω_0 the transition frequency is their energy difference. Each state's wavefunction is given by

$$\Psi_n(\mathbf{r}, t) = \psi_n(\mathbf{r}) e^{-iE_n t/\hbar}, \quad (2.7)$$

where the spatial wavefunctions $\psi_1(\mathbf{r}) \equiv |g\rangle$ and $\psi_2(\mathbf{r}) \equiv |e\rangle$, so that the full atomic wavefunction reads

$$|\Psi(\mathbf{r}, t)\rangle = c_g(t) |g\rangle e^{-iE_g t/\hbar} + c_e(t) |e\rangle e^{-iE_e t/\hbar} \quad (2.8)$$

with $|c_g(t)|^2 + |c_e(t)|^2 = 1$.

2.2.1 Interaction with Radiation

The interaction Hamiltonian for a two-level system in the dipole approximation is

$$\hat{H}_{\text{int}} = -\mathbf{d} \cdot \mathbf{E}_R(t), \quad (2.9)$$

where \mathbf{R} is the position of the atom and

$$\mathbf{d} = \langle g | \mathbf{d} | e \rangle |g\rangle \langle e| + \langle e | \mathbf{d} | g \rangle |e\rangle \langle g| \quad (2.10)$$

the dipole operator. As discussed at the end of the preceding section, $\mathbf{d}_{ge} = \langle g | \mathbf{d} | e \rangle$ can be found from equation (2.5).

With $\mathbf{E}_R(t) = \epsilon E_0 \cos(\omega t)$, we find by substituting into Schrödinger's equation (1.8)

$$\begin{aligned} i\dot{c}_g(t) &= \Omega \cos(\omega t) e^{-i\omega_0 t} c_e(t) \\ i\dot{c}_e(t) &= \Omega^* \cos(\omega t) e^{i\omega_0 t} c_g(t) \end{aligned} \quad (2.11)$$

where

$$\Omega = E_0 \frac{\mathbf{d}_{g,e} \cdot \boldsymbol{\epsilon}}{\hbar} \quad (2.12)$$

is the Rabi frequency.

Starting out with all population in the ground state ($|c_g(0)|^2 = 1$), if the light field is weak such that for all times $|c_e(t)|^2 \ll 1$, we can use a perturbation theory approach, which is treated in detail in [Foot \(e.g. 2005\)](#), [Gerry and Knight \(e.g. 2005\)](#). Adopting the rotating-wave approximation ([RWA](#)), the probability to find the two-level atom in its excited state is

$$|c_e(t)|^2 = |\Omega|^2 \frac{\sin^2(\omega_0 - \omega)}{(\omega_0 - \omega)}, \quad (2.13)$$

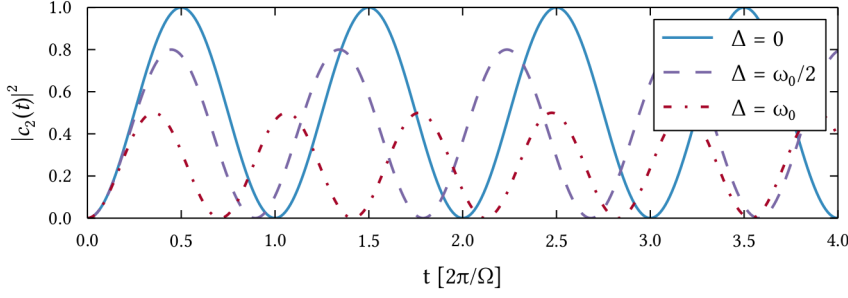


Figure 2.3: Rabi oscillations in a two-level system for different light field detunings $\Delta = \omega - \omega_0$.

where we see that the excitation probability goes inversely proportional with the square of the detuning between field and atomic resonance.

As stated in the last section, in this thesis we are for the most part concerned with transition rates rather than probabilities. Therefore, we follow [Gerry and Knight \(2005, p. 79–81\)](#) in assuming $\omega \approx \omega_0$ and replacing the last factor of (2.13) with a δ -function. This way, we obtain Fermi's golden rule, which gives the transition rate between $|e\rangle$ and $|g\rangle$ as

$$\gamma = \frac{\pi}{2} |\Omega|^2. \quad (2.14)$$

2.2.2 Interaction with a Strong Coherent Field

If the two-level system is driven by a strong classical (coherent) field (cf. sec. 1.3.2), we can no longer assume that $c_e(t) \approx 0$. Then, equations (2.11) yield

$$\frac{d^2 c_e(t)}{dt^2} + i(\omega - \omega_0) \frac{dc_e(t)}{dt} + \left| \frac{\Omega}{2} \right|^2 c_e = 0. \quad (2.15)$$

We define the detuning $\Delta = \omega - \omega_0$ and, assuming that $c_e(0) = 0$, find

$$|c_e(t)|^2 = \frac{\Omega^2}{\Omega^2 + \Delta^2} \sin^2 \left(\frac{\sqrt{\Omega^2 + \Delta^2} t}{2} \right). \quad (2.16)$$

Here we notice that the oscillation depends on Δ and introduce the effective Rabi frequency $\tilde{\Omega} = \sqrt{\Omega^2 + \Delta^2}$. As we see in figure 2.3, the oscillation is slowest for $\Delta = 0$ and it is only then that we reach a full population reversal.

2.2.3 Two-Level Atom as a Spin-1/2 System

In figure 2.4 we have seen that we can represent the state of a system by a vector rotating in a three-dimensional space. We expand on this picture by defining the operators

$$\hat{s}_+ = |e\rangle \langle g| \quad \text{and} \quad \hat{s}_- = |g\rangle \langle e| \quad (2.17)$$



Figure 2.4: In the Bloch sphere representation, the state of a two-level system $|\Psi\rangle = \cos(\theta/2)|g\rangle + \exp(i\varphi)\sin(\theta/2)|e\rangle$ is represented by the Bloch vector (θ, φ) . Coherent operations on $|\Psi\rangle$ correspond to rotations on the sphere.

as well as

$$\hat{s}_z = \frac{1}{2}(|e\rangle\langle e| - |g\rangle\langle g|). \quad (2.18)$$

We find that they obey the same commutation relations as spin- $\frac{1}{2}$ angular momentum operators (Agarwal, 2013):

$$[\hat{s}_+, \hat{s}_-] = 2\hat{s}_z, \quad [\hat{s}_z, \hat{s}_+] = \hat{s}_+, \quad [\hat{s}_z, \hat{s}_-] = -\hat{s}_-. \quad (2.19)$$

We can therefore think of a two-level atom as a spin- $1/2$ system, and identify $|g\rangle \equiv |\downarrow\rangle$ and $|e\rangle \equiv |\uparrow\rangle$.

Before we move on to systems of many such atoms, we introduce the well-known concept of π - and $\pi/2$ -pulses. Say initially the atom is in state $|\uparrow\rangle$, i. e. the Bloch vector points towards the “north pole”. If we drive the system on resonance for $T_\pi = 1/(2\Omega)$, afterwards the atom will be in state $|\downarrow\rangle$, i. e. the spin has been rotated by an angle of π and hence a pulse of length T_π is called a π -pulse. Likewise, a rotation for $T_{\pi/2} = 1/(4\Omega)$ brings the Bloch vector to the equator, leaving the atom in a superposition state $1/\sqrt{2}(|\uparrow\rangle + \exp(i\varphi)|\downarrow\rangle)$ where the phase φ depends on the phase of the $\pi/2$ -pulse.

As can be seen from figures 2.3 and 2.4, the experimental realization of these pulses requires knowledge of the exact value of ω_0 . This will be the topic of section 9.2.4.

2.3 COLLECTIVE SPIN STATES

Up to this point, we have treated only a single atom and in the last section have seen that a two-level atom is equivalent to a spin- $1/2$ system. Now, we combine N_a atoms to a collective spin state (CSS).

2.3.1 Total Spin and Holstein-Primakoff Approximation

By adding all N_a spins, we can assign a total spin $\mathbf{S} = \sum_{k=1}^{N_a} \mathbf{s}_k$ (with \mathbf{s}_k the Bloch vector of the k^{th} atom) to a given CSS. In general, $|\mathbf{S}|$ is not constant. If, however, most spins point in the same direction, $|\mathbf{S}| \approx N_a/2 = \text{const.}$ and we can represent the CSS on a Bloch sphere as introduced in figure 2.4. If N_a is very large, the Holstein-Primakoff approximation (Holstein and Primakoff, 1940) can be employed (Christensen, 2014, p. 23–24): If all atomic spins are aligned along the same axis, e. g. x , then $\langle \hat{S}_y \rangle \approx S = N_a/2$ and \hat{S}_x can be taken as a classical quantity. By accordingly rescaling \hat{S}_y and \hat{S}_z we find

$$\left[\frac{\hat{S}_y}{\sqrt{\langle \hat{S}_x \rangle}}, \frac{\hat{S}_z}{\sqrt{\langle \hat{S}_x \rangle}} \right] = i\hbar, \quad (2.20)$$

just like for the phase space operators \hat{q} and \hat{p} in section 1.2. This connects the CSS to quantum phase space.

2.3.2 Atomic Fock States

In analogy to \hat{a}^\dagger (cf. sec. 1.1), we introduce the ensemble creation operator

$$\hat{A}^\dagger = \frac{1}{\sqrt{N_a}} \sum_{k=1}^{N_a} \hat{A}_k^\dagger, \quad (2.21)$$

where $\hat{A}_k^\dagger = |\uparrow\rangle_k \langle \downarrow|_k$ is the individual atomic creation operator (Duan et al., 2001b). It is implicitly understood² that \hat{A}_k only acts on the k^{th} atom, e. g.

$$\hat{A}_2^\dagger |\downarrow\downarrow\downarrow\rangle = |\downarrow\uparrow\downarrow\rangle. \quad (2.22)$$

When the number of excitations n is small compared to N_a ,

$$\left[\hat{A}, A^\dagger \right] = \frac{1}{N_a} \sum_{k=1}^{N_a} (|\downarrow\rangle_k \langle \downarrow|_k - |\uparrow\rangle_k \langle \uparrow|_k) \approx 1 \quad (2.23)$$

which is in analogy to the commutation relation for the photon creation and annihilation operators (eq. 1.3). The states created by \hat{A}^\dagger can therefore rightfully be called atomic Fock states (AFSs).

In this thesis, we will mostly be concerned with the first excited state ($n = 1$)

$$\hat{A}^\dagger \bigotimes_{k=0}^{N_a} |\downarrow\rangle_k = \frac{1}{\sqrt{N_a}} \sum_{k=1}^{N_a} \bigotimes_{l=0}^{k-1} |\downarrow\rangle_l \otimes |\uparrow\rangle_k \otimes \bigotimes_{l=k+1}^{N_a} |\downarrow\rangle_l \quad (2.24)$$

$$= \frac{1}{\sqrt{N_a}} \sum_{k=1}^{N_a} |\downarrow\downarrow \dots \downarrow \underbrace{\uparrow}_{k^{\text{th}} \text{ atom}} \downarrow \dots \downarrow\rangle \equiv |\Psi_{\text{SES}}\rangle. \quad (2.25)$$

² As is convention for \hat{a} and \hat{a}^\dagger as well.

where a single excitation is shared among all N_a atoms – the single excitation state (SES). Just like was the case for the photonic Fock state $|n = 1\rangle$, the SES's Wigner function is negative at the origin of phase space (cf. fig. 1.4).

To further our analogy with photonic Fock states, we note that here the mode is comprised of all N_a atoms, and $\bigotimes_{k=0}^{N_a} |\downarrow\rangle_k = |0\rangle_A$ is the equivalent to the vacuum state $|0\rangle$. We also point out that the definition of \hat{A}^\dagger in equation (2.21) symmetrizes the excitation, i. e. upon measurement in the SES each individual atom has the same probability N_a^{-1} to be found in $|\uparrow\rangle$. If one attempts to create an SES in the laboratory, it is thus a challenge to ensure this indistinguishability despite the fact that the atoms might in principle be distinguishable by their spatial position (cf. sec. 5.1 and 8.3).

Having established the general theoretical framework, we now take a first step towards experiment.

2.4 ATOM TRAPPING AND COOLING

The trapping and cooling of atoms with the help of light and magnetic fields has opened up the field of ultracold atoms, ranging from precision spectroscopy over Bose-Einstein condensates to new generations of atomic clocks. In this section, we will very briefly review the methods employed in our experiment and describe their implementation. A more detailed introduction can be found in the classic [Metcalf and van der Straten \(1999\)](#) and [Grimm et al. \(2000\)](#), which the following sections are based on.

2.4.1 Doppler Cooling

Each atomic absorption and emission event goes along with momentum transfer. Doppler cooling exploits the recoil atoms experience when absorbing photons to slow and therefore cool them. In a coarse, qualitative picture, we imagine an atom moving along a laser beam whose frequency ω is red-detuned with respect to one of the atom's resonance frequencies ω_0 , i. e. $\omega_0 - \omega > 0$. If the atom is co-propagating, ω will be red-shifted from resonance even further. If on the other hand the atom is moving contrary to the light with sufficient velocity, $\omega_0 \approx \omega$ and a photon can be absorbed, slowing the atom's movement.

Even though the emission event following each absorption event increases the atom's momentum in a random direction, we see that the atom's velocity along the beam axis will on average decrease.

This method of cooling works up to the Doppler limit, which corresponds to the optimum between laser detuning and temperature. It is given by

$$k_B T_D = \frac{\hbar\Gamma}{2} \quad (2.26)$$

with k_B the Boltzmann constant ([Foot, 2005](#), sec. 9.3.1). For the D_2 -line of cesium, $T_D = 125 \mu\text{K}$ ([Steck, 2010](#)).

To employ Doppler cooling simultaneously for a large number of stationary atoms, we need to confine the latter in a small volume of space.

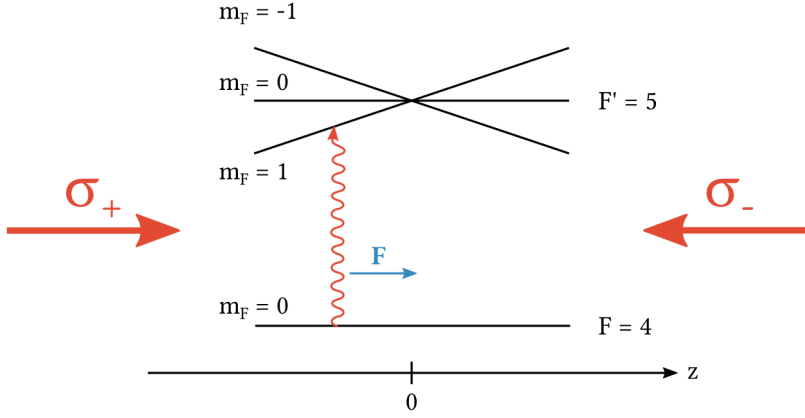


Figure 2.5: Principle operation of a MOT in one dimension: The quadrupole field lifts the degeneracy of the magnetic sublevels in the way depicted. Two circularly polarized, red-detuned laser beams are overlapped with the center of the field. Atoms on the negative part of the z -axis are tuned in resonance with the laser not only by their relative velocity, but also the Zeeman shift. Therefore, atoms are not only cooled, but trapped. (Graphic adapted from [Esteve, 2013](#))

2.4.2 Magneto-Optical Traps

Since they are robust and comparably easy to construct and operate, magneto-optical traps (MOTs) are the workhorse of ultracold atomic physics ([Metcalf and van der Straten, 1999](#)). They combine optical pumping, radiative forces, and an inhomogeneous magnetic quadrupole field as sketched in figure 2.5 to cool and confine atoms. Especially advantageous is that their capture range is so wide (≥ 1 K) that atoms can be loaded from a room temperature background vapor.

The prerequisite for the operation of a MOT is the existence of a (strong) closed optical transition. For cesium, this is $|F = 4\rangle \rightarrow |F' = 5\rangle$, which a laser commonly termed the *cooler* drives. Since the latter is detuned from resonance, it can also excite atoms into $|F' = 4\rangle$ from which atoms can decay into $|F = 3\rangle$. Therefore, a second laser – the *repumper* – is necessary to bring atoms back into the cooling cycle by driving $|F = 3\rangle \rightarrow |F' = 4\rangle$.

For the experiments described in this thesis, a standard six beam MOT is used ([Béguin, 2015, sec. 12.2](#)), whose optical setup is sketched in figure 2.7. Two external cavity diode lasers (ECDLs, cf. app. D) serve as the cooler and the repumper. The former is beatnote locked (cf. app. D.2) to the latter, which in turn is locked to the $|F = 3\rangle \rightarrow |F' = 2\rangle \times |F' = 3\rangle$ cross-transition via Doppler-free saturation polarization spectroscopy (cf. app. D.2) and serves as the main frequency reference for all lasers in the setup. The output of both ECDLs each passes through an acousto-optical modulator (AOM) for modulation and switching before it is coupled into a fiber. The light is mixed on a fiber beamsplitter and distributed equally onto the six MOT beams (cf. fig. 2.6b). The MOT operation is controlled via the LabView VI *SteMOT* (formerly *CaMOT*), which also provides the main time reference for

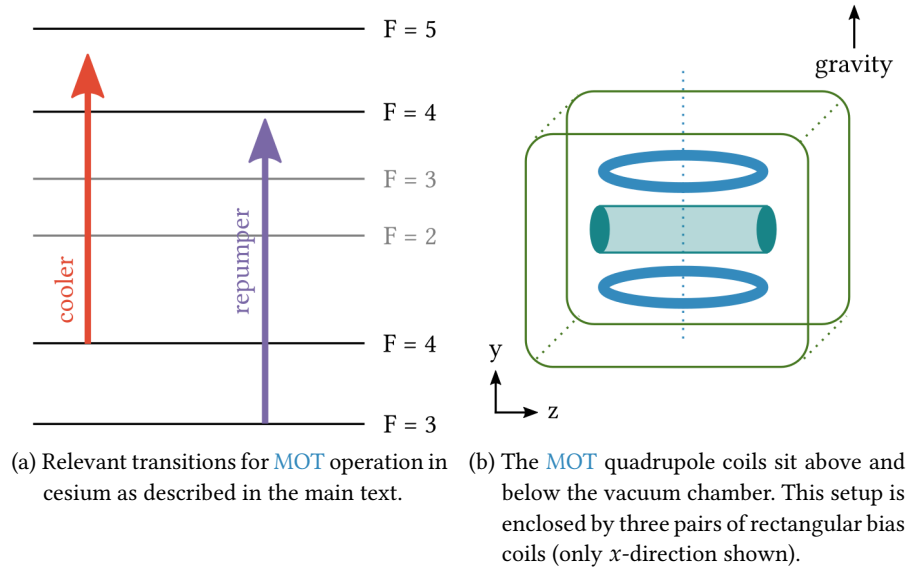


Figure 2.6

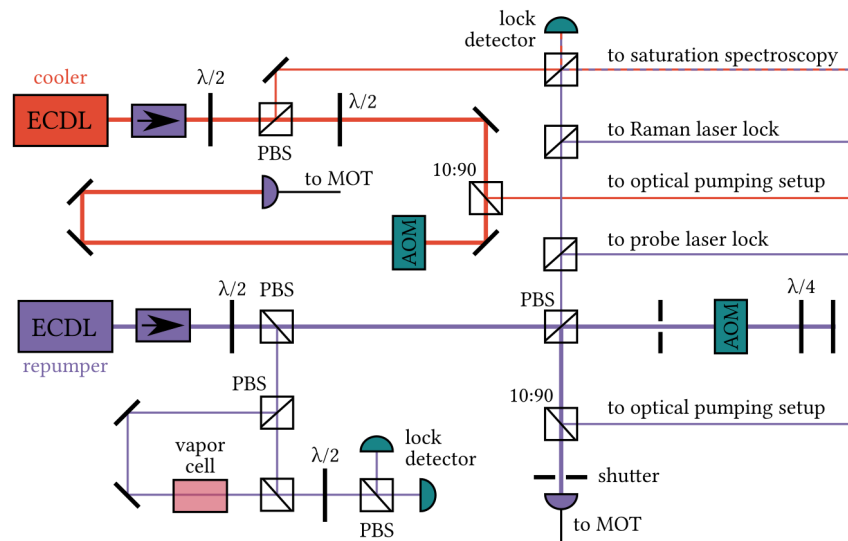


Figure 2.7: The MOT setup consists of two ECDL whose light is mixed and split into 6 beams using a fiber beamsplitter.

Light from the repumper is distributed throughout the setup as the main frequency reference. Light from both lasers is also used for optical pumping (dashed lines), which is detailed in figure 9.1.

There are six bias field coils in Helmholtz configuration on the outside of the setup which are used to move the MOT.

our experiments, i. e. all **TTL** and other control signals – most of which are controlled via the LabView *VI DIO* – are sent at timestamps defined relative to the *SteMOT* stages.

The quadrupole field is provided by a pair of coils in anti-Helmholtz configuration (fig. 2.6b). If a stronger bias field is needed then can be applied by the bias coils, the quadrupole coils can be switched into a Helmholtz configuration.

A bias field is provided by six coils in Helmholtz configuration (fig. 2.6b). They allow one to cancel the earth's and other stray magnetic fields, apply a bias field for the atoms in the nanofiber trap (cf. sec. 9.2.3), and to finetune the position of the **MOT** to maximize loading into the nanofiber trap (cf. sec. 5.4). They are controlled using a digital-to-analog converter (**DAC**), which can be switched between two different settings (I_x, I_y, I_z) via a **TTL** signal.

2.4.3 Dipole Traps

While a **MOT** is an excellent tool to cool and accumulate atoms, it is not suitable for quantum state preparation as scattering affects the atoms' electronic state. In traps using the dipole force exerted on atoms by far-detuned light, scattering rates are negligible. Further, the trapping potential can be made independent of the atom's internal state and a rich variety of trapping geometries can be realized – especially in combination with photonic waveguides like nanofibers, which we will discuss in detail in section 5.1. Here, we now give a brief introduction into dipole traps based on the classic review by Grimm et al. (2000).

A two level atom with transition frequency ω_0 (cf. sec. 2.2) placed in a classical far-detuned light field $\mathbf{E}(\mathbf{r}, t)$ of frequency ω experiences a dipole force. Assuming negligible saturation and $|\Delta| = |\omega - \omega_0| \ll \omega_0$ so the rotating-wave approximation is valid this force can be described by the potential

$$U_{\text{dip}}(\mathbf{r}) = \frac{3\pi c^2}{2\omega_0^3} \frac{\Gamma}{\Delta} I(\mathbf{r}) \quad (2.27)$$

where $I(\mathbf{r}) = |\mathbf{E}(\mathbf{r}, t)|^2$ is the light intensity at position \mathbf{r} and

$$\Gamma = \frac{\omega_0^3}{3\pi\hbar c^3} |\langle e|\mu|g\rangle|^2 \quad (2.28)$$

is the spontaneous decay rate of the excited level. The scattering rate is given by

$$\Gamma_{\text{sc}}(\mathbf{r}) = \frac{3\pi c^2}{2\hbar\omega_0^3} \left(\frac{\Gamma}{\Delta}\right)^2 I(\mathbf{r}). \quad (2.29)$$

From (2.27) and (2.29) we see that since $\Gamma_{\text{sc}} \propto I/\Delta^2$ and $U_{\text{dip}} \propto I/\Delta$, a large detuning Δ and a high light intensity I are desirable. Furthermore, a positive (negative) detuning Δ results in a repulsive (attractive) potential.

In a perturbation theory treatment, the potential (2.27) appears as an energy shift (*ac Stark shift*) of the atom's ground (−) and excited (+) state:

$$\Delta_E = \pm \frac{3\pi c^2 \Gamma}{2\omega_0^3 \Delta} I. \quad (2.30)$$

Blue-detuned and red-detuned traps can also be combined. In our experiment, we create such a two-colour dipole trap around the tapered section of a nanofiber. This is discussed in detail in chapter 5.

2.4.4 Sub-Doppler Cooling

Since its trap potentials are conservative, we cannot simply load a dipole trap by superimposing a cloud of ultracold atoms, but need to provide a dispersive force, i. e. friction. Furthermore, although the temperature of the atoms in a MOT is below the Doppler limit already (Metcalf and van der Straten, 1999, ch. 10), they are barely cold enough to be confined by the shallow trap potentials of the dual-color dipole trap (cf. sec. 5.2).

Much thought has gone into the development of a trap loading procedure, and many of the intricate details can be found in Béguin (2015, sec. C.3.4). Here, we attempt to provide a merely qualitative picture.

From equation (2.30) we see that in general, only the groundstates experience an attractive force.³ We therefore need atoms to be in the groundstates for as much time as possible. Also from equation (2.30) we see that if an atom drops into a trapping potential, its groundstate energy changes, bringing it out of resonance with both cooler and repumper. To provide a dispersive force, i. e. to further slow the atom, we can detune cooler and repumper to match this shift.⁴

Additionally, we can increase the amount of time atoms spend in the ground state: In the mode of MOT operation we described in section 2.4.2, most atoms are in a bright state with respect to the cooler, which lends the name *bright MOT*. By balancing the power of cooler and repumper, we can control which fraction of time atoms spend on the cooling transition. This way, we can tune the MOT into a *gray* mode of operation, where the atoms spend more time in the dark state, where they are also less prone to heating through scattering. Consequently, at the end of the sub-Doppler cooling procedure (which in practice is a much more complex sequence than we could discuss here), most atoms confined in the nanofiber trap are in the $|F = 3\rangle$ hyperfine groundstate (cf. sec. 9.1.1).

As a final note we remark that in principle, sub-Doppler cooling is only limited by the recoil energy (Cohen-Tannoudji, 1998)

$$E_{\text{recoil}} = k_B T_{\text{recoil}} = \frac{\hbar^2 k^2}{2m} \quad (2.31)$$

³ In dual-color dipole traps, one can find so-called “magic wavelengths” which also provide a trapping potential for the excited state, cf. sec. 5.2.

⁴ Since the dipole force in the nanofiber trap is spatially inhomogeneous (cf. sec. 5.2), this cooling effect is local, but this does not need to concern one here.

where k is the photon's wavevector. For cesium $T_{\text{recoil}} \approx 200$ nK (Steck, 2010). We will estimate the temperature of the atoms in our trap during our “atomic mirror” experiment (cf. fig. 7.7).

Indem wir vom Wahrscheinlichen sprechen, ist ja das Unwahrscheinliche immer schon inbegriffen und zwar als Grenzfall des Möglichen, und wenn es einmal eintritt, das Unwahrscheinliche, so besteht für unsereinen keinerlei Grund zur Verwunderung, zur Erschütterung, zur Mystifikation.¹

— from Max Frisch: *Homo Faber*

In the first two chapters, we have presented an overview of a quantum theory of light and atoms, introducing the important concepts of quantum states and quantum phase space. Although we made a digression into experimental techniques at the end of chapter 2, so far our treatment has been theoretical in nature. On the following pages, we will now show how one can investigate quantum systems and catch a glimpse of quantum phase space in the laboratory.

We begin with a general overview of quantum measurement, thereby introducing a consistent terminology. Then we present and analyze homodyne measurement, which in the subsequent section we use to illustrate our discussion of quantum noise and quantum limits. Finally, we turn to heterodyne detection and introduce the experimental realization of the two-color heterodyne scheme which we will employ throughout this thesis.

3.1 INTRODUCTION

It is well known that according to quantum mechanics all one can measure are the eigenvalues of operators (e. g. Nielsen and Chuang, 2000, sec. 2.2.3). The question of how this comes about is the notorious “measurement problem”, which is the root of much debate and far from being resolved (Esfeld, 2012, Friebe, 2015). From the experimenter’s point of view, however, things are not looking quite as bleak. In this section, we will introduce different kinds of quantum measurements and some terminology.

The first type is a strong projective measurement. This corresponds literally to the case which is described by the measurement postulate of quantum mechanics: If a measurement of an observable A (corresponding to an operator \hat{A} with eigenstates $|\Psi_j\rangle$ and eigenvalues A_j , i. e. $\hat{A}|\Psi_j\rangle = A_j|\Psi_j\rangle$) is performed on a system initially in $|\Psi\rangle = \sum_j p_j |\Psi_j\rangle$, this measurement will yield A_j with probability $|p_j|^2$ and the system will “collapse” into $|\Psi_j\rangle$ (Sakurai and Napolitano, 2011, sec. 1.4).

¹ When we speak of probabilities, the improbable is always included as the limit of the possible. And if the improbable occurs, there is no need for wonder, astonishment or mystification.

The projection destroys any information about the conjugate variable (cf. [Sakurai and Napolitano, 2011](#), ch. 1), which is a consequence of Heisenberg’s uncertainty relation. A simple example is a photo detector absorbing a photon: Say we have a mode of the electric field in state $|\Psi\rangle = 1/\sqrt{2}(|0\rangle + \exp(i\varphi)|1\rangle)$. The action of the photo detector is the projection of $|\Psi\rangle$ onto $|\text{noclick}\rangle \langle 0| + |\text{click}\rangle \langle 1|$. Since the photon is absorbed, this is a maximally destructive measurement, but we also measure the photon number in the mode with maximum accuracy, losing all information on the phase φ in the process (cf. eq. 1.21).

In contrast, during a weak continuous measurement, in each instant of time we only gain partial information on the system’s state. Therefore, there is no instant “collapse” into one eigenstate, but rather the system dephases as the amount of information gained increases. Again, this back-action is the consequence of Heisenberg’s uncertainty relation. We emphasize (and shall see in our example in section 3.3) that at the point in time the system’s state is unambiguously determined, the system has completely dephased into the measured eigenstate ([Clerk et al., 2010a](#)), i. e. considering the final state of the system there is no difference to a strong projective measurement: If eigenvalue A_j was measured, the system is in $|\Psi_j\rangle$.

A special kind of measurement are those termed quantum non-demolition (QND), where the eigenstates of the measurement operator are stationary states of the system, i. e. $[\hat{H}, \hat{A}] = 0$. With [Clerk et al. \(2010a\)](#) we emphasize that QND does not necessarily mean that the system’s state is not changed: A collapse into one of the operator’s eigenstates will happen unless the system was in such an eigenstate before, and it is the measured eigenvalue which does not change. Experimentally, for a measurement to be QND one only considers the commutator between the ideal Hamiltonian of the system, i. e. one ignores dissipation by coupling to the environment ([Clerk et al., 2010a](#)).

After introducing the homodyne detection method in the next section we will give an illustration of a weak continuous QND measurement in section 3.3.

3.2 HOMODYNE DETECTION

In this section, we present a method for measuring the quadrature operators (sec. 1.2) and hence the quantum state of light using a simple interferometer. While we will use more sophisticated variants of interferometric quantum measurements in the experiments, homodyne measurement is an important concept for the tomography of the single excitation state (cf. sec. 8.3.1) and due to its simplicity lends itself as a model to discuss fundamental aspects of quantum measurement and noise as we shall do in section 3.3. Our treatment follows [Leonhardt \(1997\)](#); an instructive and insightful discussion geared towards experiment can be found in [Béguin \(2015, ch. 3\)](#).

A schematic setup of a balanced homodyne detection is depicted in figure 3.1: A signal \hat{a}_{sig} and a strong coherent beam α_{LO} called the local oscillator (LO) are overlapped on a balanced beam splitter. The two signals \hat{a}_1 and \hat{a}_2

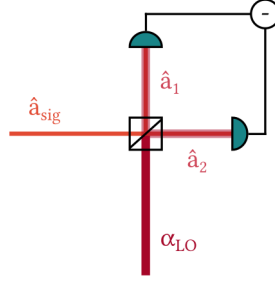


Figure 3.1: Balanced homodyne detector

are each detected by a photo diode. What is recorded is the difference of the resulting photocurrents $I_{21} = I_2 - I_1$.

A very simple analysis in terms of classical fields

$$E_{\text{LO}} = A_{\text{LO}} e^{i\omega t} \quad (3.1)$$

$$E_{\text{sig}} = A_{\text{sig}}(t) e^{i\omega t} \quad (3.2)$$

where without loss of generality A_{LO} is real and the signal amplitude $A_{\text{sig}} = |A_{\text{sig}}(t)| e^{i\theta(t)}$ carries changing amplitude and phase yields

$$I_{21}(t) = I_2 - I_1 \quad (3.3)$$

$$= \left| \frac{E_{\text{LO}} - E_{\text{sig}}}{\sqrt{2}} \right|^2 - \left| \frac{E_{\text{LO}} + E_{\text{sig}}}{\sqrt{2}} \right|^2 \quad (3.4)$$

$$= 2A_{\text{LO}} |A_{\text{sig}}(t)| \cos(\theta(t)) \quad (3.5)$$

and shows the main feature: The homodyne signal $I(t)$ contains $A_{\text{sig}}(t)$ amplified by a factor A_{LO} . In the case where the signal's magnitude is constant, θ_0 is a small phase shift and if we experimentally choose $\theta = \pi/2 + \theta_0$ for maximum sensitivity, the normalized homodyne signal is (cf. Clerk et al., 2010a, p. 1167)

$$I(t) = \int_0^t \bar{I}_{21} = \theta_0 t, \text{ i. e. } \theta_0 = \frac{I(t)}{t}. \quad (3.6)$$

A quantum mechanical analysis reveals the connection of $I(t)$ to quantum phase space (cf. sec. 1.2). Below detector saturation, the photocurrent I is proportional to the number of impinging photons, i. e.

$$\hat{n}_1 = \hat{a}_1^\dagger \hat{a}_1 \text{ and } \hat{n}_2 = \hat{a}_2^\dagger \hat{a}_2, \quad (3.7)$$

where

$$\hat{a}_1^\dagger = \frac{\hat{a}_{\text{sig}} - \alpha_{\text{LO}}}{\sqrt{2}} \text{ and } \hat{a}_2^\dagger = \frac{\hat{a}_{\text{sig}} + \alpha_{\text{LO}}}{\sqrt{2}} \quad (3.8)$$

are the creation operators for the light fields after the beam splitter (following our discussion in section 1.3.2, we treat the strong LO classically). Adopting the shorthand notation $\hat{a} = \hat{a}_{\text{sig}}$, we can calculate the difference current

$$\begin{aligned}
I_{21} &\propto \hat{n}_2 - \hat{n}_1 \\
&= \hat{n}_{21} \\
&= \frac{\hat{a}^\dagger \hat{a} + \hat{a}^\dagger \alpha_{\text{LO}} + \alpha_{\text{LO}}^* \hat{a} + \alpha_{\text{LO}}^* \alpha_{\text{LO}}}{2} \\
&\quad - \frac{\hat{a}^\dagger \hat{a} - \hat{a}^\dagger \alpha_{\text{LO}} - \alpha_{\text{LO}}^* \hat{a} + \alpha_{\text{LO}}^* \alpha_{\text{LO}}}{2} \\
&= \alpha_{\text{LO}}^* \hat{a} + \alpha_{\text{LO}} \hat{a}^\dagger.
\end{aligned} \tag{3.9}$$

Using equations (1.6), we can connect this result to the quantum phase space operators:

$$\hat{n}_{21} = \alpha_{\text{LO}}^* \frac{\hat{q} + i\hat{p}}{\sqrt{2}} + \alpha_{\text{LO}} \frac{\hat{q} - i\hat{p}}{\sqrt{2}}. \tag{3.10}$$

Writing α_{LO} as $|\alpha_{\text{LO}}| e^{i\theta}$ and using equation (1.5), we obtain our main result:

$$\begin{aligned}
\hat{n}_{21} &= \frac{|\alpha_{\text{LO}}|}{\sqrt{2}} (\hat{q} \cos \theta + i\hat{p} \cos \theta) \\
&= \sqrt{2} |\alpha_{\text{LO}}| \hat{q}_\theta.
\end{aligned} \tag{3.11}$$

The last line shows a simple relationship between I_{21} and the phase space operator \hat{q}_θ (with $\hat{q}_0 = \hat{q}$ and $\hat{q}_{\pi/2} = \hat{p}$) of the *signal* light field. The phase θ is provided by the LO, which is therefore required to be phase stable relative to the signal. In practice, this is achieved easiest by deriving both fields from the laser; the relative phase is then controlled via the path lengths. We further see that the detector signal I_{21} is proportional to the LO's intensity. Therefore the homodyne detector serves as an optical amplifier, lifting the potentially very weak signal \hat{a}_{sig} well above the inherent electronic noise of the photo detectors.² In order to scale the signal in absence of accurate knowledge of the LO's intensity, one can simultaneously record the sum of the photocurrents, which for a strong LO gives its intensity:

$$\begin{aligned}
I_2 + I_1 &\propto \hat{n}_2 + \hat{n}_1 = \hat{a}^\dagger \hat{a} + \alpha_{\text{LO}}^* \alpha_{\text{LO}} \\
&= \hat{n}_{\text{sig}} + |\alpha_{\text{LO}}|^2 \approx |\alpha_{\text{LO}}|^2.
\end{aligned} \tag{3.12}$$

Relating this discussion to the very beginning of section 1.1, we see that the LO selects a single light mode $u(x, t)$ (eq. 1.1) for measurement. This has the experimentally convenient consequence that the balanced homodyne signal is immune to stray light (as long as the photodiodes are not saturated).

3.3 QUANTUM NOISE AND QUANTUM LIMITS

We will discuss a simple example of a weak continuous QND measurement given by Clerk et al. (2010a) to expand on the concepts introduced in section

² We will return to this discussion in section 3.4 when we describe in more detail the properties of the detectors used in our experiment.

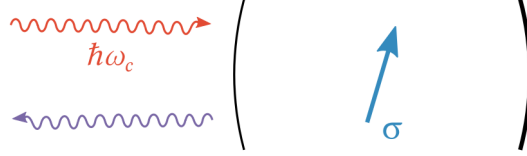


Figure 3.2: A single spin is placed in a one-sided cavity and interrogated with a strong coherent beam. The reflected light is sent to a homodyne detector as introduced in section 3.2.

3.1. The situation, which is related to the experiments we perform in this thesis, is sketched in figure 3.2: A spin-1/2 qubit is placed inside a one-sided cavity and interrogated with light. The system Hamiltonian is

$$\hat{H} = \frac{1}{2}\hbar\omega\hat{\sigma}_z + \hbar\omega_c(1 + A\hat{\sigma}_z)\hat{a}^\dagger\hat{a} + \hat{H}_{\text{env}}, \quad (3.13)$$

where A is the coupling of the qubit to the cavity and \hat{H}_{env} the electromagnetic modes in the environment. The latter damps the cavity, which we can parametrize by a leakage rate κ . We consider the case that $\omega_c/\kappa \gg 1$, i. e. the cavity's quality factor $Q = \omega_c/\kappa$ is very large.

If we probe the cavity with light of frequency ω_c , starting with Clerk et al. (2010b, eq. E42)³ the reflection coefficient is

$$r = \frac{\omega_c - \omega_c(1 + A\hat{\sigma}_z - \frac{\kappa}{2})}{\omega_c - \omega_c(1 + A\hat{\sigma}_z + \frac{\kappa}{2})} = -\frac{1 + 2iAQ\hat{\sigma}_z}{1 - 2iAQ\hat{\sigma}_z}. \quad (3.14)$$

Since the cavity is lossless, $|r| = 1$ and for small A

$$r = -e^{-i\theta} \text{ with } \theta \approx 4QA\hat{\sigma}_z = (A\omega_c\hat{\sigma}_z)t_{\text{WD}}. \quad (3.15)$$

Here we have introduced the Wigner delay time $t_{\text{WD}} = 4\kappa^{-1}$ which can be understood as the time the qubit interacts with the cavity field.

The phase shift θ can be measured using homodyne detection as introduced in the previous section. If $[\hat{H}, \hat{\sigma}_z] = 0$, $\hat{\sigma}_z$ is a constant of motion, allowing for a QND measurement.⁴ $\hat{\sigma}_z$ has eigenvalues ± 1 , so the possible results of the measurement of θ are

$$\theta_0 = \pm A\omega_c t_{\text{WD}}. \quad (3.16)$$

Because A is very small, $|\theta_0| \ll 1$ and we need to measure for a finite time t in order to determine the qubit's state. Using (3.6), $\langle I \rangle = \pm\theta_0$, and considering the ideal case of a shot noise limited probe, $\Delta I = \sqrt{S_{\theta\theta}t}$. Here, $S_{\theta\theta} = (\Delta\theta)^2 t = 1/4\bar{n}$ is the phase imprecision spectral density, i. e. given a mean photon flux \bar{n} the variance of the phase measurement will be $(\Delta\theta)^2 = S_{\theta\theta}/t$ (cf. sec. 1.3.2, eq. 1.20).

³ See chapter 7 of Walls and Milburn (2007) for a more detailed derivation.

⁴ As we have noted in section 3.1, it is not necessary that $[\hat{H}_{\text{env}}, \hat{\sigma}_z] = 0$ for the measurement to be QND, but for simplicity we assume that the qubit is not dephased by the environment, i. e. $\tau_1 = \infty$.

The measurement rate Γ_{meas} , i. e. the rate at which the accessible information grows during the measurement, is equal to half the signal to noise ratio (SNR)⁵:

$$\Gamma_{\text{meas}} := \frac{1}{2} \text{SNR} = \frac{1}{2} \frac{\langle I \rangle^2}{(\Delta I)^2} = \frac{\theta_0^2}{2S_{\theta\theta}t'} \quad (3.17)$$

To study the effect the measurement has on the qubit, we re-arrange (3.13) as follows:

$$\hat{H} = \frac{\hbar}{2} \left(\omega + 2A\omega_c \hat{a}^\dagger \hat{a} \right) \hat{\sigma}_z + \hbar\omega_c \hat{a}^\dagger \hat{a} + \hat{H}_{\text{env}}. \quad (3.18)$$

From this it is apparent that the probe light induces an ac Stark shift (cf. sec. 2.4.3, eq. (2.30)), i. e. depending on the number of photons present in the cavity the qubit's splitting frequency is shifted. This is the back-action of the measurement onto the system.

Even though in the case at hand no transitions can be induced (QND measurement), fluctuations in $\hat{n} = \hat{a}^\dagger \hat{a}$ will dephase the qubit. In the limit of weak coupling (small A) the accumulated phase is (Clerk et al., 2010a, eq. 3.26)

$$\langle e^{i\varphi} \rangle = \exp \left(-2(A\omega_c t_{\text{WD}})^2 S_{\hat{n}\hat{n}} t \right), \quad (3.19)$$

where $S_{\hat{n}\hat{n}} = \bar{n}$ is the photon shot noise spectral density, i. e. similar to above $(\Delta n)^2 = S_{\hat{n}\hat{n}}/t$ (cf. sec. 1.3.2). From (3.19) we define the dephasing rate

$$\Gamma_\varphi := 2(A\omega_c t_{\text{WD}})^2 S_{\hat{n}\hat{n}} = 2\theta_0^2 S_{\hat{n}\hat{n}} \quad (3.20)$$

and immediately find that in the ideal limit

$$\frac{\Gamma_\varphi}{\Gamma_{\text{meas}}} = 1, \quad (3.21)$$

i. e. as Clerk et al. (2010a) put it: “The best you can possibly do is [to] measure as quickly as you dephase.”

Without going into further detail, we note that in order to reach the quantum limit (3.21) it is necessary that all available information is used. This is the case in the one-sided cavity discussed here, but not if *both* mirrors are slightly transmissive. Then, an equal amount of information on the qubit's state is leaking out of the cavity on both sides, and if only one of these channels is measured, $\Gamma_\varphi/\Gamma_{\text{meas}} = 2$, i. e. the dephasing due to back-action is doubled (Clerk et al., 2010a, eq. 3.44).

3.3.1 Projection Noise

Before we end our discussion, we briefly consider the case where we do not have a single, but N spin particles in the cavity. This is the case in our

⁵ Several instructive motivations for this choice of definition are given in Clerk et al. (2010b, app. F)

experiment, where we have N two-level atoms (cf. sec. 2.3). Then, in addition to noise on the probe and in the detection electronics, another source of noise arises if one measures the population in one of the levels. Since in the measurement process each individual atom will be projected into either $|\uparrow\rangle$ or $|\downarrow\rangle$, for a system of N atoms where the probability to find an atom in $|\uparrow\rangle$ is $p_{|\uparrow\rangle}$, the probability to measure $N_{|\uparrow\rangle}$ is⁶ (Itano et al., 1993)

$$P(N_{|\uparrow\rangle}) = \binom{N}{N_{|\uparrow\rangle}} (p_{|\uparrow\rangle})^{N_{|\uparrow\rangle}} (1 - p_{|\uparrow\rangle})^{(N - N_{|\uparrow\rangle})}. \quad (3.22)$$

The variance of (3.22) is the *projection noise*

$$\sigma^2 = N p_{|\uparrow\rangle} (1 - p_{|\uparrow\rangle}). \quad (3.23)$$

We see that not surprisingly (3.23) is maximal if $p_{|\uparrow\rangle} = 0.5$ (yielding $\sigma^2 = N/4$) and that the projection noise scales with N . Thus, we say that a measurement method is “projection noise limited” if the noise on population measurements grows linearly with the number of atoms (cf. Windpassinger et al., 2008, Christensen, 2014).

3.4 HETERODYNE DETECTION

In the previous sections we have seen that homodyne detection is a powerful tool. However, there are several drawbacks: In general, the noise level is highest at DC and in the spectral region directly above, e. g. due to (classical) noise which stems from the various electronic circuits involved in generating the light. Second, it is clear that the detected *total* intensity at DC is dependent on ambient and stray light.

Furthermore, in our experiments we are not interested in the state of the light field itself, but the state of an atomic ensemble. While we have seen an example of how to accomplish this with homodyne detection in the previous section, especially in the case of a nanofiber trap, where strong trap light is co-propagating with the weak probe in the very same guided mode, it is important that somehow the probe signal can be filtered out.

All of these issues are circumvented by the heterodyne detection method. Here, the LO and signal light field are detuned by $\Delta\omega = \omega_{\text{sig}} - \omega_{\text{LO}}$, typically several 10 MHz.

Similar to our derivation for homodyne detection in section 3.2, the LO and signal light field are given by

$$E_{\text{LO}} = A_{\text{LO}} e^{i\omega_{\text{LO}} t}, \quad (3.24)$$

$$E_{\text{sig}} = A_{\text{sig}}(t) e^{i\omega_{\text{sig}} t} \quad (3.25)$$

⁶ Itano et al. (1993) show that this classical treatment yields the correct result.

and the detected intensity signal⁷ is

$$I(t) = |E_{\text{LO}} + E_{\text{sig}}|^2 \quad (3.26)$$

$$= |A_{\text{LO}}|^2 + |A_{\text{sig}}(t)|^2 + 2\text{Re}(E_{\text{LO}}^* E_{\text{sig}}). \quad (3.27)$$

Using

$$E_{\text{LO}}^* E_{\text{sig}} = A_{\text{LO}}^* A_{\text{sig}}(t) e^{i(\omega_{\text{sig}} - \omega_{\text{LO}})t} \quad (3.28)$$

we see that

$$I(t) = \text{DC} + 2\text{Re}(A_{\text{LO}}^* A_{\text{sig}}(t)) \cos(\Delta\omega t), \quad (3.29)$$

i. e. we detect a signal oscillating with $\Delta\omega$ – far removed from **DC** and thus spectrally in a quiet region – on top of a **DC** offset. In addition, the electrical amplification in the photo detectors we use is tailored precisely around $\Delta\omega$. Although it is crucial that the amplification stages are not saturated by light beating with the **LO** at other nearby frequencies, stray light and far-detuned light (like the nanofiber trap) in the same mode are not detrimental to detection efficiency or noise.

By demodulating with $\sin(\Delta\omega t)$, we extract from (3.29) our signal of interest. As was the case for the homodyne signal (eq. 3.5), $A_{\text{sig}}(t)$ is optically amplified by the **LO**:

$$I_{\text{het}}(t) = 2A_{\text{LO}} A_{\text{sig}}(t). \quad (3.30)$$

Now it is straightforward so see how one can use this variant to probe state populations in an atomic ensemble: If the probe light is tuned on resonance with e. g. the $|F = 4\rangle \rightarrow |F' = 5\rangle$ transition, $A_{\text{sig}}(t)$ is an absorption signal proportional to the number of atoms in $|F = 4\rangle$ (cf. fig. 5.5).

Before we move on to our quantum limited probe, we would like to understand how and where exactly the light amplification happens in heterodyne (or, for that matter, homodyne) detection. To this end, we briefly have to consider how light is detected. Since there are no detectors capable of following the fast oscillations of electromagnetic waves in the optical domain, light can only be detected by absorbing it in a material, thereby creating a photocurrent. We have already used that this current I is proportional to the number of photons in the mode, i. e. $\langle I \rangle \propto \langle \hat{n} \rangle$. Hence, photodiodes are known as square-law detectors, detecting the field intensity instead of the field amplitude, thereby losing all information on the phase – which, as we have seen, we can circumvent with interferometric detection methods.

In general, photo detectors have a finite efficiency, commonly called the quantum efficiency η_{QE} . While a state of the art photon counter like the one we use in our experiment can reach $\eta_{\text{QE}} = 0.8$ for specific wavelengths (fig. 10.9), detectors capable of standing more than a few 100,000 photons per

⁷ We point out that one can also perform a balanced heterodyne detection. While in fact one of the detectors in our setup is built in such a configuration, for the measurements conducted there is no fundamental difference.

second exhibit significantly lower detection efficiencies. Nevertheless, the quantum efficiency of heterodyne detection is practically unity (Hammerer et al., 2010).

To understand how this is accomplished, we observe that the field amplitude on the detector is the sum of signal and LO. It is then the non-linear detection which provides the amplification (cf. eq. 3.26). Further, by mixing the very weak signal with the strong LO, the former is lifted well above the electronic noise of the detector – while for photon counting, dark counts are a significant source of noise (cf. sec. 10.4.1), in the limit of a strong LO its shot noise dominates all other noise. Thus, what one measures in the absence of a signal is the vacuum (cf. eq. 1.7 and e. g. fig. 6.11), to which a photon counter is not sensitive.

3.4.1 Two-Color Heterodyne Detection

In the previous section we have seen how heterodyne measurement can be used for absorption spectroscopy. To perform QND measurements on CSS, however, it is necessary to avoid scattering photons off the atoms. Therefore, the probe light has to be detuned from resonance (cf. sec. 5.1). While it is possible to reach the projection noise limit (cf. sec. 3.3.1) using the method described in the last section with a far-detuned probe (e. g. Windpassinger et al., 2008), the latter induces an ac Stark shift (sec. 2.4.3, eq. 2.30), which – as we have seen in section 3.3 – constitutes additional back-action on the atoms, dephasing the system faster than the measurement process itself.

To avoid this, one can expand the heterodyne detection scheme to a two-color version,⁸ where the probe light is split into two sidebands detuned equally around the atomic resonance ω_0 , thus cancelling the differential ac Stark shift.

Since this method is described in formidable detail in chapters 3 and section 16.3 of Béguin (2015) (a much briefer summary is presented in Béguin et al. (2014b)), here we will only give a general introduction, highlighting the main features and the experimental realization.

The implementation is sketched in figure 3.3. The probe sidebands are detuned by $\Omega = 62.5 \text{ MHz} \approx 12\Gamma$, where Ω was chosen to be an integer fraction of the 500 MHz input of the DDS generating the RF-signal, therefore phase jitter is avoided (Béguin, 2015, p. 221). The frequency of the probe laser ω is calculated to be on resonance with the strong, closed $|F = 4\rangle \rightarrow$

⁸ As due to shared nomenclature this can lead to confusion, we note that Oblak (2010), Christensen (2014) et al. also used a two-color heterodyne scheme, but with one sideband detuned from $|F = 3\rangle \rightarrow |F' = 2\rangle$ and one detuned from $|F = 4\rangle \rightarrow |F' = 5\rangle$. This cancels the ac Stark shift on the hyperfine groundstates, enabling QND population *difference* measurements, but not *population* measurements on $|F = 4\rangle$. We will return to this discussion at the end of section 8.3.1.

$|F' = 5\rangle$ transition and then finetuned as to not dephase the atomic state.⁹ We briefly describe this measurement in section 9.2.5.

Similar to the analysis we performed in the previous section, we have

$$E_{\text{LO}} = A_{\text{L}} e^{i\omega t} \quad (3.31)$$

$$E_{\text{sig}} = A_1 e^{i(\omega+\Omega)t+i\varphi} + A_2 e^{i(\omega+\Omega)t-i\varphi}, \quad (3.32)$$

where φ is the phaseshift imprinted on the light by the atoms (note that atomic dispersion is antisymmetric around resonance). If a single atom leads to a phaseshift φ_0 , the number of atoms in $|F = 4\rangle$ is

$$N_{|F=4\rangle} = \frac{\varphi}{\varphi_0}, \quad (3.33)$$

i. e. we perform a population measurement. Indeed, if carefully calibrated and paired with a statistical model, one can determine $N_{|F=4\rangle}$ with sub-Poissonian precision (Béguin et al., 2014a).

In light of our analyses in the past sections, we see from (3.32) that what we will find on the detector are four signals, one each at DC, Ω , 2Ω , and 2ω . As before, we discard DC. Further, 2ω is too fast to be detected and 2Ω is not amplified by the LO, leaving as in the previous section the signal oscillating at Ω .

Again from (3.32) we see that the signal at Ω is the sum of each sideband's beat with the LO. As the analysis given in Béguin (2015, sec. 16.3.1) reveals, this leads to cancellation of common classical phase noise from the measurement signal, i. e. if the sideband's intensity is balanced, phase shifts (relative to the reference phase φ_{ref} provided by the LO) acquired by both sidebands are converted into amplitude modulation. This is important in the case of a nanofiber, as e. g. its length changes due to temperature fluctuations (cf. sec. 4.2.1) and mechanical oscillations can affect the guided light (cf. the footnote in sec. 5.3). To maintain maximum visibility, we balance the length of the two interferometer arms as to operate at the white light position.

The detector signal is amplified electrically and mixed down using the same RF signal used to drive the AOM. With the help of an I - Q -demodulator, both quadrature components of the signal are acquired¹⁰ and recorded on an oscilloscope (Agilent Infiniium 54832D). The two quadrature components obtained are given by Béguin (2015, p. 224) and read

$$S_q(t) = A_{\text{LO}} (\epsilon \cos(\varphi_{\text{ref}}) \cos(\varphi)), \quad (3.34)$$

$$S_p(t) = A_{\text{LO}} (\epsilon \cos(\varphi_{\text{ref}}) \sin(\varphi)), \quad (3.35)$$

⁹ Since it will be very relevant later, we already note that if the probe light is H polarized (cf. sec. 4.2.3) – which it usually is to obtain a high light-atom coupling strength (cf. sec. 4.3.2) – and strong, despite the large detuning from resonance atoms will be pumped into the extreme m_F -levels. For a description of this process, see 9.1.2; for an application, see towards the end of section 8.3.1.

¹⁰ It is a feature of heterodyne detection that one can access both light field quadratures at the same time, without changing the length of the interferometer (cf. sec. 3.2). Of course, since $[\hat{q}, \hat{p}] = i\hbar$ (sec. 1.2), it is not possible to measure \hat{q} and \hat{p} *simultaneously*. Rather, due to the oscillating signal, we rapidly alternate between probing \hat{q} and \hat{p} .

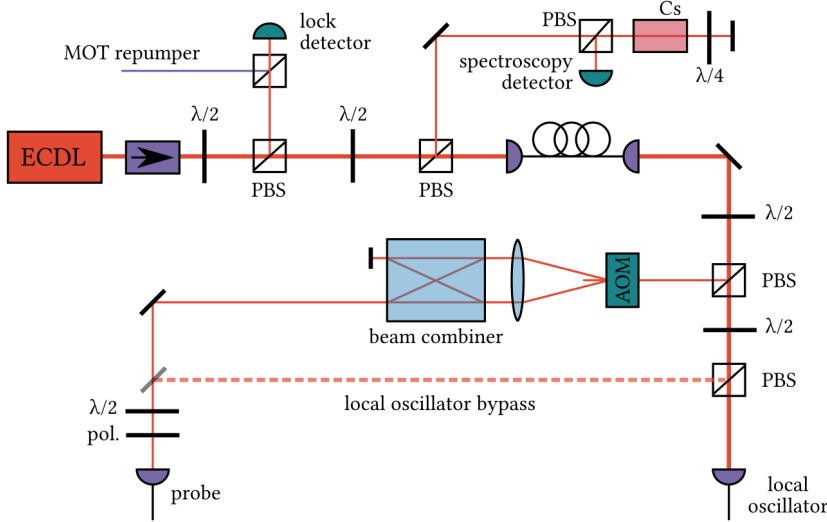


Figure 3.3: The setup for the two-color heterodyne probe light generation consists of a single ECDL beatnote locked to the MOT repumper (cf. app. D) as the common source for both LO and probe light. After the light is sent through a fiber for mode cleaning, the LO is split off and through a fiber reaches the interferometer part. An AOM modulates the desired sidebands onto the probe light, afterwards the two sidebands are combined. (If one sideband is blocked, the setup is reduced to a regular heterodyne measurement.) The balancing between the sidebands is controlled via the waveplate/polarizer combination in front of the probe fiber input. It is possible to send the LO through the probe fiber if high optical powers are necessary for alignment. In the interferometric part (not shown), both LO and probe light are split on 50/50 beamsplitters. The LO goes a long way to reach the whitelight point, this arm is stabilized with a piezo driven mirror. Probe light propagates in both directions through the atomic ensemble trapped around the nanofiber.

where $\epsilon = (A_1 + A_2)/2$. To measure φ , we lock the interferometer such that $\varphi_{\text{ref}} = 0$ and obtain

$$\varphi = \arctan \left(\frac{S_p(t)}{S_q(t)} \right). \quad (3.36)$$

To summarize, we have introduced two different methods of probing an atomic ensemble with light using heterodyne detection. With a single sideband, we can perform absorption spectroscopy by observing the change in amplitude probe light experiences when passing through the atoms. By employing two far-detuned sidebands, we detect the phase-shift imprinted by the atoms on the probe signal.

Sections 3.1 and 3.3 greatly benefited from the author's participation in the "Quantum Noise and Quantum Measurement" seminar led by Albert Schliesser.

Part II

NANOFIBER TRAPPED ATOMS

We begin by introducing our experimental platform, tapered optical nanofibers. We cover their properties, how to trap atoms in their vicinity, and present experimental data on some characteristics of these traps. In doing so, we introduce our setup. We end the part by presenting our methods for aligning and controlling light polarization and determination of the number of trapped atoms.

An optical nanofiber is an optical fiber with a diameter below the wavelength of the light it guides (eg. [Tong et al., 2012](#)). The strong confinement of light leads to optical properties remarkably different from standard fibers, most notably a large longitudinal polarization component and large evanescent fields, i. e. a significant fraction of the light is guided on the outside of the fiber.

Due to these optical properties and their straightforward integration using standard fiber technology, nanofibers are an exciting platform for atomic physics (e. g. [Vetsch et al., 2010](#), [Christensen, 2014](#), [Béguin, 2015](#)). On the one hand, it is possible to use the evanescent field to create a dipole trap around the fiber where atoms are tightly localized in a one-dimensional chain. In contrast to free-space dipole traps, the length of this chain is not limited by the Rayleigh length. On the other hand, the light is confined to an area comparable to the absorption cross-section of an atom, yielding a single atom optical depth (OD) about two orders of magnitude higher than in a comparable free-space dipole trap ([Béguin et al., 2014a](#)). In the context of quantum memories, this value is the figure of merit (sec. [5.1](#), [Hammerer et al. \(2010\)](#)). Furthermore, the complex polarization properties allow one to drive all atomic transitions through the fiber and the spontaneous emission on some transitions exhibits a chirality which can be exploited (sec. [4.2.3](#), [Le Kien and Rauschenbeutel \(2014a\)](#), [Mitsch et al. \(2014b\)](#)).

In this chapter, we first briefly describe the fabrication of nanofibers. Then, we outline their optical properties relevant to the experiment and treat the radiative interaction between nanofiber modes and atoms trapped in its vicinity. The creation and operation of a dipole trap around a nanofiber will be treated in chapter [5](#). We will discuss the benefits of a nanofiber for quantum physics in general in section [5.1](#) and more specifically for the two experiments described in this thesis – the atomic mirror and the creation of a single-excitation state – individually in sections [6.3](#) and [8.3](#).

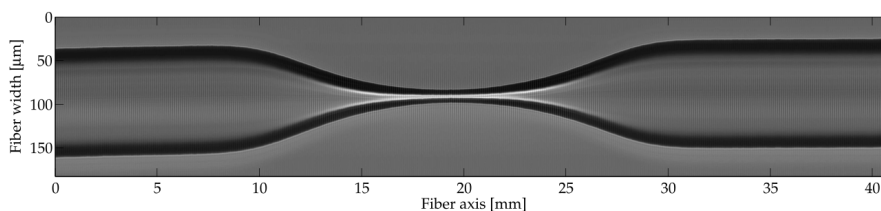


Figure 4.1: Microscope image of a nanofiber manufactured from a 100 μm diameter standard optical fiber (Image taken from [Sørensen, 2013](#)).

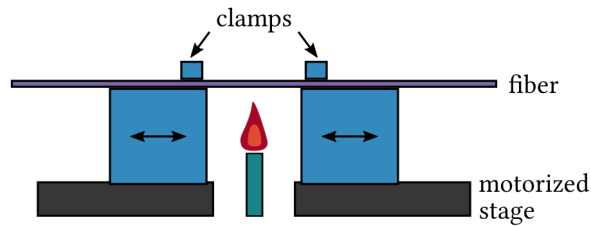


Figure 4.2: A typical nanofiber pulling rig consists of two motorized stages and a hydrogen torch.

4.1 FABRICATION

Nanofibers are manufactured top-down by heating and pulling standard optical fibers. Several methods are reviewed in [Brambilla \(2010\)](#). Here, we very briefly describe the flame-brushing technique which is the most widely used. The principle setup of a fiber pulling rig is depicted in [figure 4.2](#): The optical fiber is stripped and clamped down onto two motorized stages. A hydrogen torch is used to heat a small section of the fiber which at the same time is pulled. The resulting shape is controlled by the position and duration of heating and the speed and sequence of pulling (cf. [sec. 4.2.1](#)).

Due to this fabrication method optical nanofibers are “pigtailed” at both ends, i. e. there is at least a short section of regular fiber which can e. g. be spliced onto other fibers or to which a fiber coupler can be attached using standard techniques. Furthermore, due to negligible surface roughness optical nanofibers are mechanically robust ([Brambilla, 2010](#)).

At [QUANTOP](#) fiber production with a modified flame-brushing technique where the hydrogen torch is replaced by a ceramic oven is investigated ([Sørensen et al., 2014](#), [Sørensen, 2013](#)). The key difference is the larger, more uniform heating region which might be advantageous for the creation of more homogenous fiber shapes. While at the time of writing none of these fibers were yet in use for an atomic physics experiment, test measurements indicate that this fabrication method yields fibers with competitive properties ([Pedersen, 2015](#)).

For completeness, we briefly note that it is possible to further structure the nanofiber section (e.g. [Sumetsky et al., 2011](#), [Schell et al., 2015](#)) or to twist the nanofiber section into a loop, forming a ring resonator (cf. [Sumetsky et al., 2006](#), [Pedersen, 2015](#)). The latter is a promising path to further enhanced optical depths for atomic physics experiments ([sec. 11.2.1](#)).

4.2 LIGHT PROPAGATION

Given that the diameter d is smaller than the light’s wavelength λ it is obvious that the modes supported by a nanofiber will be drastically different from modes in standard optical fibers. In the introduction to this chapter we already mentioned that e. g. a large fraction of light will be guided *outside* of the fiber. This is illustrated in [figure 4.3](#) where we show a direct image

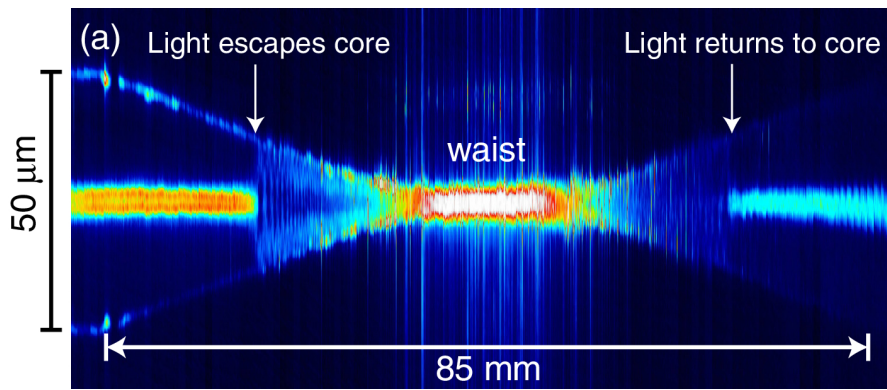


Figure 4.3: High resolution recording of Rayleigh scattering from a nanofiber. Light propagates from left to right. Modes which are not supported by the nanofiber section are lost (cf. sec. 4.2.1), hence less light leaves the fiber (Image taken from Hoffman et al., 2015).

obtained by Hoffman et al. (2015). While in a standard optical fiber light is guided by the core-cladding interface, below a certain diameter light escapes into the cladding and is guided by the cladding-air interface.

In this section we will present the implications of this change in guidance on the transmission properties and mode shapes as we will have to investigate the coupling of atoms to these modes. For a more detailed presentation we refer to Sagué Cassany (2008) and Béguin (2011).

4.2.1 Transmission and Thermal Properties

Transmission through a nanofiber is a crucial figure of merit if one wants to place it inside a vacuum chamber where only heat conduction through the nanofiber itself remains as a channel for excess thermal energy. To create a dual-color dipole trap for atoms, up to 20 mW of optical power need to be sent through the tapered section, so even the absorption of a few percent leads to heating. The resulting length change is significant and can directly be measured in an interferometer (e. g. Sørensen, 2013). Especially dangerous to a nanofiber are dust particles or other scatterers on its surface as well as “kinks” which can form during vibration. In both cases, absorption increases locally and the fiber melts. An extensive investigation of thermal properties of optical nanofibers can be found in Pedersen (2015).

Typical nanofibers for atomic physics experiments exhibit transmission well above 90%. The key to low losses is the shape of the tapered section, i. e. the transition region. Ideally, the light is transferred adiabatically into the nanofiber guided modes. Significant effort has been put into sophisticated algorithms to determine the optimal fiber shape and fabrication procedure (see e. g. Nagai and Aoki, 2014, Sørensen, 2013, Knudsen and Pedersen, 2014). At the time of writing, the highest reported transmission was $99.95 \pm 0.02\%$ which allows for transmission of more than 400 mW of optical power in high vacuum (Hoffman et al., 2014).

The fiber used in the experiments reported in this thesis was fabricated in 2010 in the group of Arno Rauschenbeutel at the University of Mainz and measured to 92% transmission at $\lambda = 852$ nm (Béguin, 2015, ch. 10).

4.2.2 Modes

A step-index fiber (cf. Saleh and Teich, 2007, ch. 9) consists of a core with refractive index n_{core} and a cladding with refractive index $n_{\text{cladding}} < n_{\text{core}}$. In these fibers, light rays are guided by total internal reflection at the core-cladding boundary if their angle of incidence is greater than the critical angle $\Theta_c = \arcsin(n_{\text{cladding}}/n_{\text{core}})$.

In general, two types of rays are distinguished: Meridional rays are confined to a plane which contains the fiber axis, while this is not the case for skewed rays. The latter thus follow a helical trajectory.

In the case of a nanofiber, there is only a silica core and no distinct cladding left, so that $n_{\text{core}} = 1.4469$ and $n_{\text{cladding}} = 1$ (cladding-air guidance, cf. fig. 4.3). This leads to a large critical angle $\Theta_c \approx 43.7^\circ$. Since the light entering the nanofiber is guided through a step-index fiber with $n_{\text{cladding}} = 1.4$, which thus has a critical angle $\Theta_c \approx 80^\circ$, we can make use of the paraxial approximation when calculating the supported modes. As we will see, this is an especially good approximation in the case of the fundamental and lower order modes.

The modes propagating through a step-index fiber can be calculated from Maxwell's equations as first principles. In this section, owing to the limited space and the fact that this is presented in great detail both in e.g. Sagué Cassany (2008) and Béguin (2015), we only set up the problem to then sketch some relevant parts of this calculation, thereby stating the results on which we build in the remainder of this thesis. We mainly follow Saleh and Teich (2007, ch. 9) and Sagué Cassany (2008).

To determine the modes supported by the fiber, we start with the Helmholtz equation in cylindrical coordinates

$$\frac{\partial^2 E}{\partial r^2} + \frac{1}{r} \frac{\partial E}{\partial r} + \frac{1}{r^2} \frac{\partial^2 E}{\partial \phi^2} + \frac{\partial^2 E}{\partial z^2} + n^2 k_0^2 E = 0 \quad (4.1)$$

where $k_0 = \omega/c$ is the wavevector of the propagating field in vacuum. We assume a wave travelling in z -direction which is periodic in ϕ with 2π , i. e.

$$E_z(r, \phi, z, t) = u(r) e^{i(\omega t - \beta z)} e^{-il\phi}. \quad (4.2)$$

Here, ω is the angular frequency of the wave, β is the propagation constant in the axial direction and $l \in \mathbb{Z}$. Inserting (4.2) into (4.1), we find

$$\frac{\partial^2 u(r)}{\partial r^2} + \frac{1}{r} \frac{\partial u(r)}{\partial r} + (n^2 k_0^2 - \beta^2 - \frac{l^2}{r^2}) u(r) = 0. \quad (4.3)$$

Since a mode is only guided when $n_2 k_0 < \beta < n_1 k_0$, we introduce

$$\begin{aligned} \kappa &= \sqrt{n_1^2 k_0^2 - \beta^2} \in \mathbb{R}, \\ \gamma &= \sqrt{\beta^2 - n_2^2 k_0^2} \in \mathbb{R}, \end{aligned}$$

which leads to two equations describing the propagation inside the core and cladding, respectively:

$$\frac{\partial^2 u(r)}{\partial r^2} + \frac{1}{r} \frac{\partial u(r)}{\partial r} + (\kappa^2 - \frac{l^2}{r^2})u(r) = 0, r < a \quad (4.4)$$

$$\frac{\partial^2 u(r)}{\partial r^2} + \frac{1}{r} \frac{\partial u(r)}{\partial r} - (\gamma^2 + \frac{l^2}{r^2})u(r) = 0, r > a. \quad (4.5)$$

Here, a is the fiber radius.

Equations (4.4) and (4.5) are variants of the (modified) Bessel differential equation with solutions

$$u(r) = \begin{cases} AJ_l(\kappa r) + BY_l(\kappa r) & r < a \\ CI_l(\gamma r) + DK_l(\gamma r) & r > a, \end{cases} \quad (4.6)$$

where J_l and Y_l (I_l and K_l) are the (modified) Bessel functions of first and second kind, respectively (Weisstein, a,b). Since $Y_l \rightarrow -\infty$ when $r \rightarrow 0$ and $I_l \rightarrow \infty$ when $r \rightarrow \infty$, we set $B = C = 0$. The complete solution for the electric field in z -direction then reads

$$E_z(r, \phi, z, t) = \begin{cases} AJ_l(\kappa r)e^{i(\omega t - \beta z)}e^{-il\phi} & r < a \\ DK_l(\gamma r)e^{i(\omega t - \beta z)}e^{-il\phi} & r > a. \end{cases} \quad (4.7)$$

The magnetic field component H_z can be calculated strictly analogously.

To determine E_ϕ and E_r as well as H_ϕ and H_r , we use Maxwell's equations $\nabla \times H = \epsilon(r)\partial_t E$ and $\nabla \times E = -\mu_0\partial_t H$ in cylindrical coordinates to set up a system of in total twelve differential equations of the form

$$E_r(r, \phi, z, t) = \begin{cases} -\frac{\beta}{\kappa} \left[iAJ_l'(\kappa r) - \frac{\omega\mu_0 l}{\beta} F \frac{J_l(\kappa r)}{\kappa r} \right] e^{i(\omega t - \beta z - l\phi)}, & r < a \\ \frac{\beta}{\gamma} \left[iDK_l'(\gamma r) - \frac{\omega\mu_0 l}{\beta} G \frac{K_l(\gamma r)}{\gamma r} \right] e^{i(\omega t - \beta z - l\phi)}, & r > a \end{cases} \quad (4.8)$$

which are stated explicitly in Sagué Cassany (2008, p. 129/30). By requiring that the boundary conditions

$$E_{\phi,z}(r \rightarrow a^-) = E_{\phi,z}(r \rightarrow a^+), \quad (4.9)$$

$$H_{\phi,z}(r \rightarrow a^-) = H_{\phi,z}(r \rightarrow a^+), \quad (4.10)$$

$$P = \frac{\omega}{2\pi} \int_0^{2\pi} dt \int_S S_z dS \quad (4.11)$$

with S_z the component of the Poynting vector along the fiber axis and P the total transmitted power are fulfilled, conditions for the constants A , D , F , and G are found. From these, an equation for the propagation constant β can be derived:

$$\begin{aligned} \left(\frac{J_l'(\kappa a)}{\kappa a J_l(\kappa a)} + \frac{K_l'(\gamma a)}{\gamma a K_l(\gamma a)} \right) \left(\frac{n_1^2 J_l'(\kappa a)}{\kappa a J_l(\kappa a)} + \frac{n_2^2 K_l'(\gamma a)}{\gamma a K_l(\gamma a)} \right) \\ = l^2 [(\kappa a)^{-2} + (\gamma a)^{-2}]^2 \left(\frac{\beta}{k_0} \right)^2. \end{aligned} \quad (4.12)$$

This is the so-called mode condition, for which sets of solutions exist for a given l . These are discussed in [Béguin \(2015, ch. 6\)](#) and [Sagué Cassany \(2008, ch. 1\)](#). Here, we immediately restrict our discussion to the fundamental mode HE_{11} which is the only mode that exists regardless of the nanofiber's diameter. Hence, the nanofiber is pulled below the cut-off diameter for all higher order modes (for an experimental demonstration, cf. [Sørensen, 2013, ch. 4](#)).

We further only discuss the properties of the evanescent field in detail, as we are interested in the coupling of atoms positioned in the vicinity of the fiber surface to the guided mode. The evanescent field is described by the mode profile function $e(\mathbf{r})$, whose components in cylindrical coordinates $(\hat{r}, \hat{\phi}, \hat{z})$ read ([Le Kien and Rauschenbeutel, 2014a, app. A](#))

$$\begin{aligned} e_r &= iC [(1-s)K_0(\gamma r) + (1+s)K_2(\gamma r)], \\ e_\phi &= -C [(1-s)K_0(\gamma r) - (1+s)K_2(\gamma r)], \\ e_z &= C \frac{2\gamma}{\beta} K_1(\gamma r), \end{aligned} \quad (4.13)$$

where

$$s = \frac{(\kappa^2 a^2)^{-1} + (\gamma^2 a^2)^{-1}}{J_1'(\kappa a) [\kappa a J_1(\kappa a)]^{-1} + K_1'(\gamma a) [\gamma a K_1(\gamma a)]^{-1}} \quad (4.14)$$

and C such that

$$\int_0^{2\pi} d\phi \int_0^\infty dr r n^2(r) |e|^2 = 1 \quad (4.15)$$

where $n(r)$ is a step-function with values $n(r) = n_1$ for $r < a$ and $n(r) = 1$ otherwise. Since C will drop out in all subsequent calculations, we will not carry out this normalization. An explicit expression is given in [Béguin \(2015, eq. 6.25\)](#).

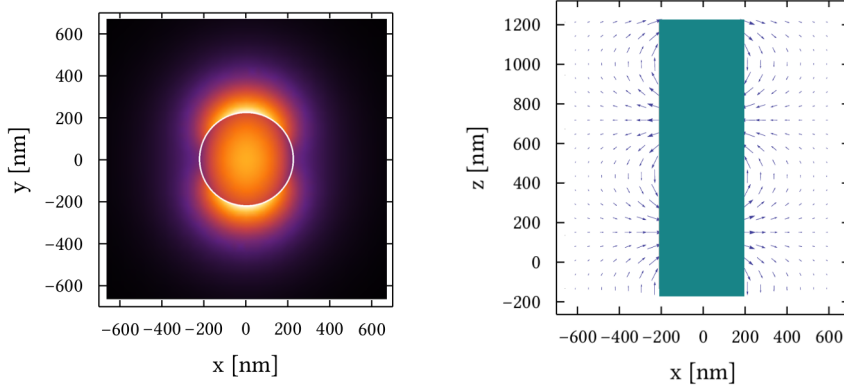
4.2.3 Polarization

To determine the polarization in the evanescent field, it is convenient to choose two orthogonal polarizations. A natural choice given [\(4.13\)](#) is the so-called quasicircular polarization basis, with basis vectors

$$\tilde{\sigma}_{l,\pm} = e_r \hat{r} + l e_\phi \hat{\phi} \pm e_z \hat{z} \quad (4.16)$$

describing a field propagating along the z -axis in the direction given by the sign in front of the z -component, rotating in the direction given by $l \in (-1, 1)$. We also see that polarization in the evanescent field of a nanofiber is a local property.

However, this choice of polarization is inconvenient for two reasons: First, it is difficult to describe coupling to atoms, where we would like to treat (linear) pi - and (circular) σ_\pm -transitions (cf. [sec. 4.3.1](#)). Second, it is experimentally easier to align the polarization at the nanofiber to be linear (cf. [sec. 5.6](#)).



(a) Field intensity for V -polarized light. The intensity profile for H -polarized light is identical, but rotated by 90° . (b) Polarization H in the x - z -plane. (Adapted from Béguin (2015).)

Figure 4.4

Consequently, we choose the quasilinear basis which can be obtained from (4.16) by (Le Kien and Rauschenbeutel, 2014a, app. A)

$$\tilde{x}_\pm = \frac{\tilde{\sigma}_{1,\pm} \exp(i\varphi) + \tilde{\sigma}_{-1,\pm} \exp(-i\varphi)}{\sqrt{2}} \quad (4.17)$$

$$\tilde{y}_\pm = \frac{\tilde{\sigma}_{1,\pm} \exp(i\varphi) - \tilde{\sigma}_{-1,\pm} \exp(-i\varphi)}{i\sqrt{2}} \quad (4.18)$$

with mode profile functions

$$\begin{aligned} e^{\pm,x} &= \sqrt{2} (e_r \cos \varphi \hat{r} + i e_\varphi \sin \varphi \hat{\phi} \pm e_z \cos \varphi \hat{z}) \\ e^{\pm,y} &= \sqrt{2} (e_r \sin \varphi \hat{r} - i e_\varphi \cos \varphi \hat{\phi} \pm e_z \sin \varphi \hat{z}). \end{aligned} \quad (4.19)$$

To prevent confusion and ambiguity in terminology, we from here on through the remainder of this thesis refer to light quasilinearly polarized in the reference frame of the nanofiber as V for light polarized along the y -axis (cf. fig. 4.4a) and H for light polarized along the x -axis. This reflects the configuration in the laboratory frame, where y coincides with the gravity axis and the x -axis is parallel to the floor (cf. fig. 4.5).

4.3 INTERACTION OF GUIDED MODES WITH ATOMS

The coupling of modes with emitters in its vicinity is what makes nanofibers an interesting platform. While atoms are a natural choice considering their inherent indistinguishability and the vast amount of previous work on their manipulation (and the resulting ease thereof, cf. sec. 5.1), coupling of e. g. nitrogen vacancy centers (Liebermeister et al., 2014), quantum dots (Yalla et al., 2012), and nanocrystals (Joos and Glorieux, 2015) has been reported. Outside of quantum physics the interaction of nanofibers with a rich variety of emitters is studied (cf. sec. 4.4).

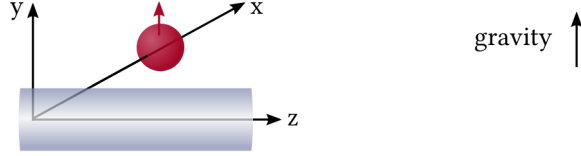


Figure 4.5: In the coordinate system used throughout this thesis, the z -axis is the fiber axis. We quantize atoms along y , which coincides with the gravity axis.

4.3.1 Light Polarization in the Atom's Reference Frame

In section 4.2.3 we have seen that the polarization of light in the evanescent field is not only non-transversal, but also a local property. We will now investigate the polarization for an atom placed on the positive x -axis. Contrary to convention, we quantize the atom along the y -axis, which in our experiment is also the gravity axis and the direction of the magnetic bias field. We will use this convention throughout this thesis (fig. 4.5).

From (4.19) we find the mode profile functions on the positive x -axis ($\varphi = 0$) in the cartesian coordinate system (x, y, z) to be [Le Kien and Rauschenbeutel \(cf. 2014a\)](#)

$$\mathbf{e}^{(\pm, H)} = \sqrt{2} (i |e_r|, 0, \pm |e_z|)^T$$

$$\mathbf{e}^{(\pm, V)} = \sqrt{2} (0, i |e_\phi|, 0)^T. \quad (4.20)$$

$$(4.21)$$

We see that in the atom's reference frame, V appears as linearly polarized, whereas H is rotating.

For an atom on the negative x -axis, V is linearly polarized as well, but for H the direction of rotation reverses, i. e. H appears as

$$\mathbf{e}^{(\pm, H)} = \sqrt{2} (i |e_r|, 0, \mp |e_z|)^T. \quad (4.22)$$

This reversal is a consequence of the choice of y as the quantization axis, which breaks the system's symmetry, and – as we will show in the next section – has dramatic consequences for the coupling between the nanofiber's guided mode and atoms.

We point out that in a more complete treatment, one has to consider that photons – which we made no mention of – propagating along the fiber carry not only spin angular momentum, but also orbital angular momentum. See [Béguin \(2015, ch. 8\)](#) for an extensive discussion of this topic.

4.3.2 Directionality of Spontaneous Emission

The emission of a single cesium atom into the fundamental guided mode of a nanofiber is studied in detail in [Le Kien et al. \(2005\)](#) and [Le Kien and Rauschenbeutel \(2014a\)](#), whose main result we will now summarize. We treat the case of a two-level atom positioned on the positive part of the x -axis and

light propagating along the positive z -direction, as is depicted in figure 4.5. As the basis of polarization of guided modes we choose H and V ; again the quantization axis for the atom is y .

The total scattering rate of the atom is given by

$$\Gamma_{\text{total}} = \gamma + \Gamma_{\text{fs}}, \quad (4.23)$$

where Γ_{fs} is the emission into free space and γ the rate of spontaneous emission into guided modes. The latter is given by (cf. eq. 2.14)

$$\gamma^{(\pm, \xi)} = \frac{\omega_0 \beta'_0}{2\epsilon_0 \hbar} \left| \mathbf{d} \cdot \mathbf{e}^{(\omega_0, \pm, \xi)} \right|^2, \quad (4.24)$$

where ω_0 is the atomic resonance frequency and $\beta' = \partial\beta/\partial\omega$ is the derivative of the propagation constant β with respect to ω (cf. eq. 4.12). In the superscript of the mode function \mathbf{e} , $\xi \in (H, V)$ is the polarization of the mode and the sign denotes the direction of propagation ($\pm z$). Thus, γ can be split into four components:

$$\gamma = \gamma^{(-, H)} + \gamma^{(-, V)} + \gamma^{(+, H)} + \gamma^{(+, V)}. \quad (4.25)$$

σ_{\pm} -transitions

We first treat σ_{\pm} transitions and let $q = m_{F'} - m_F = \pm 1$ denote the circularity in the atom's reference frame. In the reference frame of the fiber, the atom's dipole matrix-element vector is

$$\mathbf{d}_q = \frac{d_q}{\sqrt{2}} (i, 0, -q)^T, \quad (4.26)$$

where d_q is the spherical tensor component in the atom's reference frame, i. e.

$$d_q = \frac{-q(d_z + iq d_x)}{\sqrt{2}}. \quad (4.27)$$

What determines the coupling of a fiber mode to a component of the atom's dipole matrix-element is (cf. eq. 4.24)

$$\mathbf{d}_q \cdot \mathbf{e}^{(\pm, \xi)} = \frac{d_q}{\sqrt{2}} \left(i e_x^{(\pm, \xi)} - q e_z^{(\pm, \xi)} \right). \quad (4.28)$$

For V -polarized modes, $e_x^{(\pm, V)} = e_z^{(\pm, V)} = 0$ (eq. (4.20)) and (4.24) yields $\gamma^{\pm V} = 0$, i. e. as expected from section 4.3.1 σ_{\pm} transitions do not couple to V -polarized modes.

However, $e_x^{(\pm, H)} = i\sqrt{2}|e_r|$ and $e_z^{(0, \pm, H)} = \pm\sqrt{2}|e_z|$, which together with (4.24) leads to

$$\gamma^{(\pm H)} = \frac{\omega_0 \beta'_0}{2\epsilon_0 \hbar} d_q^2 (|e_r| \pm q |e_z|)^2. \quad (4.29)$$

We see that the rate of spontaneous emission of σ_{\pm} light into guided H -polarized modes depends on both the circularity of the emitted light and

the mode's propagation direction. From (4.29) it is clear that this remarkable feature is a consequence of the longitudinal component of the mode's polarization.

It is straightforward to calculate the ratio

$$\frac{\gamma^{(+H)}}{\gamma^{(-H)}} \Big|_{q=1} = \left(\frac{|e_r| + |e_z|}{|e_r| - |e_z|} \right)^2 = \frac{\gamma^{(-H)}}{\gamma^{(+H)}} \Big|_{q=-1}, \quad (4.30)$$

which we plot in figure 4.6 both for the fiber used in our experiment as well as nanofibers of different diameter. We see from (4.30) that the directionality is a feature of the mode, but point out that the atom's emission frequency ω_0 enters as a parameter.

The directionality of emission into H -polarized modes has been studied and confirmed experimentally by Mitsch et al. (2014b) for the $|F' = 5, m_F = 5\rangle \rightarrow |F = 4, m_F = 4\rangle$ transition in cesium, which is an excellent approximation of a two-level atom (cf. sec. 2.2).

What is left to consider is the case of an identical atom placed symmetrically on the negative part of the x -axis. In this case, $e_x^{(pm,H)} = i\sqrt{2}|e_r|$ and $e_z^{(\pm,H)} = \mp\sqrt{2}|e_z|$. Now we have to consider our discussion about light polarization in the atom's reference frame: If we were to expect emission from a σ_+ transition from an atom on the positive x -axis, in the reference frame of the nanofiber this is equivalent to emission from a σ_- transition for an atom placed on the negative x -axis. If we substitute $q \rightarrow \tilde{q} = -q$, we arrive at the same directionality.

H as a Mixture of σ_{\pm} -polarized Light

We remark that the ratio between forward and backward scattering can also be understood by expressing H – locally at the atom's position and in the latter's reference frame – as a mixture of σ_+ and σ_- polarized light. The ratio is given by (4.30), i. e.

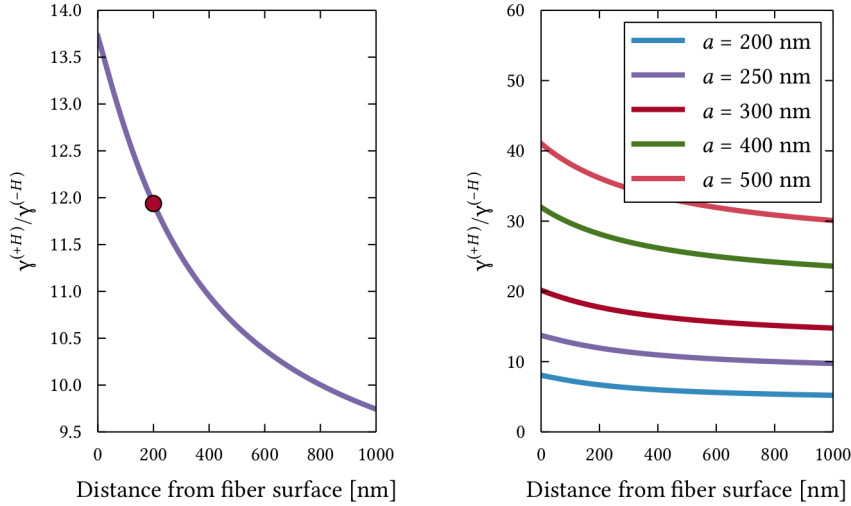
$$\begin{aligned} H &= \frac{\gamma^{(+H)} \Big|_{q=+1}}{\gamma^{(+H)} \Big|_{q=+1} + \gamma^{(+H)} \Big|_{q=-1}} \sigma_+ + \frac{\gamma^{(+H)} \Big|_{q=-1}}{\gamma^{(-H)} \Big|_{q=+1} + \gamma^{(+H)} \Big|_{q=-1}} \sigma_- \\ &= 0.9227\sigma_+ + 0.0773\sigma_-, \end{aligned} \quad (4.31)$$

where in the second line we give the ratio as it appears in our experiment (cf. fig. 4.6a).

So while in many cases, we can neglect the contribution of the σ_- -polarized component and treat H as σ_+ , for a complete analysis e. g. of optical pumping this has to be taken into account (cf. sec. 8.3).

π -transitions

For π -transitions, the atom's dipole tensor in the fiber's reference frame is $(0, d_0, 0)^T$, where again d_0 is the spherical tensor component in the atom's reference frame. We immediately see that π -transitions do not couple to H -polarized modes. Since both the mode function and the atom's dipole tensor



- (a) Calculation for the nanofiber used in the experiment ($a = 250$ nm). The atom's position in the trap (cf. fig. 5.1b) is marked with a red dot. We thus expect a twelve-fold enhancement of forward-scattering for σ_+ transitions.
- (b) Directionality of emission of σ_+ polarized light into the fundamental mode HE_{11} for different nanofiber radii.

Figure 4.6: Since $\gamma^{(+H)}/\gamma^{(-H)}$ is determined by the magnitude of the fiber guided mode's longitudinal component, it is sensitive to the fiber radius a . For a given fiber, the ratio $\gamma^{(+H)}/\gamma^{(-H)}$ depends on the distance of the atom above the fiber surface.

All calculations were performed for a fiber with $n_1 = 1.4469$, $n_2 = 1.0$ and emitted light of wavelength $\lambda = 852.35$ nm.

The left figure is similar to figure 11 of [Le Kien and Rauschenbeutel \(2014a\)](#). We thank Jean-Baptiste Béguin for the algorithm to find the propagation constant β .

have only one non-zero component, the emission couples equally into the forward and backward propagating V -polarized mode, i. e.

$$\gamma^{+V} = \gamma^{-V} \Rightarrow \frac{\gamma^{+V}}{\gamma^{-V}} \Big|_{q=0} = 1. \quad (4.32)$$

Expanding on our remark above, we can again relate this to the mixture of polarization in the atom's reference frame: Since V is a balanced mixture of two counterrotating circular polarization components (sec. 4.2.3), the modes $+V$ and $-V$ are indistinguishable in the atom's reference frame and no directionality can arise.

Coupling Strength

Using the same approach as before, we can also find the relative coupling strengths of H and V light. To this end, we calculate

$$\frac{\gamma^{+H} \Big|_{q=+1}}{\gamma^{+V} \Big|_{q=0}} = \left(\frac{d_1}{d_0} \cdot \frac{|e_r| + |e_z|}{|e_\phi|} \right)^2 \approx 5 \cdot \left(\frac{d_1}{d_0} \right)^2, \quad (4.33)$$

where in the last step we have assumed (cf. fig. 4.6) that the atom is placed 200 nm above the fiber surface and probed with light of wavelength $\lambda = 852.35$ nm. We find that the coupling of H to the atoms's σ_+ -transitions is significantly stronger than that to π -transitions. This can be understood qualitatively by considering that if the atoms are positioned on the x -axis, they are placed in the region of lowest intensity of the V polarized component of the evanescent field (cf. fig. 4.4a).

4.3.3 Chains of Atoms

So far, we have considered the case of a single atom coupled to the fundamental mode of a nanofiber. If instead multiple atoms are present, their emission properties can be drastically altered. Here, we will briefly discuss if, when, and how this is the case.

Generally, atoms around a nanofiber can be treated as independent emitters as long as they are not arranged in a periodic structure yielding Bragg resonances (Le Kien and Rauschenbeutel, 2014b). While we discuss these structures in part III and present a theoretical treatment there, the lattice created by our dual-color dipole trap as described in the next chapter is far from any such resonance.

Another interesting ensemble phenomenon is superradiance, which can occur when multiple emitters are coupled to the very same photonic mode. Then, their radiative decay rate can be greatly enhanced compared to a single, independent emitter (cf. Gross and Haroche, 1982, Goban et al., 2015). As the coupling of atoms to the guided modes of a nanofiber is weak compared to their coupling to radiation modes, superradiance is not observed.

4.4 FURTHER APPLICATIONS

In this chapter, we have presented the foundations for atomic quantum physics around a nanofiber. After introducing a method to trap atoms in the next chapter we will at lengths discuss two atomic physics experiments and in chapter 11 explore future directions for this line of research. Hence it might very well seem that atomic physics is the only application of optical nanofibers. To rectify this impression we will in this section give a short review of selected other applications.

The investigation of scatterers in the evanescent field of nanofibers is not limited to atoms. To this end, either the interaction of particles with the evanescent field is studied directly or the fiber surface is functionalized, i. e. covered with a material that interacts with the particles of interest. [Edwards et al. \(2014\)](#), who demonstrate a proof of concept for Raman scattering spectroscopy, highlight the low cost and ease of fabrication¹ as well as the small size of nanofibers as advantageous for sensing applications. The mechanical robustness of nanofibers also allows for their placement in liquids. [Driscoll et al. \(2015\)](#) report the sensing of aluminum nanorods in an aqueous solution and emphasize that since the particles only float by the nanofiber instead of attaching to its surface, this variant compares favorably in lifetime and reusability.

The robustness and large evanescent field are also exploited to drive whispering gallery mode (WGM) resonators. While these can be studied in their own right (for an interesting example see e. g. [Peng et al., 2014](#)), they are frequently used for sensing ([Foreman et al., 2015](#)) and in optomechanics. An example of the latter is reported by [Li et al. \(2015\)](#) who couple light from a nanofiber into a silica microsphere WGM resonator suspended from a cantilever by bringing the latter less than 1 μm above the fiber surface. Through an active feedback system the dipole forces between the nanofiber and the microsphere are controlled in such that their mechanical oscillation – either the microsphere’s center of mass motion, the nanofiber’s mechanical modes, or both simultaneously – is cooled.

A third area of application is the study of nonlinear optics in nano- and microfibers ([Brambilla, 2015](#)). For example, [Lee et al. \(2012\)](#) report third harmonic generation in silica microfibres with a diameter below 2.5 μm . To this end, several modes have to be phase-matched. Interestingly, it is the transition region (cf. fig. 4.3) where the signal is generated.

This section greatly benefited from the author’s participation in the “Optical Nanofiber Applications: From Quantum to Bio Technology” workshop held in May 2015 in Okinawa, Japan. Funding by the Okinawa Institute of Science and Technology and travel funding by QUANTOP is gratefully acknowledged.

¹ As long as the nanofiber is not placed in vacuum, transmission losses of several 10% are tolerable which greatly reduces the demands on the fabrication process.

[I]n order to carry out logic the information bearing degrees of freedom must interact strongly with each other. At the same time, to preserve coherence, they cannot interact with anything else, including the physical framework that holds the bits in their positions. That is a tall order!

— Rolf Landauer: *The physical nature of information*

As introduced in section 2.4.3 atoms placed in oscillating electromagnetic fields experience a dipole force which can be used for trapping. By combining two evanescent fields created by a blue and a red detuned laser beam sent through a nanofiber, we can trap atoms at an in principle arbitrary distance from the fiber surface. Such a dual-color dipole trap was proposed by [Le Kien et al. \(2004\)](#) and first realized by [Vetsch et al. \(2010\)](#). In the past years it was the topic of many experimental efforts, a large portion of which is mentioned within this thesis and can therefore be found in the [bibliography](#).

We start this chapter by recapitulating the motivation to use nanofiber trapped atoms for quantum physics. Subsequently, we discuss in more detail the trap configuration and its experimental realization. Following a description of the trap operation, we present some experimentally determined properties, most notably the radial trap frequency. Towards the end of the chapter, we describe in detail how to align and maintain the polarization of the trap lasers and explain our method of counting the number of trapped atoms.

Before we begin, we note that while the trapping of atoms in a dipole trap around the nanofiber is advantageous in many regards, it is by no means necessary. A large number of experiments can be performed with a MOT cloud around the tapered section, ranging from fundamental interaction studies (e. g. [Sagué Cassany \(2008\)](#) and resulting publications; or [Béguin \(2015\)](#)) to the demonstration of a memory for light ([Gouraud et al., 2015](#)). In terms of retrieval efficiency, the latter (10 %) compares favorably to the virtually identical experiment with dipole trapped atoms, where [Sayrin et al. \(2015\)](#) reported 3 %, although with a much lower number of atoms. As we shall see in the next section, in many experimental scenarios the latter is a key advantage.

5.1 NANOFIBER TRAPPED ATOMS AS A LIGHT-MATTER INTERFACE

Before we dive into the setup, operation and properties of our nanofiber trap, we will take a step back and discuss why a few thousand cesium atoms trapped around a nanofiber are an excellent light-matter interface which in

the context of quantum memories – or, more humbly, quantum state engineering – is in some important ways superior to prior cavity and free-space realizations.

As is summarized in the quote at the beginning of this chapter, the sorcerer’s stone of quantum information research is a quantum system which is completely isolated from its surroundings, entirely detached from the Universe, yet interacts strongly with the particles we use to communicate with it. Depending on the desired application, very good approximations to these ideal systems can be created (cf. [Haroche and Raimond, 2006](#)).

As we have discussed in chapter 2, atoms are ideal candidates to form the system. First of all, they are inherently indistinguishable, i. e. all atoms of the same species have identical properties. However, in many situations atoms can gain individuality (cf. [French, 2015](#)) by their spatio-temporal location, e. g. if atoms are trapped in distant lattice sites which can be resolved optically. More subtly, this is also the case for atomic vapors in a Gaussian beam dipole trap, where atoms at the intensity maximum are more likely to scatter a photon compared to those further out. The nanofiber trap removes these mechanisms: All atoms couple to the very same single photonic mode – by monitoring the output of the fiber, it is impossible to know where the atom emitting the photon was located along the fiber¹ – and the light field intensity at each atom’s location is identical to a much better degree than in a Gaussian beam. We will return to this important feature in section 8.3 when we discuss how to eliminate individuality gained from different absorption probabilities for atoms along the fiber.

More practical, the internal state of atoms can be controlled with high precision and they can be trapped and cooled relatively easily. Since atoms are electrically neutral, large numbers of identical qubits can be gathered in a small region and they are immune to electric charges. The latter is important in the context of a nanofiber since its surface is in general charged, which e. g. poses great difficulties when one tries to trap ions nearby ([Colombe, 2015](#)). While the effect of surface charges on the atoms is negligible compared to the ac-Stark shifts caused by the dipole trap (cf. sec. 2.4.3), the nanofiber exerts attracting van-der-Waals forces on the atoms which have to be taken into account.

Cesium is an excellent choice for quantum state engineering since its two hyperfine groundstates are stable, form an excellent approximation of a two-level system (cf. sec. 2.2), can be addressed by technologically well-controllable microwaves (sec. 9.2) and due to their large splitting be separated optically (cf. sec. 6.4 and 9.1).

The absence of scattering in a far-detuned dipole trap (sec. 2.4.3) is what allows for long coherence times and the preparation of quantum superpositions. Compared to a freespace dipole trap, the standing wave configuration (sec. 5.2) with only a single atom per lattice site (sec. 5.5.1) removes collisions between atoms as a source of decoherence – only collisions with back-

¹ Unless the timestamp of the detection event carries information on location, cf. the discussion towards the end of section 8.3.

ground vapor remain. It is also possible to realize trap configurations where the atoms are not confined to pointlike positions and can move along the fiber freely. We will briefly discuss some variants in section 11.2.2.²

As stated above, the light field is identical for all atoms to very good approximation and therefore the dipole trap induced ac Stark shifts are identical for all atoms, eliminating a disadvantage of Gaussian beam dipole traps. The resulting fictitious magnetic fields can however still be problematic (cf. sec. 9.2). Due to the close proximity to the fiber and the large³ overlap of the evanescent field with the atomic absorption cross-section atoms in the dual-color dipole trap couple strongly to the guided mode. This coupling can be maximized via the trap laser powers (sec. 5.2); the advantage of the resulting high single-atom optical depth for quantum state engineering (Hammerer et al., 2010) will be discussed in more detail in 8.3. A much more elaborate version of this discussion can be found in Béguin (2015, sec. 15.1).

We note that much of what we said about nanofibers is true for hollow core fibers as well. The main advantage of nanofiber based traps is the easier loading process which allows for higher repetition rates (cf. sec. 5.4.1) and optical accessibility from all spatial directions, all of which comes at the expense of a much more involved optical setup for the trap light (cf. e.g. Vorrath et al., 2010). In addition, nanofibers can be integrated into fiber based optical setups without the need for waveguide couplers (cf. sec. 4.1 and sec. 11.2.4). The latter and their more involved fabrication is a drawback hollow core fibers share with so-called “alligator” waveguides pioneered by Yu et al. (2014) which are otherwise very similar to nanofibers.

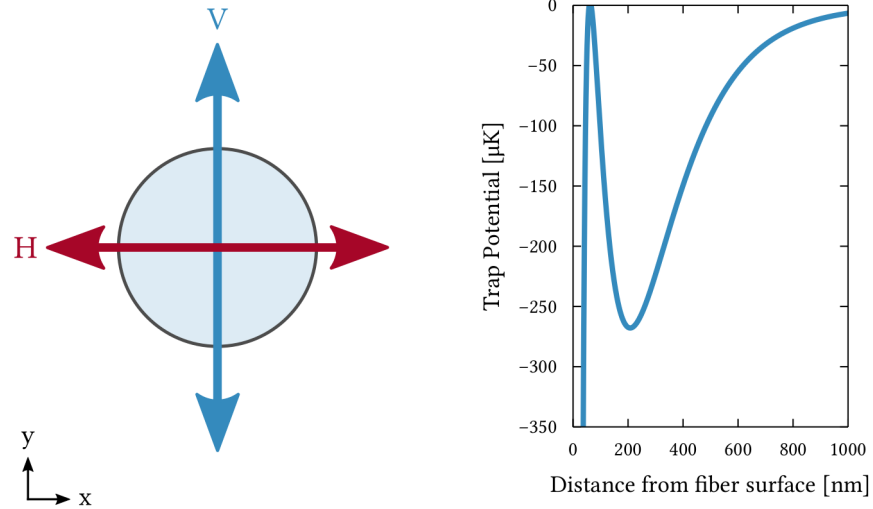
It almost goes without saying that photons in the infrared or visible domain are ideal candidates as the means of communication with an isolated quantum system: As non-interacting bosonic particles they can travel long distances undisturbed – both through fibers and free space – and are the prime carrier of quantum information (cf. Haroche and Raimond, 2006, Nielsen and Chuang, 2000). More practically speaking, the creation of light with arbitrary frequencies in the range of the atom’s resonances is a superbly mastered trade, as is the manipulation of its polarization. In section 3.4.1 we have already introduced a scheme where back-action through ac Stark shifts is evaded allowing for QND measurements. There, we have also discussed the detection of light.

5.2 TRAP CONFIGURATION AND POTENTIAL

To trap atoms around the nanofiber by means of a dipole trap, it is clear that we need to engineer a potential by combining an attractive force – preferably long-range – with a (short-range) repulsive one that keeps the atoms well above the fiber surface and out of reach of the van der Waals attraction.

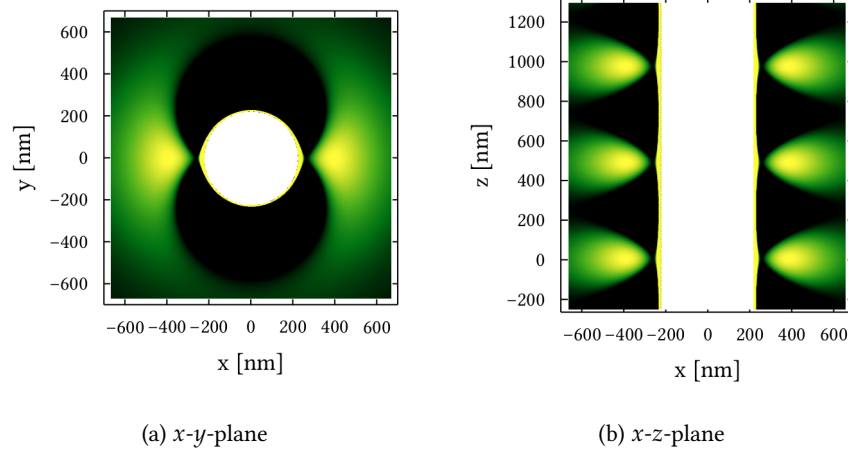
² We note here that a standing wave configuration has the further advantage that vector light shifts induced by the blue-detuned trap light are cancelled, cf. (cf. Béguin, 2015, sec. C.2.3) and sec. 4.2.3.

³ It is on the order of 100.



(a) Polarization alignment of the red and blue trap laser. The atoms are thus trapped on the sides of the nanofiber (cf. fig. 5.2). (b) Calculated trap potential for the caterpillar trap configuration with orthogonal quasilinearly polarized trap light for $P_{\text{blue}} = 14 \text{ mW}$ and $P_{\text{red}} = 2 \times 1.3 \text{ mW}$. The atoms are located about 200 nm above the fiber surface.

Figure 5.1: Laser configuration and trap potential for the caterpillar trap used for the experiments in this thesis.



(a) x - y -plane (b) x - z -plane

Figure 5.2: Calculated trap potentials for the caterpillar trap configuration with orthogonal quasilinearly polarized trap light. The atoms are trapped in two rows on opposite sides of the nanofiber. Each of the anharmonic trap sites contains at most one atom (sec. 5.5.1).

In this section, we will briefly outline the realization of this concept used for the experiments described in this thesis. An in-depth discussion rich in historical remarks and references can be found in [Béguin \(2015, ch. 15\)](#).

The configuration in the pioneering work by [Vetsch et al. \(2010\)](#) which we also utilize is that of orthogonally quasilinearly polarized trap light (fig. [5.1a](#)). Other possible configurations include parallel quasilinear polarization ([Goban et al., 2012](#)) or arbitrary angles between the quasilinearly polarized light found by maximizing the atomic ensemble’s optical depth ([Lee et al., 2015](#)). Non-caterpillar type traps created by using higher order nanofiber modes will briefly be discussed in section [11.2.2](#).

The distance of the atoms above the fiber surface and hence their coupling to the guided mode (cf. sec. [4.3](#)) is controlled by balancing the power of the blue-detuned trap light P_{blue} and the power of the red-detuned trap light P_{red} . In figures [5.1b](#) and [5.2](#) we show the calculated⁴ trap potentials for the nominal light powers used in the experiments described in this thesis. In practice, we first adjust P_{blue} to the desired value and then adjust P_{red} for maximum observed OD.

While we will not go into detail, we remark that the complex rotating polarization in the evanescent field of the nanofiber gives rise to vector light shifts, which appear as fictitious magnetic fields. Due to the standing wave configuration, in the caterpillar trap these shifts are cancelled at the nodes. Since the fictitious magnetic fields couples the Zeeman levels, if they are to be addressed separately, a several gauss strong magnetic bias field has to be applied.

The trap presented here is not state-insensitive, i. e. there is no stable trapping potential for excited states and the atomic sublevels are inhomogeneously broadened. A configuration with “magic” wavelengths ($\lambda_{\text{red}} = 937$ nm, $\lambda_{\text{blue}} = 686$ nm), where differential scalar light shifts are evaded completely and vector shifts are greatly suppressed (cf. [Béguin, 2015, sec. C.3](#)) was reported by [Goban et al. \(2012\)](#). We do not utilize such a configuration since we are mainly interested in achieving high groundstate coherence times, consequently we exploit the reduced scattering due to farther detuned trap light.

5.3 OPTICAL SETUP

The trap light is provided by two free running external cavity diode lasers (ECDLs) (cf. app. [D](#)). One is operated at nominally 1057 nm, the other at 780 nm. In the following we will refer to these as the *red* and *blue trap laser*, respectively.

The blue trap laser is sent through a waveplate/polarizer combination for power adjustment, a fiber for mode cleaning, and enters the nanofiber from port B. The setup of the red trap laser is similar, with the addition of an AOM. The latter protects the ECDL from back-reflected light and can be used to switch off the trap (cf. sec. [5.5.3](#)). After the mode cleaning fiber the trap light is split on a polarizing beamsplitter (PBS) and enters the nanofiber from both

⁴ We thank Jean-Baptiste Béguin for access to the Mathematica scripts

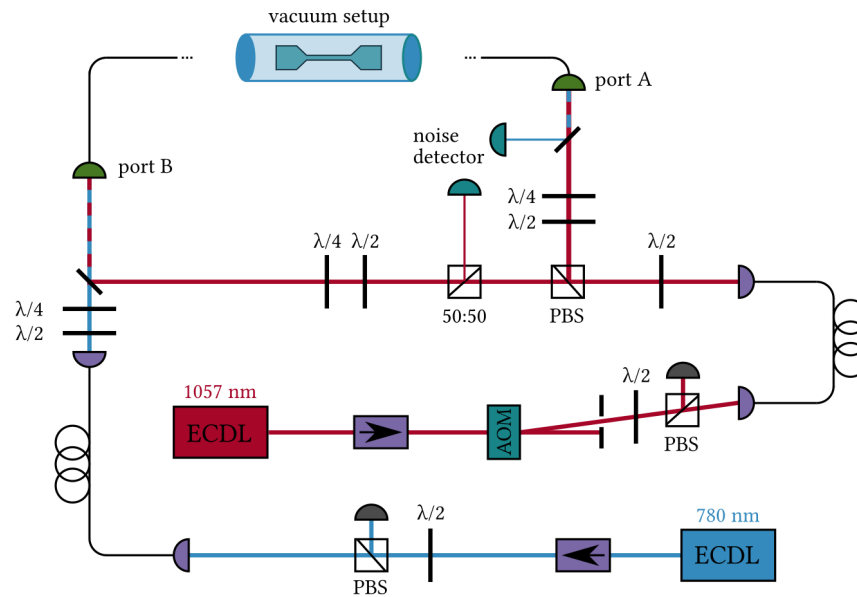


Figure 5.3: The trapping setup consists of two ECDLs, which are each power-adjusted, mode-cleaned and coupled into the nanofiber ports. Numerous passive optical elements not essential for the operation of the setup have been omitted.

ports in order to form a standing wave. The power balancing between the two arms is controlled manually with a waveplate in front of the PBS.

As indicated in figure 5.3 both colors of trap light leaving the nanofiber are sent onto a balanced photodetector. While the blue-detuned trap light is split off with a dichroic mirror at port A, the red-detuned trap light leaving the nanofiber at port A is split off by a beamsplitter cube. This enables monitoring of the noise of the lasers as it is critical for the trap quality that both ECDLs are operated at the shot noise limit.⁵ To this end, the home-built photodetector is designed with two different photodiodes optimized to the respective wavelengths. The gain is tailored such that it is possible to only operate a single diode without saturating the amplification stages. At the time of writing, a small circuit was in development which integrates the detector signal over the relevant frequency range (0 to 10 MHz) and whose output can be recorded together with the measurement data. This information can later be used to omit individual measurements taken with noisy trap light from large datasets acquired over several hours.

Since the assembly for the red trap forms a Sagnac type interferometer, changes in the pathlength – e. g. due to heating of the nanofiber – lead to changes in the standing wave interference pattern. Due to unavoidable back-reflections (mainly from the nanofiber input fibercouplers) which mix the counterpropagating beams this can be detected as a change in intensity on

⁵ We remark that especially on the red trap light, low frequency oscillations are visible which we attribute to mechanical oscillations of the nanofiber.

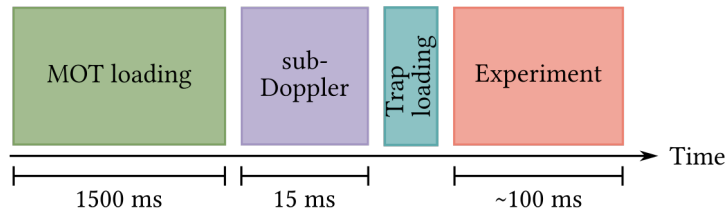


Figure 5.4: The standard trapping sequence consists of four stages with a total duration of about 2 s. Possible speedup is discussed in section 5.4.1.

the noise detector DC signal. It might prove beneficial to the trap lifetime and coherence times to actively stabilize the pathlength.

5.4 TRAP OPERATION

While the dipole trap light is always present in the nanofiber, the trap lifetime is on the order of 100 ms (sec. 5.5.2) and therefore atoms need to be loaded into the trap repeatedly.

The trapping sequence is controlled via the LabView VI *SteMOT* (cf. sec. 2.4.2). As is visualized in figure 5.4 it can be divided into four steps: First, the MOT is loaded from the background vapor in the vacuum cell (cf. sec. 2.4.2). Subsequently, a sub-Doppler cooling procedure as described in section 2.4.4 is run which loads atoms into the nanofiber trap. At the end of this sequence the MOT beams have been switched off and the atom cloud dissolves. Afterwards, a time-window of up to 100 ms is available to conduct experiments. However, most experiments described in this thesis will be conducted in a short time window 10 ms after the MOT has been switched off, when the number of trapped atoms is highest (cf. sec. 5.5.2) and enough time has passed such that there are no MOT atoms remaining near the nanofiber.

The number of trapped atoms depends on at least four parameters: The depth of the trap potentials, the overlap between MOT and nanofiber⁶, and both density and temperature of the MOT cloud. While the former is solely determined by the power ratio, noise level, and polarization alignment (cf. sec. 4.2.3) of the trap lasers, the latter is a combination of the background vapor pressure inside the vacuum chamber, the alignment of the MOT beams with the magnetic field (cf. sec. 2.4.2), and the effectiveness of the sub-Doppler cooling procedure (cf. sec. 2.4.4).

Whereas the MOT performance and trap loading have to be refined only occasionally, the trap powers are repeatedly adjusted. In both cases, the figure of merit is the measured OD. In general, we find that subsequent trap loadings yield comparable atom numbers while over several hours a significant difference can accumulate, presumably due to changing vapor pressure in the vacuum chamber. This has to be taken into account for all measurements sensitive to the number of atoms (cf. e. g. sec. 6.4.1.3).

⁶ The optimum is found empirically. The work by Béguin (2015) suggests that it is optimal if the center of the MOT is positioned somewhat off the nanofiber.

5.4.1 Repetition Rate

For virtually all of the measurements described in this thesis many realizations need to be prepared and measured to obtain a meaningful result. Especially in the case of the single excitation experiment a large number of data points needs to be acquired to uncover the state's Wigner function amidst the noise (sec. 8.3.1). Thus, a high repetition rate is desirable and we will now discuss the limitations and prospects.

In the standard sequence (fig. 5.4) MOT loading is by far the longest process. However, once the background vapor pressure is high enough and a sufficient MOT size has been reached this time can be reduced to a few 100 ms without compromising on the OD too much. In contrast, the length of the sub-Doppler cooling phase (≈ 15 ms) is fixed (cf. sec. 2.4.4) albeit short compared to the trap lifetime which determines the window for experiments (up to 100 ms, sec. 5.5.2).

In conclusion, a repetition rate of about 2 Hz is feasible. We also note that processing and saving of the data becomes a significant source of delay whenever files have to be written to a harddrive. To circumvent this problem, at the time of writing a new data processing module based on a field programmable gate array (FPGA) was in development.

5.5 SOME PROPERTIES

In the following we will characterize the dual-color trap by determining two quantities crucial for the experiments to follow: its lifetime and the attainable optical depth (OD). Furthermore, we present the first measurement of the radial trap frequency in our nanofiber setup. We will however not experimentally investigate the interaction of atoms with guided modes which has already been studied and discussed in great detail in Béguin (2015).

5.5.1 Filling Factor

The dual-color dipole trap around the nanofiber is quite shallow (sec. 5.2). Therefore, already a slight mechanical disturbance will remove atoms from the trap. This brings the trap into the so-called collisional blockade regime (Schlosser et al., 2002): If two atoms are initially loaded into the same trap site, upon collision their recoil will be enough for them to overcome the potential barrier. Only if an odd number – most commonly, a single atom – is loaded, one atom can stay behind. For a much more detailed analysis see Béguin (2015, sec. C.4).

Therefore, on average 50% of all trap sites are filled. Taken both linear chains together this leads to a 75% probability for finding an atom at a given trap site position along the fiber axis.

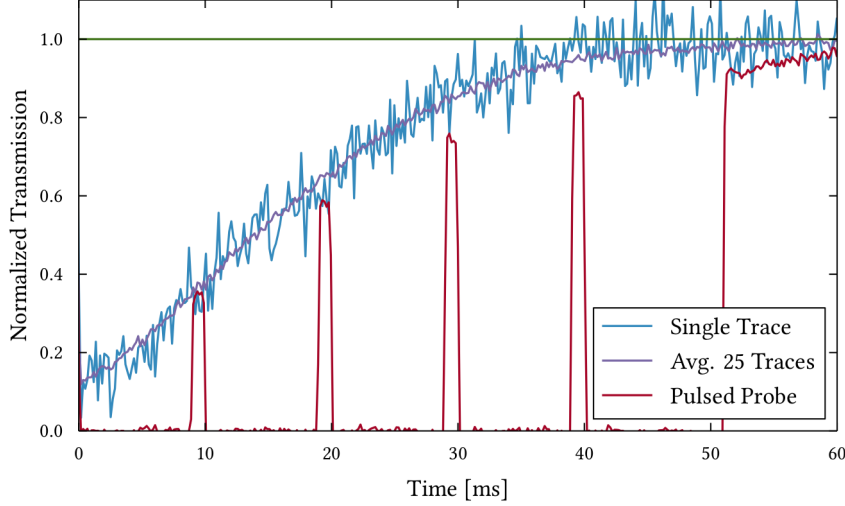


Figure 5.5: Transmission measurement for a total of 60 ms, starting 5 ms after trap loading. The onset OD is ≈ 2 , the trap decay has a time constant of about 20 ms. For comparison, we also show a measurement with a pulsed probe, which reveals a small effect of probe light on the trap decay.

5.5.2 Lifetime

As we see in figure 5.5, atoms stay in the trap for several 10 ms, and trap lifetimes of more than 100 ms have been observed. The lifetime of the atoms in the nanofiber trap depends on several key parameters: The accuracy of polarization alignment (cf. sec. 5.6), the noise on the trap lasers (cf. sec. 5.3) and the trap light power balance. Further, strong probing disturbs the atoms.

5.5.3 Radial Trap Frequency

To determine the radial trap frequency we use a conceptually simple method (Oblak, 2010, Ch. 9): We pump atoms into $|F = 4\rangle$ and monitor the phase shift of the probe laser, which is resonant to the $|F = 4\rangle \rightarrow |F' = 5\rangle$ transition, using the two-color heterodyne method (sec. 3.4.1). By switching off the AOM in its beam path (cf. fig. 5.3) we briefly block the red detuned dipole trap. During this time T_{off} the atoms are pushed away from the fiber by the blue detuned trap laser and thus will oscillate in their radial trap potential when the red detuned trap laser is turned back on. As the coupling of the atoms to the guided mode of the nanofiber depends on the distance of the atoms from the fiber surface, this oscillation is also visible on the phase measurement (cf. sec. 3.4.1).

Experimentally we find that we cannot switch off the red detuned trap for more than a few microseconds without losing all the atoms into free space. We adjust T_{off} for maximum contrast on the phase oscillation which we find to occur around $T_{\text{off}} = 500$ ns. The oscillation is clearly visible on the real

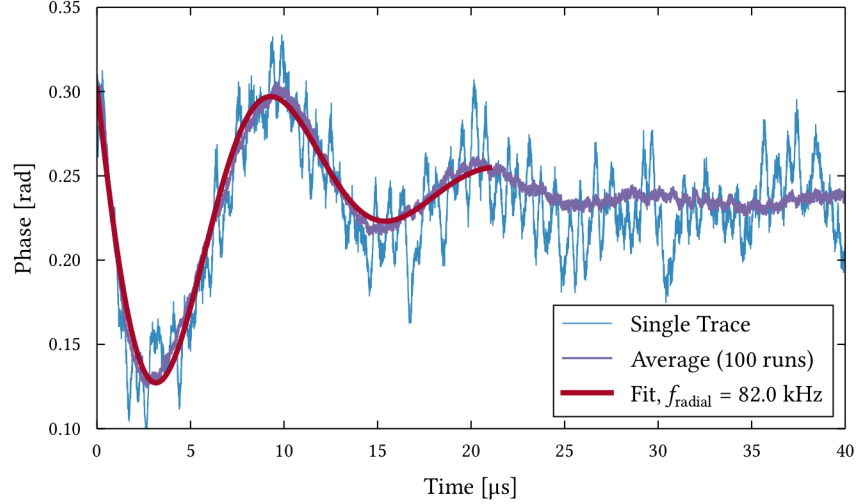


Figure 5.6: Phase shift data ($T_{\text{off}} = 500$ ns) and fit for the radial trap frequency measurement. The fit shows similar deviations as reported in (Oblak, 2010, Ch. 9) which we point to the anharmonicity of the trap potential.

time signal (fig. 5.6). We note that we can repeat the procedure several times for a single MOT loading.

To analyze we fit a simple model suggested in Oblak (2010, Ch. 9) to the data which assumes a damped harmonic oscillation:

$$A \cdot \exp\left(-\frac{t}{\tau}\right) \cdot \cos\left(\frac{2\pi}{T}(t - \varphi)\right) + C. \quad (5.1)$$

Here, A , C , and φ are fit parameters with no direct physical meaning, τ is the decay constant of the oscillation, and T the oscillation period. The data and fits are shown in figure 5.6. We find a radial trap frequency $f_{\text{radial}} = 82 \pm 2$ kHz.

This result is remarkably lower than the ones given by (Vetsch et al., 2012, Mitsch et al., 2014a) (200 kHz and 120 kHz), the latter of which was calculated for similar trap powers (here: $P_{\text{blue}} = 13$ mW and nominally $P_{\text{red}} = 2 \times 1.5$ mW). While we cannot present a conclusive reason, we point out that our measurement differs from the one presented by Oblak (2010) in that we only turn off one trap laser, i. e. not the whole trap. Further, it is conceivable that the atoms are heated due to the “push” by the blue-detuned trap laser, increasing the influence of the potential’s anharmonicity (cf. fig. 5.1b). This could be investigated by employing the temperature estimation through the measurement of the dephasing time of resonant structures (fig. 7.7).

5.6 POLARIZATION CONTROL AND ALIGNMENT

So far we have assumed certain polarization of the probe and trap lasers at the tapered section of the nanofiber without stating how one can achieve

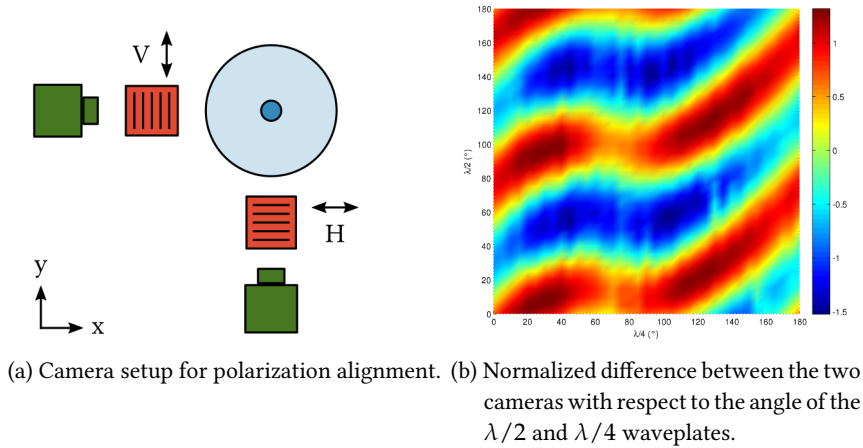


Figure 5.7

such a configuration. As it turns out, aligning and maintaining polarization at the tapered section of a nanofiber is a not necessarily hard, but tedious undertaking. In describing in detail the procedures used for this purpose, this section fills one of the very few gaps left in Béguin (2015, ch. 15).

The root of the problem lies in the fact that a nanofiber is fabricated from a non-polarization maintaining fiber (sec. 4.1) in order for it to support different polarizations at different wavelengths. In addition, light of vastly different color will propagate very differently. It can hence be deemed hopeless to attempt to adjust the polarization properties of the fiber by inducing stresses such that *all* input wavelengths of say horizontal linearly polarized light will emerge in the same polarization at the tapered section.

Therefore, all beams coupled into the nanofiber will need to be polarization adjusted individually and one has to find a way to determine their individual polarization at the tapered section. To our knowledge, the only method known and employed for this task is the use of two CCD cameras monitoring the tapered section, which are mounted at an 90 degree angle and are equipped with polarization filters (Vetsch et al., 2012) as is schematically shown in 5.7a.

To align the input waveplates for light with wavelengths of 780 nm, 852 nm and 1057 nm, respectively, we record so-called polarization maps. To this end, we install a linear polarizer and both a motorized $\lambda/2$ and $\lambda/4$ waveplate in front of one nanofiber input port. Then, we automatically step through all possible combinations of waveplate settings and record camera images. From the image files we extract the light intensity for each waveplate setting; an example of such a polarization map can be found in figure 5.7b.

By calculating the difference between the two camera maps we can find the settings for which the light at the tapered section is either maximally *V*- or *H*-polarized (cf. sec. 4.2.3) and use these settings to align the input waveplates in front of the other input port. This procedure has to be repeated for each wavelength at each nanofiber port, leading to six maps for a full calibration and alignment.

As a rough alignment method and to check whether a setting is still valid one can also monitor the intensity values on both cameras in real time. However, sensor saturation and the different maximum light intensities recorded by the cameras can be misleading.

There are several signs that the polarization is not well-aligned. If the relative polarization of the trap lasers is not correct, the number of atoms trapped will decrease significantly, although in practice it is difficult to distinguish this from the effect of e. g. excessive noise on the trap or MOT lasers. We note that it is possible to trap atoms even if the polarization is in parallel (also reported by Lee et al., 2015).

If the probe light polarization is not well-aligned with the axes defined by the trap lasers one can observe birefringence as the light will propagate more slowly on the axis where it couples strongly to the atoms (cf. Dawkins et al., 2011). This can be detected as a polarization rotation which therefore is a telltale sign of misaligned polarization.

5.7 COUNTING THE TRAPPED ATOMS

For all experiments described in this thesis it is necessary to know how many atoms exactly are trapped around the nanofiber. The answer to this question is one of the main results of Béguin (2015), culminating in a method to create and detect a sub-Poissonian atom number distribution (Béguin et al., 2014a). In this section, we briefly describe how the absolute number of atoms can be determined.

Since it is not possible to optically resolve the atoms in their lattice sites (Béguin, 2015) the information has to be obtained by sending light through the fiber. The most straightforward approach is to probe the ensemble well above saturation ($P > P_{\text{sat}}$) and to measure how much light is absorbed (P_{abs}). If p is the power radiated by a single fully saturated atom, $N_{\text{at}} = P_{\text{abs}} / p$ is the number of atoms (e. g. Vetsch et al., 2010, Goban et al., 2012).

The method employed in this thesis, which is more robust and much faster, uses optical pumping to infer the number of atoms (Béguin, 2015, Béguin et al., 2014a). To this end, all $N_{\text{at,total}}$ atoms are initially prepared in the $|4\rangle$ hyperfine groundstate. Then the ensemble is weakly probed resonantly on the $|4\rangle \rightarrow |4'\rangle$ transition. Since atoms in $|4'\rangle$ can decay into $|3\rangle$ which is red-detuned 9.192 GHz relative to $|4\rangle$ and therefore a dark state, the optical depth $d(t)$ (OD) will decrease over time. Via Lambert-Beer's law the latter is connected to the transmission

$$T(t) = \frac{\Phi_{\text{out}}(t)}{\Phi_{\text{in}}} e^{-d(t)}, \quad (5.2)$$

where Φ_{in} (Φ_{out}) is the photon flux into (out of) the nanofiber. The OD $d(t)$ is directly related to the number of atoms in $|4\rangle$ $N_{\text{at}}(t)$ ($N_{\text{at}}(0) = N_{\text{at,total}}$) via the OD per single atom α_{at} :

$$d(t) = N_{\text{at}}(t)\alpha_{\text{at}}. \quad (5.3)$$

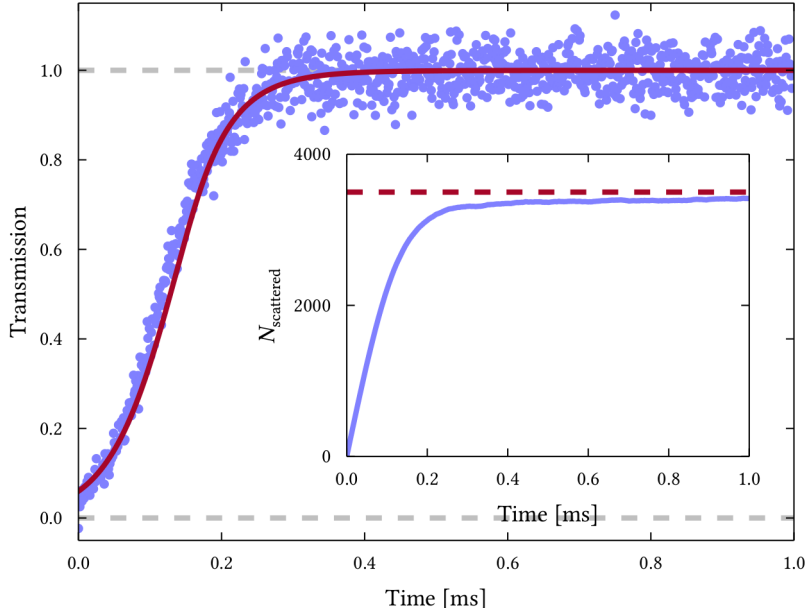


Figure 5.8: Example of an atom number measurement (213 runs). The inset shows the number of scattered photons as a function of time.

If an atom on average scatters k photons before it is pumped into $|3\rangle$ (this is independent of the m_F sublevel, i. e. identical for all atoms; see [Béguin \(2015, sec. 17.1.5\)](#) for a more detailed discussion), $N_{\text{at}}(t)$ changes as

$$\frac{d}{dt}N_{\text{at}}(t) = -\frac{1}{k}(\Phi_{\text{in}} - \Phi_{\text{out}}(t)). \quad (5.4)$$

Together with (5.2) and (5.3) this yields

$$\frac{d}{dt}d(t) = -\frac{\alpha_{\text{at}}}{k}\Phi_{\text{in}}[1 - e^{-d(t)}]. \quad (5.5)$$

For the transmission through the ensemble, which is the quantity we can experimentally measure via single-sideband heterodyne detection (sec. 3.4), we find

$$T(N_{\text{at,total}}, \alpha_{\text{at}}, t) = \left(1 + \left[e^{\alpha_{\text{at}}N_{\text{at,total}}} - 1\right] e^{-\alpha_{\text{at}}\Phi_{\text{in}}tk^{-1}}\right)^{-1} \quad (5.6)$$

with $k = 2.4$ (for the derivation see [Béguin, 2015, sec. 17.1.3](#)).

An example of such a measurement is presented in figure 5.8. From the transmission signal of about 200 consecutive measurements, using (5.6) the number of atoms⁷ is determined to be

$$N_{\text{at,total}} = 1458 \pm 3. \quad (5.7)$$

⁷ We point out that these methods only yield an *effective* atom number, since they depend on the coupling of the atoms to the guided mode of the nanofiber, which due to motion in the trap potential is not identical for all trapped atoms. We note that as long as we only probe ensembles through the guided mode this restriction has no significance as the experimenter has no way (and therefore no need) to distinguish between an effective and a “real” number of atoms.

The error is mainly due to the uncertainty in overall quantum efficiency of the detection, which in our experiment is 10%. This systematic error dominates all others, but is an inherent property of the experimental setup, i. e. it does not vary between runs (Béguin et al., 2014a).

Part III

AN ATOMIC MIRROR

We present the first realization and investigation of scattering off resonantly structured atoms trapped near a photonic waveguide. Starting out from a brief introduction into theory and a review of previous work, we describe our structuring method based on optical pumping and introduce the methods used for detection and analysis. Subsequently we discuss our quest for a high reflection coefficient, thereby detailing the underlying physical processes. Then, we present our investigation into the limited lifetime of the Bragg superstructure. We conclude with an outlook on possible applications and alternative structuring methods.

BRAGG SCATTERING OFF A ONE-DIMENSIONAL ATOMIC CRYSTAL

As described in the previous chapter, atoms are trapped around the nanofiber in two linear chains. Cast in the language of solid state physics we have a one-dimensional lattice potential with a monoatomic basis where the lattice constant is determined by the wavelength of the red detuned trap. One can now ask whether it is possible to observe solid state phenomena in such a system.

A prominent example of these are Bragg reflections. Pioneered in the early 1910s by Max von Laue ([Friedrich et al. \(1913\)](#), Nobel Prize 1914) and William Henry and William Lawrence Bragg (Nobel Prize 1915) with x-rays on crystals, it is the prime method to investigate highly spatially ordered structures.

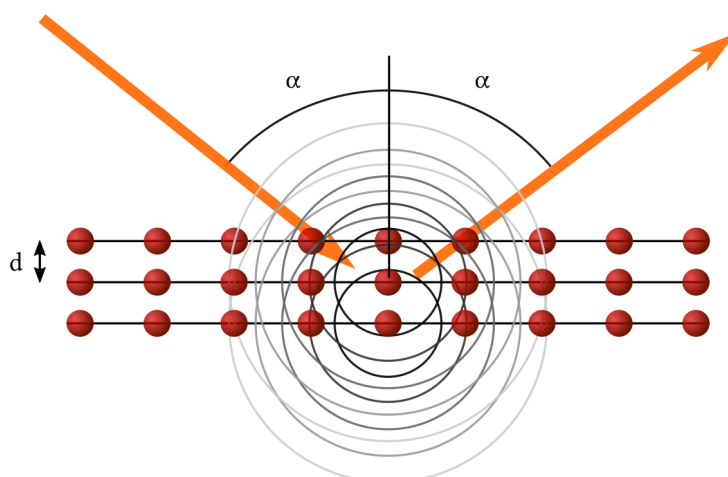


Figure 6.1: Illustration of the Bragg condition.

In short, the idea is sketched in figure 6.1: If both the wavelength λ of the incoming light and the angle of incidence α are chosen correctly the reflections from all layers interfere constructively. This is captured by the simple yet powerful equation

$$n \cdot \lambda = 2 \cdot d \cdot \sin(\alpha) \quad (6.1)$$

known as Bragg condition. By scanning over a range of angles and wavelengths and recording the pairs (α, λ) for which reflections are observed, one can learn about the lattice constant d . More sophisticated methods like the von Laue and Debye-Scherrer methods to both of which (6.1) is central allow one to determine the full crystallographic structure (cf. e. g. [Gross and Marx, 2012](#)).

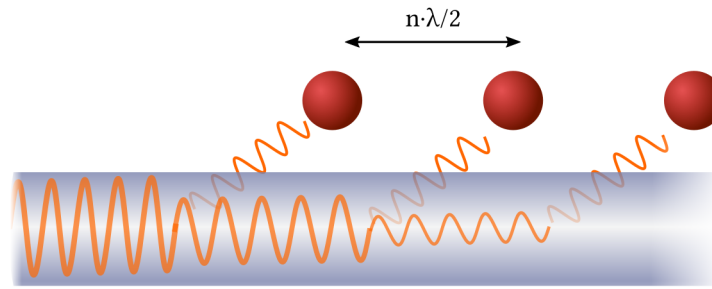


Figure 6.2: Emission from regularly spaced scatterers interferes coherently.

In this chapter we summarize our work on Bragg reflections in nanofiber trapped ensembles which is reported in [Sørensen et al. \(2015a\)](#) and has been presented at several conferences and workshops¹. A more thorough investigation can be found in [Sørensen \(2015\)](#); some preliminary results were also discussed in [Béguin \(2015\)](#). Reflection from unstructured ensembles of atoms trapped around a nanofiber was previously studied by [Goban et al. \(2012\)](#), [Reitz et al. \(2014\)](#).

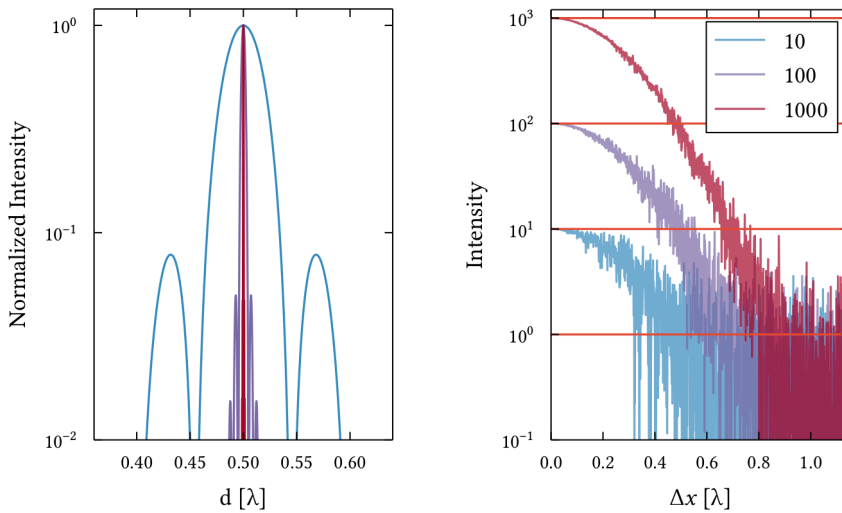
We start this chapter with a theoretical introduction and continue by reviewing Bragg reflections in optical lattices. Then we describe our novel approach, discuss the optical pumping scheme used for Bragg lattice preparation, and give an overview of our detection and analysis methods.

6.1 COHERENT ENHANCEMENT OF ATOMIC EMISSION

Bragg scattering is an interference effect that appears for spatially regularly placed scatterers much smaller than the wavelength of light (cf. [Friedrich et al., 1913](#)). For an optically thin ensemble of N randomly placed scatterers coupled to a common photonic mode the back-reflected intensity scales with N . If however the scatterers are placed regularly with lattice constant $\lambda/2$, the intensity scales as N^2 (figs. 6.2 and 6.3). The backreflection intensity I depends on the degree of localization (e. g. [Egami and Billinge, 2003](#), ch. 2). A simple numerical calculation where each scatterer's position is randomized assuming a normal distribution illustrates this (fig. 6.4).

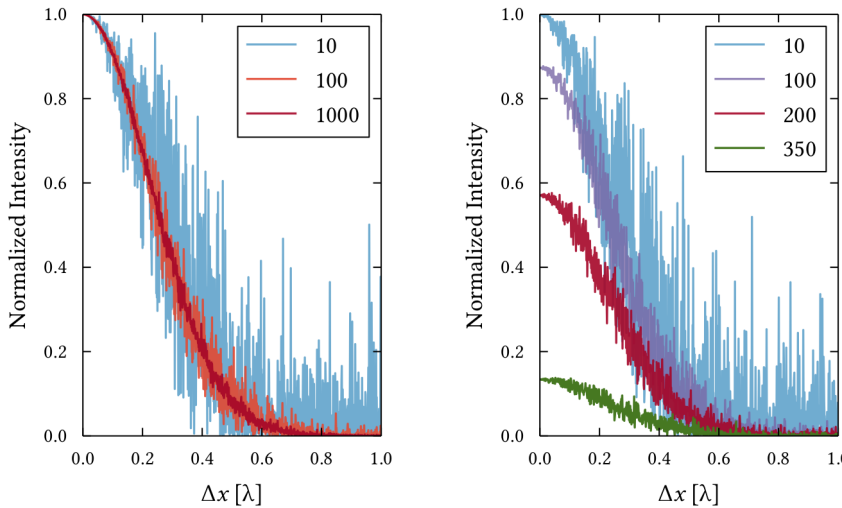
Bragg scattering can be understood via the Kronig-Penney model ([McQuarrie, 1996](#)) as the formation of a photonic bandgap ([Deutsch et al., 1995](#)). For this model to hold, light has to be scattered elastically by the atoms, which is the case as long as the atoms are not driven into saturation. Then they can be modeled as classical dipoles and the emitted light will be coherent. This regime is sometimes referred to as resonance fluorescence.

¹ Kluge et al. (2015a), Sørensen et al. (2015b), Kluge et al. (2015c), Appel et al. (2015), Kluge et al. (2015b)



(a) Reflection off N scatterers with spacing d . The larger N , the narrower the expected reflection peak.
 (b) Reflection off N scatterers spaced with $d = \lambda/2$ with localization uncertainty Δx . Intensity at perfect localization scales with N^2 .

Figure 6.3: If N scatterers are spaced in multiples of $\lambda/2$ in a spatial direction, the emission in this direction is enhanced by a factor N . Numerical simulation for optically thin ensembles. The legend in (b) is common to both subfigures.



(a) For scatterers spaced with $d = \lambda/2$, the number of scatterers has no influence on the sensitivity to delocalization.
 (b) For scatterers spaced with $d = 0.499\lambda$, the larger N the more severe is the relative loss in reflectivity.

Figure 6.4: The reflection intensity depends on the spacing between atoms and the degree of localization. Numerical simulation for optically thin ensembles with different numbers of scatterers N .

To model the system we will discuss in this and the next chapter, a transfer matrix formalism similar to [Deutsch et al. \(1995\)](#) is used. To this end, each two-level atom is modeled by

$$\underline{\underline{M}}_{a,j} = \begin{pmatrix} 1 - \beta_j & -\beta_j \\ \beta_j & 1 + \beta_j \end{pmatrix}, \quad (6.2)$$

where $j \in (1, N_a)$ is the atom's index (with N_a the total number of atoms) and

$$\beta_j = \frac{\gamma}{\Gamma_{\text{fs}} - 2i(\Delta + \Delta_j)} \quad (6.3)$$

is the scattering parameter with γ the rate of emission into the guided mode (eq. 4.24), Γ_{fs} the rate of emission into free space (cf. sec. 4.3.2), Δ the detuning of the probe light from atomic resonance, and Δ_j is a randomly drawn parameter to describe the inhomogeneous broadening of atomic transitions due to the strong trap light (for details cf. [Sørensen, 2015](#), [Sørensen et al., 2015a](#)).

Together with a matrix $\underline{\underline{M}}_{f,j}$ describing the propagation through free space, the system can be modeled as

$$\underline{\underline{M}}_{\text{ensemble}} = \prod_{j=N}^1 \underline{\underline{M}}_{f,j} \underline{\underline{M}}_{a,j} = \begin{pmatrix} M_{11} & M_{12} \\ M_{21} & M_{22} \end{pmatrix}, \quad (6.4)$$

where the reflection coefficient is given by $r = M_{12}/M_{22}$. The structuring is modeled by assigning to each atom a probability to remain in the bright state after structuring

$$p_j = \exp\left(-\zeta \cos^2\left(\frac{2\pi z_j}{\lambda_{\text{struct}}}\right)\right), \quad (6.5)$$

where the dimensionless parameter ζ is a measure for E_{struct} and z_j is the atom's position. We use this model, which was developed by Ivan Iakoupov at [QUANTOP](#), to discuss our approach (fig. 6.7) and will compare it to our experimental results in figures 7.1 and 7.2. A detailed description is beyond the scope of this thesis and can be found in [Sørensen \(2015\)](#), [Iakoupov \(2015\)](#).

6.2 BRAGG SCATTERING IN OPTICAL LATTICES

Bragg scattering has been studied in optical lattices since the advent of these systems in the early 1990s. We will give a short review of this work, as it allows us to discuss some fundamental aspects as well as key ideas and will allow us to better clarify the novelties in our approach.

6.2.1 Three-dimensional Lattices

The first studies of Bragg scattering in optical lattices were reported almost simultaneously by [Birkl et al. \(1995\)](#) and [Weidemüller et al. \(1995\)](#). Both

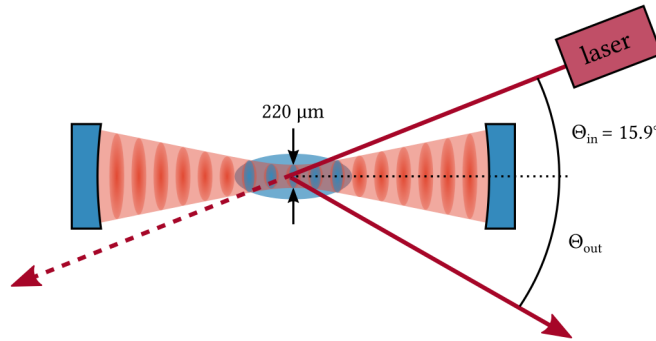


Figure 6.5: Principle setup used in Slama et al. (2005b): A standing wave dipole trap is formed inside a cavity ($\mathcal{F} = 4000$) which structures MOT atoms (blue) into disks of 115 nm width and $70\ \mu\text{m}$ radius; about 10,000 of these disks are created. The structure is illuminated with a dipole laser close to resonance at an fixed angle Θ_{in} and the reflected light recorded with a CCD camera. In Slama et al. (2006) the latter was replaced by a photo-multiplier (PMT). In addition, a photodiode was used to detect the transmitted and another PMT to detect the absorbed light. For Slama et al. (2005a) a more involved but similar system with a ring cavity and a heterodyne detection scheme was used (see text).

groups uses three-dimensional, near-resonant optical lattices, which therefore also cool the atoms. The geometry of their lattices allows both groups to probe at virtually arbitrary angles α , which allows Weidemüller et al. (1995) to use a probe far-off lattice resonance – something which is not possible in a one-dimensional configuration.

After these principal studies, both groups used Bragg scattering as a tool to study previously inaccessible properties of optical lattices (Raithel et al., 1997, Weidemüller et al., 1998), which is also an aspect of our experiment. We highlight that from the time-evolution of the Bragg peak intensities, which is a direct result of the motion of atoms in the trap, one can learn about the temperature of atoms, which allows one to study cooling mechanisms. The intensity is also a measure for long-range order (Weidemüller et al., 1998), i. e. using Bragg scattering, one can probe the “structuredness” of an atomic ensemble.

6.2.2 One-dimensional Lattices

While a one-dimensional configuration was studied by Raithel et al. (1997), it is not until Slama et al. (2005a,b, 2006) that this is investigated in more detail. Their principal setup is sketched in figure 6.5 and consists of a cigar-shaped cloud of ultracold Rubidium atoms which is structured into $N \approx 7,500$ to $N \approx 10,000$ planes via a standing wave dipole trap. The input angle Θ_{in} is restricted by the geometry, small angles close to 0° are prohibited.

The one-dimensional configuration is not the only novelty this approach has in common with the experiment described in this chapter. Slama et al. (2005a) pioneer heterodyne detection, which allows for measurement of the

coherent part of back-reflected field only, thereby clearly distinguishing Bragg reflections from incoherent scattering. They are also first to simultaneously detect in transmission (Slama et al., 2006). Due to the finite size of the discs and the non-zero Θ_{in} , only a limited number of lattice sites can be probed at a time. By using a small probe diameter and adjusting the lattice constant such that the Bragg condition is fulfilled off the atomic resonance (less absorption), in the group’s final study of Bragg scattering in this system, they reach up to 80 % intensity reflection (Schilke et al., 2011).

6.3 BRAGG SCATTERING OFF NANOFIBER TRAPPED ATOMS

In the specific case of Bragg scattering, nanofiber trapped ensembles have several advantages over the free-space optical lattices described in the previous section: Not only is it easily possible to probe and detect along the trap-axis, but we are also in the limit of a single atom per lattice site. In addition, both length and homogeneity of the atomic crystal are not limited by the Rayleigh length (cf. ch. 5). Compared to the dipole traps previously used to realize the one-dimensional case (sec. 6.2.2) the motion of atoms in radial direction is negligible on the investigated timescale (sec. 5.5.3 and sec. 7.2).

If for the moment we assume a perfect crystal – and thus leave aside the fact that each lattice site is only occupied by an atom with 75% probability (sec. 5.5.1) which introduces defects to be discussed below – the situation is quite simple: Since there is only one available light mode which is always coinciding with the sole axis of the one-dimensional crystal, the angle between the “surface” and the incoming light α is always equal to $\pi/2$ and (6.1) reduces to

$$\lambda_{\text{red}} = n \cdot \lambda. \quad (6.6)$$

Accordingly, one naively could expect to observe Bragg scattering when sending light with a proper wavelength $\lambda_{\text{probe}} = n \cdot \lambda$ into the fiber. However, atoms only scatter light relatively close to their resonance frequencies (sec. 2.2), so for cesium significant scattering will only be observed for $\lambda_{\text{probe}} \approx 852.35$ nm. Thus, λ_{red} itself ($n = 1$) is ruled out as a probing wavelength as it is by choice far detuned from any resonance (cf. sec. 5.1). Analogously, $\lambda = 530$ nm ($n = 2$) has to be discarded. Even shorter wavelengths ($n > 2$) are already in the UV which is unfeasible given our optical setup and nanofiber.²

One could now hope to make use of the probabilistic occupation of lattice sites, but as is easily seen this does not alter the issue fundamentally. Nevertheless it is clear that one has to somehow arrange the scatterers in a way that $\lambda_{\text{lattice}} = n \cdot \lambda_{\text{probe}}$. There are several proposals how to accomplish this, of which we chose the perhaps most simple: To select the atoms in “good”

² To be precise, one could also opt to use the D1 line of cesium whose resonance wavelength is 894.59 nm (fig. 2.1). In this case, the same argument applies. Additionally, due its lack of a closed transition probing changes the hyperfine groundstate populations (cf. sec. 2.1), on whose constance all Bragg schemes discussed in this chapter rely.

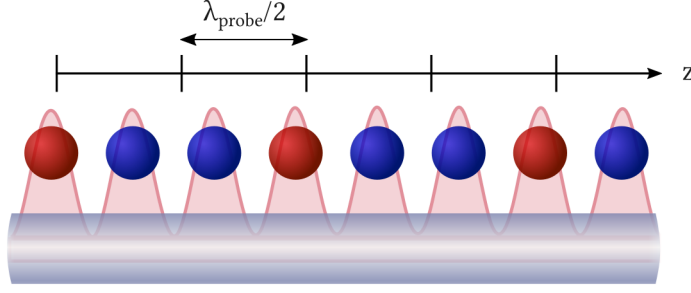


Figure 6.6: A superstructure with suitable lattice constant $d = \lambda/2$ along the fiber axis z is created by pumping atoms into dark (blue) and bright (red) states.

positions by optical pumping, i. e. to imprint a superstructure for which (6.6) is fulfilled. Other methods will briefly be discussed at the end of this chapter in section 7.3.

6.4 ENGINEERING A BRAGG SUPERSTRUCTURE

There are two stable states for cesium atoms in our nanofiber trap: The hyperfine groundstates $|F = 3\rangle$ ($|3\rangle$) and $|F = 4\rangle$ ($|4\rangle$). A probe laser tuned to the $|4\rangle \rightarrow |F' = 5\rangle$ transition only couples to atoms in $|4\rangle$; $|3\rangle$ is a dark state. This configuration is preferable to the case of a probe resonant to $|3\rangle \rightarrow |F' = 2\rangle$ with $|4\rangle$ as the dark state as the coupling of the latter transition is significantly weaker. Although we aim for strong coupling between atoms and probe light, we choose V as our polarization,³ as H exhibits strong directionality of emission (cf. sec. 4.3.2).

In summary, we aim to only have atoms in “good” positions in $|4\rangle$ and are left with two different options: We can either choose to start out with all atoms in $|3\rangle$ and then optically pump the “good” atoms into $|4\rangle$ (dubbed the *bright lattice*) or we initially bring all atoms into $|4\rangle$ and then pump the “bad” atoms to $|3\rangle$ (*dark lattice*, fig. 6.8).

In both cases we use a standing wave with $\lambda_{\text{struct}} = 852$ nm for pumping. Since only atoms at its antinodes will be affected by the structuring light, what forms in both cases is a superstructure with a lattice constant $d = \lambda_{\text{struct}}/2$, which fulfills (6.6). A quick look at figure 6.7 reveals that the *dark lattice* yields the favorable relationship of the degree of localization with respect to the number of scatterers. We therefore focus on this scheme, the *bright lattice* is discussed further in Sørensen (2015).

Since not all trap sites are occupied initially and λ_{struct} and λ_{red} are incommensurable (in the sense that the integer numbers a and b with the same ratio are much larger than the number of trap sites) the superstructure formed

³ As introduced in section 4.2.3 we take V and H as the basis for polarization and quantize the atoms along y . However, in this and the following chapter, no “special” optical properties of the nanofiber come into play: V light exclusively drives π -transitions, the emission into the forward and backward direction is balanced, and we furthermore do not apply any bias field, i. e. magnetic sublevels are degenerate.

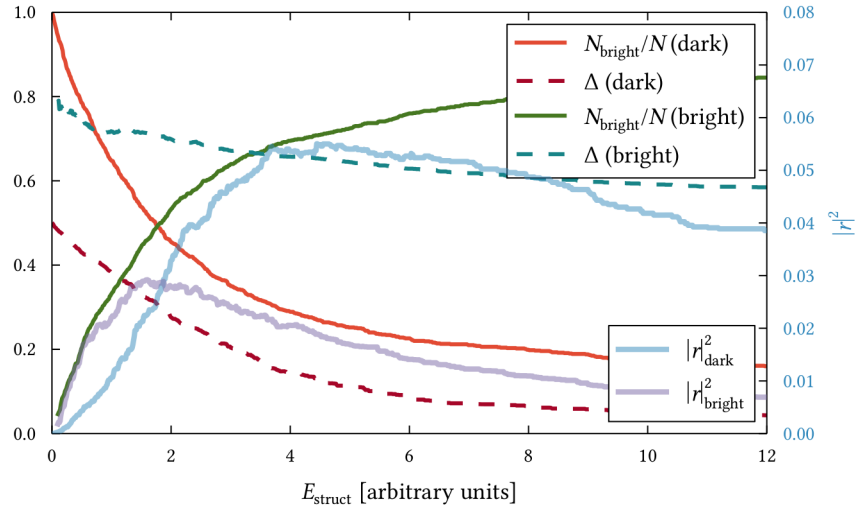


Figure 6.7: Starting out with N atoms initially, the maximum reflection occurs when the number of scatterers in the bright state N_{bright} and their localization are optimally balanced. Here, Δ denotes the average position uncertainty, i. e. $\Delta = 0$ is equivalent to precisely positioned atoms. For the *bright lattice* N_{bright} is initially 0 and grows with the energy of the structuring pulse E_{struct} while the localization deteriorates. In the *dark lattice* scheme initially we have $N_{\text{bright}} = N$ and the localization grows with E_{struct} . (Numerical simulation based on the work by Ivan Iakoupov, cf. Sørensen et al. (2015a), Iakoupov (2015).)

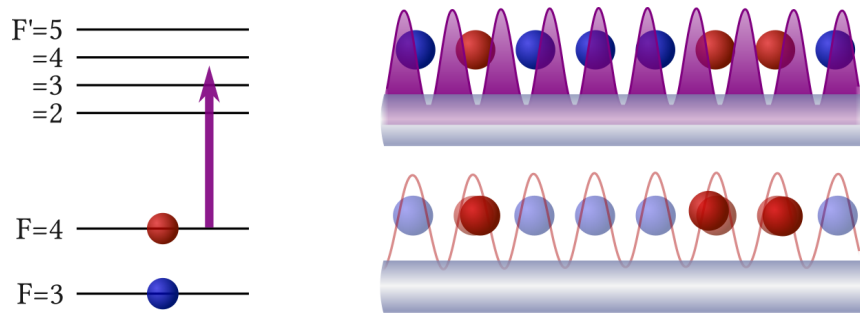


Figure 6.8: *Dark lattice* scheme: All atoms are initially prepared in the $|F = 4\rangle$ hyperfine groundstate by applying the MOT repumper. A standing wave structuring pulse pumps atoms at its antinodes into $|F = 3\rangle$, which is dark to the probe resonant with $|F = 4\rangle \rightarrow |F' = 5\rangle$.

by the atoms in $|4\rangle$ will necessarily have many vacancy defects. Following our discussion of coherent reflection enhancement in section 6.1 these are – aside from the overall lower number of scatterers N – not detrimental to reflection (cf. Weidemüller et al., 1995). In contrast, light emitted by interstitial defects, i. e. atoms at “wrong” positions, will lead to destructive interference.

As a side remark we point out that it is at first sight rather remarkable that the structuring light can propagate through the structure it creates at all since $\lambda = \lambda_{\text{struct}}$ clearly is a solution of (6.6). That this is nevertheless possible is the result of back-action of atoms on the structuring light (Deutsch et al., 1995). In the experiment discussed here, however, the influence of this force is small compared to the thermal motion of the atoms and the dipole forces exerted on the atoms in radial direction which we will discuss in section 7.2.

6.4.1 Experimental Realization

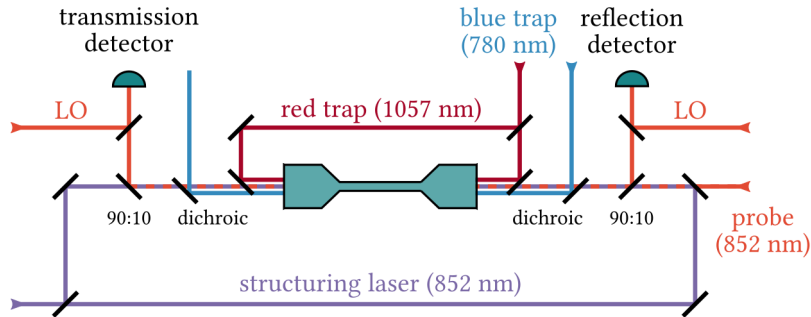


Figure 6.9: Schematic overview of the relevant parts of the setup for the atomic mirror experiment: In addition to the nanofiber trap (cf. fig. 5.3 for details) a structuring laser (cf. fig. 9.22) is coupled into the nanofiber in a standing wave configuration. The probe enters the nanofiber from one port and is detected via heterodyne measurement (sec. 3.4) in reflection and transmission.

To create the Bragg superstructure we add an additional laser to the nanofiber setup described in section 5.3 which we will refer to as the *structuring laser* in the remainder of this chapter. Again we use an external cavity diode laser as described in appendix D which is beatnote locked to the MOT repumper. The setup of the laser itself is shown in figure 9.22 while the relevant parts of the experimental apparatus for the atomic mirror experiment are sketched in figure 6.9.

The setup is controlled via two LabView VIs *SteMOT* (cf. sec. 2.4.2) and *DIO* which allow us to run TTL pulse sequences with a timing precision on the order of a few nanoseconds. The general sequence is summarized in figure 6.10 and consists of the standard procedure for trap loading (sec.

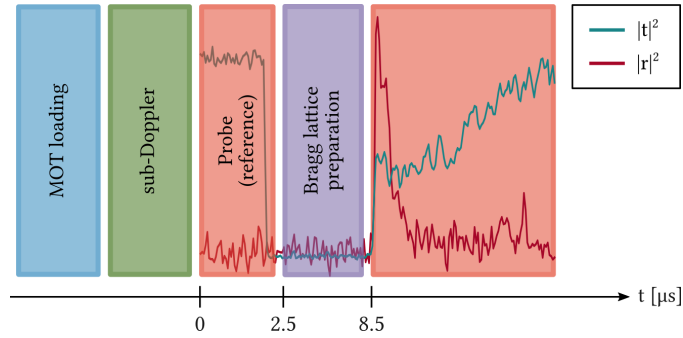


Figure 6.10: Each experimental run begins with MOT loading (2 s) and sub-Doppler cooling (15 ms), during which atoms are loaded into the nanofiber dipole trap (cf. sec. 5.4). Then we first probe for 2 μ s to obtain a transmission reference. The window for the preparation of the Bragg grating lasts 6 μ s, afterwards we probe and observe reflection and transmission. Times shown are the trigger timestamps as set in *DIO*. Shown in the background are examples of a down-mixed reflection and transmission signal (y-axis not to scale).

5.4) with subsequent Bragg lattice preparation and probing. We will devote section 7.1 to optimizing the preparation procedure.

6.4.1.1 Data Acquisition and Analysis

To detect light transmitted through and reflected off the superstructure we employ a heterodyne scheme as introduced in section 3.4: The weak probe light is mixed with a strong local oscillator (LO) derived from the same laser and the resulting intensity signal of a photodetector is recorded with a digital oscilloscope (Agilent Infiniium 54832D). The reflection and transmission signals are acquired simultaneously; typically data for 50 to 200 realizations is recorded for a given configuration. Afterwards the data is digitally demodulated (cf. sec. 3.4) and low-pass filtered with a running average timebin of typically 96 ns. An example of such a processed data set is shown in figure 6.11.⁴

Within a single timebin, only very few photons arrive at the reflection detector, therefore the shot noise is very high (cf. sec. 1.3.2). An illustration can be found in figure A.7 in the appendix, where we also demonstrate that one can obtain a clear signal already with only a few segments. It is only to reduce the relative error that we average over many more realizations.

6.4.1.2 Detector Calibration

To calculate reflection coefficients one has to relate the detector signal to an optical power at the “surface” of the atomic crystal. To this end, we shut off the trap (only the counterpropagating arm of the red trap remains to prevent atoms from attaching to the nanofiber surface) and invert the direction of

⁴ For plotting, we decrease the number of data points shown for sake of visual clarity. Usually, we display every point. Otherwise we state this information in the figure caption. The same applies if we use a different averaging timebin.

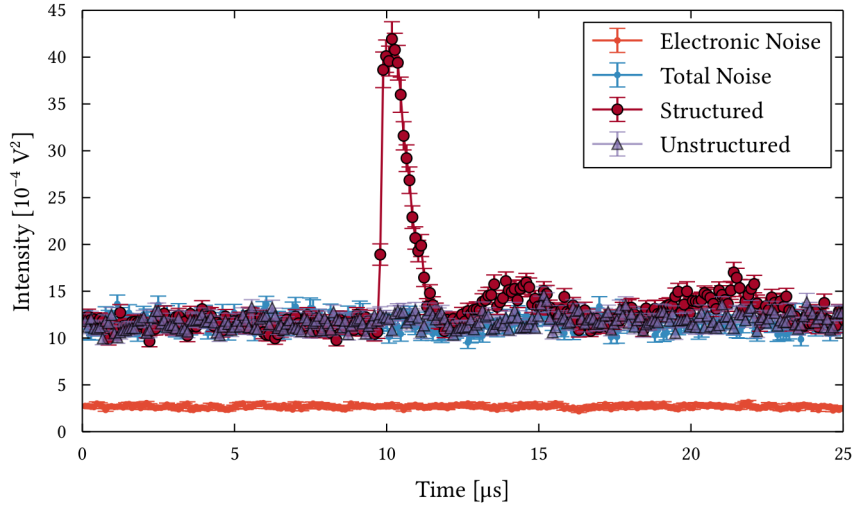


Figure 6.11: Example of a reflection measurement on the atomic mirror. The electronic noise is well below the total noise level, which is effectively the LO's shot noise (sec. 3.4).

After the Bragg grating is prepared and the probe turned on (cf. fig. 6.10) a large reflection peak appears. Its finite width and the oscillations on the reflection signal after the initial peak has dephased will be the topic of section 7.2.

The result of a measurement with a blocked structuring laser and otherwise same parameters is shown as a semi-transparent overlay. It is virtually identical to the total noise. For an investigation of unstructured reflection see Sørensen (2015), Reitz et al. (2014).

($P_{\text{struct}} = 213 \text{ nW}$, $t_{\text{struct}} = 250 \text{ ns}$, $\Delta_{\text{struct}} = -175 \text{ MHz}$, $P_{\text{probe}} = 164 \text{ pW}$, $\Delta_{\text{probe}} = 8 \text{ MHz}$. Average over 200 realizations.)

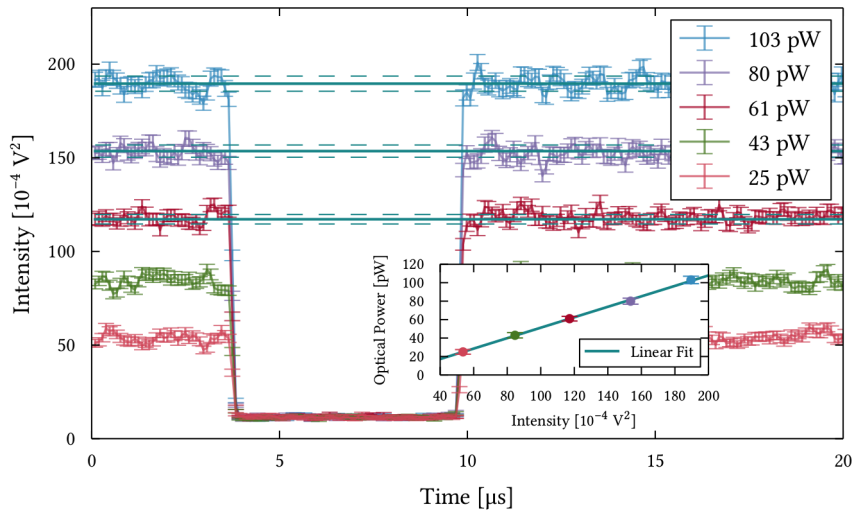


Figure 6.12: Result for the detector calibration as described in the main text. Plotted are the reflection signals for five different probe powers (measured at the nanofiber output). The inset shows the resulting relationship between optical power and measured intensity.

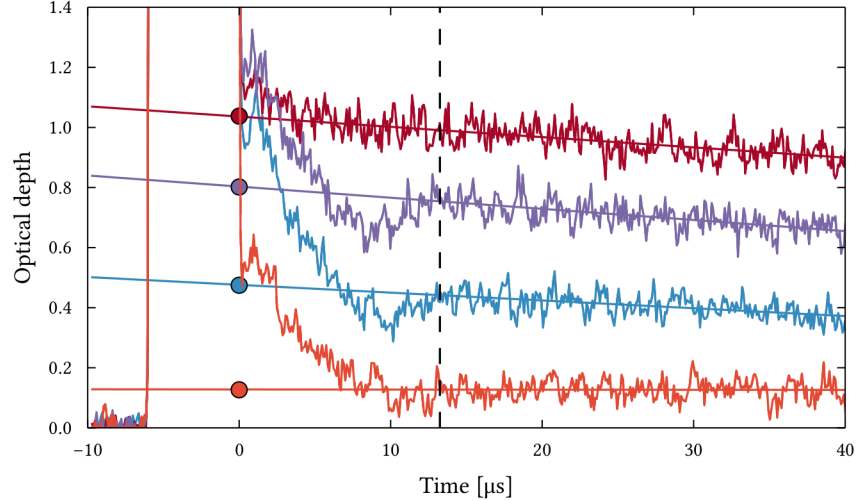


Figure 6.13: To estimate the number of atoms, we extrapolate the OD at the point in time when the probe is switched on (here, this corresponds to $t = 0 \mu\text{s}$).

probe light in the setup, i. e. the roles of the detectors are interchanged (cf. fig. 6.9). For different probe powers we determine the optical power at what is now the output of the nanofiber and also record a “reflection signal” as described above. This way we find the relationship of the detector signal to the power emerging from the atomic crystal (fig. 6.12).

While the method is conceptually simple, detector saturation and varying LO powers can introduce errors. This is discussed in detail in Sørensen (2015).

6.4.1.3 Inferring the Number of Atoms

The number of scatterers N is an important parameter if one wants to compare the results obtained for realizations across several hours or days of measurement as the number of atoms fluctuates due to changing background vapor pressure and trap laser powers (sec. 5.4).

A procedure for measuring the number of trapped atoms to high accuracy has been outlined in section 5.7, but due to the demands on probe light cannot be integrated into the Bragg mirror sequence. Instead, we chose to use the optical depth (OD) – which depends on N and is readily calculated from the transmission signal – to infer the number of atoms.

By determining the number of atoms at different points in time after trap loading using aforementioned counting method we found the relationship $N(OD)$. The extraction of the OD from the transmission signal had to be independent from probe or pumping induced dynamics in the trap (cf. sec. 7.2), therefore we chose to extrapolate the initial OD from the natural trap decay as is visualized in figure 6.13. A more detailed discussion of this crucial method can be found in Sørensen (2015).

In this chapter we present some experimental results obtained during our investigation of Bragg superstructures.

In the first part, we describe our efforts to reach a high reflection coefficient. To this end, we investigate the dependence of the reflection on several parameters, including the optical powers and number of atoms used. These experiments were the main focus of the atomic mirror experiment (Sørensen et al., 2015a) and therefore carried out in close collaboration. Consequently, a detailed analysis can also be found in Sørensen (2015).

If one thinks about using Bragg superstructures as a tool or device, e. g. as a mirror, the attainable structure lifetime is an important figure of merit. In the second part of this chapter we therefore present an investigation into the reason for the limited amount of time the reflection prevails and whether it is possible to extend it. As this sidetrack was mainly pursued by the author, we provide more detail and a collection of supplemental figures in appendix A.

Finally, we give an outlook on possible applications for Bragg superstructures and other kinds of structured formations of atoms in the vicinity of nanofibers. In light of these promising avenues we discuss the suitability of the optical pumping technique presented here as well as two alternative approaches to structure preparation.

7.1 TOWARDS HIGH REFLECTION

The goal of our experiment was to find the parameters necessary to achieve the highest possible reflection coefficient. In general these parameters are the wavelength of the structuring laser λ_{struct} which determines the lattice constant, its power P_{struct} , and the duration of the pulse T_{struct} . In addition, both the detuning of the probe from resonance Δ_{probe} and the probe power P_{probe} can be varied. In the following we present our efforts to explore this large parameter space.

7.1.1 Structuring Power and Duration

The structuring pulse energy E_{struct} is the product of the structuring pulse duration T_{struct} and power P_{struct} . It can also be instructive to think of E_{struct} in terms of the number of pump photons $N_{\text{pump}} = E_{\text{struct}}c(\hbar\lambda_{\text{struct}})^{-1}$, where c is the speed of light and \hbar is Planck's constant. We see that – as long as the phase of the structuring laser is constant over T_{struct} – E_{struct} is the relevant quantity and should be large enough such that all atoms in wrong positions are scattered.

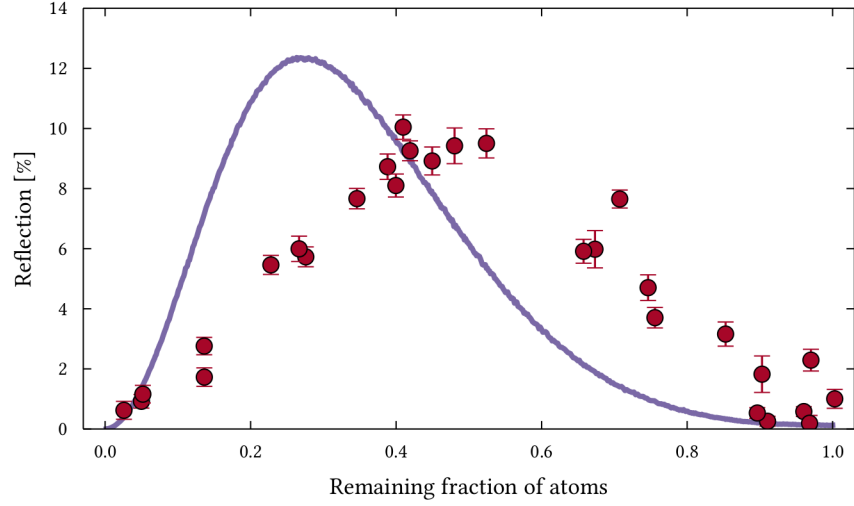


Figure 7.1: By varying P_{struct} we can, as discussed in the main text, vary the number of atoms comprising the superstructure. As predicted, we observe an optimum between the number of scatterers and their degree of localization. We find that the maximum reflection appears for 41% of atoms remaining ($N_{\text{bright}} = 530$, $N_a = 1292$). The reflection coefficient was calculated from a Debye-Waller fit as shown in figure 7.7 and corresponds to the reflection immediately after the structuring pulse was applied. In the background, we show the theoretical curve obtained with the model described in section 6.1 for the same total number of atoms N_a . The deviation is attributed to the fact that interstitial defects are not treated realistically in the model, i. e. the simple pumping model given in equation (6.5) does not sufficiently reflect the experimental situation. ($P_{\text{probe}} = 164 \text{ pW}$, $\Delta_{\text{probe}} = 8 \text{ MHz}$, $P_{\text{struct}} = 17 - 1340 \text{ nW}$, $\Delta_{\text{struct}} = -175 \text{ MHz}$. Each point is the average over 100 to 250 realizations.)

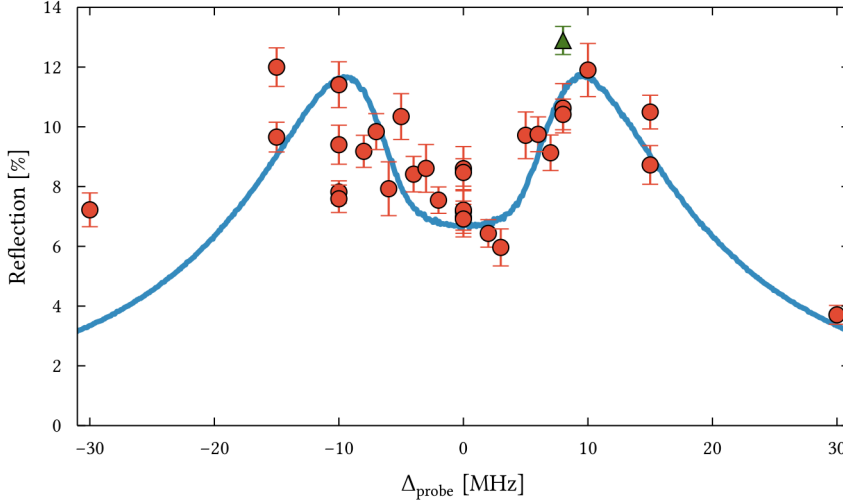


Figure 7.2: To study the effect of probe detuning, we choose P_{struct} close to the optimum (cf. fig. 7.1) and vary Δ_{probe} from -30 to 30 MHz. As expected from the discussion in the main text, we find that maximum reflection (green triangle, cf. tab. 7.1) occurs for a slightly off-resonant probe. In the background, we show the theoretical curve obtained with the model described in section 6.1 for $N_a = 1950$ and $N_{\text{bright}} = 810$ (cf. fig. 7.1) which is in good agreement with the data. ($P_{\text{probe}} = 177$ pW, $P_{\text{struct}} = 238$ nW, $\Delta_{\text{struct}} = -175$ MHz. Average over 200 realizations.)

We choose $T_{\text{struct}} = 250$ ns and use P_{struct} up to about 2 nW. We note that this choice of a fixed T_{struct} and varying P_{struct} is likely not optimal. Although our initial measurements indicated that E_{struct} indeed is the relevant quantity (cf. fig. A.1 in the appendix), a systematic and more detailed study of the forces exerted on the trapped atoms by the structuring light might yield a pulse shape (in principle, there is no need for P_{struct} to be constant) which produces better localization or less interstitial defects.

As we have discussed in figure 6.7, E_{struct} affects both the number of atoms in the bright state N_{bright} and their localization. For the dark lattice, we start with all N_a trapped atoms in the bright state ($N_{\text{bright}} = N_a$). The stronger E_{struct} , the fewer, but better localized atoms will remain. Consequently, we expected there to be an optimum tradeoff, which we indeed observe (fig. 7.1).

7.1.2 Probe Detuning and Power

Regarding the probe detuning from resonance Δ_{probe} we can distinguish two separate factors which need to be optimized:

First, λ_{probe} should be as close as possible to λ_{struct} to fulfill (6.6), although given the short length of the nanofiber lattice a small mismatch can be tolerated and hence (6.6) can be relaxed to $\lambda_{\text{struct}} \approx \lambda_{\text{probe}}$.

Second and more importantly is the fact that the scattering probability depends on Δ_{probe} as $\Delta_{\text{probe}}^{-2}$. This probability should be high enough to yield significant scattering while at the same time all atoms should be illuminated by the probe light, i. e. the penetration depth should at least be equal to the length of the lattice. Likewise, photons reflected by atoms in the back of the superstructure should have a sufficient probability to make it back to the front and emerge from the crystal.

For a more precise analysis of the second point, one has to consider that in a superstructure where the atoms are localized perfectly, a standing wave forms with the atoms at its nodes (Slama et al., 2006). Therefore, absorption is reduced and the penetration depth increases such that one would expect that $\Delta_{\text{probe}} = 0$ should yield the highest back-reflection. If one however considers that the atom's positions are not perfect and that interstitial defects are present, by our previous argument we see that slightly off-resonant probe light will propagate further into the structure.

The measurements presented in figure 7.2 confirm these assumptions. We find the highest reflection for Δ_{probe} of about 1.3 times the natural linewidth Γ .

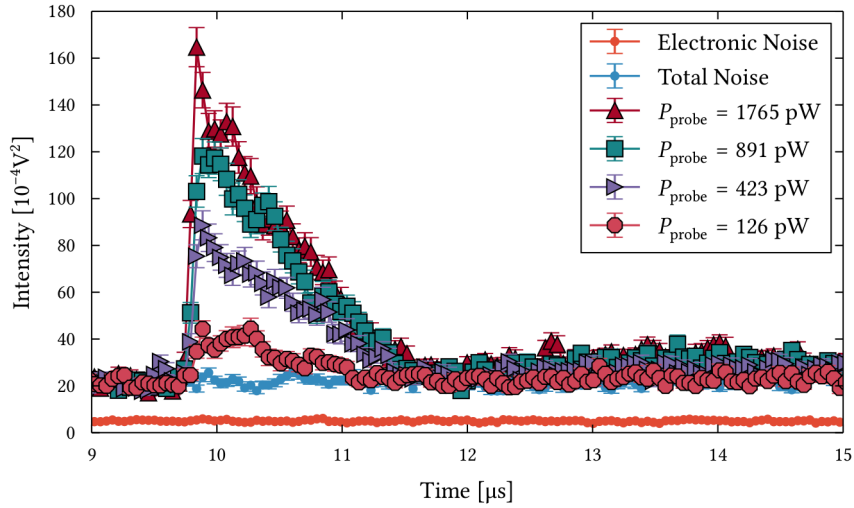
With respect to the probe power P_{probe} , well below saturation we expect $|r|^2 \propto P_{\text{probe}}$. Once the atoms comprising the superstructure are saturated an increase in probe power does not lead to higher reflection (fig. 7.3).

7.1.3 Structuring Wavelength

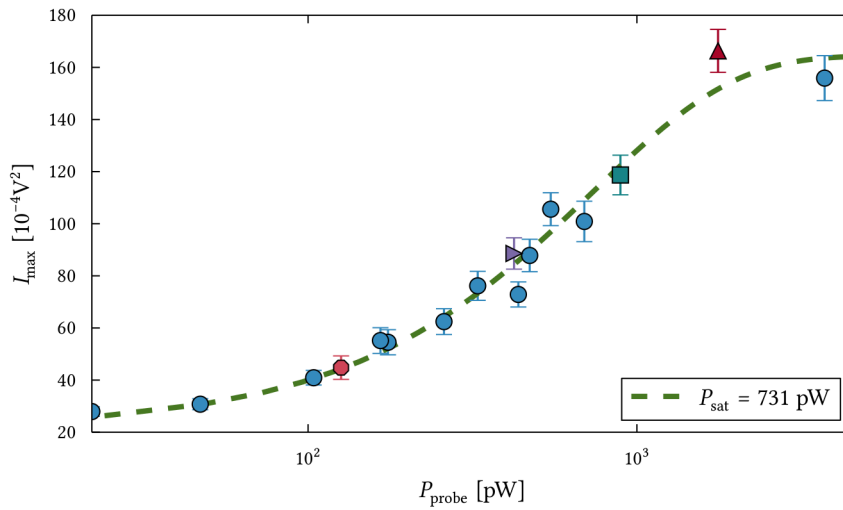
Ideally the structuring laser addresses all trapped atoms equally. This requires its wavelength λ_{struct} to be chosen not only to match λ_{probe} , but also such that no dark states exist. Since the structuring pulse is V -polarized and thus drives π -transitions (cf. sec. 4.3) only $|F' = 4, m_F = 0\rangle$ is problematic since $|F' = 4, m_F = 0\rangle \rightarrow |F = 4, m_F = 0\rangle$ is a forbidden transition.

By varying the detuning of the structuring laser Δ_{struct} (with respect to $|F = 4\rangle \rightarrow |F' = 3\rangle$) for otherwise fixed parameters we find that $\Delta_{\text{struct}} = +140$ MHz is a local and $\Delta_{\text{struct}} = -180$ MHz the global optimum (fig. 7.4). As already discussed above, due to the short length of the lattice it is sufficient if $\lambda_{\text{struct}} \approx \lambda_{\text{probe}}$. Taken together with the inherent trap structure determined by λ_{trap} there is no need for λ_{struct} to be constant during T_{struct} . Therefore, instead of choosing a fixed wavelength which addresses all atoms with varying coupling strength one could e. g. ramp or modulate λ_{struct} during T_{struct} (cf. sec. 9.1).

A slightly different path to take is to first pump atoms into specific Zeeman-sublevels of $|F = 4\rangle$, e. g. $|F = 4, m_F = 0\rangle$ (cf. sec. 9.1). Then all atoms couple to the structuring light with equal strength and E_{struct} can be expected to decrease significantly. In general, this comes at the expense of the number of atoms in the superstructure as the pumping procedure's efficiency is not 100% requiring unpumped atoms to be removed from the trap (cf. sec. 9.1.3) or detuned by applying a large magnetic bias field (cf. sec. 9.2.3).



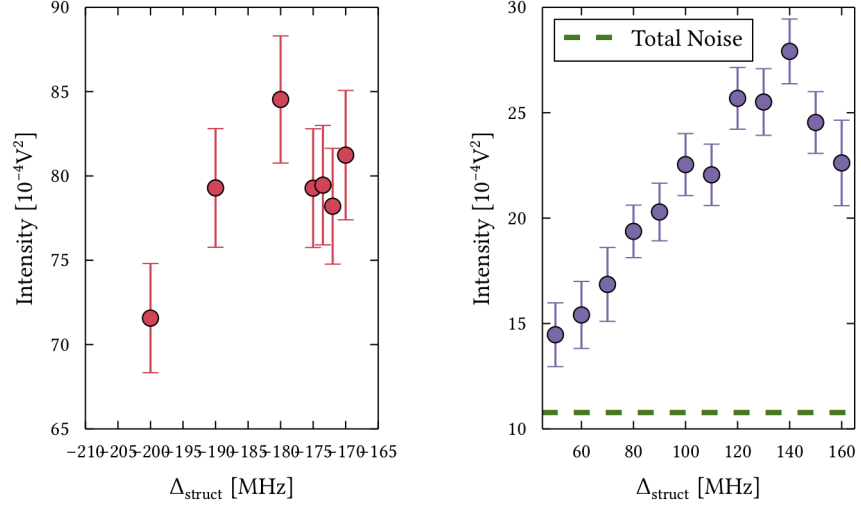
(a) Reflection signals for four vastly different P_{probe} . We see that both shape and decay time stay constant.



(b) Relationship between reflected and probe power. As expected, we find a saturation point from which on higher P_{probe} does not lead to a gain in reflected power.

Figure 7.3: $\Delta_{\text{probe}} = -5 \text{ MHz}$, $\Delta_{\text{struct}} = -175 \text{ MHz}$, $P_{\text{struct}} = 238 \text{ nW}$. Each point corresponds to the average of 100 realizations.

Data points shown in both plots are indicated by the same color.



(a) $P_{\text{probe}} = 472 \text{ pW}$, $\Delta_{\text{probe}} = -5 \text{ MHz}$, $P_{\text{struct}} = 238 \text{ nW}$.
 (b) $P_{\text{probe}} = 1100 \text{ pW}$, $\Delta_{\text{probe}} = 0 \text{ MHz}$, $P_{\text{struct}} \approx 190 \text{ nW}$.

Figure 7.4: The reflection coefficient heavily depends on λ_{struct} . We present two separate measurements covering the two frequency ranges where the highest reflection was observed.

Each point corresponds to the maximum of the reflection peak obtained from averaging 100 realizations, each analyzed with a running average timebin of 192 ns.

Since the two measurements presented here were taken several weeks apart, the obtained intensities are not directly comparable as significant improvements in polarization control, detection efficiency, and trap quality were achieved in the meantime.

In later measurements for different Δ_{probe} and P_{struct} we found $\Delta_{\text{struct}} = -175 \text{ MHz}$ to be the more optimal choice (cf. tab. 7.1), but did not repeat this systematic study.

7.1.4 Optimal Parameter Set

By utilizing the investigations into the different parameters, we empirically find a maximum reflection of $(11.6 \pm 1.1)\%$ (green triangle in fig. 7.2) for the parameter values listed in table 7.1. Considering the fact that in this case the superstructure was formed by only about 800 atoms, this is remarkably high and exceeds e. g. reflection from a common glass window. In comparison, the reflection from the unstructured about 1300 atoms which are initially loaded into the nanofiber lattice amounts to a mere $(0.10 \pm 0.01)\%$ (Sørensen et al., 2015a).

P_{struct}	204 nW
T_{struct}	250 ns
Δ_{struct}	-175 MHz
P_{probe}	177 pW
Δ_{probe}	8 MHz

Table 7.1: Optimum parameters found for the preparation of an atomic mirror in the dark lattice scheme.

7.2 DYNAMICS

Up to this point we have only considered the momentary reflection off the atomic crystal right when the probe light is turned on. In this picture the atoms form a static structure. In light of possible applications of resonantly spaced superstructures beyond Bragg reflection (cf. sec. 7.3), we will now investigate the dynamics.

In general the reflection persists for a limited time on the order of $1 \mu\text{s}$ and the highest reflection occurs at the instant the probe light first reaches the atomic ensemble. The decline in reflection can be due to either loss in structure, i. e. deteriorating localization of the atoms, or loss in scatterers. Both of these effects are caused by thermal motion of the atoms inside the trapping potentials which might be altered by the structuring laser or the probe light. Atoms can also be lost from the superstructure due to optical pumping into the dark state $|3\rangle$. Since the probe is resonant to $|4\rangle \rightarrow |5'\rangle$, we can neglect this effect.

After the initial peak has vanished, oscillations are visible on the reflection signal, hinting at a re-formation of the resonance in the superstructure. The oscillation frequency is compatible with the trap frequencies (sec. 5.5.3). More detail on this effect is provided in Sørensen (2015).

7.2.1 Effect of Probe Light

In a first step we investigate whether the probe light has any effect on the dynamics. To this end we run the usual preparation sequence (fig. 6.10), but

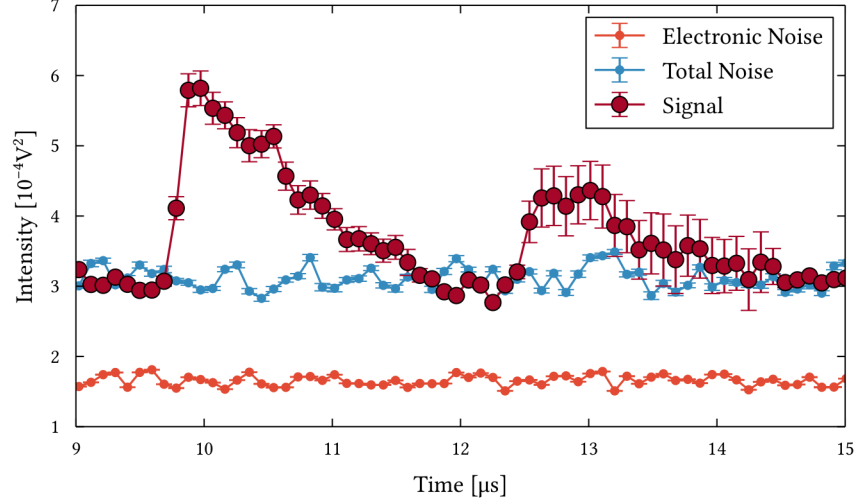


Figure 7.5: If a second structuring pulse is applied after the initial reflection peak has disappeared, a second reflection appears.

Probe light is turned off during the second structuring pulse. The corresponding transmission signal can be found in the appendix (fig. A.5).
($P_{\text{probe}} = 770 \text{ pW}$, $\Delta_{\text{probe}} = 0$, $P_{\text{struct}} = 170 \text{ nW}$, $\Delta_{\text{struct}} = 140 \text{ MHz}$.
Average over 100 runs.)

delay the probe onset by a time ΔT . If probing were to have an influence on the atomic motion, the shape of the reflection peak should vary, one could e. g. expect the peak to appear in the same shape but delayed by ΔT . If on the other hand the interaction of structured atoms with the probe laser leads to heating, there should be a difference in the observed transmission signal. (Of course, the interaction with the probe laser will always induce heating and subsequently loss of atoms from the trap, but on a timescale much larger than a $1 \mu\text{s}$, cf. fig. 5.5 and fig. A.6.)

The results of this measurement are presented in figure 7.6 for the case of a resonant probe. It is apparent that the reflection and transmission dynamics remain the same, i. e. the probe laser has no (significant) influence. The results for probe light detuned from resonance, where one could expect to see an influence from ac Stark shifts yield a similar conclusion, the corresponding figures A.3 and A.4 can be found in the appendix.

In figure 7.3 we have already found that the probe light intensity has no influence on the duration of reflection.

In conclusion we see that the superstructure's dynamics are independent of the probe light. This justifies our previous assumption that optical pumping due to probing can be neglected.

7.2.2 Effect of Structuring

In general, we do not see a difference in reflection lifetime for different structuring pulse durations T_{struct} (fig. A.1) or powers P_{struct} (fig. A.2). We also

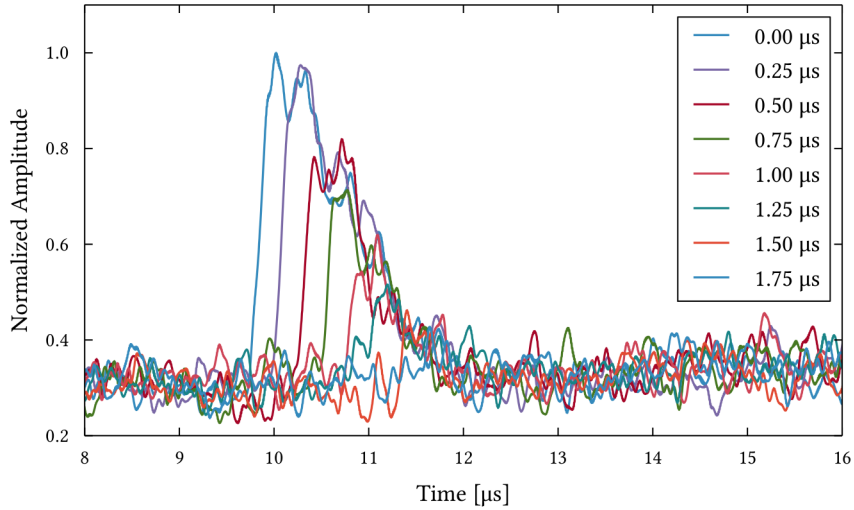
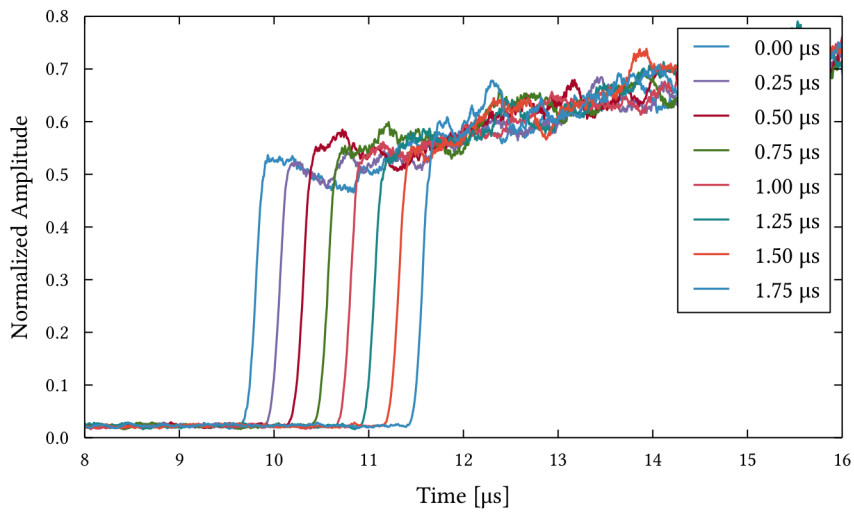
(a) Reflection for different probe delays ΔT .(b) Transmission for different probe delays ΔT .

Figure 7.6: To investigate the effect of probe light on the dynamics, we delay the probe onset by ΔT .

(Each curve corresponds to 100 runs with $\Delta_{\text{struct}} = -175$ MHz, $P_{\text{struct}} = 238$ nW, $\Delta_{\text{probe}} = 0$ MHz, $P_{\text{probe}} = 175$ pW.)

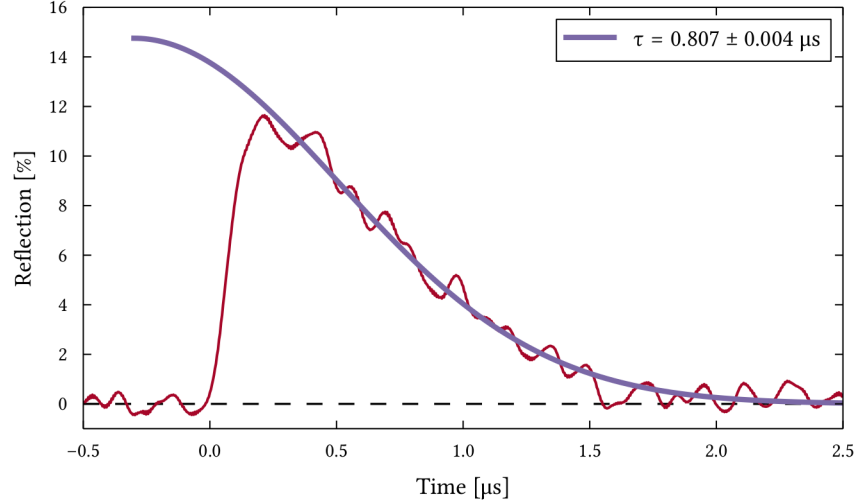


Figure 7.7: By fitting an exponential decay to the data, from equation (7.1) we find a temperature of $T = 42 \pm 2 \mu\text{K}$ for the atoms. This model was also used to extrapolate the reflection coefficients for figures 7.1 and 7.2.

observe that if we apply a second structuring pulse – without previously re-pumping all atoms back to $|F = 4\rangle$ – after the initial reflection peak has vanished, a second reflection peak appears (fig. 7.5). While its lifetime does not vary significantly from the first's, the reflection intensity is lowered, which we therefore attribute to the loss in scatterers. We note that the difference in reflection intensity observed in figure 7.5 roughly corresponds to the difference in transmission (cf. fig. A.5).

All of this warrants the conclusion that – just as we found for the probe light – the structuring pulse has no influence on the atom's dynamics. This allows us to use the decay time to infer the temperature of the atoms in the trap using the Debye-Waller factor (Birkl et al., 1995, Gross and Marx, 2012). According to this model, the reflection intensity goes as

$$I = I_0 \cdot \exp(-K^2 \sigma_z^2(t)) \quad (7.1)$$

where $K = 4\pi n \lambda_{\text{probe}}^{-1}$ is the momentum transferred onto an atom by a single photon and the width σ_z describes the localization spread of the atoms. Since the reflection vanishes on a timescale much below the trap frequency, the time evolution of σ_z can be modeled as a free ballistic expansion

$$\sigma_z^2(t) = \sigma_z^2(0) + \frac{\sigma_p^2}{2m} t^2, \quad (7.2)$$

where m is the atomic mass and σ_p the momentum distribution. As long as $\hbar\omega_{\text{trap}} \ll 2k_B T \pi$ (cf. sec. 5.5.3) the trapping potential can be modelled as an isotropic harmonic oscillator, i. e.

$$\frac{\sigma_p^2}{2m} = \frac{\hbar\omega_{\text{trap}}}{2m} \coth \frac{\hbar\omega_{\text{trap}}}{2k_B T} \approx \frac{k_B T}{m}. \quad (7.3)$$

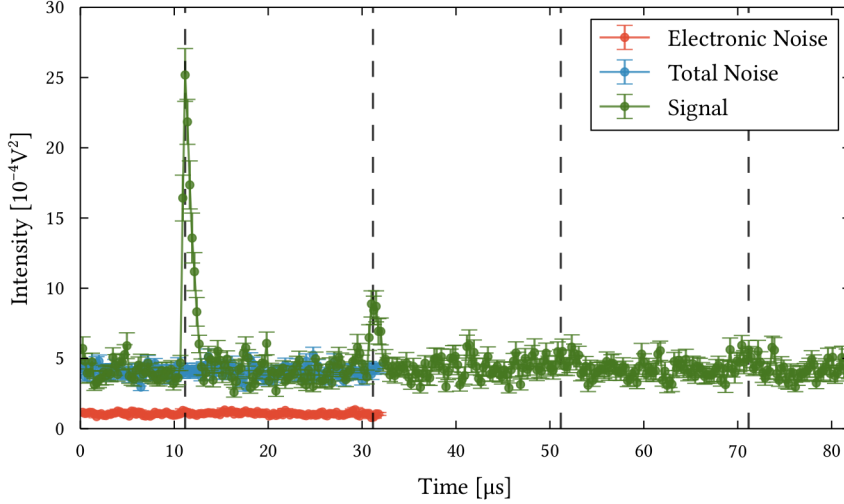


Figure 7.8: If the complete preparation sequence (repumping all atoms into $|F = 4\rangle$ and subsequently applying a structuring pulse) is run multiple times, contrary to the expectation only a few reflection peaks can be observed, with rapidly decaying maximum reflection intensity. Vertical dashed lines represent the points in time where a reflection would be expected (20 μs repetition cycle). ($\Delta_{\text{struct}} = -175$ MHz, $P_{\text{struct}} = 238$ nW, $\Delta_{\text{probe}} = 0$ MHz, $P_{\text{probe}} = 175$ pW. Average over 100 realizations.)

An example result can be found in figure 7.7, yielding $T = 42$ μK , which is well within the expected temperature range (cf. sec. 2.4.4). More details on this analysis can be found in Sørensen et al. (2015a), Sørensen (2015).

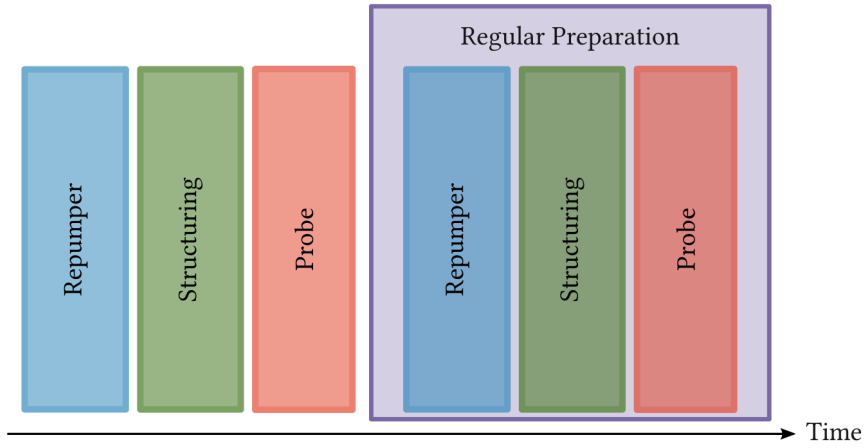
7.2.3 Repeated Preparation

In light of our discussion so far, it should be possible to repeatedly prepare and probe a mirror during the same MOT loading. We note that if the whole preparation procedure is delayed by 100 μs , no appreciable change in the decay time can be found, i. e. the inherent heating of atoms can be neglected on the timescale under consideration here (fig. A.6). However, we fail to observe multiple high-reflecting mirrors if we simply repeat the whole Bragg superstructure preparation sequence (fig. 7.8).

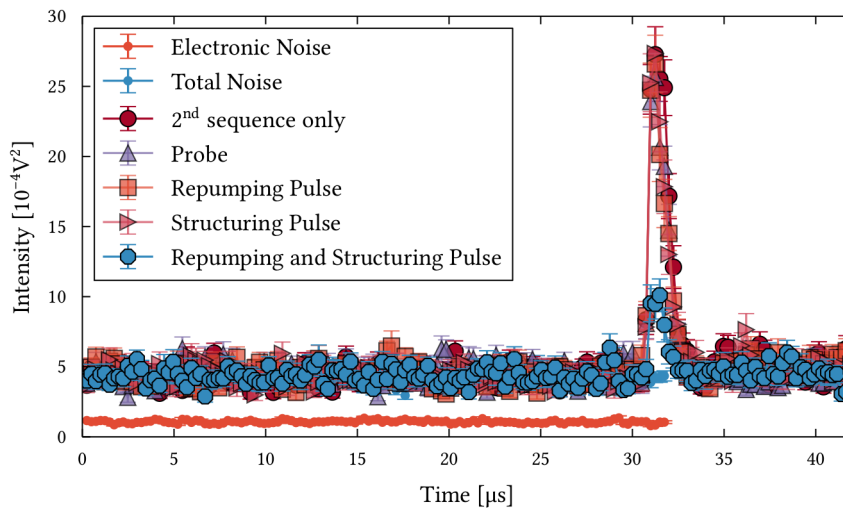
From a systematic investigation using the pulse sequence shown in figure 7.9a we conclude that atoms are heated by pumping into the dark state $|3\rangle$ (fig. 7.9b). Due to our inability to rapidly switch between a standing and running wave configuration for the structuring pulse within the experimental sequence,¹ it remains an open question whether the effect is due to the spatial structure of the pulse or a general feature of optical pumping. While an understanding of the phenomenon's dependence on P_{struct} and T_{struct} might

¹ The main experimental challenge lies in the fact that for such a measurement to be conclusive, it is necessary that the total power of the running wave is equal to that of the standing wave.

yield a pulse shape (cf. sec. 7.1.1) which reduces the effect, enabling multiple preparations of similar quality and thus higher repetition rates for the experiment, the limited lifetime of the reflection itself remains an obstacle for the applications we will discuss in the next section. Here, the alternative structuring methods discussed in sections 7.3.3 and 7.3.4 constitute promising paths.



- (a) The experimental protocol consists of two complete preparation sequences. While the second one is run in full each time, the first is used in all possible combinations.



- (b) Result for all possible variants of sequence (a) where in principal a signal from the atoms can be detected (i. e. at least some atoms are in $|4\rangle$). We see that the reflection peak only deteriorates if a structuring pulse has been applied in the first part of the sequence after the atoms have been repumped.

Figure 7.9: To find the reason why a repeated preparation of high reflectivity Bragg superstructures is not possible, we investigate which process causes the reflection to vanish.

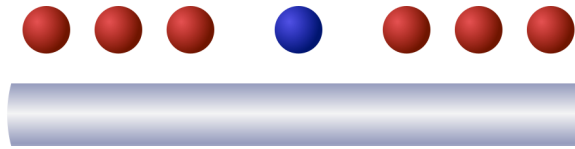


Figure 7.10: By creating gaps around a single atom inside the atomic mirror one can create a Fabry-Perot type cavity.

7.3 APPLICATIONS AND OUTLOOK

Although certainly a phenomenon worth investigating in its own right, the creation of Bragg mirrors – or, to be more general, the preparation of structures which lead to coherent enhancement of emission – near nanofibers or other photonic waveguides has recently been the basis for several proposals. In this section we discuss the suitability of our optical pumping method for these proposals as well as more advanced mirror preparation schemes.

7.3.1 Atomic Cavities

The perhaps most obvious application of atomic mirrors is the creation of atomic cavities which was studied theoretically e. g. by [Chang et al. \(2012\)](#). An atomic cavity as sketched in figure 7.10 could be used to enhance the coupling of a single or several atoms at its center to the nanofiber. The main advantage compared to regular mirrors positioned at the fiber ports (cf. [Kato and Aoki, 2015](#)) is not only the narrow reflection window optimally tailored to the atomic emission, but the switchability.

One can prepare such a system by creating a gap inside an atomic mirror which is in principle possible with a tightly focused laser beam aimed at the center of the lattice. A scheme where a single or a few atoms remain at the cavity center is conceivable. Also, with the reflection coefficients achieved with the optical pumping method presented here and the generous assumption that both cavity mirrors would yield a similar reflection, a cavity finesse $\mathcal{F} > 1$ is within reach. This is however not sufficient to reach a useful enhancement. While a larger initial number of atoms N would presumably lead to higher \mathcal{F} , for a significant increase alternative preparation schemes are necessary, some of which we will discuss below. These schemes also remove the second severe limitation which prohibits the implementation of atomic cavities with our approach: As discussed in section 7.2.3 the prepared structure dephases quickly and – since the optical pumping disturbs the atoms – cannot be prepared repeatedly.

7.3.2 Quantum State Preparation

Another interesting avenue is the use of resonantly structured atoms for quantum state preparation. In a scheme proposed by [González-Tudela et al. \(2015\)](#) an ensemble of N atoms spaced by $d = n\lambda$ is used to store excitations

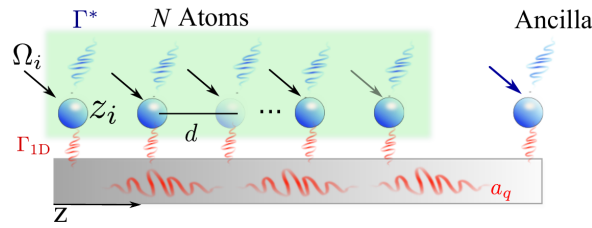


Figure 7.11: Proposal for the deterministic quantum state preparation using an atomic crystal with $d = \lambda$. The excitations are encoded in the single ancilla atom and transferred to the N storage atoms. (Image taken from González-Tudela et al., 2015, .)

in the form of a subclass of Dicke states $|D_m\rangle$ similar to the states discussed in section 2.3.2. Instead of exciting this atom chain directly, the excitation is encoded into a separate ancilla atom and upon success transferred. This allows for the deterministic generation of large numbers of excitations m , whereas e. g. the DLCZ protocol discussed in section 8.1 is probabilistic and therefore unsuitable for $m \gg 1$ (cf. sec. 10.4.2). The stored excitations can be released in form of a photonic Fock state by exploiting superradiant enhancement (cf. sec. 4.3.3).

With the optical pumping method explored in this chapter, the creation of a structure with $d = \lambda$ is not possible, at least not in a straightforward fashion. Additionally, the occupation of only 50% of the lattice sites with atoms (sec. 5.5.1) prevents the formation of a vacancy defect free atomic crystal. However, the preparation of only a single linear chain has been demonstrated (Mitsch et al., 2014a) and the addressing of a single ancilla atom by means of a focused laser beam perpendicular to the fiber axis is certainly possible. Especially self-organized lattice formation as discussed below might offer a way to create suitable structures which can also have much longer lifetimes. A different approach lies in the development of quantum state preparation schemes which are robust with respect to vacancy or interstitial defects.

7.3.3 Structuring via EIT

As discussed above and in section 7.2 the thermal motion of atoms quickly washes out the imprinted structure. Since atoms are irreversibly lost from the superstructure by structuring through optical pumping it is not possible to repair it by repeated structuring pulses.

Here, electromagnetically induced transparency (EIT) is a possible solution. As sketched in figure 7.12 the lattice is created by combining a running wave pump with a standing wave control beam (cf. Brown and Xiao, 2005). Again the atomic crystal to be scattered from is formed by atoms in $|4\rangle$. However, in this scheme the transfer of atoms between $|4\rangle$ and $|3\rangle$ is a reversible process. If the atoms's movement is slow compared to the light intensity gradient, they will be transferred adiabatically into and out of the superstructure. While this scheme is compatible with a caterpillar trap, in principle it is

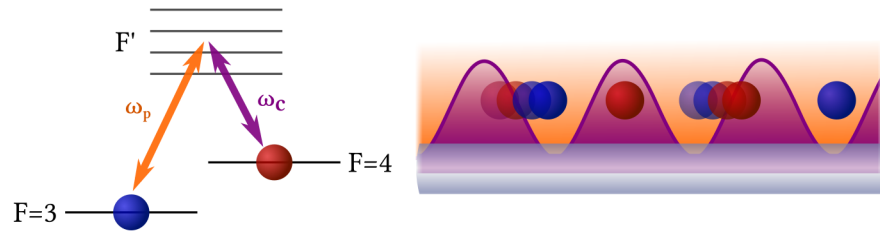


Figure 7.12: Possible configuration for the creation of an atomic mirror via EIT. Left: A standing wave control field ω_c transfers atoms into the $|F = 4\rangle$ state, which is again the bright state for the probe. Right: Atoms are dark at the antinodes and bright at the nodes and are switched adiabatically when moving relative to the control field.

also applicable to the case where the standing wave of the red-detuned trap is replaced by an equally intense, but running wave. The caterpillar configuration however guarantees that the number of scatterers comprising the superstructure stays constant to good approximation, whereas it can be expected to significantly fluctuate if atoms are not confined to a very small volume (cf. sec. 5.2).

EIT has been employed in a similar fashion in atomic vapors (cf. Bajcsy et al., 2003, Brown and Xiao, 2005, Schilke et al., 2012) as well as been observed and used in a range of experiments on the nanofiber platform (e.g. Kumar et al., 2015b, Gouraud et al., 2015, Sayrin et al., 2015). While we also observed signs of EIT in our nanofiber trapped ensemble, early attempts to create an atomic mirror failed and would have required significant experimental effort. We therefore leave this for future experiments to explore and at this point only emphasize that as long as the transfer of atoms between $|3\rangle$ and $|4\rangle$ does not lead to heating (cf. sec. 7.2.3), it should be possible to maintain a mirror for times that are long compared to the ones we observed with the optical pumping method.

7.3.4 Self-Organized Structuring

A more advanced proposal than the one just discussed is the creation of mirrors through self-organization (cf. Chang et al., 2013, Holzmann et al., 2014, Holzmann, 2015, Holzmann and Ritsch, 2015). This necessarily requires the atoms to be able to move freely along the fiber axis, i.e. a running red trap as mentioned in the previous section is needed.

For self-structuring to occur, the coupling of the atoms to the common light mode, i.e. in our case the coupling of atoms to the nanofiber, has to be on significantly stronger than what we observe. However, this regime can be reached in a straightforward fashion when the tapered section of the nanofiber is placed inside a fiber Bragg cavity such as demonstrated by Kato and Aoki (2015). Alternatively, the nanofiber can be twisted to form a loop which serves as a ring resonator. We will cover this in more detail in section 11.2.1. It is important to stress that while a resonator increases

the light-atom coupling, it also adds boundary conditions which can also lead to structuring – similar to [Slama et al. \(2005b\)](#) (fig. 6.5) and what we have presented in this chapter, where the path of the structuring laser can be viewed as a ring resonator.

This section benefited from discussions with Darrick Chang (Instituto de Ciencias Fotónicas, Barcelona) and Alejandro González-Tudela (Max-Planck-Institut für Quantenoptik, Munich).

Part IV

TOWARDS THE SINGLE EXCITATION FOCK STATE

In the beginning, we introduce the general protocol for the creation of a single excitation state. Subsequently we present a proposal for the case of nanofiber trapped atoms and an analysis thereof. Then, we turn to its experimental realization and describe our efforts regarding the preparation of the initial state using microwave and optical pumping. In doing so, we obtain estimates for the coherence times in the nanofiber trapped ensemble. Then we discuss in detail our detection scheme, where we present data on the performance of each of the components and finally predict the attainable state purity.

Our goal is the creation and characterization of a single excitation state – the first atomic Fock state as introduced in section 2.3.2 – in a nanofiber trapped atomic ensemble. In this chapter, we present the outline of the experiment building on [Christensen et al. \(2013\)](#) and [Christensen \(2014, sec. 9.5\)](#).

First we discuss how a single excitation state can be prepared in general and how this can be implemented in cesium. Subsequently, we work out a detailed proposal for nanofiber trapped atoms and discuss briefly how a tomography can be implemented. We conclude with an overview of the following chapters, where the development of certain experimental tools necessary to turn the proposal into reality will be described.

8.1 CREATING A SINGLE EXCITATION STATE

To create the single excitation state (SES) we make use of the entanglement generation step of the so-called DLCZ protocol ([Duan et al., 2001a](#), [Christensen, 2014](#)).

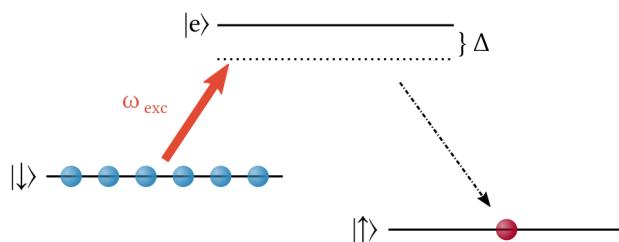


Figure 8.1: The DLCZ protocol requires two (meta)stable ground states $|\downarrow\rangle$ and $|\uparrow\rangle$, coupled through an excited state $|e\rangle$.

In our nanofiber trap, we have an optically thick ensemble of N_a (identical) cesium atoms, which possess an DLCZ suitable level structure as depicted in figure 8.1. For now, we identify the ground states $|\downarrow\rangle$ and $|\uparrow\rangle$ with a Zeeman sublevel of either one of the hyperfine groundstates of cesium, while the excited state $|e\rangle$ can be a Zeeman sublevel of either $|F' = 3\rangle$ or $|F' = 4\rangle$. We will discuss and compare different specific choices in section 8.2.

All N_a atoms are initially prepared in $|\downarrow\rangle$, so the initial state of the ensemble reads

$$|\Psi_0\rangle_A = \bigotimes_{k=1}^{N_a} |\downarrow\rangle_k, \quad (8.1)$$

which corresponds to the “atomic vacuum” $|0\rangle_A$ from section 2.3.2. All N_a atoms couple equally to a photonic mode \hat{a} , and the initial state of the full system reads

$$|\Psi_0\rangle_A = |\Psi_0\rangle_A |0\rangle_P. \quad (8.2)$$

From here on, states with a subscript A denote collective states of the atomic ensemble, states labelled with k are states of the (distinguished) k^{th} atom and states with subscript P are Fock states of the photonic mode.

A short, off-resonant laser pulse drives a Raman transition (which is a coherent process, cf. sec. 9.3) from $|\downarrow\rangle$ into $|\uparrow\rangle$, which is equivalent to the action of the ensemble creation operator \hat{A}^\dagger (cf. eq. 2.21) on $|\Psi_0\rangle$:

$$|\Psi\rangle = \hat{A}^\dagger |\Psi_0\rangle = |\downarrow\rangle_A |0\rangle_P + \sqrt{p_c} \hat{S}^\dagger \hat{a}^\dagger |\downarrow\rangle_A |0\rangle_P + o(p_c), \quad (8.3)$$

where p_c is the excitation probability and $o(p_c)$ denotes all terms where more than one atom was excited. p_c has to be chosen such that $o(p_c)$ remains small with respect to the second term. In turn, at the same time the latter should not be too small compared to the first term, to obtain an SES in a reasonable time (we will discuss further constraints on the pulse duration in section 8.3).

A detector measures whether a photon propagates in the mode \hat{a} , i. e. the projection onto |noclick> $\langle 0|_P + |\text{click}\rangle \langle 1|_P$ (cf. sec. 3.1). If the detector “clicks”, $|\Psi\rangle$ collapses into

$$|\Psi_{\text{SES}}\rangle_A = \hat{S}^\dagger |\downarrow\rangle_A, \quad (8.4)$$

i. e. the atomic ensemble is in

$$|\Psi_{\text{SES}}\rangle_A = \hat{S}^\dagger |\downarrow\rangle_A = \frac{1}{N_a} \sum_{k=1}^{N_a} |\downarrow \dots \downarrow \underbrace{\uparrow}_{k^{\text{th}} \text{ atom}} \downarrow \dots \downarrow\rangle. \quad (8.5)$$

In other words, the detection of the photon heralds the creation of the desired SES.

8.2 CHOICE OF LEVEL SET

Since the DLCZ protocol only requires a combination of two stable ground and one excited state (fig. 8.1), in the case of cesium various options are available.¹ In addition to forming a Λ -scheme, the level set has to fulfil additional requirements:

- It has to be possible to prepare the initial state with high occupation and high purity from an ensemble with randomly distributed population of m_F sublevels. This is only possible for states where $m_F = 0$ or $m_F = \pm F$ (sec. 9.1).

¹ As introduced in section 4.3.1, we use the coordinate system given in figure 4.5 and quantize the atom along the y -axis.

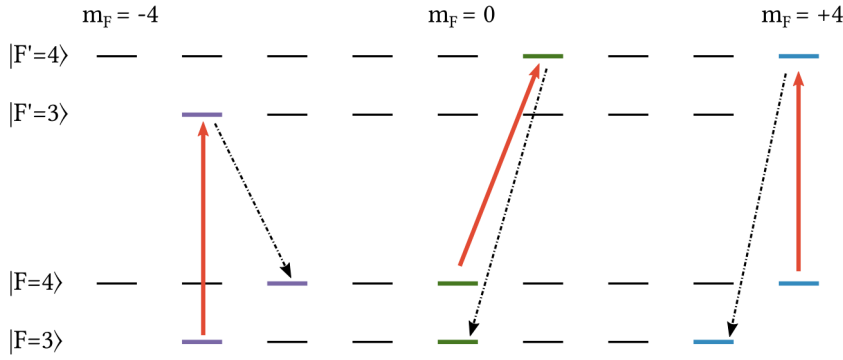


Figure 8.2: Three different choices of level sets for the implementation of the DLCZ protocol in atomic cesium.² The choice of upper levels takes into account the branching ratios and coupling strengths.

- Following the discussion in section 4.3.2, the heralding photon must be σ_{\pm} polarized to exploit the directionality of spontaneous emission.
- The excitation transition has to be reasonably strong to yield a sufficient p_c . Further, the decay into $|\uparrow\rangle$ has to dominate all other decay channels, especially those σ_{\pm} -polarized, to minimize false positives when detecting the heralding photon (cf. sec. 8.3).

Three options are shown in figure 8.2.² The two level sets with extreme Zeeman sublevels as initial states, $|F = 3, m_F = 3\rangle$ and $|F = 4, m_F = 4\rangle$, can be prepared straightforwardly by optical pumping with H polarized light (cf. sec. 4.3.2). For the excited states, the π -transitions are almost equally strong ($|F' = 4, m_F = 3\rangle$ decays symmetrically into $|F = 4, m_F = 2\rangle$ and $|F = 4, m_F = 4\rangle$ and is thus discarded). However, the branching ratios favor $|F = 4, m_F = 4\rangle$ as the initial state, since for $|F' = 3, m_F = 3\rangle$ the π -transition into $|F = 4, m_F = 3\rangle$ is the dominating decay. Furthermore, the desired σ_+ decay into $|F = 4, m_F = 2\rangle$ is extremely weak. We are thus left with the option $|0\rangle_A = |F = 4, m_F = 4\rangle$ for the initial state of the atoms.

The disadvantage of $|F, m_F = 0\rangle$, commonly known as “clock levels” for their use in the 1967 SI definition of the second,³ is the more involved preparation, which requires a combination of optical and microwave pumping (cf. sec. 9.1). However, there are also key advantages: First, the states are magnetically insensitive to first order, which ensures that inhomogeneous background magnetic fields do not render the two ensembles or atoms on either end of the same ensemble distinguishable. Secondly, due to the same reason the clock states experience less disturbance and can thus be expected to exhibit longer coherence times.

² Note that we will once more discuss polarizations and levels in terms of atom’s placed on the positive x -axis, i. e. the left-most example in figure 8.2 is shown mirrored. For details, see section 4.3.

³ “The second is the duration of 9 192 631 770 periods of the radiation corresponding to the transition between the two hyperfine levels of the ground state of the cesium 133 atom.” Refined in 1997 to a cesium atom in its ground state at 0 K.

A third advantage specific to the nanofiber is that both atomic ensembles will be in the very same state. To reiterate, for the extreme m_F -substates one ensemble will be in $m_F = +4$ while the other will be in $m_F = -4$, leading to different energy difference between the two ground states if a bias field is present (cf. Mitsch et al., 2014a, for an illustrative demonstration). Since a bias field is necessary to lift the degeneracy of m_F sublevels (cf. sec. 4.3.2) and to avoid spin flips (cf. sec. 9.2), this makes both ensembles distinguishable, requiring one to “blow out” one of the ensembles, reducing the number of atoms to half the initially loaded value (cf. sec. 9.1.3 and once again Mitsch et al. (2014a)). In section 11.1.4 we will briefly discuss examples of how the distinguishability of the two ensembles enables interesting experiments).

We thus select the clock levels for our experiment.

8.3 A SINGLE EXCITATION IN A NANOFIBER TRAPPED ATOMIC ENSEMBLE

Here we adapt and analyze the proposal by Christensen et al. (2013) for the case of nanofiber trapped atoms as introduced in chapter 5. A preliminary analysis can be found in Christensen (2014), which we now extend to include the directionality of emission (sec. 4.3.2).

To be able to individually address Zeeman sublevels, we need to lift their degeneracy by applying a large bias field along the quantization axis.⁴ Then it is possible to prepare the initial state

$$|\Psi_0\rangle_A = \bigotimes_{k=1}^{N_a} |\downarrow\rangle_k = \bigotimes_{k=1}^{N_a} |F = 4, m_F = 0\rangle_k \quad (8.6)$$

through microwave interactions and optical pumping. We need not be concerned about the details at this point, they are covered in chapter 9.

To create the SES, we have to drive the σ_+ transition $|4, 0\rangle \rightarrow |4', 1\rangle$. This requires the excitation light to be H -polarized. Since H polarized light also has a small σ_- component at the atom position of the atoms (cf. sec. 4.3.2), we also address the $|4, 0\rangle \rightarrow |4', -1\rangle$ transition, which will bring atoms into $|3, 0\rangle$, $|3, -1\rangle$ and $|3, -2\rangle$ as well as $|4, -2\rangle$. Given a sufficiently strong bias field, coherences between these levels and our Λ system of interest quickly dephase and we are left with a mixed state. Nevertheless we have to take these processes into account, since the emitted photons are close in frequency to the heralding photon.

From an experimental perspective, we can classify the unwanted decay channels into two categories: Those far-detuned from the heralding photon ($|\Delta\nu| = |\nu - \nu_{\text{hp}}| \approx \nu_{\text{clock}} = 9.192 \text{ GHz}$) which can be filtered optically (cf. sec. 10.1) on the one hand, and on the other hand those of approximately the same emission frequency ($|\Delta\nu| \approx 0$).

⁴ We again take z to be the fiber axis, place the atoms on the positive x -axis and quantize them along y . We use the nomenclature introduced in section 4.2.3 to unambiguously describe light polarization.

Following our discussion in section 2.1.2, all magnetic sublevels decay with the same rate Γ and we can simply use the branching ratios found e. g. in (Steck, 2010) to determine the emission probabilities for an atom excited into $|e\rangle = |4', 1\rangle$. In section 4.3.2 we have seen that as a result of the complex polarization properties of the nanofiber's evanescent field and the symmetry-breaking choice of y as the quantization axis, emission on σ_{\pm} transitions exhibits a distinct directionality, which we need to incorporate as well.

Before we continue our discussion with considerations on the experimental requirements, we consider the consequence of a decay into modes other than the detection mode $H+$. This can be the $-z$ direction, $V+$, or free space. In all these cases, we will never detect a photon despite the fact that an atom might have decayed into $|\uparrow\rangle$ or another magnetic sublevel. We will see in section 8.3.1 that it is only the atoms comprising the coherent state which contribute to the SES's signature in the tomography, and per the discussion above, all atoms which scattered a photon incoherently (cf. sec. 9.3) will quickly dephase. Nevertheless, they are still present and will be measured during the tomography, thereby reducing its efficiency (sec. 10.4.3). We would therefore like to keep this number small (Christensen, 2014, sec. 8.4.2, 9.5).

If we denote the probability for an atom prepared in $|e\rangle = |4', 1\rangle$ to emit on the transition $|4, 1\rangle \rightarrow |F, m_F\rangle$ as P_{F, m_F} (with $\sum_{F, m_F} P_{F, m_F} = 1$), the probability that the heralding photon is emitted in the forward direction is

$$P_{\text{hp},+} = \frac{12}{13} P_{3,0} = 0.14, \quad (8.7)$$

where the factor $12/13$ is the directionality coefficient for σ_+ transitions. Then it is straightforward to calculate the ratio

$$\frac{P_{\text{hp},+}}{P_{\Delta \approx 0,+}} = \frac{P_{\text{hp},+}}{1/13 \cdot P_{3,2}} = 40, \quad (8.8)$$

where we have per our discussion above excluded the π -transition into $|3, 1\rangle$ and again the pre-factor in the denominator reflects the directionality of σ_- -transitions. We note that this leads to a remarkable improvement compared to the situation in the free-space experiment of Christensen et al. (2013, 2014), where

$$\frac{P_{\text{hp},+}}{P_{\Delta \approx 0,+}} = \frac{P_{3,0}}{1/2 \cdot P_{3,1}} = 1.33. \quad (8.9)$$

Here, the factor $1/2$ reflects the overlap between σ_+ and π polarization. What remains is to calculate the contributions of the far-detuned decay channels

$$P_{\Delta \approx \nu_{\text{clock}},+} = \frac{12}{13} P_{4,0} + \frac{1}{13} P_{4,2} = 0.29. \quad (8.10)$$

Contributions from the decay of an atom excited to $|4, -1\rangle$ can be found strictly analogously.⁵

⁵ $\bar{P}_{\Delta \approx 0,+} = 12/13 \cdot \bar{P}_{3,-2} + 1/13 \cdot \bar{P}_{3,0} = 0.05$ and $P_{\Delta \approx \nu_{\text{clock}},+} = 1/13 \cdot \bar{P}_{4,0} + 12/13 \cdot \bar{P}_{4,2} = 0.26$, where \bar{P}_{F, m_F} is the probability to decay from $|4, -1\rangle$ into $|F, m_F\rangle$.

While the ratio $P_{\text{hp},+}/P_{\Delta\approx 0,+}$ is a fixed⁶ quantity, we can adjust

$$\frac{P_{\text{hp},+}}{P_{\Delta\approx\nu_{\text{clock}},+}} = 0.47 \quad (8.11)$$

by employing an optical bandpass filter – a cavity (or a chain thereof).

To include the excitation light – the light driving the $|4, 0\rangle \rightarrow |4', 1\rangle$ transition – we switch from probabilities to rates, where Γ_{F,m_F} is the decay rate from $|4', 1\rangle$ into $|F, m_F\rangle$ in the $+z$ direction and Γ_{exc} is the photon flux of the excitation pulse. The excitation pulse duration T_{exc} is on the order of $1/\Gamma_{\text{hp}}$, where Γ_{hp} is the rate at which heralding photons are generated and emitted in the forward direction, thereby ensuring that only a single excitation is created (we will be more precise in our analysis in section 10.4.1).

We observe that Γ_{hp} is itself a function of Γ_{exc} and the coupling strength of the excitation light to the $|\downarrow\rangle \rightarrow |e\rangle$ transition (which in turn of course is a function of the detuning Δ as introduced in figure 8.1). To maintain the atoms' indistinguishability and thus obtain the desired SES instead of a mixed state (where one specific atom is in $|\uparrow\rangle$ and all the others are in $|\downarrow\rangle$, cf. sec. 2.3.2), this coupling needs to be identical for all N_a atoms. To see this, we consider the case where the excitation light is on resonance: Clearly the atom closest to the input port has a higher chance of absorbing a photon than one further along the fiber, simply because less photons will make their way through (this is similar to the argument we encountered when discussing the reflection properties of the atomic mirror in section 7.1.2). We therefore need to choose Δ such that the ensemble is sufficiently transparent ($\text{OD} < 1$) while at the same time ensuring a reasonable

$$\Gamma_{\text{hp}} = m \cdot \Gamma_{\text{exc}} \eta_{\text{gen}} P_{\text{hp},+} \quad (8.12)$$

where we have introduced the directionality coefficient $m = 0.9227$ (cf. eq. 4.31) and the generation efficiency η_{gen} which depends on the atom's coupling strength to the guided mode α and the detuning Δ . We note that $g \equiv \Gamma_{\text{exc}} \eta_{\text{gen}}$ is a common factor to all Γ .

With this in mind, our goal then is to make

$$\frac{\Gamma_{\text{hp}}}{\eta_{\text{BP}}(\Gamma_{\text{exc}} + \Gamma_{\Delta\approx\nu_{\text{clock}}} + \tilde{\Gamma}_{\Delta\approx\nu_{\text{clock}}}) + \Gamma_{\Delta\approx 0} + \tilde{\Gamma}_{\Delta\approx 0}}, \quad (8.13)$$

where $\tilde{\Gamma}$ are the rates from decays out of $|4, -1\rangle$, as large as possible by filtering the unwanted contributions with efficiency η_{BP} .

The bandpass filter also serves a second purposes, which we see when taking into account our discussion regarding the indistinguishability of atoms in the SES in section 2.3.2. There we noted that one has to be careful not to render the atoms distinguishable by their spatial position. Obviously, by placing the detector at one output port of the fiber, there is no possibility to

⁶ The filter cavity employed to filter the far-detuned contributions has a linewidth of about 25 MHz and therefore little effect near the heralding photon frequency. Also see the discussion regarding filtering bandwidth below.

detect which atom sent the photon along the guided mode – but only as long as we do not gain information from the point in time we detect a photon.

Since we use a short excitation *pulse* (cf. sec. 8.1) of length T_{exc} on the order of microseconds, each atom will be illuminated precisely this time T_{exc} , but if the light reaches the atom closest to the input port (say, $k = 1$) at time t_1 , it will reach the last atom $k = N_a$ only at $t_1 + \Delta t$ where $\Delta t = l/c$ with $l \approx 1$ mm the length of the lattice trap and c the speed of light.⁷

If we find that the heralding photon impinges on the detector in the time interval

$$\Delta T = [T_{\text{path}} + t_1 + T_{\text{exc}}, T_{\text{path}} + t_1 + T_{\text{exc}} + \Delta t], \quad (8.14)$$

where T_{path} is the time it takes the photon to travel from the end of the lattice trap to the detector, it is more likely that it was emitted by atom $k = N_a$ than by the atom $k = 1$, simply because the interaction time of the excitation pulse with the former was Δt longer than with the latter one. The same is true if one considers the first and the second half of the atomic ensemble as separate entities.

The cavity serving as the optical bandpass now makes T_{path} a variable quantity by adding a statistical delay T_{delay} . For a cavity with finesse \mathcal{F} and lengths L , the average time a photon spends inside it is

$$\bar{T}_{\text{delay}} = \frac{\mathcal{F} \cdot 2L}{c}, \quad (8.15)$$

and since the cavities decay can be modeled as an exponential decay, $\Delta T_{\text{delay}} = \bar{T}_{\text{delay}}$. To keep all atoms in the ensemble indistinguishable, it is now important that the bandpass filter washes out the time information, i. e. the $\Delta T_{\text{delay}} \gg \Delta t$. This is e. g. the case for a cavity with $\mathcal{F} = 300$ and $L = 20$ mm like we will employ in our setup (sec. 10.1), where $\bar{T}_{\text{delay}} = 40$ ns. In addition, the time resolution of the detector used in our experiment is specified as 1000 ps by the manufacturer. We are therefore not able to resolve the spatial position of atoms along the fiber.

Additionally to what we covered so far, in the case of a nanofiber trapped ensemble one has to consider the trap light, where at least one arm of the red-detuned dipole trap is co-propagating with the excitation light and the heralding photon. Furthermore, there can be broadband contributions from scattering off color centers and similar defects inside the fiber material. Here, additional measures have to be taken, which we will discuss in chapter 10, especially in sections 10.2 and 10.4.1. We stress that the fact that these contributions are relevant here is a direct consequence of the discrete detection of light by photon counting – with heterodyne detection we were in chapter 7 able to find a handful of photons amidst residual trap light without any issue, but lacked the strong projective nature of the measurement (cf. sec. 3.4).

With this last remark we have completed our sketch of the requirements for the excitation pulse and detection setup. The latter's experimental realization will be the topic of chapter 10, where in section 10.4 we will give an

⁷ Of course, this is a very idealized and qualitative discussion, but – as we shall see – sufficient.

estimate of the attainable state purity taking into account experimental constraints such as detector dark counts, finite quantum efficiency, and finite transmission of the optical filters.

Here, we now turn to a brief description of the second part of the experiment.

8.3.1 State Tomography

To verify that a SES (and not e. g. a mixed state $|\Psi_{\text{mix}}\rangle = \otimes_{k=1}^{N_a-1} |\downarrow\rangle_k \otimes |\uparrow\rangle_{k=N_a}$) has been created and to demonstrate its non-Gaussianity (cf. sec. 1.5), we need to perform a tomography.

The term tomography describes a process in which one reconstructs the quantum state of a system through a measurement (Leonhardt, 1997, D’Ariano et al., 2003, Lvovsky and Raymer, 2009) As we have seen in section 3.1, this is not possible with just a single measurement, unless we have a priori information such as the knowledge that a system is in one of its eigenstates (cf. Braginsky and Khalili, 1992). Since copying of quantum systems is in general not possible (“no cloning theorem”, Nielsen and Chuang, 2000), this means that we have to repeatedly prepare the very same system in the very same state we want to do a tomography of. Therefore it is crucial that we can reliably create the SES, i. e. with a high purity, a quantity we will estimate for our setup in section 10.4.

In this section we will show how the ability to perform a population measurement on the $|\downarrow\rangle \equiv |F=4, m_F=0\rangle$ state is sufficient to unambiguously uncover the non-Gaussianity of the SES. As introduced in section 3.4.1, the two-color heterodyne method can be used to measure the population in the $|\downarrow\rangle = |F=4, m_F=0\rangle$ state. To this end, we first show that a measurement of the difference in population ΔN between $|\downarrow\rangle$ and $|\uparrow\rangle$ suffices as a state tomography following the proposal by Christensen et al. (2013). Then, we discuss how access to only one ground state’s population is sufficient.

To convert the CSS created in the atomic ensemble into a signature population, we apply a microwave $\pi/2$ pulse (sec. 2.2.3)

$$\hat{R}_{\pi/2} = \sum_{k=1}^{N_a} (|+\rangle_k \langle\downarrow|_k + |-\rangle_k \langle\uparrow|_k) \quad (8.16)$$

where

$$|\pm\rangle = \frac{|\downarrow\rangle \pm |\uparrow\rangle}{\sqrt{2}}. \quad (8.17)$$

At this point we already note that this is formally identical to two modes \downarrow and \uparrow interfering at a beamsplitter, where $+$ and $-$ are the output ports. We see that

$$|\Phi_{\text{SES}}\rangle = \hat{R}_{\pi/2} |\Psi_{\text{SES}}\rangle = \frac{1}{N_a} \sum_{k=1}^{N_a} |++\cdots + \underbrace{-}_{k^{\text{th}} \text{ atom}} + \cdots ++\rangle, \quad (8.18)$$

while the atomic vacuum yields

$$|\Phi_0\rangle = \hat{R}_{\pi/2} \bigotimes_{k=1}^{N_a} |\downarrow\rangle_k = \bigotimes_{k=1}^{N_a} |+\rangle_k. \quad (8.19)$$

By projecting onto a general CSS of N_a atoms with a population difference $\Delta N = N(\downarrow) - N(\uparrow)$ given by

$$|\Psi_{\Delta N}\rangle = \left(\binom{N_a}{\frac{1}{2}(N_a - \Delta N)} \right)^{-\frac{1}{2}} \sum_{\pi} | \underbrace{\downarrow\downarrow\downarrow\cdots}_{\frac{1}{2}(N_a + \Delta N)} \underbrace{\uparrow\uparrow\uparrow\cdots}_{\frac{1}{2}(N_a - \Delta N)} \rangle, \quad (8.20)$$

where π denotes all possible permutations, we find the probability distribution for our measured quantity ΔN :

$$\begin{aligned} p_{\text{vac}}(\Delta N) &= |\langle \Psi_{\Delta N} | \Phi_0 \rangle|^2 \\ &= \left(\binom{N_a}{\frac{1}{2}(N_a - \Delta N)} \right) \frac{1}{2^{N_a}} \\ &= \left(\binom{N_a}{\frac{1}{2}(N_a - \Delta N)} \right) \left(\frac{1}{2} \right)^{\frac{1}{2}(N_a - \Delta N)} \left(1 - \frac{1}{2} \right)^{\frac{1}{2}(N_a + \Delta N)} \\ &\stackrel{N_a \gg 1}{\approx} \frac{1}{\sqrt{2\pi N_a}} e^{-\frac{\Delta N^2}{2N_a}} \end{aligned} \quad (8.21)$$

where in the last line we approximated the binomial distribution with a normal distribution (cf. [Christensen, 2014](#), p. 32). Not surprisingly this is normally distributed (Gaussian) in ΔN around 0 with variance N_a . This can be understood as each atom projecting independently (cf. sec. 3.3.1).

However, for the SES

$$\begin{aligned} p_{\text{SES}}(\Delta N) &= |\langle \Psi_{\Delta N} | \Phi_{\text{SES}} \rangle|^2 = \\ &= \left| \langle \Psi_{\Delta N} | \frac{1}{N_a} \sum_{k=1}^{N_a} \sqrt{2}^{-1} (|\cdots + \underbrace{\downarrow}_{k^{\text{th}} \text{ atom}} + \cdots\rangle - |\cdots + \underbrace{\uparrow}_{k^{\text{th}} \text{ atom}} + \cdots\rangle) \right|^2 \\ &\stackrel{N_a \gg 1}{\approx} \frac{1}{\sqrt{2\pi N_a}} e^{-\frac{\Delta N^2}{2N_a}} \frac{\Delta N^2}{N_a} \\ &= p_{\text{vac}} \cdot \frac{\Delta N^2}{N_a} \end{aligned} \quad (8.22)$$

This is clearly a drastically different distribution, see figure 8.3. Thus, by measuring $p(\Delta N)$ we can distinguish a SES from a standard CSS.

With the two-color heterodyne method as we introduced it in section 3.4.1, we cannot measure ΔN directly, but only acquire knowledge about $N_{|F=4, m_F=0\rangle} = N_{|\downarrow\rangle}$. In footnote 8 we already mentioned briefly that in the experimental setup used for [Christensen et al. \(2013, 2014\)](#), both ground state populations were measured simultaneously and from the difference in the phaseshift of the two sidebands one could directly infer ΔN . While it is possible to implement this scheme in the nanofiber setup as well (in fact, the sidebands were generated with the very same setup described in appendix D.3

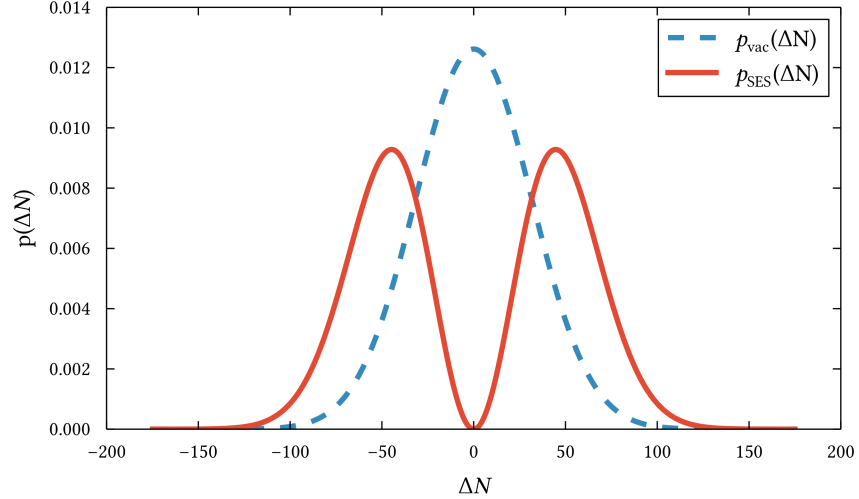


Figure 8.3: Probability distributions $p_{\text{vac}}(\Delta N)$ (eq. 8.21) and $p_{\text{SES}}(\Delta N)$ (eq. 8.22) for an ensemble of $N_a = 1000$ atoms. We note that the shapes resemble those of the corresponding Wigner functions (cf. fig. 1.3 and 1.4).

we will use for testing in chapter 10), its immunity to classical phase noise favors the two-color measurement of just a single sideband. We will now discuss how we are able to determine ΔN with access to only one groundstate's population.

There are two different methods which come to mind given the experimental methods discussed so far: Either, one measures $N_{|\downarrow\rangle}$ and, employing the method introduced in section 5.7, the total number of atoms N_a . Or one first determines $N_{|\downarrow\rangle}$, then applies a π -pulse

$$\hat{R}_\pi = \sum_{k=1}^{N_a} (|\downarrow\rangle_k \langle\uparrow|_k + |\uparrow\rangle_k \langle\downarrow|_k), \quad (8.23)$$

and finally measures the population of $|\downarrow\rangle$ a second time, which now corresponds to what was $N_{|\uparrow\rangle}$ at the time when $N_{|\downarrow\rangle}$ was determined. Correcting for atom loss from the trap in the time between the two measurements, we can determine ΔN . We point out that through the probe pulse which yields $N_{|\downarrow\rangle}$, atoms are pumped into extreme m_F states, thereby depleting $|\downarrow\rangle$.

Returning to our remark above, we see that the process we just described is similar to a balanced homodyne measurement (Béguin, 2015, ch. 4): The single excitation in $|\uparrow\rangle$ is interfered with the CSS in $|\downarrow\rangle$, and the difference signal is read out through population measurements (cf. sec. 3.2).

The reconstruction of the SES's Wigner function is an intricate process in its own right, and we will not cover it here in any detail. However, pointing to the pioneering work by McConnell et al. (2015), we summarize that one can e. g. obtain the Wigner function through the state's density matrix ρ (cf. sec. 1.4), which in turn can be reconstructed by repeating the tomogra-

phy for different angles of rotation, i. e. replacing the β 2-pulse. The Wigner function's value at our origin of quantum phase space is then given by

$$W(0,0) = \sum_n (-1)^n \rho_n n, \quad (8.24)$$

i. e. the population of all n AFSs. If only $|0\rangle$ and $|1\rangle$ have significant population, this corresponds to the difference.

8.4 SETUP REQUIREMENTS AND OVERVIEW

In this chapter we have presented the experimental protocol and now turn to its practical implementation in the laboratory. While the dual-color dipole trap for the atomic ensemble was already described in chapter 5, so far only basic optical pumping has been discussed (cf. ch. 6). Thus, we need to implement methods for more sophisticated control of the atomic ensemble's state, implement the scheme to create the SES, find a way to detect the heralding photon amidst all the light guided through the nanofiber, and eventually implement a method of state tomography to recover the Wigner function.

As was outlined in the [preface](#) this thesis covers mainly the detection of the heralding photon and the preparation of the initial state. The other tasks will be discussed only briefly in section 11.1.

Thus, chapter 9 covers state preparation. To this end, we discuss the manipulation of the atomic ensemble with light and microwaves. In doing so, we measure coherence and interaction times, which are benchmark values for the feasibility of our approach. Subsequently, in chapter 10 we will plan, model, build, and characterize the setup for the detection of the photon heralding the creation of the SES. In the final section 10.4 we show that the detection setup's performance is sufficient for its intended task.

PREPARATION

The first step in the creation of a single excitation state (SES) after loading atoms into the nanofiber trap is the preparation of the initial state. The goal is to gather as many atoms as possible in a single Zeeman sublevel of one of the hyperfine levels, i. e. in a single, well-defined state, while at the same time the population in any other state is minimal. In our case, this state is $|F = 4, m_F = 0\rangle$ (sec. 8.2).

We explore three different methods to manipulate states in our atomic ensemble: microwave interactions, optical pumping, and Raman scattering. In this chapter, we will investigate their suitability for our experiment. In doing so, we cover their basic principles of operation and develop a feasible preparation sequence for the SES. Along the way we learn about the coherence times of the spin states in the nanofiber trap and optimize the QND probe.

While atomic state manipulation is a well-studied topic, in nanofiber trapped ensembles only microwave interactions and optical pumping have been applied previously. Reitz et al. (2013) demonstrated Rabi oscillations and Ramsey interferometry; in a later work the same group used microwave interactions and optical pumping to optically separate the two linear atomic chains (Mitsch et al., 2014a).

9.1 OPTICAL PUMPING

In the context of this thesis, we use the term “optical pumping” for interactions of near-resonant single light fields in the infrared with atoms. Thus, there is no significant difference to what we described in chapter 6, other than that we from here on will no longer neglect Zeeman sublevels.¹ For the optical pumping processes, we use two lasers, which we will refer to as the *repumper* and the *depumper*.

The source for repumper light is the MOT repumper (cf. sec. 2.4.2), which can be applied externally through the six MOT beams and therefore has no well-defined polarization at the position of the atoms. Additionally, it can also be sent into the fiber, where it is *V* polarized. As shown in figure 9.1, the external repumper path can be blocked by a shutter, whereas the internal path is always open. This does not influence the cooling of the atoms as described in section 2.4.1. During the optical pumping sequences, it is tuned on resonance with the $|F = 3\rangle \rightarrow |F' = 4\rangle$ transition unless stated otherwise.

The depumper light is derived from the MOT cooler. Split off before the AOM which controls the MOT beams, it passes through an AOM in dou-

¹ As introduced in section 4.3.1, we use the coordinate system given in figure 4.5 and quantize the atom along the *y*-axis.

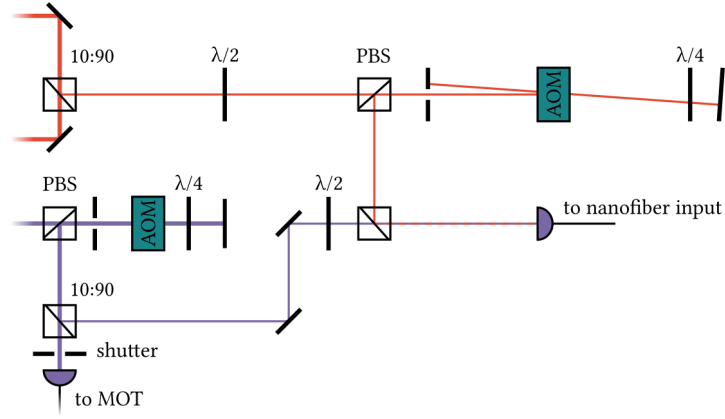


Figure 9.1: Relevant parts of the setup for optical pumping. As indicated in figure 2.7, the MOT cooler (orange) and repumper (purple) serve as the light sources for optical pumping.

While the depumper can only be applied through the nanofiber, the repumper can also be sent through the MOT beams by opening the shutter (cf. fig. 2.7 and fig. 6.8).

ble pass configuration before it enters the same fiber as the aforementioned repumper. Therefore, it is also V polarized at the atoms. To eliminate dark states and enhance the pumping efficiency in presence of a magnetic bias field, a 10 MHz signal is mixed onto the RF-signal, thus creating two sidebands.

9.1.1 Hyperfine Cleaning

Although after loading into the nanofiber trap a majority of the atoms is prepared in a Zeeman sublevel of the $|F = 3\rangle$ manifold, a fraction is found to be in $|F = 4\rangle$. By applying a pulse of the depumper, all atoms in $|F = 4, m_F \neq 0\rangle$ ($|F = 4, m_F = 0\rangle$ is a dark state) can be transferred to $|F = 3\rangle$ (fig. 9.3). Length and power are adjusted to ensure maximum depletion of $|F = 4\rangle$.

9.1.2 Pumping into $m_F = 0$

As the SES preparation starts from $|F = 4, m_F = 0\rangle$ ($|4, 0\rangle$), it is as a first step necessary to bring as many atoms as possible into a state where $m_F = 0$. This also proved necessary to observe microwave Rabi oscillations on the clock transition (cf. sec. 9.2.4).

A transfer of atoms into this central state can be achieved optically by applying the repumper and depumper simultaneously. The repumper constantly brings all atoms into $|F = 4\rangle$, while the depumper sends all atoms not in its dark state $|4, 0\rangle$ (we remind the reader that V -polarized light drives π -transitions) back into $|F = 3\rangle$. Over time, a significant fraction of atoms accumulates in the dark state.

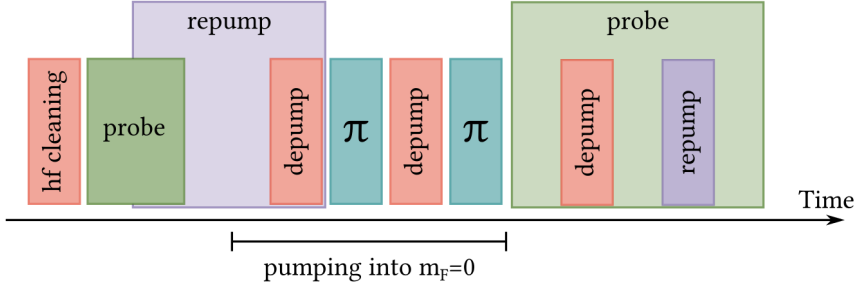


Figure 9.2: Experimental sequence to accumulate atoms in $|4, 0\rangle$ as described in the main text.

The hyperfine cleaning (sec. 9.1.1) and the sequence used to verify the process (cf. fig. 9.3) are shown as well.

To achieve and verify this experimentally, we need to jump ahead to the next section and use a microwave π -pulse. For now, we will state that such a microwave pulse swaps the population of the $|4, 0\rangle$ and $|3, 0\rangle$ state without affecting any other Zeeman sublevel (cf. sec. 2.2.3). We will describe in 9.2.4 how this is realized.

The sequence is similar to the one described in Christensen (2014, p. 63) and visualized in figure 9.2: With a cleaning pulse, we prepare all our atoms in $|3\rangle$ and turn on the probe laser, which is resonant to $|F = 4\rangle \rightarrow |F' = 5\rangle$, to obtain a reference level. Next, we repump all atoms into $|4\rangle$ and shut off the probe laser, as it is σ_{\pm} -polarized and thus pumps atoms out of $|4, 0\rangle$ into the outer m_F -levels.

Now, the depumper is switched on, and the optical pumping as described above takes place. Then, we turn off both repumper and depumper and apply a π -pulse, which transfers all atoms in $|4, 0\rangle$ into $|3, 0\rangle$. Another pulse of the depumper transfers all other atoms into $|3\rangle$, with $|4\rangle$ left empty. Finally, a second π -pulse brings the atoms in $|3, 0\rangle$ back to $|4, 0\rangle$, where they can be detected by the probe laser, which in the process transfers them out of the $m_F = 0$ state.

To verify that we did not lose or heat any atoms in the process, we first depump all atoms into $|3\rangle$ one last time, and then repump everything back into $|4\rangle$. The resulting transmission signal is presented in figure 9.3.

We estimate that we can bring about 40% of all atoms into $m_F = 0$. Since there is no value reported in the literature to compare to as a benchmark, at the time of writing it remains an open question if and by how much this fraction can be improved.

9.1.3 Blow-Away

As in Christensen (2014, p. 63), in our final preparation sequence we replace the second depumper pulse within the accumulation sequences (fig. 9.2) with a strong “blow-away” pulse, which instead of transferring atoms

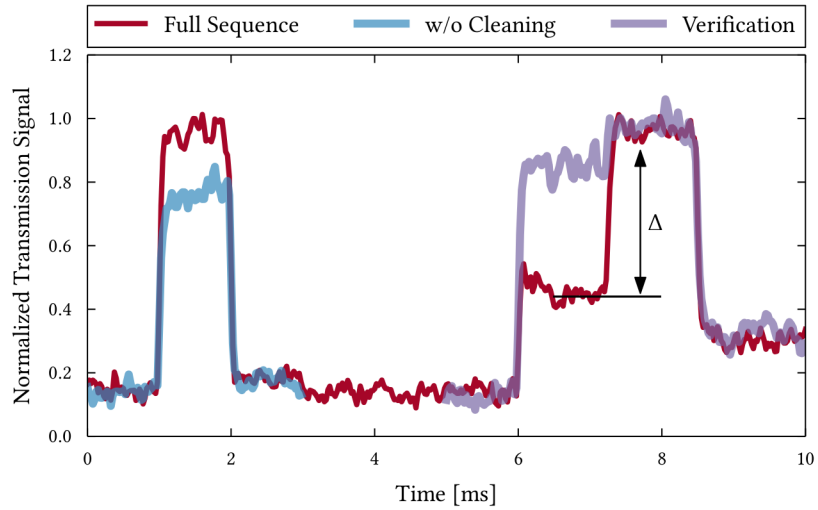


Figure 9.3: Example result for the optical pumping sequence described in figure 9.2. From the difference in transmission Δ we can estimate the fraction of atoms brought into $|4, 0\rangle$.

To verify that the sequence works as expected, we present data where only the first π -pulse was applied. We see that very few atoms remain, reflecting the fact that at the time the data presented here was taken, T_π and Ω had not yet been finetuned. The absorption signal after the last repumper pulse is identical for the full and the verification sequence, demonstrating that no atoms are lost from the trap in the process.

We further show that without applying a hyperfine cleaning pulse (sec. 9.1.1), there is a residual population in $|3\rangle$.

into $|F = 3\rangle$ removes them out of the nanofiber trap by heating (Mitsch et al., 2014a,b).

9.2 MICROWAVE

To realize a strong coherent drive for the clock levels, we have to resort to magnetic interactions since no electrical π -transitions are allowed ($|3, m_F = 0\rangle \rightarrow |4, m_F = 0\rangle$ is a dipole forbidden transition, cf. sec. 2.1.2).

Their treatment is no different than what we introduced for in section 2.2.2, just that instead of the electric dipole $\hat{\mathbf{d}}$ we have a magnetic dipole $\hat{\boldsymbol{\mu}}$ and instead of the electric component \mathbf{E} we use the magnetic part \mathbf{B} of the electromagnetic field:

$$\hat{H}_{\text{int}} = -\hat{\boldsymbol{\mu}} \cdot \mathbf{B}. \quad (9.1)$$

Since the matrix elements of $\hat{\boldsymbol{\mu}}$ are much smaller, we need to use up to 10 W of microwave power to reach appreciable Rabi frequencies.

9.2.1 Coherence Times

In principle, an SES can be prepared using microwave and optical pumping alone, as is detailed in Christensen (2014, p. 61). However, the required pulse lengths might be too long compared to the coherence times of our ensemble. We distinguish two different times:

The so-called spin-lattice relaxation time τ_1 describes the coherence of our CSS, i. e. how long it takes until the atoms comprising the state

$$|\Psi\rangle = \bigotimes_{k=1}^{N_a} |\uparrow\rangle \quad (9.2)$$

have relative to each other dephased so much – e. g. due to a spatially inhomogeneous background or drive field – that $|\Psi\rangle$ can no longer be described as a single spin vector on the Bloch sphere (cf. sec. 2.3.1). We can determine τ_1 by observing the amplitude decay of Rabi oscillations in the system (sec. 9.2.4).

The spin-spin relaxation time describes the coherence between the two levels of our system, i. e. between $|\uparrow\rangle$ and $|\downarrow\rangle$. This time is measured by applying a $\pi/2$ -pulse to $|\Psi\rangle$, thereby creating the superposition state

$$|\Psi_{\text{sup}}\rangle = \frac{|\uparrow\rangle - |\downarrow\rangle}{\sqrt{2}} \quad (9.3)$$

and observing for how long afterwards one can return back to the initial state $|\Psi\rangle$ by applying a second $\pi/2$ -pulse (sec. 9.2.5). In general, τ_2 is expected to be significantly shorter than τ_1 .

We see that in order to prepare the SES and perform a tomography, the pulse duration T_π (which is fixed by the attainable interaction strength given our microwave source) has to be well below τ_2 , i. e. the whole experiment

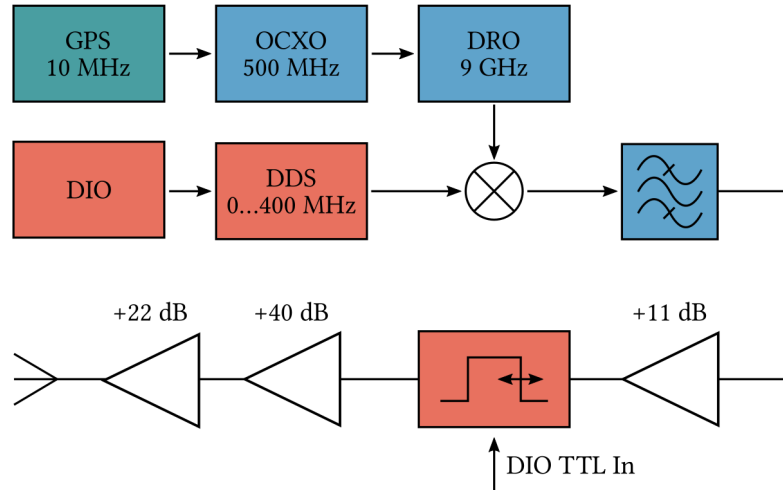


Figure 9.4: Schematic overview of the microwave setup as described in the main text.

has to be carried out within this timespan. In the following, we will therefore determine these two coherence times. In section 9.3 we will afterwards describe the first steps towards a faster method for state control.

9.2.2 Setup and Control

An introduction to our microwave setup sketched in figure 9.4 can be found in Oblak (2010, pp. 172), who also discusses in detail stability and noise considerations. In short, our setup consists of a frequency source, a switch, several amplifiers, and an antenna.

Our frequency reference is a 10 MHz signal from a GPS receiver, which as an atomic frequency standard is very stable. This signal is used to stabilize an oven controlled crystal oscillator (OCXO, Morion MV78-A50I-500MHz-G), to whose 500 MHz output signal we lock a dielectric resonance oscillator (DRO, Poseidon Scientific Instruments DROO-9.000-FR) generating a 9 GHz signal. On top of this signal, we mix the output of a direct digital synthesizer (DDS, Analog Devices) which can generate signals with frequencies ν up to 400 MHz. We use the upper sideband $9 \text{ GHz} + \nu$. Both carrier and the lower sidebands are far detuned from any atomic resonance, but would nevertheless contribute to amplifier saturation and are therefore filtered away with a cavity filter (Lorch Microwave 5CF7-9200/50-S).

The signal is pre-amplified (+11 dB) and sent through a pulse modulator (Hewlett-Packard 11720A) for switching. Afterwards, the signal is pre-amplified again (Microwave Amps AL 22-9.25-40-25) before reaching the power amplifier (Kuhne KU PA 922 XL-226), which has a maximum output of 41 dBm. By inserting a suitable attenuator in front of the second pre-amplifier, we ensure that we can drive the power amplifier well into satura-

tion when setting the DDS output to its highest value, but at the same time retain the full dynamic range.

As the antenna we use a wave-guide coupler with an open end-face, whose length was optimized for maximum free-space coupling. The small device can be placed conveniently close to the vacuum cell inside the compensation coils. With the described setup, we can reach up to 10 W of microwave power.

The integration of a microwave source into our setup made it necessary to shield parts of the photodetectors and amplifier chains used for the PLLs of the lasers, as they are highly sensitive to signals around 9 GHz (cf. app. D.2). We used aluminum and copper foil to shield the detectors and replaced the few remaining open PLL amplifiers by fully packaged variants (MiniCircuits ZX60-14012L+). In addition, we integrated notch filters into the amplifier chains.

9.2.3 Landau-Zener Sweeps

A natural choice for a first experiment with the newly integrated microwave source were Landau-Zener sweeps. Here, all atoms were prepared in $|F = 3\rangle$ and in a few milliseconds the microwave frequency was swept over several megahertz around the clock frequency $\nu_{\text{clock}} = 9.192\,631\,770$ GHz. If one simultaneously probes the ensemble on the $|F = 4\rangle \rightarrow |F' = 5\rangle$ transition, one can monitor whether and when atoms are transferred into $|F = 4\rangle$.

In the absence of a magnetic bias field the microwave has an effect similar to optical pumping, bringing all atoms from $|F = 3\rangle$ to $|F = 4\rangle$.

If a bias field $\mathbf{B} = (0, B_y, 0)^T$ is applied along the quantization axis, the energy of a state $|F, m_F\rangle$ is shifted by (anomalous Zeeman effect, Steck, 2010)

$$\Delta E_{|F, m_F\rangle} = \mu_B g_F m_F B_y, \quad (9.4)$$

with μ_B Bohr's magneton and g_F the hyperfine Landé factor (given in Steck, 2010), the degeneracy of the magnetic sublevels is lifted. Since the microwave's linewidth is narrow enough, we can resolve this (fig. 9.5).

9.2.4 Rabi Oscillations

The observation of Rabi oscillations is a major milestone towards state preparation, as it is the first truly quantum effect (cf. sec. 2.2.2) and allows one to directly infer the coherence time τ_1 (sec. 9.2.1). With the knowledge of Ω , we also obtain the π -pulse length T_π , which is necessary to perform precise rotations on the Bloch sphere (cf. sec. 2.2.3).

9.2.4.1 Clock Frequency Estimation

As Rabi frequencies for microwave interactions with the clock levels in our experiment are on the order of a few 10 kHz (Christensen, 2014, Reitz et al.,

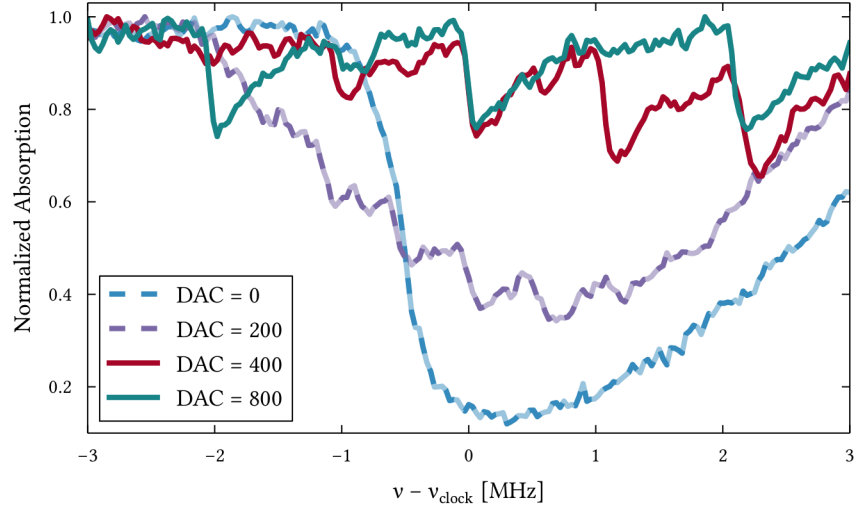


Figure 9.5: Absorption signal for 10 ms long microwave sweeps over 6 MHz centered around ν_{clock} for four different bias coil currents (given as input values for the DAC bias coil current controller, cf. sec. 2.4.2).

In absence of a bias field (DAC = 0, blue dashes), the effect of the microwave is similar to optical pumping. With increasing bias field, steps appear (DAC = 200, purple dashes) until the magnetic sublevels are clearly resolved. We see that the level splitting is linear in B . A more detailed analysis can be found in figure 9.6.

Using equation (9.4) and the well-known values for g_F (Steck, 2010), we employ this kind of measurement to calibrate our bias field (fig. 9.7).

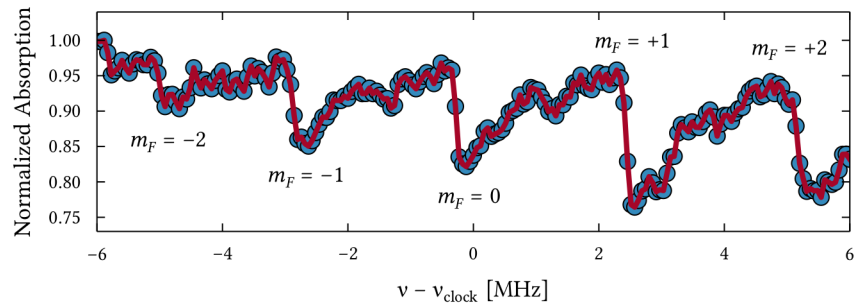
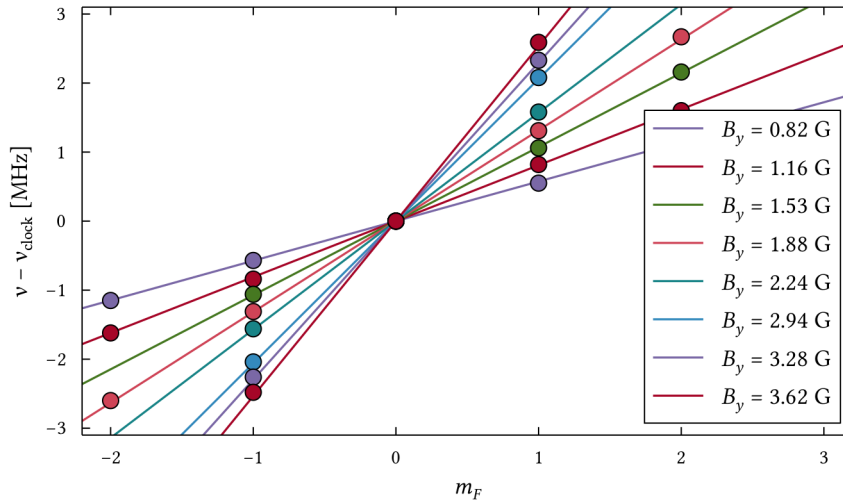
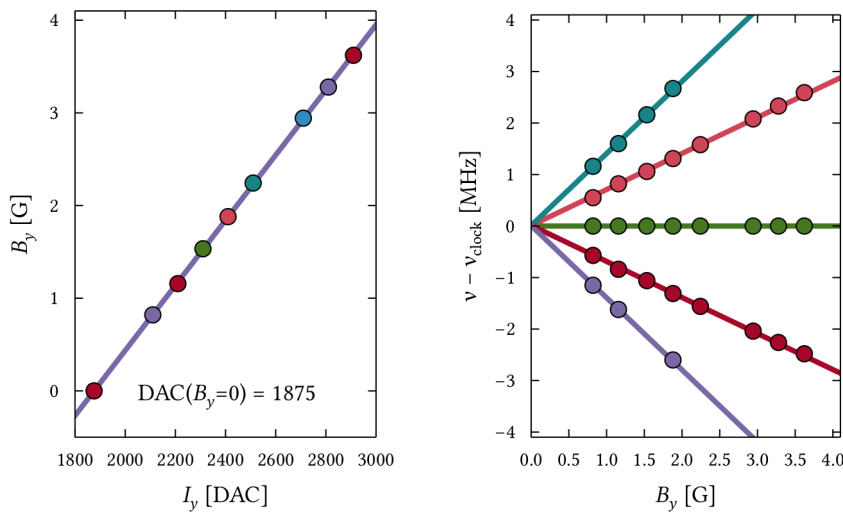


Figure 9.6: Absorption signal for a 10 ms long microwave sweep over 12 MHz centered around ν_{clock} with a bias field of 3.71 G. Data points (blue circles) are connected (red line) to guide the eye.

As indicated by the labels on the plot, each absorption line corresponds to a different $|F = 3, m_F\rangle \rightarrow |F = 4, m_F\rangle$ transition. We also see weak σ_{\pm} transitions $|F = 3, m_F\rangle \rightarrow |F = 4, \pm m_F\rangle$, indicating that the microwave's polarization at the atoms is not entirely π .



(a) Using the well known values for $\mu_B g_F$ (Steck, 2010), we can determine B_y for each Landau-Zener sweep.



(b) Using the values B_y obtained from (a), we (c) The hyperfine splitting grows linearly with can calibrate the DAC bias field controller. B_y (cf. eq. 9.4).

Figure 9.7: By analyzing Landau-Zener sweeps taken at different DAC values for the bias field current I_y , we can find $\text{DAC}(B_y)$. Common colors in (a) and (b) indicate identical data sets.

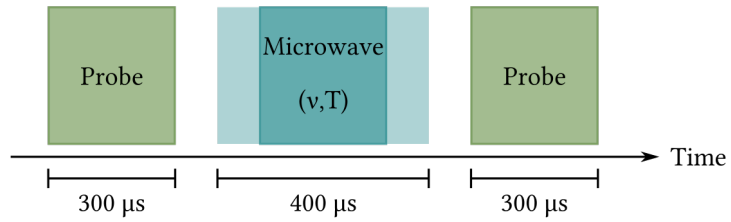


Figure 9.8: To find an estimate for the clock frequency $\tilde{\nu}_{\text{clock}}$, we prepare atoms in $|F = 3, m_F = 0\rangle$ (sec. 9.1.2) and use the shown sequence. By e. g. choosing a fixed T and varying the microwave frequency ν , the phase contrast is maximized, and ν_{max} is used as an estimate for $\tilde{\nu}_{\text{clock}}$.

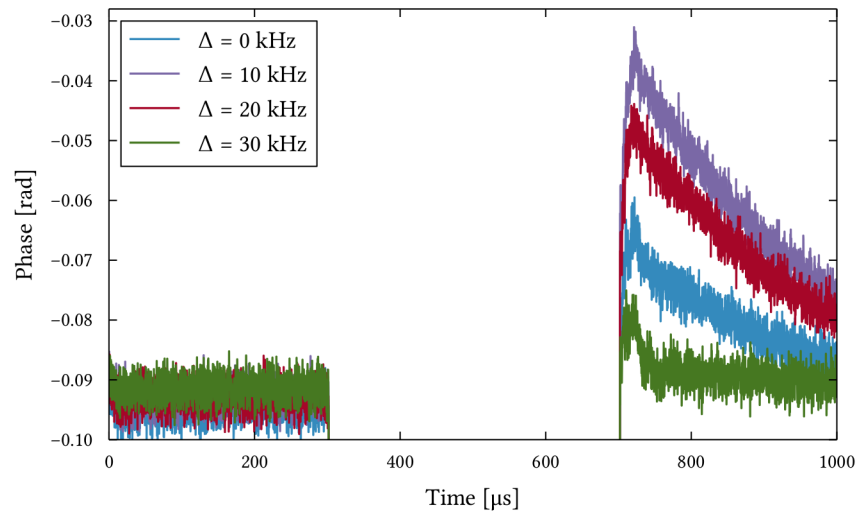


Figure 9.9: Results for clock frequency estimation using $T = 200 \mu\text{s}$ and varying as $\nu = \nu_{\text{clock}} + \Delta$. We find $\nu_{\text{max}} = +10 \text{ kHz}$.

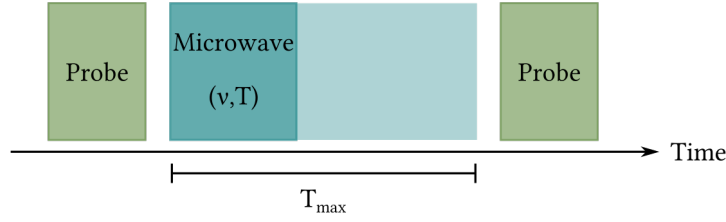


Figure 9.10: Rabi sequence: Initially, all atoms are prepared in $|F = 3, m_F = 0\rangle$ and an initial probe pulse (which as we remind ourselves measures the population in $|F = 4, m_F = 0\rangle$) is used to determine the reference phase. Then, a microwave pulse of variable frequency ν and variable duration T is applied. After a fixed time T_{\max} , we again probe the population in $|F = 4, m_F = 0\rangle$.

2013), Rabi oscillations with significant amplitude can only be observed in a narrow window around resonance (cf. eq. 2.16). Therefore, we first need to find a good estimate for the clock frequency $\tilde{\nu}_{\text{clock}}$ – i. e. the frequency we set the DDS output chain to, a value known to be drifting on a timescale of days from previous experiments – which is expected to deviate up to several kilohertz from the nominal $\nu_{\text{clock}} = 9.192\,631\,770$ GHz.

To this end, we use the sequence described in 9.8 to find a combination (T, ν) which yields a significant change in population, visible as a large phase contrast. Setting a fixed $T = 200\,\mu\text{s}$ and varying ν based on the knowledge we gained from the Landau-Zener sweeps in section 9.2.3, we find $\nu = \nu_{\text{clock}} + 10\,\text{kHz}$ to yield the highest phase shift (fig. 9.9).

9.2.4.2 Observation of Rabi Oscillations Using a Strong Projective Measurement

With a good estimate on the clock frequency, we employ the sequence shown in figure 9.10 to drive and observe Rabi oscillations. Over several hundred shots, where for each shot the pulse duration T is chosen randomly in multiples of $10\,\mu\text{s}$, we recover varying population in the upper level, clearly resembling Rabi oscillations (fig. 9.11).²

To these data points we fit the function

$$\Phi(t) = A \cdot \exp\left(-\frac{t}{\tau_1}\right) \cdot \cos(\tilde{\Omega}t) + C, \quad (9.5)$$

where τ_1 is the spin-lattice relaxation time (cf. sec. 9.2.1) and $\tilde{\Omega}$ the effective Rabi frequency. A , φ , and C are fit parameters without immediate physical significance. We remark that for τ_1 to be determined with reasonable precision, a long measurement is required, which is why we do not quote it when fitting to only a few oscillation cycles. In figure 9.12 we observe Rabi oscillations over $700\,\mu\text{s}$ and find $\tau_1 = 3 \pm 2\,\mu\text{s}$, which is in excellent agreement

² We note that $\tilde{\Omega}$ is much lower in the initial measurements than in the latest data we present in figure 9.13b. This is due to a broken stage in the old pre-amplifier, which was later replaced (cf. sec. 9.2.2).

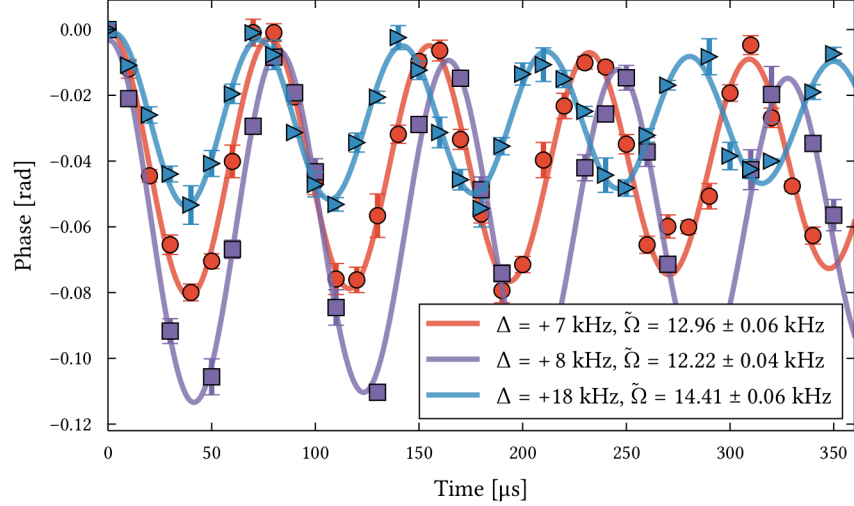


Figure 9.11: First observation of Rabi oscillations² in the nanofiber trapped ensemble of atoms ($B_y \approx 3$ G). The relationship between Rabi oscillation amplitude, effective Rabi frequency $\tilde{\Omega}$ and microwave detuning Δ clearly resembles figure 2.3. Each data point corresponds to 2 to 12 shots. Errorbars resemble the standard deviation of the mean.

with Reitz et al. (2013). We attribute the large uncertainty to an error in locking the oven controlled crystal oscillator to the GPS signal, which caused drifts of several kilohertz per half an hour and was only discovered and resolved once we began working towards the observation of Ramsey fringes (sec. 9.2.5). We also note that only a few data points were taken for each T , so we refrained from checking for interferometer lock failures and accordingly discarding data points.

Nevertheless, $\tau_1 = 3 \mu\text{s}$ is sufficient for SES preparation, since we find $\Omega = 41$ kHz and correspondingly we have $T_\pi = 24.4 \mu\text{s}$ and $T_{\pi/2} = 12.2 \mu\text{s}$. These values are more than a factor of two faster than Reitz et al. (2013) achieved in their nanofiber setup ($\Omega = 17$ kHz), which is mainly due to the stronger microwave source used here.

9.2.4.3 Observation of Rabi Oscillations in Real Time

Up to this point, we have observed Rabi oscillations by applying a pulse of certain duration and then measuring the upper state's population by probing as strong as possible to achieve a high phase contrast. In other words, we have performed a projective measurement (cf. sec. 3.1). Although to reach a negligible statistical error it was sufficient to only measure a few realizations per pulse length, the oscillations only. In this section we present the first step towards an observation in real time.

The non-destructive probing of Rabi oscillations close to the standard quantum limit was demonstrated by Windpassinger et al. (2008) in the free-space predecessor experiment which was later used for Christensen et al.

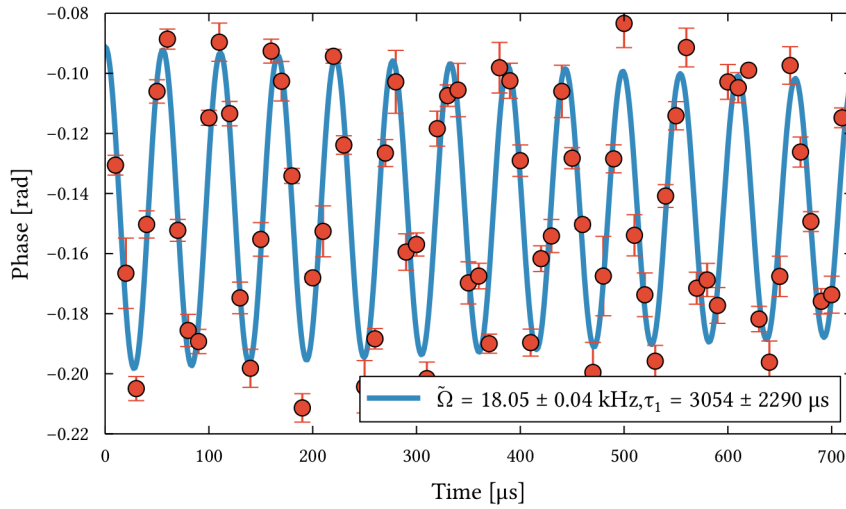
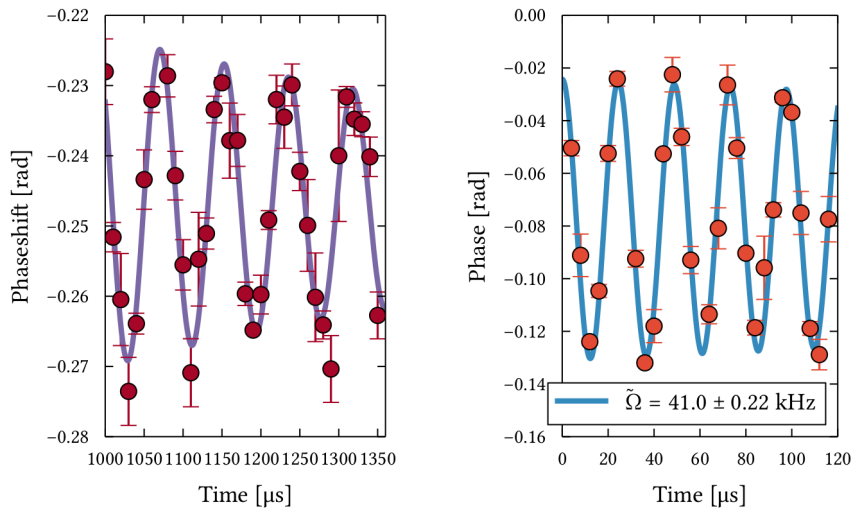


Figure 9.12: To find τ_1 , we observe Rabi oscillations² with $T_{\max} = 700 \mu\text{s}$ (cf. fig. 9.10). We find $\tau_1 = 3000 \pm 2000 \mu\text{s}$. 720 shots.



(a) Rabi oscillations after $1 \mu\text{s}$. We still observe a significant amplitude (this should be compared to fig. 9.11). 220 shots. (b) With the full microwave power, we find $\Omega = 41 \text{ kHz}$, which corresponds to $T_\pi = 24.4 \mu\text{s}$. 103 shots.

Figure 9.13

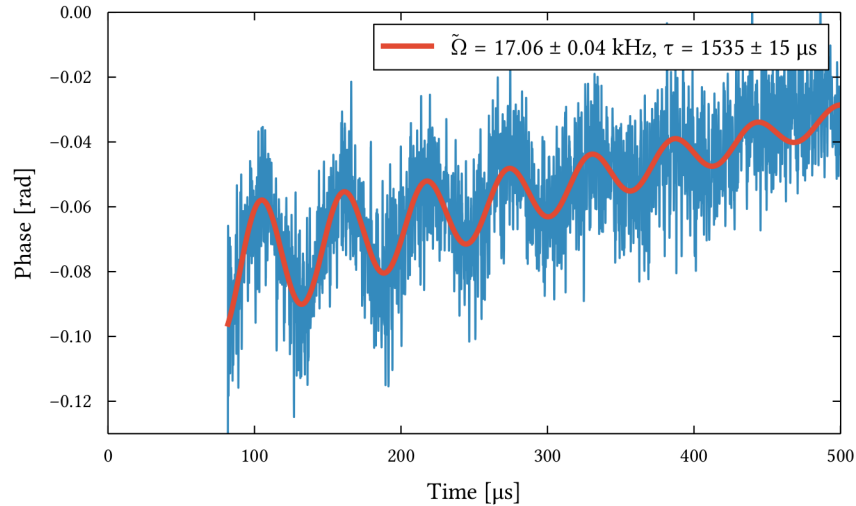


Figure 9.14: Continuous observation of Rabi oscillations² by dispersively probing the $|F = 4, m_F = 0\rangle$ population. To account for the slope, for fitting a linear term is added to (9.5). Average over 50 realizations.

(2014). This experiment is the main result of Windpassinger (2008). In short, they used a very weak laser blue-detuned from the $|F = 4\rangle \rightarrow |F'\rangle$ transition to probe the population of the $|F = 4, m_F = 0\rangle$ state in an ensemble of 10^5 cesium atoms while driving Rabi oscillations on the clock levels. By pulsing the probe as to simultaneously provide spin-echos they were able to continuously observe Rabi oscillations for up to 10 ms, reaching the projection noise limit.

Since the two-color heterodyne detection as set up in our experiment eliminates the ac-Stark shift on the atoms while preserving the dispersive signal, this major source of dephasing is absent. Indeed we are able to observe Rabi oscillations by simultaneously probing weakly (fig. 9.14); a reasonably clear signal can be obtained from as little as 10 realizations. This is an encouraging result, as at this point neither the precise clock frequency $\tilde{\nu}_{\text{clock}}$ has been found nor has the probe laser detuning been finetuned for the two-color sidebands to act as a truly QND probe. Therefore, we continue towards achieving the latter and leave this as a sidenote.

9.2.5 Ramsey Interferometry

To find a yet more precise value for the hyperfine ground state transition frequency ν_{clock} and to determine the spin-spin coherence time τ_2 (cf. sec. 9.2.1), we employ the well-known method of Ramsey interferometry. In this section we very briefly summarize the latest experimental results on this frontier.

The sequence is depicted in figure 9.15 and can be understood as the atomic analogue to a Mach-Zehnder interferometer (Haroche and Raimond, 2006, pp. 148). In figure 9.16 we show a typical result of a Ramsey measure-

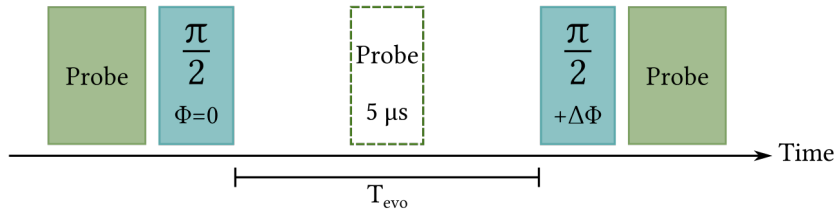


Figure 9.15: The Ramsey sequence consists of two $\pi/2$ -pulses separated by in our case $T_{\text{evo}} = 75 \mu\text{s}$. Before the start of the sequence, all atoms are prepared in $|F = 3, m_F = 0\rangle$ ($|3\rangle$) and from the first probe pulse we obtain our reference phase. The first $\pi/2$ -pulse brings the atoms into an equal superposition. If $\Delta\Phi = 0$, the second $\pi/2$ -pulse transfers the atoms into $|4\rangle$ and we expect to observe a phaseshift; if $\Delta\Phi = \pi$ they are returned to $|3\rangle$ and no phaseshift is observed. The phase contrast is a direct measure of the dephasing during T_{evo} .

To observe whether the probe sideband frequencies are chosen such that we have a QND measurement (cf. sec. 3.4.1), we add a short probe pulse during T_{evo} . If the probe does not dephase the system, we expect to see no change in fringe amplitude (fig. 9.18 and 9.19).

ment, exhibiting the expected relationship between phaseshift and phase of the second $\pi/2$ -pulse. The symmetric shape is confirmation that $\tilde{\nu}_{\text{clock}}$ was found correctly.

To estimate τ_2 , we observe the reduction of the fringe contrast with T_{evo} (cf. sec. 9.2.1). From figure 9.17 we estimate $\tau_2 \approx 500 \mu\text{s}$, which like the value obtained for τ_1 is in good agreement with Reitz et al. (2013) who state that from their measurements they estimate a τ_2 of “several 100 μs ”. In any case, $\tau_2 \gg T_\pi$, and a preparation of the SES

9.2.6 Finetuning of the Probe Sideband Frequencies

The Ramsey sequence also allows us to finetune the frequency of the probe’s sidebands, i. e. to shift the probe laser frequency such that the sideband’s ac Stark shifts on the $|F = 4, m_F = 0\rangle$ state exactly cancel, thereby realizing a true QND probe (cf. sec. 3.1 and 3.4.1).

In figures 9.18 we show Ramsey measurements where a short $5 \mu\text{s}$ probe pulse was integrated in between the two $\pi/2$ -pulses as shown in the sequence in figure 9.15. By carefully adjusting the probe laser’s frequency, we can eliminate the sidebands’ back-action on the atoms (fig. 9.19).

9.3 RAMAN

As observed in sections 9.2.4 and 9.2.5, the coherence times for CSSs prepared in the nanofiber trapped atoms are relatively short compared to the length of a microwave π -pulse. To achieve higher Rabi frequencies, the introduction of two-photon processes (commonly referred to as Raman scattering) as an additional tool for state manipulation was proposed.

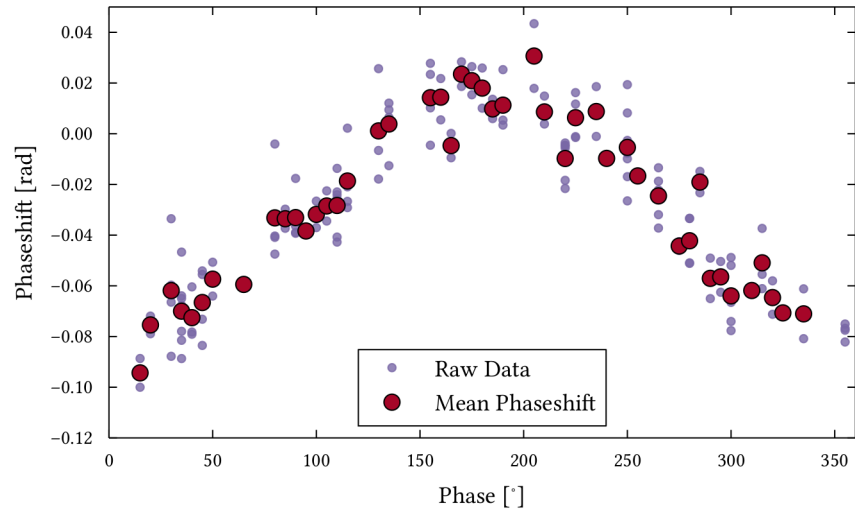


Figure 9.16: Ramsey fringes as a result of the sequence depicted in figure 9.15 for $\tilde{\nu}_{\text{clock}} = 9.192\,634\,170$ GHz. (158 shots).

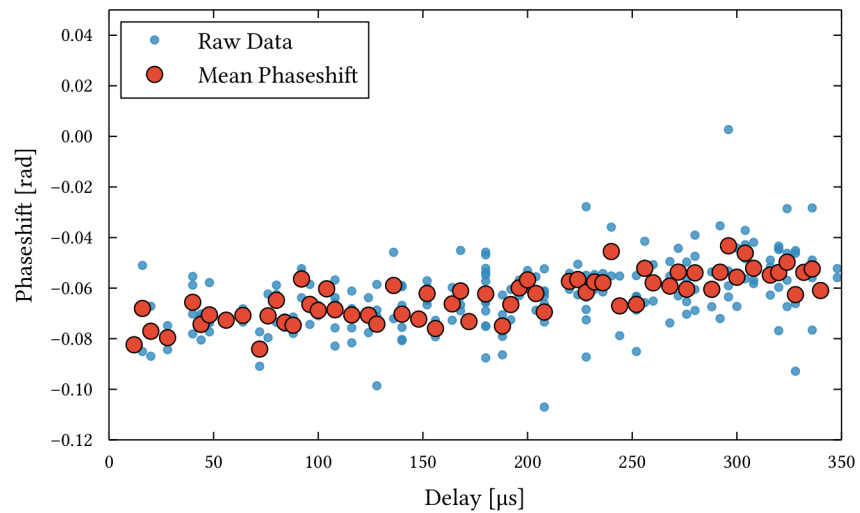


Figure 9.17: By repeating the Ramsey sequence (fig. 9.15) for different T_{evo} , we can observe how the fringe contrast (cf. fig. 9.16) varies. In $350\ \mu\text{s}$, it declines about 0.02 rad, which corresponds to a 25% decrease (cf. fig. 9.16, note that the vertical axes has the same scaling). From this we can estimate $\tau_2 \approx 500\ \mu\text{s}$ (221 shots).

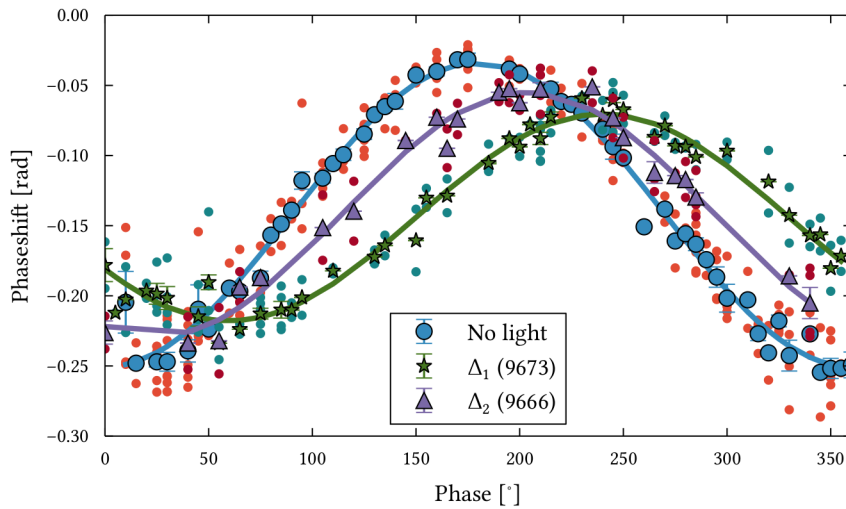


Figure 9.18: By finetuning the frequency of the probe laser, we attempt to shift the two-color sidebands symmetrically around the atomic resonance such that the ac Stark shifts cancel. To this end, we apply a short $5\ \mu\text{s}$ probe pulse during T_{evo} (fig. 9.15). In general, both the fringe amplitude and phase are affected by this probe pulse. By carefully detuning the probe laser, we attempt to minimize this disturbance (fig. 9.19). (Numbers in the legend are the four last digits of the PLL lock frequency and have no direct significance. 50 to 200 shots.)

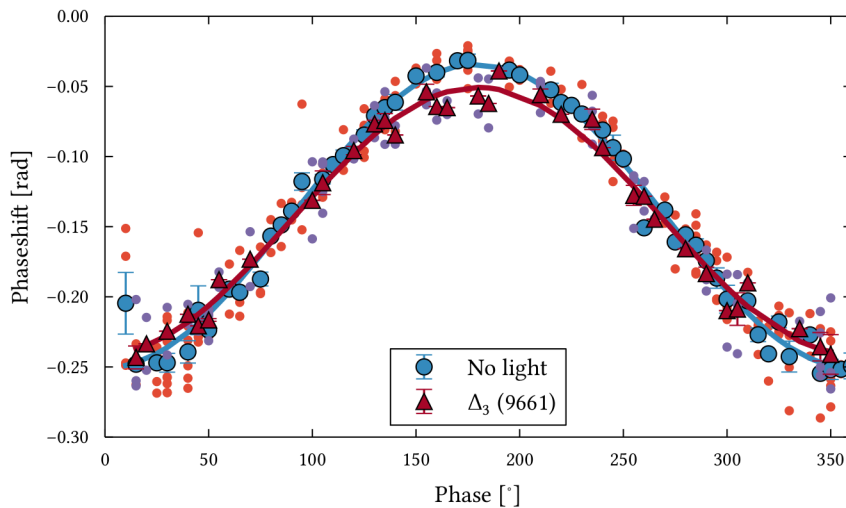


Figure 9.19: Result of the same experiment as in figure 9.18, but with optimally detuned two-color sidebands. We see that the phase is not affected anymore and only observe a slight reduction in fringe amplitude. (200 and 100 shots.)

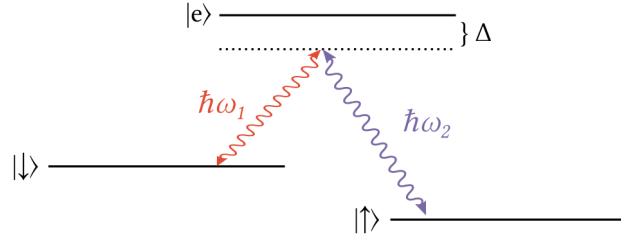


Figure 9.20: By driving the Λ -system simultaneously with light of frequency ω_1 and ω_2 , a two-photon Raman process couples $|\uparrow\rangle$ and $|\downarrow\rangle$.

In this section, we will give a brief introduction to Raman scattering and show how by simultaneously driving two optical transitions we can engineer what is effectively a coherent drive for the two-level system formed by the hyperfine groundstates $|F = 3\rangle$ and $|F = 4\rangle$, similar to the microwave interaction presented in section 9.2. Then, we will discuss the generation of the necessary light pulses with an electro-optical modulator (EOM) and the control setup. Finally, we present some preliminary measurements on the performance of the different components.

9.3.1 Coupling of Hyperfine Groundstates via Two-Photon Resonance

As discussed in section 9.2, the $|F = 3\rangle \rightarrow |F = 4\rangle$ transition is dipole-forbidden and its resonance frequency is far from the optical range. In order to effectively drive the transition by light in this domain, one thus has to couple the two levels via a common third level (cf. sec. 8.1, especially fig. 8.1). This idea is sketched in figure 9.20, where $|\downarrow\rangle$ and $|\uparrow\rangle$ represent the two-level system. By simultaneously addressing the $|\downarrow\rangle \rightarrow |e\rangle$ and $|\uparrow\rangle \rightarrow |e\rangle$ transition, it is possible to effectively drive $|\downarrow\rangle \leftrightarrow |\uparrow\rangle$. It is important to note that atoms are never excited to $|e\rangle$ in the process, i. e. it is fundamentally different from two subsequent single-photon transitions (Foot, 2005, app. E). An introduction to Raman scattering in the context of an atomic physics experiment can be found in Dotsenko (2002).

To see if and how a two-photon process as described in the previous section is identical to a strong coherent drive on the groundstates, one has to derive an effective Hamiltonian for this two-level system. To this end, one starts with the full multi-level structure of cesium (cf. fig. 2.1) and adiabatically eliminates all excited states. Briefly summarized, one first considers only the four levels $|3\rangle$, $|4\rangle$, $|3'\rangle$ and $|4'\rangle$, while $|2'\rangle$ and $|5'\rangle$, to each of which only one of the ground states couples, are added later. Here we do not present this lengthy but insightful calculation, which can be found in Sørensen (2015), and instead state its main result: For an optical power of 10 nW, we expect an effective Rabi frequency of more than 3 MHz.

This warrants further exploration, and we therefore present the first steps into the implementation of a Raman laser setup.

9.3.2 Electro-Optical Phase Modulation

To generate the Raman pulses, we utilize an electro-optical modulator (EOM). This common device uses the linear electro-optical effect, also known as Pockel's effect, to modulate the refractive index n of a crystal:

$$n(E) \approx n - \frac{1}{2} \mathfrak{r} n^3 E, \quad (9.6)$$

where E is the applied electric field and \mathfrak{r} is the Pockels coefficient, a material constant (Saleh and Teich, 2007, p. 837). Therefore, light passing through a crystal to which a voltage V is applied will experience an additional phase shift

$$\varphi(V) = -\pi \cdot \frac{V}{V_\pi}. \quad (9.7)$$

Here, V_π is the half-wave voltage, which is defined as $\varphi(V_\pi) = -\pi$ and depends on both the wavelength of light as well as the properties of the device.

When an RF-signal of the form $-V_{\text{rf}} \cdot \sin(\Omega t)$ is applied, sidebands of frequencies $\omega_{\pm n} = \omega \pm n \cdot \Omega$ are modulated onto the light of frequency ω_0 passing through the EOM:

$$E \cdot e^{i\omega t} \rightarrow E \cdot e^{i\omega t + i\alpha \sin(\Omega)t}, \quad (9.8)$$

where $\alpha = -\varphi(V_{\text{rf}})$.

To calculate the amplitude of the sidebands from (9.8), we make use of the Jacobi-Anger expansion (Weisstein, c), where J_n denotes the n^{th} order Bessel function of first kind:

$$\begin{aligned} & E e^{i\omega t + i\alpha \sin(\Omega)t} \quad (9.9) \\ & = E \cdot \left(\underbrace{J_0(\alpha) e^{i\omega t}}_{\text{carrier}} + \underbrace{\sum_{n=1}^{\infty} J_n(\alpha) e^{i(\omega+n\Omega)t}}_{\text{positive sidebands}} + \underbrace{\sum_{n=1}^{\infty} (-1)^n J_n(\alpha) e^{i(\omega-n\Omega)t}}_{\text{negative sidebands}} \right) \quad (9.10) \end{aligned}$$

We plot the intensities of the first four sidebands in figure 9.21.

9.3.3 Choice of Carrier and Modulation Frequency

One is now left with two different choices for the carrier frequency ω_0 and ω_{RF} : Either, one picks $\omega_0 = (\omega_{|\uparrow\rangle} - \omega_{|\downarrow\rangle})/2$ and $\omega_{\text{RF}} = \delta/2$, or one opts for $\omega_0 = \omega_{|\uparrow\rangle}$ and $\omega_{\text{RF}} = \omega_{|\uparrow\rangle} - \omega_{|\downarrow\rangle}$. In the first case, it is the first sidebands which have the desired frequencies $\omega_1 = \omega_{\text{RF}} + \delta/2$ and $\omega_2 = \omega_{\text{RF}} - \delta/2$, whereas in the second case the carrier and one of the first sidebands are the sources of the Raman light.

While the second alternative has the advantage that the source laser is tuned to an atomic resonance, allowing for monitoring via saturated absorption spectroscopy, the first alternative comes with inherent power balancing

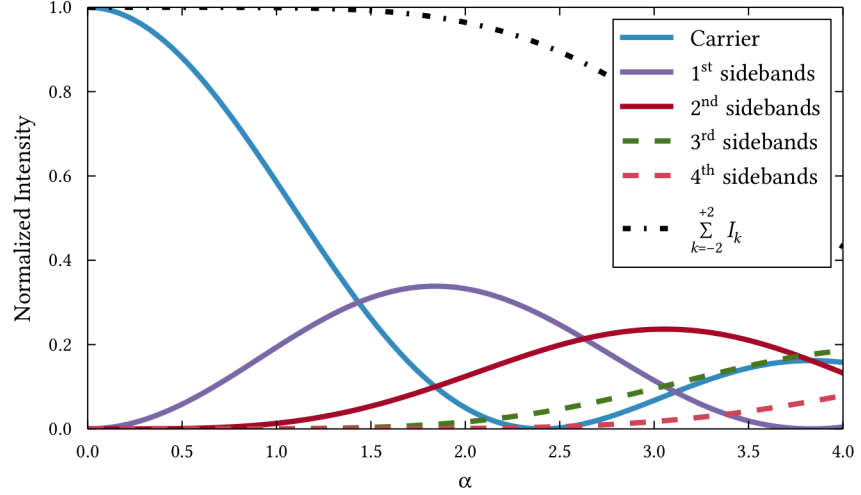


Figure 9.21: Calculated relative intensities for the carrier and the first four sidebands.

At the point of carrier depletion, about 90% of the optical power is in the first two sidebands.

between the two Raman frequencies. One further has to consider if higher order sidebands are driving unwanted transitions. We note that it is possible to separate the sidebands from the carrier and the sidebands from each other using an interferometer, but this requires much additional development and the operation of yet another lock in the setup.

For the preliminary investigations, we pick the first alternative.

9.3.4 Setup and Control

In our experiment, we use a beatnote locked external cavity diode laser (ECDL) as described in appendix D to generate light at a carrier frequency ω_0 (figure 9.22). This light is sent through a fiber coupled lithium niobate EOM (EOSPACE PM-oK5-10-PFA-PFA-850) to which an RF-signal ν_{RF} is applied. This signal is suggested to be generated by the same DDS board which is used for the microwave frequency generation (sec. 9.2.2). To this end, the DDS output signal is split off, multiplied (MiniCircuits ZX90-12-63+, $\nu_{\text{out}} = 4500$ to 6000 MHz) and sent through a bandpass filter (MiniCircuits VBF-4440+, $\nu_{\text{pass}} = 4200$ to 4700 MHz) before reaching the amplifier (MiniCircuits, 20 dB gain). This ensures that microwave and Raman pulses can be generated independently of each other: While the microwave frequency generated by the DDS is about 192 MHz, which is readily suppressed by the bandpass filter, while the EOM multiplier is driven with 383 MHz, a frequency that is too high to pass through the microwave cavity filter (cf. sec. 9.2.2).

From equation (9.10) we know that the intensity of the sidebands is $(E \cdot J_n(\alpha))^2$. As we have seen in figure 9.21, by controlling the strength of the

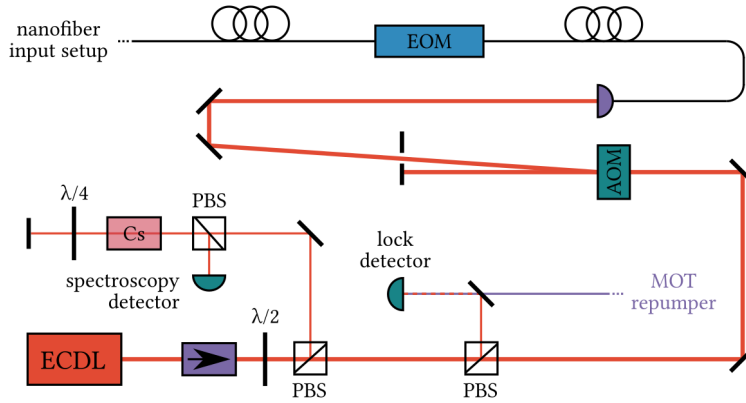


Figure 9.22: Optical setup for the creation of Raman pulses. The ECDL is beatnote locked to the MOT repumper. The saturation spectroscopy setup shown is identical to the one indicated in figure 2.7. Since as described in the main text the ECDL is locked to ω_0 , no absorption signal can be observed. However, the same laser was used as the structuring laser during the atomic mirror experiment where it was locked close to the $|F = 4\rangle \rightarrow |F^{\text{prime}} = 4\rangle$ transition (sec. 6.4.1).

modulation we can deplete the carrier band completely and shift the light into the first two sidebands. While we can neglect third and higher order sidebands in our amplitude range of interest, there is a tradeoff to be made between maximum intensity in the first order and intensity in the carrier and second order.

Since we only need about 10 nW of optical power and have several milliwatts at our hands as well as far-detuned sidebands, we choose to deplete the carrier. Using (9.7) and the definition of α , as well as taking into account input reflection and losses, we estimate carrier depletion for 17.2 dBm.

9.3.5 Preliminary Investigations

As the extraordinary optical axis of the lithium niobate crystal inside the EOM is aligned to the slow axis of the input fiber, we choose our input polarization accordingly and optimize the polarization with respect to minimum fluctuations when heating the fiber.³

To detect the sidebands, we apply an RF-signal and interfere the output of the EOM with a reference laser on a fast photo detector. By monitoring the detector signal with a spectrum analyzer, we can determine the relative intensities of the sidebands as is shown in figure 9.21. From section 3.4 and (9.10) we expect the intensity of the n^{th} sideband to be proportional to $J_n(\alpha)$. This is confirmed by our measurement as shown in figure 9.23, from which we find $P_{\text{depletion}} = 46 \text{ mW} = 16.7 \text{ dBm}$.

³ Instructions by the author on how to align the EOM based on correspondence with the manufacturer can be found on the page documentation: eospace_eom in the clock group's wiki.

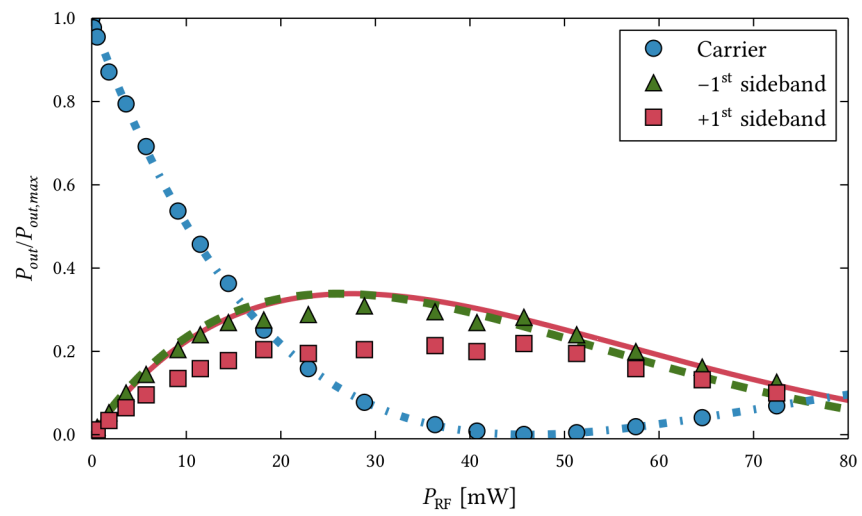


Figure 9.23: Preliminary measurement on the relative intensities of the first sidebands and the carrier for $\nu_{RF} = 4.596 \text{ MHz} = \nu_0/2$. We attribute the deviation on the +1st sideband to worse amplification and higher losses in that frequency range.

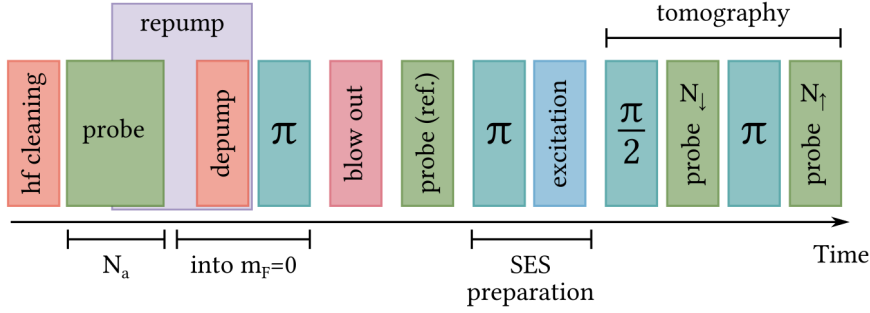


Figure 9.24: Final sequence for the SES experiment. After hyperfine cleaning (sec. 9.1.1), an estimate on N_a can be obtained (optional). Subsequently, the atoms are pumped into $m_F = 0$ (sec. 9.1.2) and the remaining atoms are removed from the trap (sec. 9.1.3). Afterwards, a reference phaseshift is obtained and all atoms are transferred into $|\downarrow\rangle$. This is the initial state $|\Psi_0\rangle$. Then, the SES is created (sec. 8.1), followed by a tomography measurement (sec. 8.3.1).

This sequence is repeated many times and data for the analysis is selected conditioned on whether a single detection event was observed during the excitation pulse.

9.4 FINAL PREPARATION SEQUENCE

In this chapter we have at lengths explored state preparation using optical pumping and microwave interactions, as well as in the last section given a brief report of our first steps towards the implementation of Raman processes.

We found that the coherence times are $\tau_1 \approx 3$ ms (fig. 9.12) and $\tau_2 \approx 500$ μ s (fig. 9.17), which together with a π -pulse length $T_\pi = 24.2$ μ s suggests that the preparation and tomography of the SES can be realized by using microwave and optical pumping alone. In figure 9.24 we give the final experimental sequence reflecting the current status at the time of writing.

Nevertheless, the implementation of Raman processes is certainly a worthwhile endeavour, especially in light of future experiments which might require state manipulation sequences consisting of many more rotations. We will briefly discuss this aspect in section 11.2.4.

DETECTION

As already discussed in chapter 8 the detection of the single excitation Fock state is equivalent to the detection of the single heralding photon emitted by the transition from $|F' = 4, m_F = 1\rangle$ to $|F = 3, m_F = 0\rangle$ ($|4', 1\rangle \rightarrow |3, 0\rangle$).¹ We therefore need to filter out all other light present in the setup, namely the trap and excitation light as well as light from the other possible decay channels. To this end, we use a standalone detection setup which was planned, built, and characterized as part of this thesis.

This setup, which is shown in its entirety in figure 10.1, consists of a filter cavity, a Volume Bragg Grating (VBG), and a single photon counting module (SPCM). In the following sections we will describe these components in detail. Subsequently the overall efficiency and the consequences for the purity of the single excitation state will be discussed.

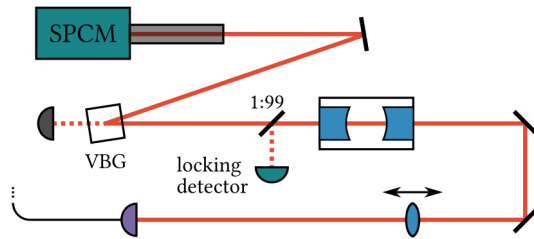


Figure 10.1: Sketch of the heralding photon detection setup. While the cavity filters out the excitation light (sec. 10.1), the VBG only reflects the heralding photon whereas the trap light is transmitted and subsequently absorbed (sec. 10.2). The SPCM photodiode is shielded from stray light by a tube which also contains focusing optics (fig. 10.10). The entire setup is enclosed in a light-tight box.

10.1 FILTER CAVITY

We use a Fabry-Perot type cavity to filter out the excitation light ($\nu_{\text{exc}}, |4, 0\rangle \rightarrow |4', 1\rangle$), which is red-detuned by 9.192 GHz from the heralding photons ($\nu_{\text{hp}}, |4', 1\rangle \rightarrow |3, 0\rangle$). To be able to efficiently perform the experiment and to reach a high state purity transmission of the latter must be as large as possible (cf. 10.4).

In the following section we detail our design choices and characterize the very filter cavity used in the final setup. Although the following considerations, calculations, and measurements were conducted ab initio for this thesis, the cavity is identical to the one described in Christensen (2012) which

¹ For the sake of clarity, we will discuss polarizations always in the reference frame of an atom positioned on the positive part of the h -axis as introduced in section 4.3.

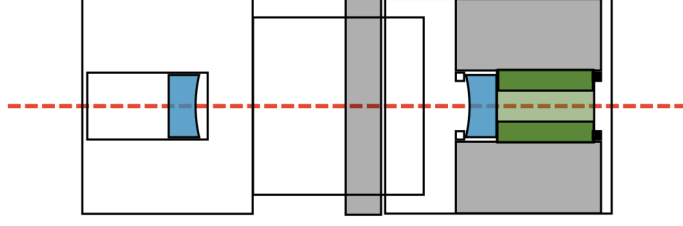


Figure 10.2: The filter cavity is formed by two mirrors (blue) mounted inside an adjustable and a regular lens tube (Thorlabs SM1Vo and 5SML10). A custom holder houses a tube shaped low-voltage piezo-electric crystal (green) which presses on the back surface of one of the mirrors.

was used for [Christensen et al. \(2014\)](#). In addition, after the work on this cavity was completed a similar model with different mirrors was constructed and tested at [QUANTOP](#) as a Bachelor's project. The results and some modeling can be found in [Appel \(2015\)](#).

10.1.1 Design

Our cavity, which is depicted schematically in figure 10.2, consists of two identical spherical mirrors with a radius of curvature of $R = 250$ mm. These are mounted inside a lens tube assembly which allows for cavity lengths from about 10 mm to 25 mm. While one mirror is fixed, the other can be shifted by applying a voltage to a piezo-electric crystal. This setup is very stable mechanically and shows negligible thermal drift on the timescales relevant to the experiment (cf. fig. 10.6).

To use the cavity as a spectral filter, we need to limit the number of its resonance frequencies ν_{res} . In general,

$$\nu_{\text{res}}(L) = n \cdot \text{FSR}(L) + m \cdot \text{TMS}(L), \quad (10.1)$$

where L is the length of the cavity ([Kogelnik and Li, 1966](#)).

$$\text{FSR}(L) = \frac{c}{2L} \quad (10.2)$$

where c is the speed of light is the free spectral range, i. e. the frequency difference between two fundamental modes, and

$$\text{TMS}(L) = \text{FSR}(L) \cdot \frac{\arccos(1 - L/R)}{\pi} \quad (10.3)$$

where R is the radius of curvature is the transversal mode spacing, i. e. the frequency difference between two neighboring higher order modes within the same FSR ([Kogelnik and Li, 1966](#)). The integers n and m , starting from 0, are the number of the FSR and the mode number within this FSR, respectively. All this is visualized in figure 10.3.

To limit the number of possible resonance frequencies it is thus desirable that

$$n \cdot \text{FSR}(L) = (n - 1) \cdot \text{FSR}(L) + m \cdot \text{TMS}(L), \quad (10.4)$$

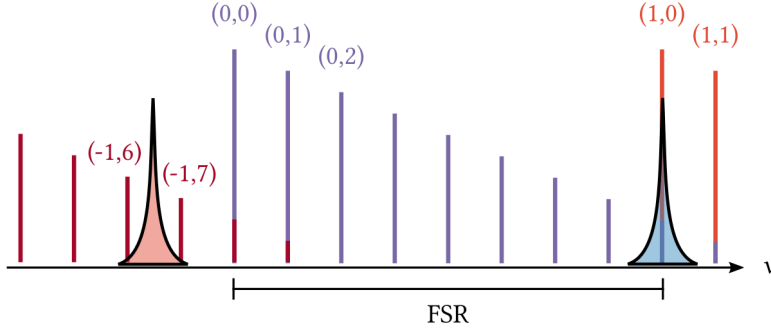


Figure 10.3: Visualization of the filter cavity's mode structure. If the heralding photon (blue) is on resonance with the fundamental mode (1,0), the excitation light lies in between the 6th and 7th order mode of the -1st FSR.

i. e. the fundamental mode of an FSR overlaps with a higher order mode of the preceding FSR.

In order for the cavity to transmit the heralding photon the fundamental mode has to be on resonance, which leads to the condition

$$\text{FSR}(L) = \frac{1}{n} \cdot \nu_{\text{hp}}. \quad (10.5)$$

At the same time the excitation light – which has a $\Delta\nu = 9.192$ GHz lower frequency – should be filtered out, i. e. its frequency should lie far away from the fundamental in between two higher order modes. The coupling into these can be suppressed almost completely through mode matching (app. B).

With this and conditions (10.4) and (10.5) we can determine the optimal pair of parameters (L, m) . We start by finding an L_0 such that

$$\text{FSR}(L_0) = \Delta\nu, \quad (10.6)$$

which leads to $L_0 \approx 20$ mm. Then we find suitable m to fulfill (10.4) and choose $m = 8$. This places the excitation frequency in between the 6th and 7th higher order mode of the preceding FSR, as depicted in figure 10.3.

We can now find L closest to the length for which (10.4) is exactly fulfilled for $m = 8$ such that condition (10.5) is met. We arrive at a cavity of length $L = 19.03$ mm. It is clear that condition (10.4) will be fulfilled only approximately for this choice of L . However, the induced frequency mismatch is below the cavity linewidth (0 MHz).

10.1.2 Adjusting the Free Spectral Range

In order to adjust and determine the length and FSR of the cavity, we employ two external cavity diode lasers (ECDLs) which can be locked at arbitrary difference frequencies in the range of 7 to 12 GHz (cf. app. D.3 for details). We send in both lasers at different intensities, such that we can discriminate them (fig. 10.4). By applying a voltage to the piezo, we scan the cavity length

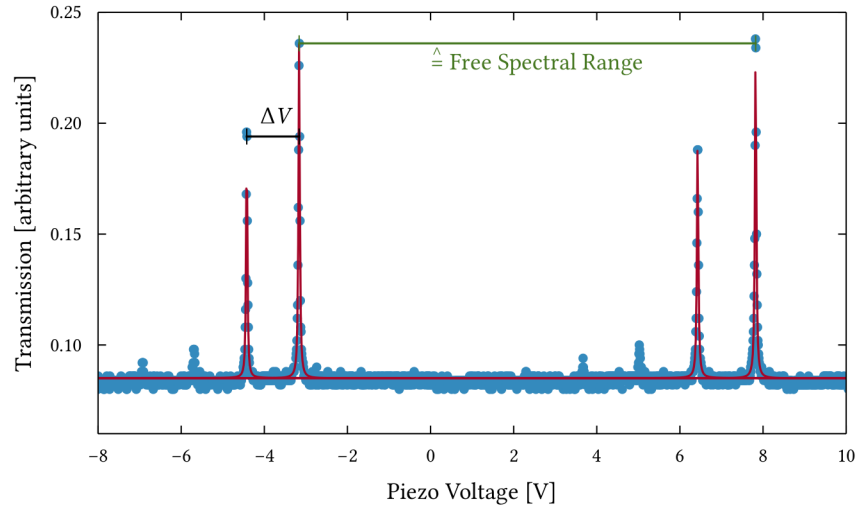


Figure 10.4: Transmission of two lasers detuned by $\Delta\nu$ with different intensities through the filter cavity for varying piezo voltage V . By fitting a Lorentzian profile to the 0th order mode transmission (red lines), we find the voltage corresponding to the highest transmission (green triangles) and determine $\Delta V(\Delta\nu)$. By repeating this procedure for several $\Delta\nu$, the FSR can be extrapolated (cf. fig. 10.5)

over about 1.5 FSRs, record the transmission spectrum and determine the voltage difference between the fundamental modes of both lasers. In doing so for several difference frequencies and performing a linear fit on the $(\Delta V, \Delta\nu)$ data, we can extrapolate the detuning for which the difference in voltage vanishes, i. e. both lasers are detuned by exactly one FSR (fig. 10.5).

10.1.3 Locking

The cavity piezo is driven through a lock circuit as described in appendix E.2, which can also generate a voltage ramp to scan the cavity length. To stabilize the cavity to maximum transmission, we use a dither lock, whose error signal is fed into the lock circuit. A description of this method can be found Christensen (e. g. in 2012), Appel (e. g. in 2015). We can control the dither lock through a TTL signal. When turned off, the circuit outputs a constant error signal such that the feedback signal remains at its current value – the piezo “freezes”.

The stability of the “frozen” cavity is important, since during the time window in which the heralding single photon is to be detected, no reference light for locking must be present in the setup. To quantify the stability, we repeatedly lock the cavity for 1 s and record the transmission for the following 4 s. One typical example of such a measurement is shown in figure 10.6. We find that the transmission remains stable for at least the first second in all measurements – much longer than needed (cf. sec. 9.4 and sec. 10.4) – and

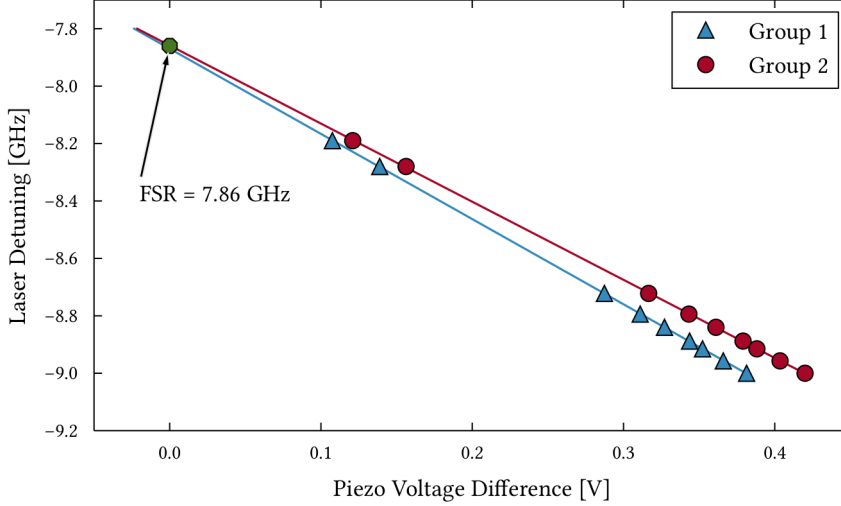


Figure 10.5: By measuring $\Delta V(\Delta\nu)$ for several laser detunings $\Delta\nu$, $\Delta V(\Delta\nu_{\text{FSR}}) = 0$ can be extrapolated through a linear fit. Due to the non-linearity of the piezo, the relationship $\Delta V(\Delta\nu)$ is different for each group of 0th order modes shown in figure 10.4. However, both share $\Delta\nu_{\text{FSR}} = 7.86 \pm 0.01$ GHz.

that in the absence of mechanical disturbance the cavity can be re-locked after 4 s.

While for testing the cavity is locked to the test laser providing light at the heralding photon frequency, to lock the cavity during the final experiment a different light source has to be used. Ideally, this light is propagating through the nanofiber to avoid additional losses by inserting e. g. a beamsampler to overlap the lock reference with the heralding photon mode.

One option is to modify the optical pumping setup (fig. 9.1) so that the MOT repumper, which is co-propagating with the heralding photon through the fiber during the cooling phases, is *H* polarized. As we noted, the repumping through the fiber did not yield different results than applying the repumper externally (sec. 9.1), therefore a rotation of the polarization from *V* to *H* is expected to be unproblematic for cooling and trap loading as well.

In case the excitation light has to be provided by a separate laser – e. g. because involved optical filtering and frequency control is necessary – it would likely be derived from the test setup (app. D.3). We will discuss the options in some more detail in section 11.1.2.

10.1.4 Transmission

Maximum transmission of light at the heralding photon frequency through the modematched and locked cavity is measured to $T_{\text{hp}} = 83.40 \pm 0.06\%$.

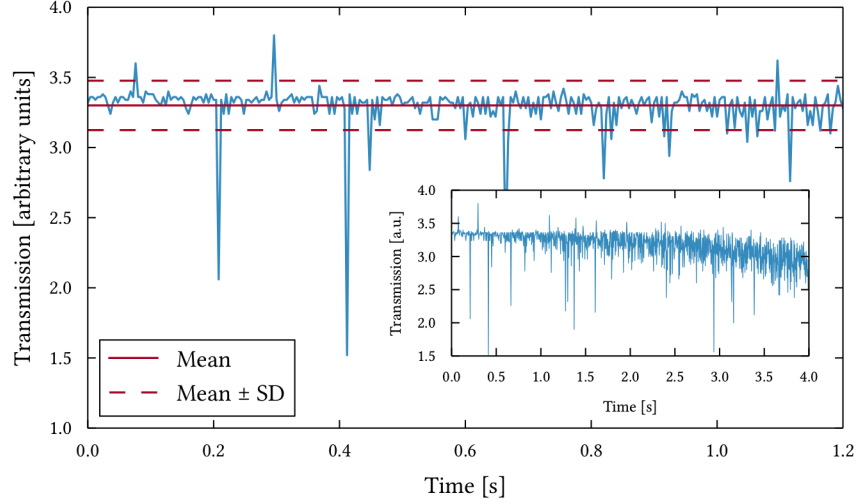


Figure 10.6: The measured transmission through the cavity varies less than 10% during the first second after the cavity lock is released. The inset shows the same transmission signal for a longer duration.

10.1.5 Linewidth

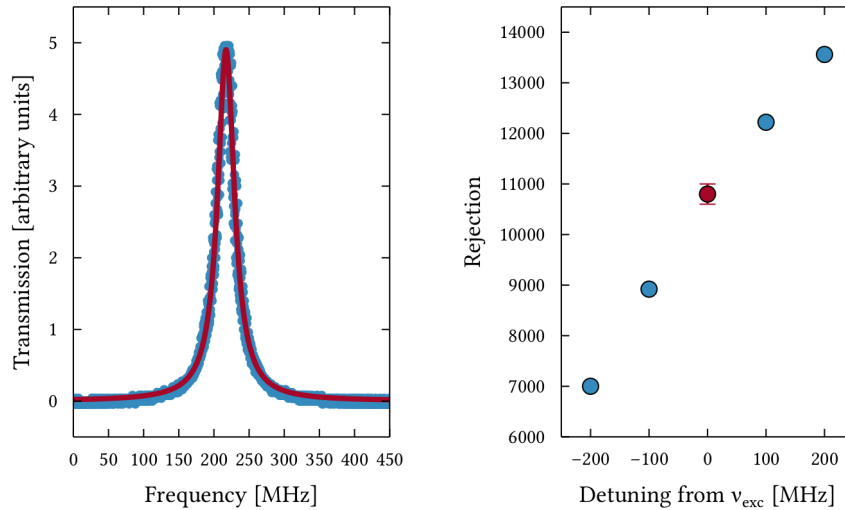
To determine the cavity linewidth, we scan over the 0th order transmission profile. Using the data acquired during the FSR measurement, we can convert from piezo voltage to wavelength (cf. fig. 10.4). We find a cavity linewidth of 29.5 MHz (fig. 10.7a).

10.1.6 Rejection

To determine the transmission of excitation light ν_{exc} through the cavity locked to the heralding photon frequency ν_{hp} , we once again use two beat-note locked ECDLs. To ensure that the excitation light is spectrally clean and does not contain photons from the laser diode pedestal, we employ both an interference filter and a filter cavity (cf. app. D.3). We can switch and modulate both lasers with AOMs.

The experimental sequence is as follows: The laser on the heralding photon frequency is switched on for 500 ms and the cavity is locked on resonance. We then freeze the lock and for 1500 ms measure the transmission of the excitation light through the cavity. To this end, we modulate the light with a frequency of 40 kHz using an AOM and employ a lock-in detector. During the time the heralding light is present in the setup, we measure the intensity of the excitation light incident on the cavity via a beamsampler. To account for any offset in the detection, we perform several runs of the sequence without any excitation light present and subtract the obtained values from each lock-in channel. We find a rejection of 1 in $10,800 \pm 200$.

In order to verify our results, we perform additional experiments. First, we block the transmission photodiode, such that no light can reach it. We obtain



(a) To obtain the cavity linewidth, a Lorentzian profile (red) is fitted to the transmission data recorded for the 0th order mode (blue). We find $\Delta\nu_{\text{FWHM}} = 29.5$ MHz, which corresponds to a finesse $\mathcal{F} = 261$. (b) Rejection of light detuned from ν_{exc} . Larger detuning moves the light away from the 0th order, thus yielding higher suppression.

Figure 10.7

a rejection ratio on the order of 1 in 230,000, which thus forms the lower bound of our measurement sensitivity. Second, we couple the light emerging from the VBG into a fiber. From measuring the transmission of the heralding light, we find that the overall transmission of the setup decreases from about 75% to about 17%. We expect to see a similar change in the rejection. Indeed, we find 1 in 60,000 instead of 1 in 10,000. We also measure the rejection ratio for different intensities of the excitation light. Last, we change the frequency difference between the lasers in steps of 100 MHz. The result can be found in figure 10.7b.

10.2 VOLUME BRAGG GRATING

A Volume Bragg Grating (VBG) is a three-dimensional holographic grating. It is commonly fabricated by creating an interference pattern of UV lasers in photo-thermo-reflective (PTR) glass. The result is a periodic variation in the refractive index which forms a Bragg grating as discussed in section 6.1. Accordingly, VBGs can be designed to either be reflective or transmissive. A thorough review of their fabrication and the diverse range of applications can be found in Glebov et al. (2012).

The narrow spectral window on the order of a few gigahertz combined with high reflection coefficients of 95% and above makes VBGs ideal devices to filter out the trapping lasers of nanofiber dual-color dipole traps (cf. e. g. Lee et al., 2015). In our filtering setup, we use a reflective VBG with a speci-

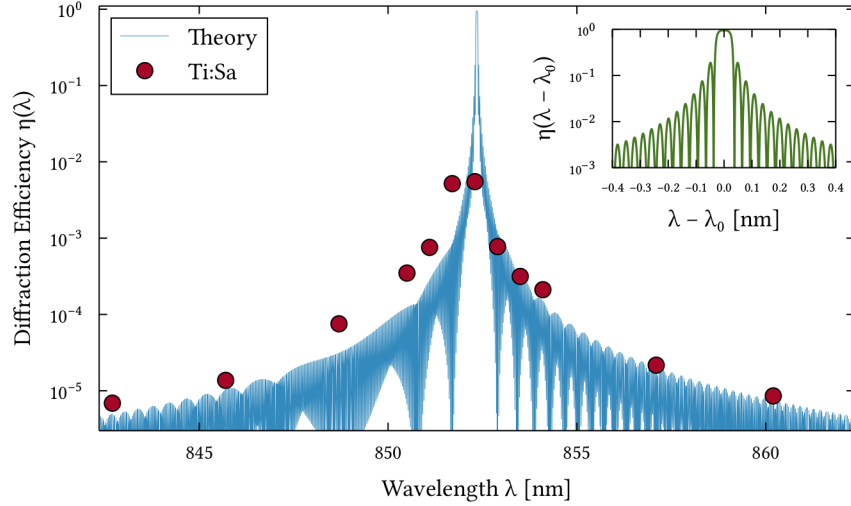


Figure 10.8: Reflection efficiency η of the VBG for light of different wavelengths. Experimental data was acquired with a Ti:Sa, a photodetector and a lock-in amplifier. The theoretical curve is the result of a coupled wave theory approach (cf. app. C).

fied peak diffraction efficiency $\eta = (99 \pm 0.5)\%$ at the central wavelength $\lambda_0 = 852.35$ nm (OptiGrate RBG-852-99, for further details see appendix C).

We perform a number of test measurements with different light sources to determine the spectral dependency of the diffraction efficiency η . Using an external cavity diode laser (ECDL, cf. app. D), we determine a peak efficiency $\eta_{\max} = 96\%$ and $\eta_{830} = 10^{-6}$ for $\lambda = 830$ nm. We also align the grating to maximum efficiency at λ_0 and then scan over the range from $\lambda = 750$ nm to $\lambda = 870$ nm using a titanium sapphire laser (Ti:Sa). We then compare our experimental data to a theoretical model based on a coupled wave theory approach Kogelnik (1969), which is described in more detail in appendix C. The results are presented in figure 10.8.

10.3 SINGLE PHOTON DETECTION

To detect the heralding photon, we use a single photon counting module (SPCM). The key specifications of the device (Laser Components COUNT-20C) are a detection efficiency of about 50% for our wavelength of interest, a dead time of 42 ns, and a dark count rate of 17 Hz. A full plot of the detection efficiency with respect to wavelength is shown in figure 10.9.

The SPCM is controlled by a circuit that ensures the count rate stays below the damage threshold specified by the manufacturer (20 MHz). Otherwise, the device is switched off and an error signal is sent. A detailed description of the control circuit which was developed as part of this thesis can be found in appendix E.1.

While the whole detection setup is placed inside a box and thus shielded from room and external stray light (cf. fig. 10.1), the SPCM has to be pro-

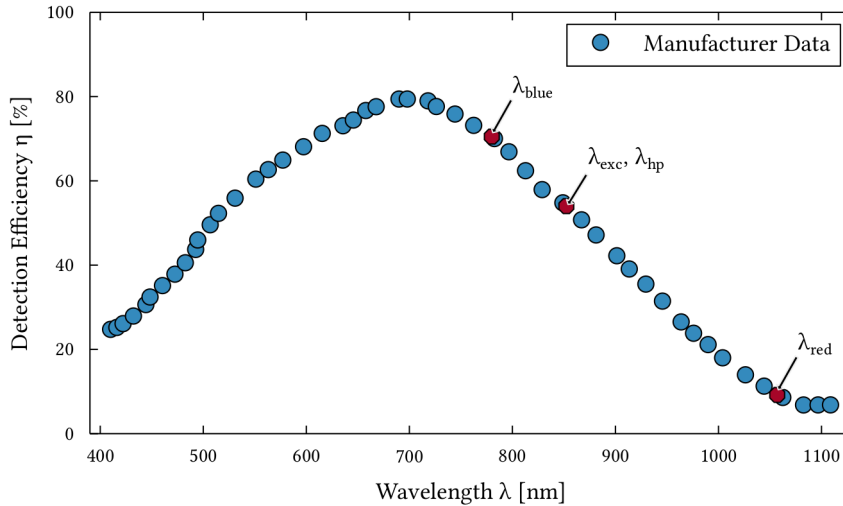


Figure 10.9: SPCM detection efficiency η as function of light wavelength λ . While $\eta(\lambda_{\text{red}})$ is below 10 %, special care has to be taken that blue-detuned trap light does not reach the detector.

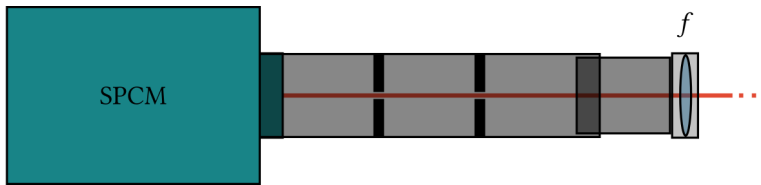


Figure 10.10: The SPCM is mounted on a custom aluminum base (not shown). To shield the detector from stray light, a lens tube assembly with apertures is used. The lens used to focus the light onto the diode is mounted inside an adjustable tube.

tected from light scattering off the VBG and other optical elements. To this end, we mount a tube in front of the device, which not only includes a focusing lens, but also two apertures (fig. 10.10).

10.4 EXPECTED STATE PURITY

With all elements of the detection setup discussed and characterized, we can now estimate its performance. The following discussion builds on Christensen (chapters 8 and 9 of 2014), incorporating our calculations made in section 8.3.

10.4.1 False Positives

In the following, we give probabilities per unit time, i. e.

$$P(\text{click}) := \frac{n \cdot \eta_{\text{QE}}}{\tau} \tag{10.7}$$

gives the expected number of “clicks” a detector with efficiency η_{QE} fires when n photons impinge during a time interval τ . Furthermore, we only discuss what is happening inside the detection setup shown in figure 10.1. Therefore, all rates Γ are given at the output of the fiber and have to be corrected for e. g. coupling losses. The latter will be summed up as an effective transmission efficiency $\tilde{\eta}$, which in most cases can be obtained directly from experiment.

The rate at which heralding photons arrive at the detection setup Γ_{hp} depends on the rate of excitation photons arriving at the atomic ensemble $\Gamma_{\text{exc},0}$ – the sole completely freely tunable parameter – and the generation efficiency η_{gen} as introduced in section 8.1:

$$\Gamma_{\text{hp}} = \Gamma_{\text{hp}}(\Gamma_{\text{exc},0}) = \Gamma_{\text{exc},0} \cdot \eta_{\text{gen}} \cdot \tilde{\eta}, \quad (10.8)$$

where $\tilde{\eta}$ is the coupling efficiency into the single mode fiber which guides the light to the detection setup, also including losses on the way from the output port of the nanofiber to the input coupler.

The probability to detect a heralding photon then is

$$\begin{aligned} P(\text{click}|\text{hp}) &= \Gamma_{\text{hp}}(\Gamma_{\text{exc},0}) \cdot T_{\text{hp}} \cdot \eta_{\text{VBG}}(\lambda_{\text{hp}}) \cdot \eta_{\text{SPCM}}(\lambda_{\text{hp}}) \\ &= \Gamma_{\text{hp}} \cdot 0.834 \cdot 0.96 \cdot 0.54 = 0.43 \cdot \Gamma_{\text{hp}}(\Gamma_{\text{exc},0}), \end{aligned} \quad (10.9)$$

where T_{hp} is the transmission of the heralding photon through the filter cavity, η_{VBG} the diffraction efficiency of the VBG at the heralding photon frequency, and η_{SPCM} the quantum efficiency of the SPCM.

Excitation light arrives at the detection setup with a rate of

$$\Gamma_{\text{exc}} = \Gamma_{\text{exc},0} \cdot \tilde{\eta} \quad (10.10)$$

and is detected with probability

$$\begin{aligned} P(\text{click}|\text{exc}) &= \Gamma_{\text{exc}} \cdot T_{\text{exc}} \cdot \eta_{\text{VBG}}(\lambda_{\text{exc}}) \cdot \eta_{\text{SPCM}}(\lambda_{\text{exc}}) \\ &= \Gamma_{\text{exc}} \cdot 11,000^{-1} \cdot 0.96 \cdot 0.54 = 4.3 \cdot 10^{-5} \cdot \Gamma_{\text{exc}}. \end{aligned} \quad (10.11)$$

We further have to consider the contributions from the other decay channels (cf. eq. 8.13), where we have

$$\begin{aligned} P(\text{click}|\text{other}) &\approx (\Gamma_{\Delta \approx 0} + \tilde{\Gamma}_{\Delta \approx 0}) \cdot T_{\text{hp}} \cdot \eta_{\text{VBG}}(\lambda_{\text{hp}}) \cdot \eta_{\text{SPCM}}(\lambda_{\text{hp}}) \\ &\quad + (\Gamma_{\Delta \approx \nu_{\text{clock}}} + \tilde{\Gamma}_{\Delta \approx \nu_{\text{clock}}}) \cdot T_{\text{exc}} \cdot \eta_{\text{VBG}}(\lambda_{\text{exc}}) \cdot \eta_{\text{SPCM}}(\lambda_{\text{exc}}) \\ &= 0.43 \cdot (\Gamma_{\Delta \approx 0} + \tilde{\Gamma}_{\Delta \approx 0}) + 4.3 \cdot 10^{-5} \cdot (\Gamma_{\Delta \approx \nu_{\text{clock}}} + \tilde{\Gamma}_{\Delta \approx \nu_{\text{clock}}}). \end{aligned} \quad (10.12)$$

For the traps, the ideal configuration is the one where the blue detuned trap is counterpropagating to the heralding photon, therefore only contributions from one arm of the red trap have to be taken into account. Before trap light is sent towards the detection setup, it is filtered by a dichroic

mirror. In addition, the wavelength is vastly different, so the coupling efficiency into the fiber transporting light into the detection setup will be significantly lower than for the heralding photon. For the same reason, the light at 1057 nm will not be focused on the SPCM.

The contribution from the single red trap arm is

$$\begin{aligned} P(\text{click}|\text{trap}) &= \Gamma_{\text{red}} \cdot T_{1057\text{ nm}} \cdot \eta_{\text{VBG}}(1057\text{ nm}) \cdot \eta_{\text{SPCM}}(1057\text{ nm}) \\ &\approx \Gamma_{\text{red}} \cdot 1 \cdot 10^{-6} \cdot 0.092, \end{aligned}$$

and we can estimate

$$\begin{aligned} \Gamma_{\text{red}} &= \frac{1.3\text{ mW} \cdot 1057\text{ nm}}{h \cdot c} \cdot \eta_{\text{dichroic}} \cdot \tilde{\eta} \\ &\approx 6.92\text{ PHz} \cdot 10^{-3} \cdot 0.01 \end{aligned} \quad (10.13)$$

$$\approx 69.2\text{ GHz}, \quad (10.14)$$

leaving

$$P(\text{click}|\text{trap}) \approx 6.4\text{ kHz}. \quad (10.15)$$

In addition to the clicks generated directly by the trap light, we have to take into account broadband resonance fluorescence from the fiber, which is predominantly generated by scattering of the high intensity trap light off color centers and other defects in the fiber material. At the time of writing this effect had been brought to our attention by several other groups who employed photon counting in combination with a nanofiber, which experienced it to be a major problem – it might well be that it proves to be a roadblock for the experiment described here as well.

It is always possible to circumvent this problem by switching off the trap lasers during the SES generation, but not without compromising the coupling of atoms to the trap, whose homogeneity is not only a prerequisite for state generation, but even more so for its subsequent tomography (cf. sec. 5.1). While we will not include the – at the time of writing unknown – contributions from resonance fluorescence in our estimate of the state purity, at the end of this analysis we will be able to estimate how many more false positive detection events we can tolerate.

With (10.9), (10.11), (10.13), and the detector dark count rate $\Gamma_{\text{dark}} = 17\text{ Hz}$ we can determine the attainable state purity. To this end, we observe that given a detection event the state of the atomic ensemble is not $|\Psi_{\text{SES}}\rangle$ as given in equation (8.5), but the mixed state (Christensen, 2014, sec. 8.4.1)

$$|\Psi_{\text{click}}\rangle = p |\Psi_{\text{SES}}\rangle + (1 - p) |\Psi_0\rangle, \quad (10.16)$$

with

$$p = \frac{P(\text{click}|\text{hp})}{P(\text{click})}. \quad (10.17)$$

In the last step, we have introduced the total rate of detector clicks

$$\begin{aligned} P(\text{click}) &= P(\text{click}|\text{hp}) + P(\text{click}|\text{exc}) + P(\text{click}|\text{trap}) \\ &\quad + P(\text{click}|\text{other}) + \Gamma_{\text{dark}}. \end{aligned} \quad (10.18)$$

10.4.2 *Multiple Excitations*

So far we have analyzed the detrimental effects of detector clicks caused by light other than the heralding photon, which we have tried to eliminate with the filtering setup developed in this chapter. To give an estimate for $\Gamma_{\text{exc},0}$ (or, more general, the generation efficiency η_{gen} as defined at the end of section 8.3), we need to take into account the effect of higher-order atomic Fock states (AFSs) we inevitably create with non-zero probability when sending more than one excitation photon down the fiber (cf. sec. 8.1). This requires us to expand our “steady state” rate picture to include some time-dependency.

Again following (Christensen, 2014), we define – given an excitation pulse containing N_{exc} photons in time T_{exc} , i. e. $\Gamma_{\text{exc},0} = N_{\text{exc}}/T_{\text{exc}}$ – the probability to have created the n^{th} order AFS albeit detecting only a single heralding photon

$$P(n|\text{click}) = \frac{p_{\text{hp}}(n)p(\text{click}|n)}{p(\text{click})}, \quad (10.19)$$

where $p_{\text{hp}}(n)$ is the probability to scatter n heralding photons into the forward direction. With Christensen (2014, sec. 5.3) we take

$$p_{\text{hp}}(n) = (1 - P_{\text{hp}}^+)(P_{\text{hp}}^+)^n, \quad (10.20)$$

where the superscript $+$ denotes the probability normalized with respect to forward scattering, as a thermal distribution. The probabilities for all other near-resonant decays are treated the same way. We approximate the contributions from dark counts, trap light, and excitation light as Poisson distributed, i. e.

$$p_{\text{dte}}(n) = \frac{p_f^n \exp(-p_f)}{n!} \quad (10.21)$$

with

$$p_f = (\Gamma_{\text{dark}} + P(\text{click}|\text{trap}) + P(\text{click}|\text{exc})) \cdot T_{\text{exc}}, \quad (10.22)$$

i. e. p_f is the probability to find false positive events from either one of the three contributions.² With

$$p_{\Delta \approx 0}(n) = (1 - P_{\Delta \approx 0}^+)(P_{\Delta \approx 0}^+)^n, \quad (10.23)$$

where $P_{\Delta \approx 0}^+ = P_{\Delta \approx 0,+}^+ + \tilde{P}_{\Delta \approx 0,+}^+$ (cf. sec. 8.3) and $p_d = 0.43$ the detection efficiency (cf. eq. 10.12), if k photons are emitted, the probability to detect n is

$$p_{\text{other}}(n) = \sum_{k=n}^{\infty} p_{\Delta \approx 0}(k) \binom{k}{k-n} (1 - p_d)^{k-n} p_d^n \quad (10.24)$$

$$= \frac{(1 - P_{\Delta \approx 0}^+)(P_{\Delta \approx 0}^+ p_d)^n}{(1 - P_{\Delta \approx 0}^+(1 - p_d))^{n+1}}. \quad (10.25)$$

² Since $P(\text{click}|\text{trap})$ and $P(\text{click}|\text{exc})$ are the dominating contributions, we neglect $P_{\Delta \approx \nu_{\text{clock}}}^+$.

Finally, we can give the probability to obtain a single click given n emitted heralding photons:

$$p(\text{click}|n) = np_d(1-p_d)^{n-1} \overbrace{p_{\text{other}}(0)p_{\text{dte}}(0)}^{\text{no false positives}} + (1-p_d)^n \underbrace{(p_{\text{other}}(1)p_{\text{dte}}(0) + p_{\text{other}}(0)p_{\text{dte}}(1))}_{\text{one false positive}}. \quad (10.26)$$

The normalization to $\sum_n p(n|\text{click})$ is given by [Christensen \(2014, p. 107\)](#) and using the shorthand notation $\tilde{p}_d = 1 - p_d$ we find

$$p(n|\text{click}) = \frac{\tilde{p}_d p_{\text{hp}}^n (1 - \tilde{p}_d p_{\text{hp}}) \cdot [np_d \tilde{p}_d^{-1} + p_f + p_d P_{\Delta \approx 0}^+ (1 - \tilde{p}_d P_{\Delta \approx 0}^+)^{-1}]}{p_f + p_d P_{\Delta \approx 0}^+ (1 - \tilde{p}_d P_{\Delta \approx 0}^+)^{-1} + p_d p_{\text{hp}} (1 - \tilde{p}_d p_{\text{hp}})^{-1}}. \quad (10.27)$$

For comparison with the purity estimated by [Christensen \(2014, p. 124\)](#), we state the different probabilities:

$$\begin{aligned} p_{\text{hp}} &= \Gamma_{\text{exc},0} \cdot \eta_{\text{gen}} \cdot T_{\text{exc}} \cdot m \cdot P_{\text{hp},+} \\ P_{\Delta \approx 0}^+ &= \Gamma_{\text{exc},0} \cdot \eta_{\text{gen}} \cdot T_{\text{exc}} \cdot (m P_{\Delta \approx 0,+} + (1-m) \tilde{P}_{\Delta \approx 0,+}) \\ p_d &= 0.43 \\ p_f &= (\Gamma_{\text{dark}} + P(\text{click}|\text{trap}) + P(\text{click}|\text{exc})) \cdot T_{\text{exc}}, \end{aligned}$$

where $m = 0.9227$ describes the mixture of states (cf. sec. 4.3.2). We already see that p_f is a significant contribution, warranting a more careful investigation of the count rate the red trap produces on the detector. We note that the integration of a second VBG can drastically decrease p_f , although it remains to be evaluated whether the increased loss for the heralding photon is a good trade-off.

For an excitation pulse of $T_{\text{exc}} = 100$ ns containing just 280 photons, we find (adopting the same value for η_{gen} as [Christensen \(2014\)](#)) that

$$p(n=0|\text{click}) = 0.18, \quad (10.28)$$

$$p(n=1|\text{click}) = 0.61, \quad (10.29)$$

$$p(n=2|\text{click}) = 0.17, \quad (10.30)$$

which is far worse than the $p(n=1|\text{click}) = 0.911$ estimated by [Christensen \(2014\)](#). This is, besides our assumption of a large rate of false positives caused by trap light, due to the large $P_{\Delta \approx 0}^+$. Here, [Christensen \(2014\)](#) suggests to apply a very large bias field. We instead suggest to carefully analyze the filter cavity transmission for each transition and exploring the option of adding a second filter cavity as was used in the former setup.

10.4.3 Conclusion

From our analysis, we find an expected state purity above the threshold $p = 0.5$ necessary to observe a negative Wigner function ([Christensen, 2014](#)).

We note that while we have attempted to obtain a conservative estimate, we did not consider e. g. the different filter cavity rejection ratios for the differently detuned decays into the $|F = 4\rangle$ manifold (cf. fig. 10.7b) or the precise values for the transmission of near-resonant decays. However, these contributions can be expected to be reasonably small in comparison to the resonance fluorescence mentioned above.

In addition to the non-unity state purity estimated in the previous two sections, the finite quantum efficiency of the state detection has to be taken into account, i. e.

$$p_{\text{meas}} = \epsilon p_{\text{state}}, \quad (10.31)$$

where ϵ is the detection efficiency with contributions from noise on the measurement signal, atoms scattered out of the coherent state (cf. sec. 8.3), and the ac Stark shift induced on the atoms by the excitation pulse. In absence of experimental data on these quantities we refrain from a more detailed analysis, but note that in advantage to the free-space dipole trap used in the previous experiment, in the nanofiber variant presented here the coupling of atoms to the excitation light is larger, which reduces number of excitations photons necessary, and the probe and excitation mode's overlap is unity, while before a factor $\epsilon_{mm} = 0.75$ reduced the detection efficiency (Christensen, 2014, sec. 8.4.2). Further, due to the much smaller number of atoms, classical noise is greatly reduced (Christensen, 2014, sec. 9.1).

CONCLUSION

In the [first part](#), we have laid out the foundations of our experiments. By summarizing a quantum theory of light, we have introduced the phase space formulation of quantum mechanics and the concept of non-classicality and non-Gaussian states. In treating the radiative and non-radiative interaction of atoms with light, we prepared our treatment of nanofiber trapped atoms and collective spin states and introduced atom trapping and cooling. Finally, we gave a summary of some fundamental aspects of quantum measurement and introduced our heterodyne detection methods.

In the [second part](#), our focus was on the nanofiber and the trapping of atoms in its vicinity. It is here that we studied in detail the emission properties of atoms in the evanescent field, deriving the directionality of emission we later exploited. After introducing the dual-color nanofiber lattice trap, we reported a first and direct measurement of the radial trap frequency.

The [third part](#) was concerned with the creation of a Bragg superstructure in the atomic ensemble and the investigation of coherent back-reflections off it – the creation of an “atomic mirror”. To this end, we developed and optimized the preparation sequence and subsequently studied the atom’s dynamics, concluding that the optical pumping scheme pioneered here is unsuitable for the proposed applications we briefly discussed. Therefore, a short outlook on alternatives was given.

In the [fourth part](#) we documented our work towards the preparation and tomography of a single excitation state. After adapting and working out in detail a proposal for this experiment, we implemented the creation of the initial state using optical and microwave interactions. Along the way, we observed Rabi oscillations (where we took a first step towards their non-destructive observation in real time) and presented the steps towards a [QND](#) tomography. In this part, we also described the development of the optical filtering setup for the heralding photon detection, concluding with an estimate on the attainable state purity.

In the following [outlook](#), we will outline the next steps towards the single excitation state and briefly present some possible avenues of future research with ultracold atoms trapped around a tapered optical nanofiber.

Hilbert space is a big place.

— *Carlton Caves*

In the final chapter of this thesis we first outline the next steps in the quest for a single excitation (SES) and other exotic quantum states. While an in-depth discussion is beyond the scope of this thesis, we try to give an overview of the experimental challenges ahead. The remainder of the chapter contains some thoughts on possible future directions for the nanofiber platform.

11.1 QUANTUM STATE PREPARATION

With the detection setup in place (ch. 10) and the preparation of the initial state accomplished up to further optimization (ch. 9), two important experimental ingredients are still missing: To push population measurement down to the projection noise limit and to implement the excitation pulse necessary to create SESs.

At the time of writing, the projection noise limit was already in sight. While for large numbers of atoms N_a the noise scaling was already linear (cf. sec. 3.3.1), at low N_a excess noise on the probe light appeared as an obstacle. With the sideband creation process identified as the source, a reconstruction of the probe light generation setup (cf. fig. 3.3) was underway.

11.1.1 Squeezed State

As soon as the projection noise limit is reached, the next step is the generation of a spin squeezed state (SSS). While this state is still Gaussian, it is distinctly non-classical as it cannot exist without entanglement (e. g. Sørensen and Mølmer, 2001, Dellantonio, 2015). Therefore, the realization of an SSS will be a significant achievement in its own right.

The creation of an SSS through two-color QND measurement similar¹ to the one employed here goes back to Saffman et al. (2009), Louchet-Chauvet et al. (2010) and is discussed in detail by Christensen (2014, sec. 5.1, 7.3). In rough terms, by probing the state population multiple times in rapid succession, we find that noise on the later measurements is below the projection noise limit. Hence,

$$p_{\text{SSS}}(\Delta N) = \frac{1}{\sqrt{2\pi\xi N_a}} e^{-\frac{\Delta N^2}{2\xi N_a}}, \quad (11.1)$$

¹ For the differences, see our discussion towards the end of section 8.3.1.

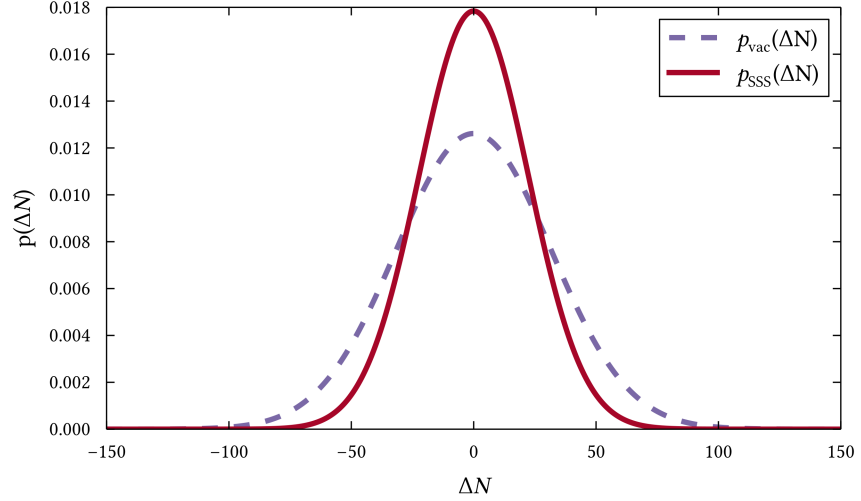


Figure 11.1: spin squeezed states are the prime examples of Gaussian, but clearly non-classical state. Here we show $p_{\text{SSS}}(\Delta N)$ for a squeezed state with $\zeta = 1/2$ compared to $p_{\text{vac}}(\Delta N)$, i. e. the expected distribution for a CSS (cf. fig. 8.3).

where ζ is the factor by which the variance is decreased compared to a CSS (fig. 11.1).

11.1.2 Single Excitation State

Once an SSS has been observed, the next milestone is the creation of an SES. To this end, two options are available: Either the excitation light is derived from the MOT cooler similar to the optical pumping light (cf. fig. 2.7 and fig. 9.1), or a separate laser is employed.

First steps towards the latter choice were taken as part of the work for this thesis by setting up a new ECDL,² which has the advantage that the whole setup can be tailored towards its single purpose, especially with regard to bandwidth filtering and AOM rejection.

At the same time, an investigation into resonance fluorescence is warranted. As briefly discussed in section 10.4.1, a high number of trap light photons scattered by color centers and other defects in the nanofiber has been observed by other groups working in the field. While large parts of this broadband light are filtered by the detection setup as we designed it, if too many photons are within the bandwidth of the heralding photon, the state purity is decreased. Possible ways to circumvent that have been discussed in section 10.4.1, and we also refer to our discussion regarding the detection bandwidth in section 8.3.

² Which is simultaneously also the new master laser for the test setup described in appendix D.3. The locking reference would be provided again by the MOT repumper, with the light picked up at the beamsplitter in front of the Raman laser lock detector depicted in figure 9.22.

With these two steps taken, given a successful realization of an *SSS* no further roadblocks are expected on the way to a tomography of the *SES*. With regard to the analysis, one can build on the work leading up to and presented in [Christensen \(2014\)](#).

11.1.3 *Single Photon Source*

Once a single excitation is stored in the atomic ensemble, the *DLCZ* protocol provides a procedure to retrieve it, i. e. to emit a single photon into the guided mode [Duan et al. \(2001a\)](#), [Bimbard et al. \(2014\)](#). To this end, a laser pulse near-resonant with the $|3\rangle \rightarrow |4'\rangle$ transition is sent through the nanofiber. To verify that what is retrieved is indeed a Fock state, one can perform a tomography using optical homodyne measurement ([Bimbard et al., 2014](#)) or measure the $g^{(2)}$ -function ([Albrecht et al., 2015](#)).

If both generation and retrieval efficiency yield sufficient rates, the system can serve as a single photon source which is deterministic in the sense that although the creation of the excitation is probabilistic, the success is heralded and the time of emission can be chosen freely within the excitation lifetime. Possible applications include e. g. an implementation of the full *DLCZ* protocol in a quantum network (cf. sec. 11.2.4) or use to realize an experiment on Boson sampling, where a large number of deterministic single photon sources operating in parallel is required ([Gard et al., 2015](#)).

11.1.4 *Beyond a Single Excitation*

While the nanofiber's predecessor at *QUANTOP* (as we already mentioned in the [introduction](#)) failed to reveal the non-Gaussianity of the *SES*, there are – as we have seen throughout this thesis – good reasons to believe that for the nanofiber setup this experiment is just the beginning.

With the proposal by [González-Tudela et al. \(2015\)](#) we discussed in section 7.3.2, a first hint on how one could store and retrieve higher order excitation states (for which the *DLCZ* protocol is not suitable, cf. sec. 10.4.2) has been brought to our attention. As this path incorporates self-structuring, which has recently attracted much attention (cf. again the [Introduction](#)), this is certainly a promising path towards states “more exotic” than an *SES*.

Another exciting avenue to explore further is – as we already mentioned in passing in section 8.2 – the separate addressing of the two linear chains trapped around the nanofiber demonstrated by [Mitsch et al. \(2014a\)](#). Here, it is conceivable to prepare different quantum states in each of them and even perform entanglement swapping (cf. [Krauter et al., 2013](#)). To this end, a barrier to overcome is the very large magnetic bias field necessary for separation paired with the requirement to keep the field strengths homogeneous along the fiber axis (i. e. to cancel all stray magnetic fields) to not render atoms distinguishable. A second challenge is to achieve and maintain clean light polarization (cf. sec. 5.6) to prevent mixing when addressing the ensembles optically.

11.2 FUTURE DIRECTIONS FOR NANOFIBER TRAPPED ATOMS

Both in the preceding section 11.1 and – in the context of the atomic mirror experiment – in section 7.3 we discussed possible future directions for experiments on the nanofiber platform. In the last section of this thesis we add to these discussions a number of more far-fetched goals. After starting out with the already mentioned quest for larger optical depths using resonators we briefly discuss trap geometries beyond the caterpillar configuration, hybrid systems, the use of nanofiber trapped atomic ensembles as building blocks for quantum networks, and conclude with an outlook on applications in quantum simulation. Our brief review is by no means exhaustive (e. g. we do not cover applications in precision measurement of which there is a long-standing tradition at QUANTOP or experiments utilizing many nanofibers in close proximity to each other) it nevertheless shows that the field of nanofiber based atomic physics is just opening up – with plenty of promises for a bright and exciting future.

11.2.1 *Cavities and Loop Resonators*

While we have stretched the absence of a cavity as an advantage of the nanofiber platform for quantum state engineering in section 5.1 in the discussion of future directions for the atomic mirror experiment, namely the exploration of self-organized systems and the engineering of superradiant states for quantum state engineering, the low coupling efficiency into guided fiber modes appeared as an obstacle (sec. 7.3).

One obvious way out was pioneered by Kato and Aoki (2015), who spliced commercially available fiber Bragg gratings onto the regular diameter ends of the nanofiber (cf. sec. 4.1). The photonic band gap of these gratings can be tuned via temperature. Since they can in principle – at the expense of a larger mode volume – be placed reasonably far away from the nanofiber section this is no obstacle. Kato and Aoki (2015) demonstrate the versatility of this approach and show that one can reach the strong coupling regime. Since the light of the nanofiber trap is far detuned from the atomic resonance the Bragg gratings appear transparent. Thus the combination of a fiber Bragg cavities with the caterpillar trap described in chapter 5 requires no new developments in terms of technology or experimental techniques while opening a path to extremely large optical depths on multiple transitions (Kato and Aoki, 2015).

Another approach is the creation of nanofiber loop resonators which are appealing both from a puristic point of view – they require nothing but a nanofiber and are equally conceptually simple – and due to the fact that they support two counterpropagating fundamental modes (compared to one mode in the aforementioned cavity) which can be driven and read out independently. First steps into their exploration have been undertaken at QUANTOP, although the development into an experimental platform will require significant effort.

A first set of challenges is mostly technological: While the formation of loops is relatively easy, their fixation is not. To achieve consistent coupling the point where the loop closes has to remain static which requires the fiber to be glued or otherwise attached to a stable base in close proximity to the nanofiber section to avoid mechanical oscillations. Closely related is the need to control and tune the loop resonator's resonance frequency which contrary to what we said before requires the loop diameter to be somewhat variable. Here one can build on the work on microfiber loop resonators by [Sumetsky et al. \(2005, 2006\)](#). In the case of nanofiber loop resonator traps resonance frequency tuning and stabilization is complicated by the substantial elongation and contraction of the nanofiber due to heating by trap light (cf. sec. 4.2.1).

The second set of challenges are the optical properties. With decreasing loop diameter the radial symmetry of light intensity disappears as whispering gallery modes (WGMs) form and become significant (cf. [Béguin, 2015](#), p. 284). This likely requires that a loop resonator trap has to be engineered to place the atoms above and below instead of inside and outside of the loop in order to maintain homogeneous coupling strengths. With regard to modeling the light intensities one can draw on the large body of work regarding WGM resonators (cf. [Foreman et al., 2015](#), and references therein).

11.2.2 Traps Using Higher Order Modes

While the caterpillar geometry as described in chapter 5 is the current method of choice (cf. [Mitsch et al., 2014a](#), [Kato and Aoki, 2015](#), [Lee et al., 2015](#)) and a state-compensated variant without vector light shifts has been demonstrated ([Goban et al., 2012](#)), new schemes which make use of higher-order modes are conceivable. The latter have been mentioned only briefly in section 4.2.2 where we chose a fiber diameter so small that only a single fundamental mode HE_{11} remained. A full discussion of their optical properties can be found in [Sagué Cassany \(2008\)](#), [Béguin \(2015\)](#); experimentally they were investigated by [Hoffman et al. \(2015\)](#), [Frawley et al. \(2012\)](#). Interactions of atoms with guided modes was studied theoretically by [Masalov and Minogin \(2013\)](#) and experimentally by [Kumar et al. \(2015a\)](#).

In general, higher order modes allow for different trap geometries due to their polarization properties and exhibit a more far-reaching evanescent field which is expected to contribute favorably to the trap lifetime. Several proposals exist, although at the time of writing all of these had yet to be tested experimentally. [Fu et al. \(2008\)](#) suggest a caterpillar trap with blue-detuned light in the HE_{11} -mode and the red-detuned light in a superposition of HE_{11} and TE_{01} , where the two arrays of trap potentials are shifted with respect to each other by half a lattice constant, although for realistic powers the trap will be more shallow than the HE_{11}/HE_{11} caterpillar. [Sagué et al. \(2008\)](#) show that it is possible to construct a trap for cesium using higher-order modes with only a single blue-detuned laser. This is especially interesting since they propose a wavelength of $\lambda = 850$ nm which would allow

the operation of the whole experiment with a single light source as long as scattering is not detrimental to the desired application.

Both [Reitz and Rauschenbeutel \(2012\)](#), [Phelan et al. \(2013\)](#) suggest a helical trap created by exciting HE and TM modes. This can be interesting for applications where the distance between the atoms along the fiber axis has to be able to vary.

With the methods used by [Hoffman et al. \(2015\)](#), [Frawley et al. \(2012\)](#) the excitation of higher-order modes can straightforwardly be integrated into an existing nanofiber trapping setup. However, beyond the mere realization of such a novel trap possible applications remain sparse and far-fetched. [Reitz and Rauschenbeutel \(2012\)](#) cite several proposals, e. g. the investigation of stable states formed by charged particles and polar molecules (cf. sec. 7.3.4) or the study of long-range interactions in a Bose-Einstein condensate (BEC) as a type of quantum simulation. While the relatively unproblematic combination of a MOT and a nanofiber (cf. sec. 5.4) gives hope that a BEC can be created in the vicinity of a nanofiber as well, it is likely to require a better control of the heating of nanofiber trapped atoms and investigations of the interaction of the fiber surface with the BEC (cf. [Hennessy and Busch, 2012](#)).

11.2.3 Hybrid Systems

The interfacing of two different quantum systems has attracted increasing attention in recent years and many such combinations have been realized experimentally. While on the one hand a stepping stone towards (hybrid) quantum networks (cf. sec. 11.2.4), on the other hand hybrid systems frequently allow to bring one of the systems into a regime which would not be accessible to experiment otherwise.

At [QUANTOP](#) the coupling of nanofiber trapped atoms to an optomechanical cavity ([Aspelmeyer et al., 2014](#)) is the prime candidate for such a system ([Hammerer et al., 2009](#)) – in fact, at the time of writing a hybrid system of a room temperature cesium vapor cell with an optomechanical membrane was investigated. The coupling of ultracold atoms confined in an optical lattice to a membrane was investigated by ([Camerer et al., 2011](#), [Vogell et al., 2015](#)), where in the latter experiment both systems were spatially separated. Nanofiber trapped atoms are especially interesting if one can connect the interfacing fiber directly to the nanofiber, thereby eliminating a main source of losses for the signal carrying light.

We conclude this section with an interesting sidenote which shows how nanofibers can be used as a tool to realize hybrid system previously deemed impossible: A project by [Orozco \(2015\)](#) currently attempts to couple cold atoms to a superconducting resonator. Here, the main challenge is the light sensitivity of the superconductor, which is heated out of its state by impinging photons, which prohibits the operation of a MOT nearby. The proposed solution to this problem is a several centimeter long nanofiber. The dipole trap around the nanofiber is loaded from a multi-stage MOT at one end and

transports the atoms (“conveyor belt”) to the superconducting circuit placed at the other.

11.2.4 *Quantum Networks*

Even though many well-controllable quantum systems have been realized in the past decades there is always a technological limit on the size of their phase space (Kimble, 2008). Here, quantum networks, i. e. separate quantum systems (nodes) linked together via quantum channels, can be used to overcome these barriers and hence open an exciting avenue towards distributed quantum computing and simulation (Kimble, 2008) and the exploration of fundamental questions in quantum information (e. g. Hayden and May, 2013). For the very same reasons as discussed in section 5.1 atoms and photons are ideal candidates – if not necessarily for eventual large scale application, then certainly as a well-understood test bed.

Ensembles of atoms trapped around nanofibers are particularly promising building blocks since they are in principle easily integrated into fiber based networks (sec. 4.1) – photons traveling along a single mode fiber being the key example of a quantum link. Based on our discussion in chapter 8 and section 11.1.3 one can readily imagine how a nanofiber trapped atomic ensemble could be used as a quantum memory by fully implementing the DLCZ protocol (Duan et al., 2001a) (cf. sec. 11.1.3).

A first experimental challenge is the physically large setup for trapping and state control which makes it difficult to realize a network beyond two or three nodes. A reduction of the current approach (which uses a minimum of five individual lasers to generate eight different frequencies of light) both in space requirements and technological overhead is therefore necessary. Additionally, individual state control – where external light sources need to be coupled into each ensemble’s nanofiber – and the need for reliable light polarization require novel technological solutions if one does not want to give up the advantage of inherent fiber connectivity – which is what all experiments known to the author at the time of writing do. To this end, advances in the field of photonic devices and conceivable means of state control from the outside (e. g. by external optical pumping, sec. 6.4.1, or via microwave, sec. 9.2) might offer a way out, although especially the polarization control stands out as a daunting issue (cf. sec. 5.6).

Another roadblock to circumvent is the short lifetime of the trapped ensemble. Generally, many gate operations have to be performed within its coherence time for a quantum system to be feasible for a quantum algorithm (Nielsen and Chuang, 2000). As we have seen in chapter 9, while we can greatly improve on the rate at which rotations can be performed by employing two-photon processes, the coherence time poses a challenge, especially if the nanofiber trapped atomic ensemble ought to function as a quantum memory which ideally should outlast other quantum systems. To this end, investigations into cooling nanofiber trapped atoms into their motional ground state might provide a solution. In a network it is furthermore required that

the communicating nodes are in a suitable state simultaneously, i. e. that the loading of the nanofiber traps is synced and occurs at a reasonable repetition rate, which can be achieved without adding much complexity (cf. sec. 5.4.1).

A first step towards the integration of nanofiber trapped atoms into quantum networks beyond the mere construction of a second setup could be the implementation of the complete [DLCZ](#) protocol or the demonstration of continuous variable state teleportation similar to the experiment by [Krauter et al. \(2013\)](#) which was performed at [QUANTOP](#) in cesium vapor cells.

11.2.5 *Quantum Simulation*

As the introductory quote to this chapter conveys, Hilbert space is indeed a big place, and both calculations and simulations of quantum systems quickly reach the limits of classical computers. To this end, quantum simulation provides a way to test physical models, e. g. providing insight into parameter ranges not accessible for real systems.

In a quantum simulation, a quantitative model for a physical system is mapped onto a different system (a prominent example is the mapping of the Bose-Hubbard model onto ultracold atoms confined in an optical lattice), in other words it is always a model which is simulated, and it needs to be verified separately that both the simulation and the model as well as the model and the system of interest are in fact ([Johnson et al., 2014](#)).

We mentioned one such proposal above (sec. 11.2.2) and here point to the recent publication by [Douglas et al. \(2015\)](#), who predict the formation of “effective cavities” by atoms placed near a one-dimensional photonic crystal waveguide. While not directly applicable to a nanofiber, this proposal nevertheless underlines that it is the one-dimensional configuration paired with long-range interactions which make nanofiber trapped atoms a promising platform.

APPENDIX

In this appendix, we document some additional results for the “Atomic Mirror” experiment described in part III which might be valuable for future investigations.

A.1 STRUCTURING PULSE DURATION

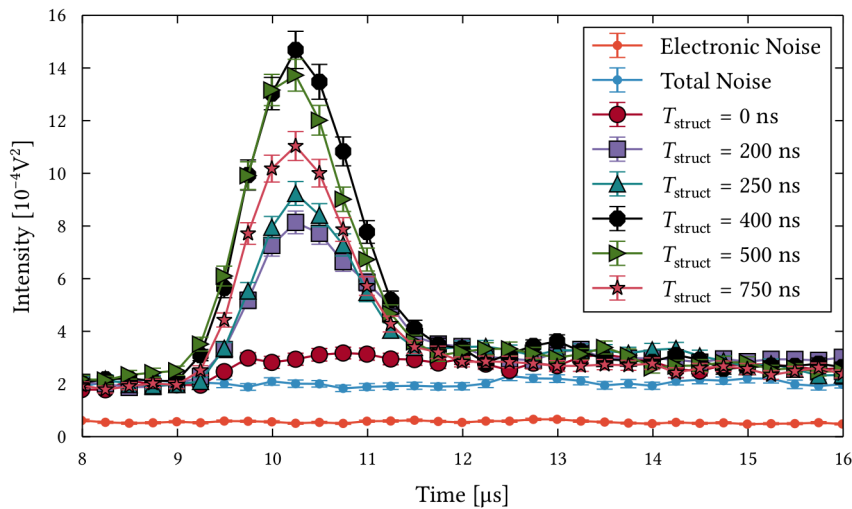


Figure A.1: Reflection signal for different T_{struct} . We see that the lifetime of the reflection does not depend on T_{struct} .

Here, we observe that highest reflection occurs for $T_{\text{struct}} = 400$ ns and $T_{\text{struct}} = 500$ ns. In later experiments we found that a reduction to $T_{\text{struct}} = 250$ ns combined with an increase in P_{struct} as to keep E_{struct} constant yields higher peak reflection.

We note that this data was taken at an early stage of the experiment and – as can be seen from the relatively slow rise of the reflection peak – there was an overlap of the structuring pulse with the probe pulse. However, this unknown overlap is constant for all measurements.

($\Delta_{\text{probe}} = 0$ MHz, $P_{\text{probe}} = 1100$ pW, $P_{\text{struct}} \approx 45$ nW, $\Delta_{\text{struct}} = -31.34$ MHz = $6 \cdot \Gamma$. Each curve corresponds to the average over 200 realizations with a timebin of 100 ns. Every 50th data point shown for visual clarity.)

A.2 STRUCTURING PULSE POWER

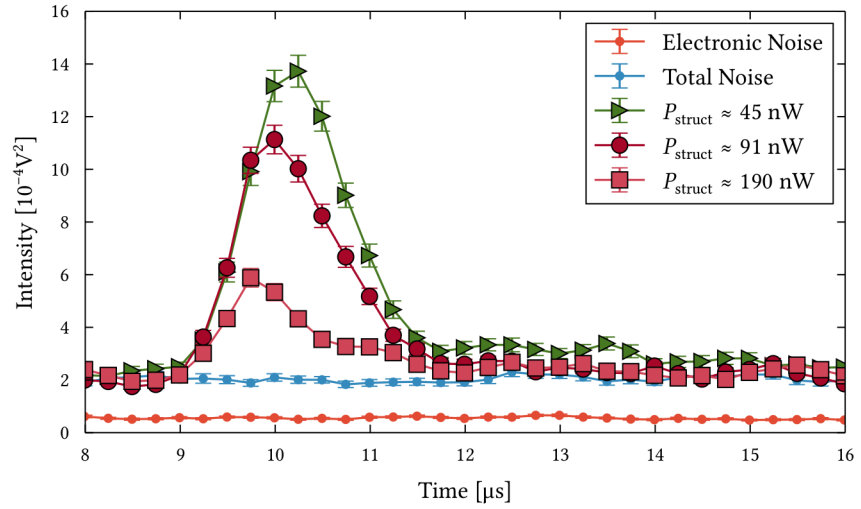


Figure A.2: Reflection signal for different P_{struct} . The power of the structuring pulse has no influence on the reflection lifetime.

We note that this data was taken at an early stage of the experiment and – as can be seen from the relatively slow rise of the reflection peak – there was an overlap of the structuring pulse with the probe pulse. However, this unknown overlap is constant for all measurements.

($\Delta_{\text{probe}} = 0 \text{ MHz}$, $P_{\text{probe}} = 1100 \text{ pW}$, $\Delta_{\text{struct}} = -31.34 \text{ MHz} = 6 \cdot \Gamma$, $T_{\text{struct}} = 500 \text{ ns}$. Each curve corresponds to the average over 200 realizations with a timebin of 100 ns. Every 50th data point shown for visual clarity.)

A.3 EFFECT OF PROBE LIGHT DETUNING ON DYNAMICS

In section 7.2.1 we concluded that probe light has no influence on the dynamics. Figures A.3 and A.4 show the results which indicate that this is true also if the probe is detuned from resonance.

As in the main text, we omit errorbars for clarity of presentation.

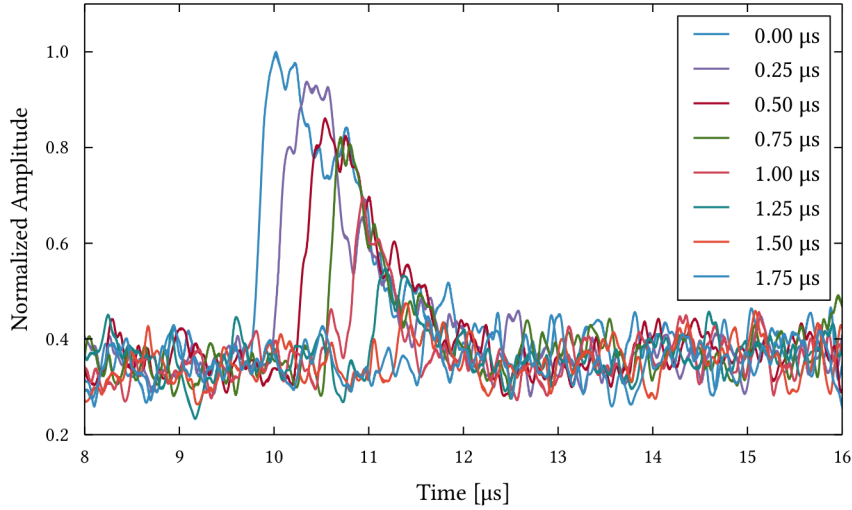
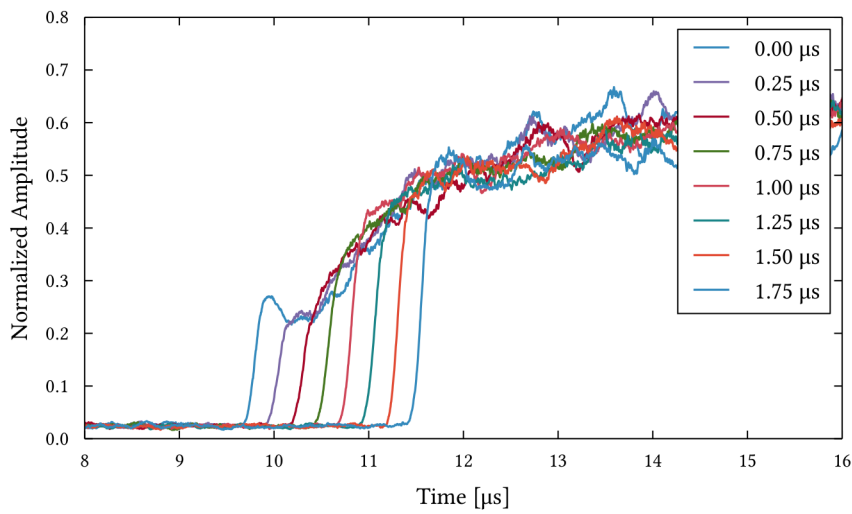
(a) Reflection for different probe delays Δt (b) Transmission for different probe delays Δt

Figure A.3: Each curve corresponds to 100 runs with $\Delta_{\text{struct}} = -175$ MHz, $P_{\text{struct}} = 238$ nW, $\Delta_{\text{probe}} = -8$ MHz, $P_{\text{probe}} = 175$ pW.

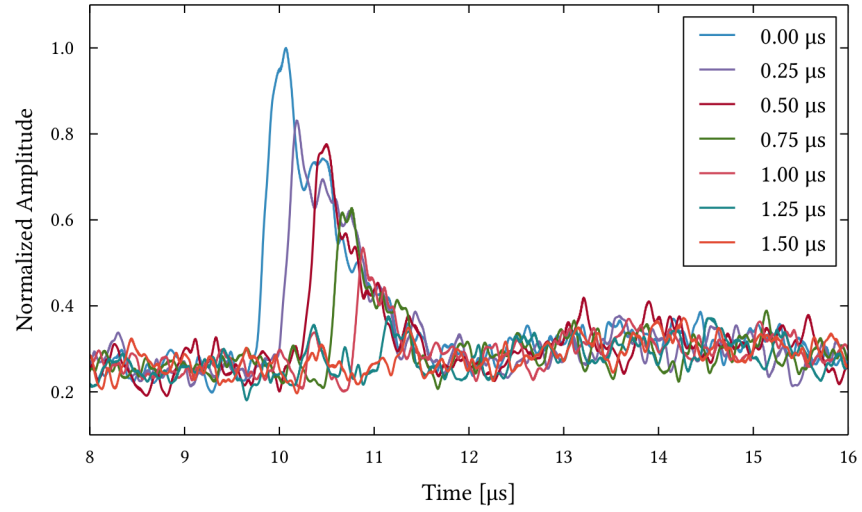
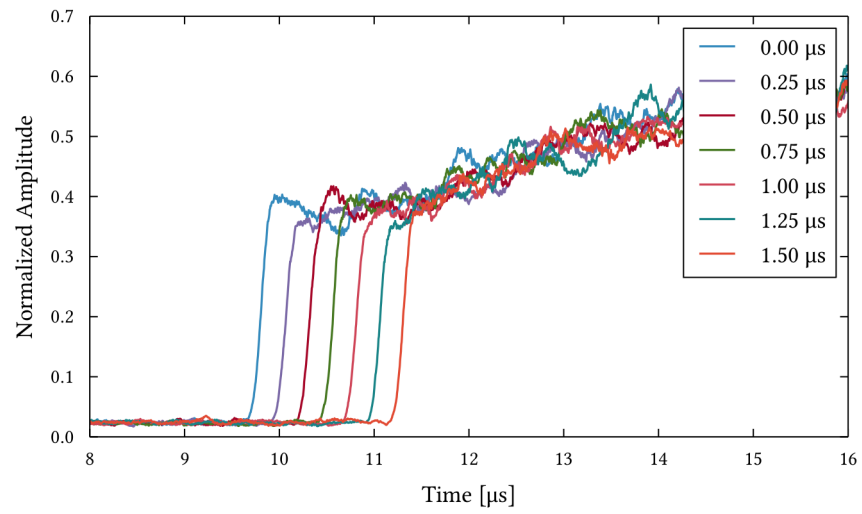
(a) Reflection for different probe delays Δt (b) Transmission for different probe delays Δt

Figure A.4: Each curve corresponds to 100 runs with $\Delta_{\text{struct}} = -175$ MHz, $P_{\text{struct}} = 238$ nW, $\Delta_{\text{probe}} = +8$ MHz, $P_{\text{probe}} = 175$ pW.

A.4 TRANSMISSION SIGNAL REPEATED PREPARATION

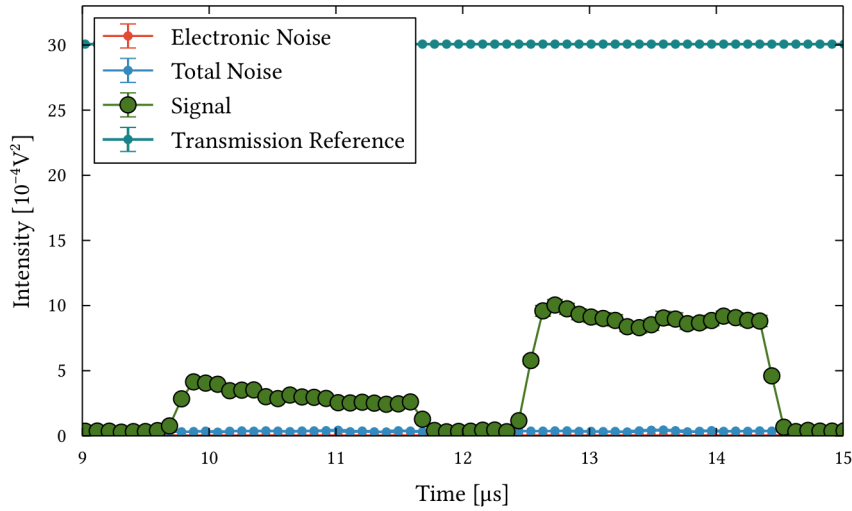
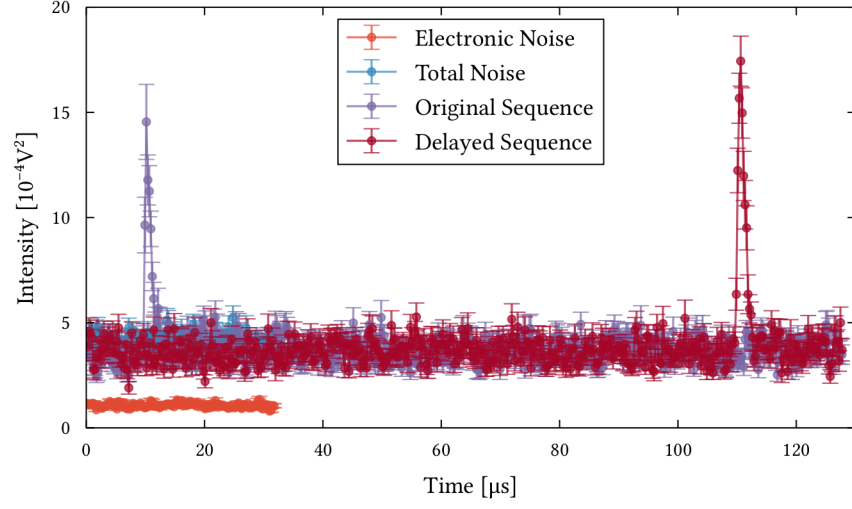


Figure A.5: Transmission signal for figure 7.5. The intensity increases by a factor of ≈ 2.5 due to loss of atoms into the dark state, while the reflected intensity is approximately halved. If the structure was perfect, given the loss in scatterers, the reflection would be expected to decrease by a factor of ≈ 1.6 .

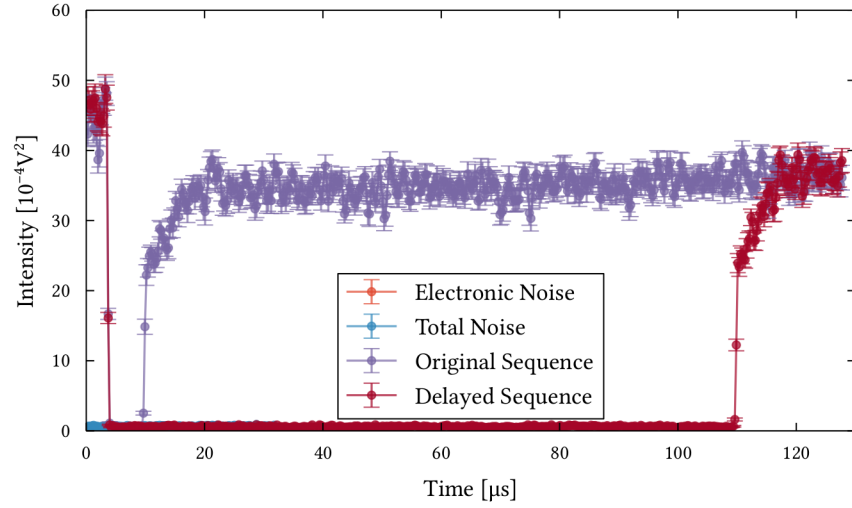
($P_{\text{probe}} = 770 \text{ pW}$, $\Delta_{\text{probe}} = 0$, $P_{\text{struct}} = 170 \text{ nW}$, $\Delta_{\text{struct}} = 140 \text{ MHz}$, each curve is the average over 100 runs.)

A.5 ATOMS DO NOT HEAT WITHOUT STRUCTURING

From figure A.6 we see that the preparation and subsequent probing of a Bragg structure does not increase the loss of atoms from the trap on the timescale relevant to the experiment.



(a) Reflection Signal



(b) Transmission Signal

Figure A.6: To verify that the inherent heating and subsequent loss of atoms from the trap is not relevant on the timescale of the conducted experiment, we delay the full preparation sequence (cf. fig. 6.10) by $100\ \mu\text{s}$, i. e. we postpone the start of the structuring pulse.

($P_{\text{probe}} = 9999\ \text{pW}$, $\Delta_{\text{probe}} = 8\ \text{MHz}$, $P_{\text{struct}} = 9999\ \text{nW}$, $\Delta_{\text{struct}} = -175\ \text{MHz}$, $T_{\text{struct}} = 250\ \text{ns}$. Each curve is the average over 100 runs with a running average of $T = 500\ \text{ns}$. Every 62nd data point shown for visual clarity.)

A.6 DETECTING A BRAGG REFLECTION IN A FEW SHOTS

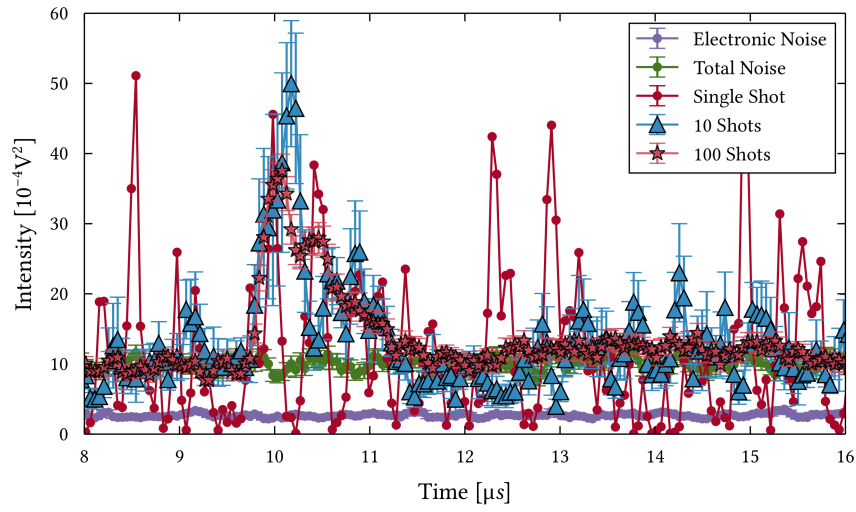


Figure A.7: While it is not possible to detect a reflection in a single shot, we see that an average over 10 realizations is already sufficient to yield an unambiguous signal.

MODE MATCHING

In order to optimize the transmission of the heralding photon through the filter cavity described in section 10.1 and to suppress coupling into higher order modes, we have to match the Gaussian TEM₀₀ mode emerging from the fiber (cf. fig. 10.1) to the fundamental mode of the cavity. We use a thin lens with focal length f placed at distance d from the cavity incoupling mirror, to perform the necessary transformation. Here we describe the calculation necessary to obtain the position of the lens.

To find the optimal pair (f, d) , we first determine the beam parameters q_{fiber} and q_{cavity} . While the latter can be obtained through a simple calculation,

$$q_{0,\text{cavity}} = \frac{i}{2} \sqrt{L(2R - L)} = 47.7991 i, \quad (\text{B.1})$$

the beam profile emerging from the fiber can only be determined experimentally. We use a beatnote locked external cavity diode laser (ECDL, see D) as our light source and measure the beam diameter at multiple points after the fiber. We fit a Gaussian profile to the data and find

$$q_{\text{fiber}} = -880.904 + 1551.26 i \quad (\text{B.2})$$

at the fiber mount. We now find (f, d, d_{tot}) such that

$$\underline{\underline{T}}(f, d, d_{\text{tot}}) \cdot q_{\text{cavity}}, \quad (\text{B.3})$$

where $\underline{\underline{T}}$ is the transfer matrix with the focal length f , distance from cavity incoupling mirror d and the total distance between fiber mount and cavity d_{tot} as parameters. $\underline{\underline{T}}$ consists of a sequence of different transformations, namely the propagations through a homogenous medium P_d , refraction at both spherical and flat surfaces with radius of curvature r and index of refraction n , $R_{r,n}$, and transfer through a thin lens L_f :

$$\underline{\underline{T}}(f, d, d_{\text{tot}}) = P_{d_{\text{tot}}-d} \cdot L_f \cdot P_d \cdot R_{\infty,n} \cdot P_{d_{\text{mirror}}} \cdot R_{R,n} \cdot P_{L/2}. \quad (\text{B.4})$$

The subscripts denote the relevant parameters. As a starting parameter we choose $d_{\text{tot}} = 500$ mm as this is a suitable length for our experimental setup and solve for possible combinations of f and d . We choose a round focal length of $f = 300$ mm and find $d = 306$ mm and $d_{\text{tot}} = 550$ mm. With this, we can suppress transmission through higher order modes below 1%.

A theoretical model to estimate the coupling into higher order modes can be found in Appel (2015).

In the following we describe in detail the modeling of the reflective Volume Bragg Grating (VBG) employed to filter the trap lights (cf. sec. 10.2). The calculations are based on the coupled wave theory approach by Kogelnik (1969), the notation follows Ciapurin et al. (2005).

The holographic grating is fully characterized by its thickness t , the refractive index of the bulk material n , the refractive index modulation amplitude δn , the grating period Λ , and the angle between the grating normal and the surface normal Φ . For the grating used in the experiment, these parameters have the values listed in table C.1.

The diffraction efficiency η of a holographic reflection grating is (Kogelnik, 1969, Ciapurin et al., 2005)

$$\eta(\xi, \nu) = \left(1 + \frac{1 - \xi^2/\nu^2}{\sinh^2(\sqrt{\nu^2 - \xi^2})} \right)^{-1}. \quad (\text{C.1})$$

In the case of negligible absorption in the bulk material, which is the case at hand, we have (Kogelnik, 1969)

$$\begin{aligned} \xi(\theta, \lambda) &= -\frac{t}{2} \cdot \frac{\vartheta(\theta, \lambda)}{c_S(\theta, \lambda)}, \\ \text{and } \nu(\theta, \lambda) &= \frac{\delta n \cdot t}{\lambda} \cdot \frac{i\pi}{\cos(\theta) \cdot c_S(\theta, \lambda)}, \end{aligned}$$

where θ is the angle between the incoming light beam and the surface normal, λ is the wavelength of the light,

$$\begin{aligned} c_S(\theta, \lambda) &= \cos(\theta) - \frac{\lambda}{\Lambda \cdot n} \cdot \cos(\Phi), \\ \text{and } \vartheta(\theta, \lambda) &= \frac{2\pi}{\Lambda} \cdot \cos(\Phi - \theta) - \pi \cdot \frac{\lambda}{\Lambda \cdot n}. \end{aligned}$$

We now adopt the following shorthand notation for (C.1):

$$\eta(\theta, \lambda) = \eta(\xi(\theta, \lambda), \nu(\theta, \lambda)).$$

t	$8 \pm 1 \text{ mm}$
n	1.486
δn	75 ppm
Λ	287.2 nm
Φ	$2.6 \pm 0.5^\circ$

Table C.1: Parameters for OptiGrate RBG-852-99

To find the Bragg angle θ_B – i. e. the angle for which the Bragg condition is fulfilled exactly – for our wavelength of interest $\lambda_0 = 852.34$ nm, we evaluate $\eta(\theta, \lambda_0)$ around $\theta = 0$. We find that η takes on its maximum at $\tilde{\theta} = -.449^\circ$, therefore $\theta_B = \Phi - \tilde{\theta} = 3.049^\circ$.

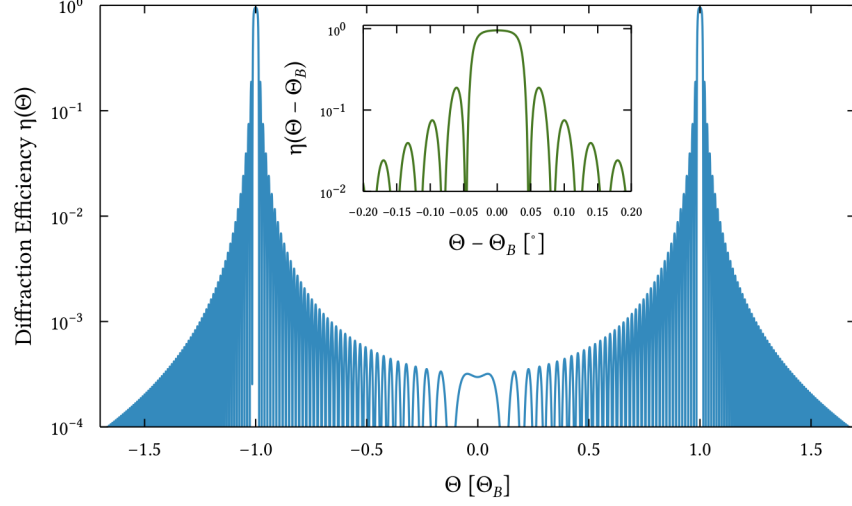


Figure C.1: Calculated $\eta(\theta, \lambda_0)$ for a VBG with the properties summarized in table C.1.

A full plot of the angular dependence of η at λ_0 is shown in figure C.1. As one would expect, we find two maxima. The full width at half maximum is $\theta_{\text{FWHM}} = 0.08^\circ$.

The knowledge of θ_B allows us to determine the spectral dependance of the diffraction efficiency around its maximum, which is presented in figure 10.8 in the main text along with experimental data that verifies our calculations. The full width at half maximum is $\lambda_{\text{FWHM}} = 0.06$ nm, i. e. $\nu_{\text{FWHM}} = 25$ GHz.

We note that our results are in good agreement with the calculations and measurements presented in Kyung (2010), which have previously been carried out with identical gratings.

In both the experiments and preliminary measurements we utilize external cavity diode lasers (ECDLs) that have been constructed at NBI based on a design by Ricci et al. (1995). In this appendix we briefly describe their design and provide reference for the techniques used for frequency stabilization and locking.

D.1 DESIGN

The basic layout of our ECDLs is sketched in Ricci et al. (1995), Petrov (2006): Mounted on a copper baseplate are both a diode mount and a grating holder made from the same material. While the diode is clamped fixed, the grating glued onto the holder can be moved coarsely by turning the screw, and finely with a small low-voltage Piezo crystal.

The grating is positioned in the so-called Littrow configuration, where the cavity is formed by the first diffraction order. Compared to the Littman-Metcalf configuration, where instead a mirror is used to steer the first diffraction order back into the laser diode, the Littrow configuration yields more optical power at the expense of beam steering.

Ricci et al. (1995) In all ECDLs used for the work described in this thesis, standard laser diodes with typically 100 to 150 mW optical output power were used. When free running, these diodes emit predominantly at an inherent, temperature dependent “native” frequency and exhibit a several nanometer broad pedestal.

To be able to tune the laser diode emission frequency, the laser baseplate is mounted on top of a Peltier element. A temperature sensor attached to the diode mount is used as the main reference for temperature stabilization, optionally a second sensor can be glued to the baseplate. Thermal stability is also important to keep the cavity length constant. In general, the temperature is chosen to lie well above room temperature, so as to provide a sufficient difference to the room temperature bath. For free running, i. e. not frequency locked lasers, a temperature lock point close to room temperature is favorable, which comes at the expense of slower stabilization, but yields better stability in the long run.

The laser frequency is determined by the 0th order mode of the cavity, which selects a narrow gain window in frequency space. If the emission of the diode at a given temperature is sufficient, it can be driven above the lasing threshold. In practice, the procedure is as follows:

1. At a current around the threshold (typically around 30 mA), the diode emission is overlapped with the Xth order of the grating at the laser output. Once this is the case, a “flash” occurs when lasing sets in.

2. A spectroscopy cell is placed at the laser output and the current set well above the threshold. While scanning the piezo crystal over its full range at a few Hertz, the emission from the spectroscopy cell is monitored. By turning the coarse screw, changing the current and changing the temperature, the laser is tuned until a strong emission from the cell is observed, i. e. the laser is scanning over an atomic transition. If a saturation spectroscopy is available, one can check immediately that it is indeed the correct transition. However, it is usually possible to tune a properly injected laser to the other hyperfine transition by changing the temperature and current.
3. To ensure optimal injection, a sine shaped current with a frequency of a few Hertz is applied to the DC modulation input of the laser current controller. A photodetector is placed at the output of the laser, and the laser current is set such that the modulation drives the laser across the threshold point. This is clearly visible as a “kink” in the intensity recorded by the photodetector when the emission goes from linear to exponential. Then, the threshold is pushed to lower currents by changing the baseplate alignment.
4. If necessary, the previous two steps are repeated iteratively.

D.2 FREQUENCY STABILIZATION

To address the various transitions in atoms, it is necessary to actively stabilize – lock – the lasers to precise frequencies. In general, the temperature of each laser is controlled through an independent feedback loop, and the frequency is stabilized with a **PI** control, addressing both the piezo (slow) and – via a **FET** – the diode current (fast). Since the latter can only “pull down” the current, it is advantageous to slightly increase the diode current setpoint after locking.

We use three different methods to generate the error signals: Absorption saturation spectroscopy (Foot, 2005, e. g.), Doppler-free saturation polarization spectroscopy (Wieman and Hänsch, 1976, Béguin, 2015), and – to lock a laser to a frequency reference provided by another – phase-lock loops (**PLLs**) (Appel et al., 2009, Oblak, 2010).

D.3 TEST SETUP

The setup we used for various test experiments consists of three, for all practical matters identical **ECDLs**, which we will refer to by the codenames Blue, Purple and Orange. A schematic of the complete setup can be found in (Oblak, 2010, Christensen, 2014).

Blue is locked to the $|F = 3\rangle \rightarrow |F' = 3 \times 2\rangle$ transition via absorption saturation spectroscopy and serves as the frequency normal. Purple is locked to Blue via beatnote locking and covers the frequency range of the $|F = 3\rangle \rightarrow |F' = ?\rangle$ transitions, while Orange is locked to Purple and can address the

$|F = 4\rangle \rightarrow |F' = ?\rangle$ transitions. One can therefore easily choose an arbitrary frequency difference between Purple and Orange. In order to be able to tune and ensure single mode operation of the two lasers, they can be monitored through both absorption saturation spectroscopy and a cavity.

Orange and Purple are each fed through an acousto-optical modulator (AOM) and a waveplate, then the two beams are combined and coupled into a fiber. To filter out the pedestal of the diode (cf. D.1), Orange can be sent through a different path with an interference filter, a lockable filter cavity similar to the one described in section 10.1 ($l = 8$ mm, FSR ≈ 17 GHz) and an additional AOM.

In addition, it is also possible to add a free-floating ECDL operating at 830 nm into the fiber.

It is customary at [QUANTOP](#) to design and implement the electronics used to control the experiments and to collect data in-house. Thus, during the setup of the experiments described in this thesis, several devices had to be adapted or re-designed.

We document this work by describing the device's functions, its application, and the relevant design decisions. In the case of the [SPCM](#) control circuit (sec. [E.1](#), where all steps beyond the basic circuit design were carried out by the author, we also document the circuit diagram, board layout, and code written for the device.

E.1 SPCM CONTROL CIRCUIT

To prevent the sensitive single photon counting modules ([SPCMs](#)) from permanent damage, we use a control circuit which monitors the count rate and accordingly controls both the gate and the power supply.

The previously used counter module was not only too slow to perform reliably for photons impinging in rapid succession, but in addition not suitable for the new [SPCM](#) used for the heralding photon detection (sec. [10.3](#)): On the one hand, the power supply was limited to 5 V (with 12 V required). On the other hand, the Laser Components COUNT-20C only guarantees a pulse length of 15 ns at 3 V, which is both too short and too low for commercially available counting modules. The idea to stretch and amplify the pulses prior to counting had to be discarded as the response time of such a circuit was well above the [SPCM](#) dead time (42 ns), i. e. it could not be guaranteed that all pulses were detected and counted.

As part of the work described in this thesis, we thus developed a completely new version of an [SPCM](#) control circuit which will be used for all [SPCMs](#) at [QUANTOP](#). While the circuit was designed by Jürgen Appel, all further steps towards implementation – namely the selection of suitable parts, routing of the board, coordination of the [PCB](#) fabrication, soldering, programming, and testing – were carried out by the author. Assistance by Henrik Bertelsen and Bent Neumann Jensen of the [NBI](#)'s electronics workshop is thankfully acknowledged.

FUNCTIONALITY AND APPLICATION Every [SPCM](#)'s avalanche photo diode ([APD](#)) has a maximum light intensity it can stand without damage. Commonly, this is given as a maximum count rate and lies in the region of a few 10 MHz. Although some [SPCMs](#) like the Laser Components COUNT-20C have a built-in [APD](#) current-limiter, external damage prevention is advisable. First and foremost, the control circuit thus has to ensure that the

SPCM is turned off before the damage threshold is reached. In addition, it should issue warnings at different count levels, control the gate of the SPCM, and relay all information to the computer running the experimental sequence. The circuit described here in addition can give audio feedback to assist with optical alignment.

DESIGN The circuit (fig. E.2) consists of two main components: A complex programmable logic device (CPLD) with a 100 MHz external clock used mainly for pulse counting, and a microcontroller to handle all remaining tasks.

The CPLD (CoolRunner XPLA3, Xilinx XCR3064XL-10VQG44I) is directly connected to the output of the SPCM, which it synchronously monitors with a time resolution of 10 ns (well below the maximum count rate 20 MHz). The counter itself is asynchronous and implemented in gray code, which ensures that the counter value read by the microcontroller is at most one photon off (lst. E.3). In addition to counting, the CPLD controls the gate of the SPCM. To this end, it asynchronously monitors both a TTL gate port controlled by the experiment and a TTL input from the microcontroller which indicates whether the SPCM's gate can safely be opened (lst. E.4). Alternatively, the circuit design allows for the CPLD itself to take over the threshold control and to then indicate towards the microcontroller whether the SPCM ought to be shut off.

The microcontroller (Atmel ATmega644P) is externally clocked at 20 MHz. In addition to the line used to communicate the status of the SPCM and the 8-bit counter bus, there are four communication channels between microcontroller and CPLD for future use (lst. E.1). In the implementation described here, the main task of the microcontroller is to frequently read out the counter, calculate the current count rate, and accordingly close the gate or turn off the power supply of the SPCM (lst. E.5). In the implementation presented here, every 10 μ s the following interrupt is executed:

1. If the gate is currently closed, open the gate.
2. Read out the CPLD counter ports and calculate how many pulses were detected since the last interrupt.
3. If the number of pulses exceeds the maximum (conservatively set to 20, i. e. $2 \text{ MHz} \ll 20 \text{ MHz}$), the SPCM's gate is closed and the warning level is increased by 2. If the number of pulses is below this threshold, the warning level is decreased by 1.
4. If the warning level exceeds 4, the power supply for the SPCM is shut off and the interrupt effectively disabled, i. e. sequence described here is not executed anymore. To reset the SPCM and microcontroller, a physical button has to be pushed by the experimenter. A reset via USB or a TTL signal is not possible by choice.

The current count rate and warning level are displayed on an LCD controlled by the microcontroller. In addition, an LED indicates whether the microcontroller has released the gate.

The power supply can be switched from 5 V supplied through the board to an external input, which allows the operation of the circuit with a wide variety of SPCMs. The switching itself is done by a high-power transistor, which is directly connected to the microcontroller. Both an LED and a TTL signal indicate the status of the power supply to the experimenter.

To issue acoustical warnings, the control circuit has a piezo buzzer. Since its frequency is tunable, it can be used to acoustically indicate the current count rate, which can be useful when aligning the SPCM. Furthermore, the control circuit has a USB port, which is handled by the microcontroller as a serial bus. This part has been copied from the NBI master laser controller designed by Jürgen Appel.

E.1.1 CPLD Code

The files are stored in the folder *Regular* in the SVN repository located at `kahuna:/data/svn/PhotonCounter`.

Listing E.1: *main.ucf*: Port definition for the CPLD.

```

1 NET "clk" TNM_NET = clk;
2 TIMESPEC TS_clk = PERIOD "clk" 10 ns HIGH 50%;
3
4 #PINLOCK_BEGIN
5
6 # COUNTING
7 NET "clk"          LOC = "S:PIN40";
8 NET "pd_in"       LOC = "S:PIN35";
9
10 NET "counter_out <0>" LOC = "S:PIN34";
11 NET "counter_out <1>" LOC = "S:PIN33";
12 NET "counter_out <2>" LOC = "S:PIN31";
13 NET "counter_out <3>" LOC = "S:PIN30";
14 NET "counter_out <4>" LOC = "S:PIN28";
15 NET "counter_out <5>" LOC = "S:PIN27";
16 NET "counter_out <6>" LOC = "S:PIN25";
17 NET "counter_out <7>" LOC = "S:PIN23";
18
19 # GATE CONTROL
20 NET "gate_in"      LOC = "S:PIN2";
21 NET "gate_out"    LOC = "S:PIN3";
22 NET "status_in"   LOC = "S:PIN44";
23
24 # COMMUNICATION PORTS (UNUSED)
25 #NET "com0"        LOC = "S:PIN22";
26 #NET "com1"        LOC = "S:PIN21";
27 #NET "com2"        LOC = "S:PIN20";
28 #NET "com3"        LOC = "S:PIN19";
29
30 #PINLOCK_END

```

Listing E.2: *main.vhd*: Main control.

```

1 library IEEE;
2 use IEEE.STD_LOGIC_1164.ALL;
3 use IEEE.NUMERIC_STD.ALL;
4
5 entity main is
6 port (
7   signal clk          : in std_logic;
8   signal pd_in       : in std_logic;
9   signal counter_out  : out std_logic_vector(7 downto 0) := (others => '0');
10  signal gate_in      : in std_logic;
11  signal gate_out     : out std_logic;
12  signal status_in    : in std_logic

```

```

13 );
14 end main;
15
16 architecture Behavioral of main is
17
18 component gate_control -- Simple AND-gate (asynchronous)
19     port (
20         gate_in  : in std_logic;
21         gate_out : out std_logic;
22         status_in : in std_logic
23     );
24     end component;
25
26 component sampling_gray_counter -- Gray Counter (sampling, synchronous)
27     port (
28         clk          : in std_logic;
29         pd_in       : in std_logic;
30         counter_out : out std_logic_vector(7 downto 0) := (others => '0')
31     );
32     end component;
33
34 begin
35
36 gate_controller : gate_control
37 port map (
38     gate_in => gate_in,
39     gate_out => gate_out,
40     status_in => status_in
41 );
42
43 gray_counter : sampling_gray_counter
44 port map (
45     clk => clk,
46     pd_in => pd_in,
47     counter_out => counter_out
48 );
49
50 end Behavioral;

```

Listing E.3: *sampling_gray_counter.vhd*: Synchronous gray counter. Based on <http://www.altera.com/support/examples/vhdl/vhdl-gray-counter.html>.

```

1 library IEEE;
2 use IEEE.STD_LOGIC_1164.ALL;
3
4 entity sampling_gray_counter is
5     port (
6         signal clk          : in std_logic;
7         signal pd_in       : in std_logic;
8         signal counter_out : out std_logic_vector(7 downto 0) := (others => '0');
9     );
10 end sampling_gray_counter;
11
12 architecture Behavioral of sampling_gray_counter is
13
14 -- we detect the photons by reading pd_input every clock cycle and
15 -- comparing the current with the previous value
16 signal previous_state : std_logic := '0';
17
18 -- 8-bit counter plus one control bit at counter(0)
19 signal counter : std_logic_vector(8 downto 0) := "00000001";
20
21 -- we need to know if there are 1s in lower bits (see explanation in detect_photon)
22 signal no_ones_below : std_logic_vector(7 downto 0) := (others => '1');
23
24 -- we need to know if the counter is overflowing
25 signal counter_monitor : std_logic;
26
27 begin
28
29 -- check whether one or both of the two highest bits are 1 (see explanation in detect_photon)
30 counter_monitor <= counter(7) or counter(8);
31 -- there is never a '1' below the lowest entry, triggers update
32 no_ones_below(0) <= '1';
33
34 detect_photon : process(clk) -- synchronous detection
35 begin
36     if (rising_edge(clk)) then
37         if ((pd_in = '1') and (previous_state = '0')) then
38             -- found a photon, increment counter
39             counter(0) <= not counter(0); -- toggle control bit
40             for i in 1 to 8 loop
41                 -- bit is 0 if
42                 -- a) currently 0 and lower part doesn't look like 1000...
43                 -- b) currently 1 and lower part does look like 1000...

```

```

43         -- bit is 1 if
44         -- c) currently 0 and lower part does look like 1000...
45         -- d) currently 1 and lower part doesn't look like 1000...
46         counter(i) <= counter(i) xor (counter(i-1) and no_ones_below(
47             i-1));
48     end loop;
49     -- the highest bit is 0 if
50     -- a) currently 0 and counter is not in 11000000
51     -- b) currently 1 and counter is in 11000000
52     -- the highest bit is 1 if
53     -- c) currently 0 and counter is in 11000000 (can't happen)
54     -- d) currently 1 and counter is not in 11000000
55     counter(8) <= counter(8) xor (counter_monitor and no_ones_below(7));
56
57     -- set the previous state to 1
58     previous_state <= '1';
59     elsif ((pd_in = '0') and (previous_state = '1')) then -- "arm" counter by
60         previous_state <= '0'; -- setting the previous state to 0
61     else
62         null;
63     end if;
64     counter_out <= counter(8 downto 1); -- output current counter value
65 else
66     null;
67 end if;
68 end process detect_photon;
69
70 counter_control : process(counter, no_ones_below)
71 begin
72     for j in 1 to 7 loop
73         no_ones_below(j) <= no_ones_below(j-1) and not counter(j-1);
74     end loop;
75 end process counter_control;
76
77 end Behavioral;

```

Listing E.4: *gate_control.vhd*: A simple (asynchronous) AND gate.

```

1  library IEEE;
2  use IEEE.STD_LOGIC_1164.ALL;
3
4  entity gate_control is
5      port (
6          signal gate_in      : in std_logic;
7          signal gate_out     : out std_logic;
8          signal status_in    : in std_logic);
9  end gate_control;
10
11 architecture Behavioral of gate_control is
12
13 begin
14
15 gate_control: process(gate_in, status_in)
16 begin
17     if (gate_in = '1' and status_in = '1') then
18         gate_out <= '1';
19     else
20         gate_out <= '0';
21     end if;
22 end process gate_control;
23
24 end Behavioral;

```

E.1.2 Microcontroller Code

The files are stored in the folder `PhotonCounter_Failsafe_2015` in the [SVN](#) repository located at `kahuna : /data/svn/avr/`.

Listing E.5: *Photoncounter_Failsafe.c*:

```

1  /*
2  Title :   SPCM Controller (PhotonCounter Failsafe 2015)
3  Author:   J rgen Appel <jappel@nbi.dk>, Kilian Kluge <kkluge@nbi.dk>
4  File:
5  Software: AVR-GCC
6  Target:   atmega644P
7  */
8

```

```

9 #include <string.h>           // for string functions
10 #include <avr/io.h>          // for the PORTs and PINs
11 #include <avr/interrupt.h>   // for interrupts
12 #include <avr/eeprom.h>      // to store the led period
13 #include <util/delay.h>      // for __delay_ms
14 #include <util/atomic.h>     // for interrupts
15
16 #include <stdlib.h>
17
18 #include "uart.h"
19 #include "lcd.h"
20
21 /* CONFIGURATION */
22 const uint8_t max_counts = 100; // maximum counts per 10us, 100 = 10 MHz (max. 20 MHz)
23 const char* const spcm_idn = "Box SPCM"; // Unique name of the watched SPCM
24
25 /* END CONFIGURATION */
26
27 /* Global Variables */
28
29 #define MAX_COMMANDLENGTH 40
30 volatile char newcommand;      // flag that announces reception of a command via USB
31 char command[MAX_COMMANDLENGTH]; // pointer to buffer that holds the received text */
32
33 volatile uint8_t warning_level; // warning level */
34 volatile uint8_t power_status;  // is the SPCM powered? */
35 volatile uint8_t acoustic_feedback; // acoustic feedback */
36 volatile uint8_t counting;      // Are we counting? */
37
38 volatile uint32_t counts;
39
40 // This is a B minor scale, from B4 to B6, with half-periods in us
41 const uint16_t tone[16] = { 1000, 900, 850, 750, 700, 650, 550, 500, 451, 425, 379, 338, 319,
42 284, 253, 402 };
43 /* 0 = B4, 7 = B5, 14 = B6 */
44
45 /*
46 .....
47 Serial Stuff
48 .....
49 */
50
51 void receive_commands(void) {
52     newcommand=0;
53     uart_cts_on();
54 };
55
56 void init_serial(void) { /* initializes the serial communication port */
57     uart_init();
58     receive_commands();
59 };
60
61 ISR(USART0_RX_vect){ /* Interrupt routine: is called whenever a character is received*/
62     char ch;
63     static char local_command[MAX_COMMANDLENGTH];
64     static uint8_t length=0;
65
66     ch=UDR0;
67     if (ch == '\r') return; /* ignore carriage returns */
68
69     if (ch == '\b') { /* backspace */
70         if (length>0) length--;
71         return;
72     }
73
74     if (ch == '\n') { /* new line means: command complete */
75         if (length==0) return;
76
77         local_command[length]='\0';
78         strncpy(command, local_command, sizeof(command));
79         length=0;
80         newcommand=1;
81         uart_cts_off(); /* Don't receive now */
82         return;
83     }
84
85     if (length<MAX_COMMANDLENGTH-1) {
86         local_command[length++] = ch;
87     }
88 };
89
90 /*
91 .....
92 */

```

```

89 /*          AUXILIARY FUNCTIONS JUST FOR HUMANS
90          */
91          */
92 void open_gate(void) { // to avoid conflicting instructions, this is only called by the 10us
interrupt
93     PORTB |= (1 << PB4); // GATE
94     PORTB |= (1 << PB1); // LED
95 };
96
97 void close_gate(void) { // this can be called everywhere, but is only permanent if "counting"
is set to 0
98     PORTB &= ~(1 << PB4); // GATE
99     PORTB &= ~(1 << PB1); // LED
100 };
101
102 void power_on(void) { // this is called once when starting up, and then only by the reset
command/interrupt
103     PORTB &= ~(1 << PB2); // not PD_ENABLE
104     PORTB &= ~(1 << PB0); // ERROR LED/BNC
105     power_status = 1;
106 };
107
108 void power_off(void) { // this can be called everywhere, and is permanent until the
controller is reset
109     PORTB |= (1 << PB2); // not PD_ENABLE
110     PORTB |= (1 << PB0); // ERROR LED/BNC
111     close_gate();
112     counting = 0;
113     power_status = 0;
114     warning_level = 0; // We're safe now, plus it helps to avoid confusion in display
routines
115 };
116
117
118 /*
119          */
120          */
121          */
122          */
123          */
124          */
125          */
126          */
127          */
128          */
129          */
130          */
131          */
132          */
133          */
134          */
135          */
136          */
137          */
138          */
139          */
140          */
141          */
142          */
143          */
144          */
145          */
146          */
147          */
148          */
149          */
150          */
151          */
152          */
153          */
154          */
155          */
156          */
157          */
158          */
159          */
160          */
161          */
162          */
163          */
164          */
165          */
166          */
167          */
168          */
169          */
170          */
171          */
172          */
173          */
174          */
175          */
176          */
177          */
178          */
179          */
180          */
181          */
182          */
183          */
184          */
185          */
186          */
187          */
188          */
189          */
190          */
191          */
192          */
193          */
194          */
195          */
196          */
197          */
198          */
199          */
200          */
201          */
202          */
203          */
204          */
205          */
206          */
207          */
208          */
209          */
210          */
211          */
212          */
213          */
214          */
215          */
216          */
217          */
218          */
219          */
220          */
221          */
222          */
223          */
224          */
225          */
226          */
227          */
228          */
229          */
230          */
231          */
232          */
233          */
234          */
235          */
236          */
237          */
238          */
239          */
240          */
241          */
242          */
243          */
244          */
245          */
246          */
247          */
248          */
249          */
250          */
251          */
252          */
253          */
254          */
255          */
256          */
257          */
258          */
259          */
260          */
261          */
262          */
263          */
264          */
265          */
266          */
267          */
268          */
269          */
270          */
271          */
272          */
273          */
274          */
275          */
276          */
277          */
278          */
279          */
280          */
281          */
282          */
283          */
284          */
285          */
286          */
287          */
288          */
289          */
290          */
291          */
292          */
293          */
294          */
295          */
296          */
297          */
298          */
299          */
300          */
301          */
302          */
303          */
304          */
305          */
306          */
307          */
308          */
309          */
310          */
311          */
312          */
313          */
314          */
315          */
316          */
317          */
318          */
319          */
320          */
321          */
322          */
323          */
324          */
325          */
326          */
327          */
328          */
329          */
330          */
331          */
332          */
333          */
334          */
335          */
336          */
337          */
338          */
339          */
340          */
341          */
342          */
343          */
344          */
345          */
346          */
347          */
348          */
349          */
350          */
351          */
352          */
353          */
354          */
355          */
356          */
357          */
358          */
359          */
360          */
361          */
362          */
363          */
364          */
365          */
366          */
367          */
368          */
369          */
370          */
371          */
372          */
373          */
374          */
375          */
376          */
377          */
378          */
379          */
380          */
381          */
382          */
383          */
384          */
385          */
386          */
387          */
388          */
389          */
390          */
391          */
392          */
393          */
394          */
395          */
396          */
397          */
398          */
399          */
400          */
401          */
402          */
403          */
404          */
405          */
406          */
407          */
408          */
409          */
410          */
411          */
412          */
413          */
414          */
415          */
416          */
417          */
418          */
419          */
420          */
421          */
422          */
423          */
424          */
425          */
426          */
427          */
428          */
429          */
430          */
431          */
432          */
433          */
434          */
435          */
436          */
437          */
438          */
439          */
440          */
441          */
442          */
443          */
444          */
445          */
446          */
447          */
448          */
449          */
450          */
451          */
452          */
453          */
454          */
455          */
456          */
457          */
458          */
459          */
460          */
461          */
462          */
463          */
464          */
465          */
466          */
467          */
468          */
469          */
470          */
471          */
472          */
473          */
474          */
475          */
476          */
477          */
478          */
479          */
480          */
481          */
482          */
483          */
484          */
485          */
486          */
487          */
488          */
489          */
490          */
491          */
492          */
493          */
494          */
495          */
496          */
497          */
498          */
499          */
500          */
501          */
502          */
503          */
504          */
505          */
506          */
507          */
508          */
509          */
510          */
511          */
512          */
513          */
514          */
515          */
516          */
517          */
518          */
519          */
520          */
521          */
522          */
523          */
524          */
525          */
526          */
527          */
528          */
529          */
530          */
531          */
532          */
533          */
534          */
535          */
536          */
537          */
538          */
539          */
540          */
541          */
542          */
543          */
544          */
545          */
546          */
547          */
548          */
549          */
550          */
551          */
552          */
553          */
554          */
555          */
556          */
557          */
558          */
559          */
560          */
561          */
562          */
563          */
564          */
565          */
566          */
567          */
568          */
569          */
570          */
571          */
572          */
573          */
574          */
575          */
576          */
577          */
578          */
579          */
580          */
581          */
582          */
583          */
584          */
585          */
586          */
587          */
588          */
589          */
590          */
591          */
592          */
593          */
594          */
595          */
596          */
597          */
598          */
599          */
600          */
601          */
602          */
603          */
604          */
605          */
606          */
607          */
608          */
609          */
610          */
611          */
612          */
613          */
614          */
615          */
616          */
617          */
618          */
619          */
620          */
621          */
622          */
623          */
624          */
625          */
626          */
627          */
628          */
629          */
630          */
631          */
632          */
633          */
634          */
635          */
636          */
637          */
638          */
639          */
640          */
641          */
642          */
643          */
644          */
645          */
646          */
647          */
648          */
649          */
650          */
651          */
652          */
653          */
654          */
655          */
656          */
657          */
658          */
659          */
660          */
661          */
662          */
663          */
664          */
665          */
666          */
667          */
668          */
669          */
670          */
671          */
672          */
673          */
674          */
675          */
676          */
677          */
678          */
679          */
680          */
681          */
682          */
683          */
684          */
685          */
686          */
687          */
688          */
689          */
690          */
691          */
692          */
693          */
694          */
695          */
696          */
697          */
698          */
699          */
700          */
701          */
702          */
703          */
704          */
705          */
706          */
707          */
708          */
709          */
710          */
711          */
712          */
713          */
714          */
715          */
716          */
717          */
718          */
719          */
720          */
721          */
722          */
723          */
724          */
725          */
726          */
727          */
728          */
729          */
730          */
731          */
732          */
733          */
734          */
735          */
736          */
737          */
738          */
739          */
740          */
741          */
742          */
743          */
744          */
745          */
746          */
747          */
748          */
749          */
750          */
751          */
752          */
753          */
754          */
755          */
756          */
757          */
758          */
759          */
760          */
761          */
762          */
763          */
764          */
765          */
766          */
767          */
768          */
769          */
770          */
771          */
772          */
773          */
774          */
775          */
776          */
777          */
778          */
779          */
780          */
781          */
782          */
783          */
784          */
785          */
786          */
787          */
788          */
789          */
790          */
791          */
792          */
793          */
794          */
795          */
796          */
797          */
798          */
799          */
800          */
801          */
802          */
803          */
804          */
805          */
806          */
807          */
808          */
809          */
810          */
811          */
812          */
813          */
814          */
815          */
816          */
817          */
818          */
819          */
820          */
821          */
822          */
823          */
824          */
825          */
826          */
827          */
828          */
829          */
830          */
831          */
832          */
833          */
834          */
835          */
836          */
837          */
838          */
839          */
840          */
841          */
842          */
843          */
844          */
845          */
846          */
847          */
848          */
849          */
850          */
851          */
852          */
853          */
854          */
855          */
856          */
857          */
858          */
859          */
860          */
861          */
862          */
863          */
864          */
865          */
866          */
867          */
868          */
869          */
870          */
871          */
872          */
873          */
874          */
875          */
876          */
877          */
878          */
879          */
880          */
881          */
882          */
883          */
884          */
885          */
886          */
887          */
888          */
889          */
890          */
891          */
892          */
893          */
894          */
895          */
896          */
897          */
898          */
899          */
900          */
901          */
902          */
903          */
904          */
905          */
906          */
907          */
908          */
909          */
910          */
911          */
912          */
913          */
914          */
915          */
916          */
917          */
918          */
919          */
920          */
921          */
922          */
923          */
924          */
925          */
926          */
927          */
928          */
929          */
930          */
931          */
932          */
933          */
934          */
935          */
936          */
937          */
938          */
939          */
940          */
941          */
942          */
943          */
944          */
945          */
946          */
947          */
948          */
949          */
950          */
951          */
952          */
953          */
954          */
955          */
956          */
957          */
958          */
959          */
960          */
961          */
962          */
963          */
964          */
965          */
966          */
967          */
968          */
969          */
970          */
971          */
972          */
973          */
974          */
975          */
976          */
977          */
978          */
979          */
980          */
981          */
982          */
983          */
984          */
985          */
986          */
987          */
988          */
989          */
990          */
991          */
992          */
993          */
994          */
995          */
996          */
997          */
998          */
999          */
1000          */

```

```

165     /* TESTING GOES HERE */
166     //PORTB ^= _BV(PB4); /* toggle Gate */
167     //PORTB ^= _BV(PB0); /* toggle Error LED */
168 }
169 else {
170     close_gate(); // make sure that gate is closed
171 };
172 };
173 };
174
175 void init_10us_interrupt(void) { /* programs interrupt to be called every 10 s */
176     TCCR0A = _BV(WGM01); /* Timer0 in Mode CTC */
177     TCCR0B = _BV(CS00); /* Timer0: Clock=no prescaler */
178     OCR0A = 200-1; /* Make an Interrupt every 200 clock cycles */
179     TIMSK0 = _BV(OCIE0A); /* Enable interrupts on match with OCR0A */
180
181     warning_level = 0;
182     counts = 0;
183 };
184
185
186 /*
187 .....
188 .....
189 .....
190 .....
191 .....
192 .....
193 .....
194 .....
195 .....
196 .....
197 .....
198 .....
199 .....
200 .....
201 .....
202 .....
203 .....
204 .....
205 .....
206 .....
207 .....
208 .....
209 .....
210 .....
211 .....
212 .....
213 .....
214 .....
215 .....
216 .....
217 .....
218 .....
219 .....
220 .....
221 .....
222 .....
223 .....
224 .....
225 .....
226 .....
227 .....
228 .....
229 .....
230 .....
231 .....
232 .....
233 .....
234 .....
235 .....
236 .....
237 .....
238 .....
239 .....
240 .....
241 .....
242 .....
243 .....
244 .....
245 .....
246 .....
247 .....
248 .....
249 .....
250 .....
251 .....
252 .....
253 .....
254 .....
255 .....
256 .....
257 .....
258 .....
259 .....
260 .....
261 .....
262 .....
263 .....
264 .....
265 .....
266 .....
267 .....
268 .....
269 .....
270 .....
271 .....
272 .....
273 .....
274 .....
275 .....
276 .....
277 .....
278 .....
279 .....
280 .....
281 .....
282 .....
283 .....
284 .....
285 .....
286 .....
287 .....
288 .....
289 .....
290 .....
291 .....
292 .....
293 .....
294 .....
295 .....
296 .....
297 .....
298 .....
299 .....
300 .....
301 .....
302 .....
303 .....
304 .....
305 .....
306 .....
307 .....
308 .....
309 .....
310 .....
311 .....
312 .....
313 .....
314 .....
315 .....
316 .....
317 .....
318 .....
319 .....
320 .....
321 .....
322 .....
323 .....
324 .....
325 .....
326 .....
327 .....
328 .....
329 .....
330 .....
331 .....
332 .....
333 .....
334 .....
335 .....
336 .....
337 .....
338 .....
339 .....
340 .....
341 .....
342 .....
343 .....
344 .....
345 .....
346 .....
347 .....
348 .....
349 .....
350 .....
351 .....
352 .....
353 .....
354 .....
355 .....
356 .....
357 .....
358 .....
359 .....
360 .....
361 .....
362 .....
363 .....
364 .....
365 .....
366 .....
367 .....
368 .....
369 .....
370 .....
371 .....
372 .....
373 .....
374 .....
375 .....
376 .....
377 .....
378 .....
379 .....
380 .....
381 .....
382 .....
383 .....
384 .....
385 .....
386 .....
387 .....
388 .....
389 .....
390 .....
391 .....
392 .....
393 .....
394 .....
395 .....
396 .....
397 .....
398 .....
399 .....
400 .....
401 .....
402 .....
403 .....
404 .....
405 .....
406 .....
407 .....
408 .....
409 .....
410 .....
411 .....
412 .....
413 .....
414 .....
415 .....
416 .....
417 .....
418 .....
419 .....
420 .....
421 .....
422 .....
423 .....
424 .....
425 .....
426 .....
427 .....
428 .....
429 .....
430 .....
431 .....
432 .....
433 .....
434 .....
435 .....
436 .....
437 .....
438 .....
439 .....
440 .....
441 .....
442 .....
443 .....
444 .....
445 .....
446 .....
447 .....
448 .....
449 .....
450 .....
451 .....
452 .....
453 .....
454 .....
455 .....
456 .....
457 .....
458 .....
459 .....
460 .....
461 .....
462 .....
463 .....
464 .....
465 .....
466 .....
467 .....
468 .....
469 .....
470 .....
471 .....
472 .....
473 .....
474 .....
475 .....
476 .....
477 .....
478 .....
479 .....
480 .....
481 .....
482 .....
483 .....
484 .....
485 .....
486 .....
487 .....
488 .....
489 .....
490 .....
491 .....
492 .....
493 .....
494 .....
495 .....
496 .....
497 .....
498 .....
499 .....
500 .....
501 .....
502 .....
503 .....
504 .....
505 .....
506 .....
507 .....
508 .....
509 .....
510 .....
511 .....
512 .....
513 .....
514 .....
515 .....
516 .....
517 .....
518 .....
519 .....
520 .....
521 .....
522 .....
523 .....
524 .....
525 .....
526 .....
527 .....
528 .....
529 .....
530 .....
531 .....
532 .....
533 .....
534 .....
535 .....
536 .....
537 .....
538 .....
539 .....
540 .....
541 .....
542 .....
543 .....
544 .....
545 .....
546 .....
547 .....
548 .....
549 .....
550 .....
551 .....
552 .....
553 .....
554 .....
555 .....
556 .....
557 .....
558 .....
559 .....
560 .....
561 .....
562 .....
563 .....
564 .....
565 .....
566 .....
567 .....
568 .....
569 .....
570 .....
571 .....
572 .....
573 .....
574 .....
575 .....
576 .....
577 .....
578 .....
579 .....
580 .....
581 .....
582 .....
583 .....
584 .....
585 .....
586 .....
587 .....
588 .....
589 .....
590 .....
591 .....
592 .....
593 .....
594 .....
595 .....
596 .....
597 .....
598 .....
599 .....
600 .....
601 .....
602 .....
603 .....
604 .....
605 .....
606 .....
607 .....
608 .....
609 .....
610 .....
611 .....
612 .....
613 .....
614 .....
615 .....
616 .....
617 .....
618 .....
619 .....
620 .....
621 .....
622 .....
623 .....
624 .....
625 .....
626 .....
627 .....
628 .....
629 .....
630 .....
631 .....
632 .....
633 .....
634 .....
635 .....
636 .....
637 .....
638 .....
639 .....
640 .....
641 .....
642 .....
643 .....
644 .....
645 .....
646 .....
647 .....
648 .....
649 .....
650 .....
651 .....
652 .....
653 .....
654 .....
655 .....
656 .....
657 .....
658 .....
659 .....
660 .....
661 .....
662 .....
663 .....
664 .....
665 .....
666 .....
667 .....
668 .....
669 .....
670 .....
671 .....
672 .....
673 .....
674 .....
675 .....
676 .....
677 .....
678 .....
679 .....
680 .....
681 .....
682 .....
683 .....
684 .....
685 .....
686 .....
687 .....
688 .....
689 .....
690 .....
691 .....
692 .....
693 .....
694 .....
695 .....
696 .....
697 .....
698 .....
699 .....
700 .....
701 .....
702 .....
703 .....
704 .....
705 .....
706 .....
707 .....
708 .....
709 .....
710 .....
711 .....
712 .....
713 .....
714 .....
715 .....
716 .....
717 .....
718 .....
719 .....
720 .....
721 .....
722 .....
723 .....
724 .....
725 .....
726 .....
727 .....
728 .....
729 .....
730 .....
731 .....
732 .....
733 .....
734 .....
735 .....
736 .....
737 .....
738 .....
739 .....
740 .....
741 .....
742 .....
743 .....
744 .....
745 .....
746 .....
747 .....
748 .....
749 .....
750 .....
751 .....
752 .....
753 .....
754 .....
755 .....
756 .....
757 .....
758 .....
759 .....
760 .....
761 .....
762 .....
763 .....
764 .....
765 .....
766 .....
767 .....
768 .....
769 .....
770 .....
771 .....
772 .....
773 .....
774 .....
775 .....
776 .....
777 .....
778 .....
779 .....
780 .....
781 .....
782 .....
783 .....
784 .....
785 .....
786 .....
787 .....
788 .....
789 .....
790 .....
791 .....
792 .....
793 .....
794 .....
795 .....
796 .....
797 .....
798 .....
799 .....
800 .....
801 .....
802 .....
803 .....
804 .....
805 .....
806 .....
807 .....
808 .....
809 .....
810 .....
811 .....
812 .....
813 .....
814 .....
815 .....
816 .....
817 .....
818 .....
819 .....
820 .....
821 .....
822 .....
823 .....
824 .....
825 .....
826 .....
827 .....
828 .....
829 .....
830 .....
831 .....
832 .....
833 .....
834 .....
835 .....
836 .....
837 .....
838 .....
839 .....
840 .....
841 .....
842 .....
843 .....
844 .....
845 .....
846 .....
847 .....
848 .....
849 .....
850 .....
851 .....
852 .....
853 .....
854 .....
855 .....
856 .....
857 .....
858 .....
859 .....
860 .....
861 .....
862 .....
863 .....
864 .....
865 .....
866 .....
867 .....
868 .....
869 .....
870 .....
871 .....
872 .....
873 .....
874 .....
875 .....
876 .....
877 .....
878 .....
879 .....
880 .....
881 .....
882 .....
883 .....
884 .....
885 .....
886 .....
887 .....
888 .....
889 .....
890 .....
891 .....
892 .....
893 .....
894 .....
895 .....
896 .....
897 .....
898 .....
899 .....
900 .....
901 .....
902 .....
903 .....
904 .....
905 .....
906 .....
907 .....
908 .....
909 .....
910 .....
911 .....
912 .....
913 .....
914 .....
915 .....
916 .....
917 .....
918 .....
919 .....
920 .....
921 .....
922 .....
923 .....
924 .....
925 .....
926 .....
927 .....
928 .....
929 .....
930 .....
931 .....
932 .....
933 .....
934 .....
935 .....
936 .....
937 .....
938 .....
939 .....
940 .....
941 .....
942 .....
943 .....
944 .....
945 .....
946 .....
947 .....
948 .....
949 .....
950 .....
951 .....
952 .....
953 .....
954 .....
955 .....
956 .....
957 .....
958 .....
959 .....
960 .....
961 .....
962 .....
963 .....
964 .....
965 .....
966 .....
967 .....
968 .....
969 .....
970 .....
971 .....
972 .....
973 .....
974 .....
975 .....
976 .....
977 .....
978 .....
979 .....
980 .....
981 .....
982 .....
983 .....
984 .....
985 .....
986 .....
987 .....
988 .....
989 .....
990 .....
991 .....
992 .....
993 .....
994 .....
995 .....
996 .....
997 .....
998 .....
999 .....
1000 .....

```

```

246 /*
      .....
      */
247
248 void beep(uint16_t ms) {
249     PORTB |= _BV(PB3); /* beep */
250     for (uint16_t i=0; i<ms; i++) {
251         _delay_ms(1);
252     };
253     PORTB &= ~_BV(PB3); /* silence */
254 };
255
256 void newbeep(uint16_t ms, uint8_t tnum) { // Beeps with tone number tnum
257     uint16_t cycles = (1000*ms)/tone[tnum];
258     for (uint16_t i=0; i<cycles; i++) {
259         PORTB ^= _BV(PB3); // toggle buzzer
260         for (int j=0; j < tone[tnum]; j++) {
261             _delay_us(1); // delay has to be a constant
262         };
263     };
264     PORTB &= ~(1 << PB3); // ensure buzzer is off
265 };
266
267 /*
      .....
      */
268 /*          COMMANDS          */
269 /*
      .....
      */
270 //PGM_P cmd_idn(void) {
271 void cmd_idn(void) {
272     uart_sendstr_P("PhotonCounterControl 2015");
273     uart_crlf();
274     uart_sendstr_P("Proudly watching ");
275     uart_sendstr_P(spcm_idn);
276     uart_crlf();
277     //return 0;
278 };
279
280 //PGM_P cmd_stat(void) {
281 void cmd_stat(void) {
282     uart_sendstr_P("Power: ");
283     if (power_status == 1) {
284         uart_sendstr_P("ON");
285     }
286     else if (power_status == 0) {
287         uart_sendstr_P("OFF");
288     }
289     else {
290         uart_sendstr_P("ERROR");
291     };
292     uart_crlf();
293     uart_sendstr_P("Maximum Counts per 100s: ");
294     uart_sendlongint(max_counts);
295     uart_crlf();
296     uart_sendstr_P("Acoustic Feedback: ");
297     if (acoustic_feedback == 0) {
298         uart_sendstr_P("Quiet");
299     }
300     else if (acoustic_feedback == 1) {
301         uart_sendstr_P("Beep");
302     }
303     else if (acoustic_feedback == 2) {
304         uart_sendstr_P("Alignment");
305     }
306     else {
307         uart_sendstr_P("ERROR");
308     };
309     uart_crlf();
310     //return 0;
311 };
312
313 //PGM_P cmd_acf(const char* parameter) {
314 void cmd_acf(const char* parameter) {
315     if (strncasecmp_P(parameter, PSTR("BEEP"), 4) == 0) { // Beep for each detected photon
316         acoustic_feedback = 1;
317         uart_sendstr_P("Beep Mode");
318         uart_crlf();
319     }
320     else if (strncasecmp_P(parameter, PSTR("ALIGN"), 5) == 0) { // Frequency according to count
321         rate
322         acoustic_feedback = 2;
323         uart_sendstr_P("Alignment Mode");
324         uart_crlf();
325     }
326     else if (strncasecmp_P(parameter, PSTR("OFF"), 3) == 0) { // Quiet mode
327         acoustic_feedback = 0;
328         uart_sendstr_P("Quiet Mode");

```

```

328     uart_crlf();
329 }
330 else { // Unknown
331     uart_sendstr_P("Unknown. Use OFF, BEEP, or ALIGN.");
332     uart_crlf();
333 };
334 // return 0;
335 };
336
337 //PGM_P cmd_reset(void) {
338 void cmd_reset(void) {
339     uart_sendstr_P("Not Implemented. Use Switch.");
340     uart_crlf();
341     // return 0;
342 }
343
344 /*
345 .....
346 .....
347 .....
348 .....
349 .....
350 .....
351 .....
352 .....
353 .....
354 .....
355 .....
356 .....
357 .....
358 .....
359 .....
360 .....
361 .....
362 .....
363 .....
364 .....
365 .....
366 .....
367 .....
368 .....
369 .....
370 .....
371 .....
372 .....
373 .....
374 .....
375 .....
376 .....
377 .....
378 .....
379 .....
380 .....
381 .....
382 .....
383 .....
384 .....
385 .....
386 .....
387 .....
388 .....
389 .....
390 .....
391 .....
392 .....
393 .....
394 .....
395 .....
396 .....
397 .....
398 .....
399 .....
400 .....
401 .....
402 .....
403 .....
404 .....
405 .....
406 .....
407 .....
408 .....
409 .....
410 .....
411 .....
412 .....

```

```

347 int main(void) {
348     /* initialize LCD display */
349     init_lcd();
350     lcd_clrscr();
351     lcd_gotoxy(0,0);
352     lcd_puts_P("Photon Counter");
353     lcd_gotoxy(0,1);
354     lcd_puts_P("Control Circuit");
355     _delay_ms(1000);
356     lcd_clrscr();
357     lcd_gotoxy(0,0);
358     lcd_puts_P("(c) 2015");
359     lcd_gotoxy(0,1);
360     lcd_puts_P("jappel, kkluge");
361     /* initialize interrupts etc. */
362     init_10us_interrupt();
363     init_serial();
364     /* initialize variables */
365     uint8_t display_mode = 0;
366     // uint8_t * error;
367     uint32_t rate_counts = 0;
368     uint32_t count_rate = 0;
369     /* initialize ports */
370     DDRA = ( 0 << PA0) // in: graycounter0
371     | ( 0 << PA1) // in: graycounter1
372     | ( 0 << PA2) // in: graycounter2
373     | ( 0 << PA3) // in: graycounter3
374     | ( 0 << PA4) // in: graycounter4
375     | ( 0 << PA5) // in: graycounter5
376     | ( 0 << PA6) // in: graycounter6
377     | ( 0 << PA7); // in: graycounter7
378     DDRB = ( 1 << PB0) // out: Error LED/BNC
379     | ( 1 << PB1) // out: Gate LED
380     | ( 1 << PB2) // out: NOT "PD enable" (Power Control SPCM)
381     | ( 1 << PB3) // out: Buzzer
382     | ( 1 << PB4) // out: Gate
383     | ( 0 << PB5) // in: MOSI
384     | ( 0 << PB6) // in: MISO
385     | ( 0 << PB7); // in: SCK
386     DDRC |= ( 0 << PC3); // in: Reset Switch
387     DDRD |= ( 0 << PD2) // in: CPLD Communication Port 0
388     | ( 0 << PD3) // in: CPLD Communication Port 1
389     | ( 1 << PD4) // out: CPLD Communication Port 2
390     | ( 1 << PD5); // out: CPLD Communication Port 3
391     /* testing goes here */
392     /* prepare for main loop */
393     _delay_ms(1000);
394     display0();
395     lcd_backlight(0);
396     // signal startup
397     newbeep(750,7);

```

```

413 newbeep(25,8);
414 newbeep(25,15);
415 newbeep(500,7);
416
417 power_on();
418
419 sei(); // enable interrupts
420 counting = 1;
421
422 while (1) { /* Main loop, loop forever */
423     _delay_ms(10);
424
425     /* Display Messages */
426     /* There are 3 display modes: 0 is for regular operation, 1 for warnings, and 2 for power
         off */
427     if (warning_level > 0) {
428         if (display_mode == 0) { // If we just start warning, change display
429             lcd_backlight(1);
430             lcd_gotoxy(0,0);
431             lcd_puts_P("WARNING!");
432             display_mode = 1;
433         };
434         if (display_mode == 1) {
435             lcd_gotoxy(0,1);
436             lcd_puts( (const char*) warning_level);
437         };
438     } else {
439         if (display_mode == 1) { // We're back to normal after warning phase
440             display0();
441             display_mode = 0;
442             lcd_backlight(0);
443         };
444     };
445
446     if (display_mode == 0) { // We're in normal display operation
447         lcd_gotoxy(0,1);
448         lcd_print_number(4,4,counts);
449         count_rate = (counts-rate_counts)*100;
450         // lcd_print_number(4,4,count_rate);
451         // lcd_gotoxy(6,1);
452         // lcd_print_number(4,4,counts-rate_counts);
453     };
454
455     if (power_status == 0) { // Power Off
456         if (display_mode < 2) { // Just entering this mode
457             lcd_backlight(1);
458             lcd_clrscr();
459             lcd_gotoxy(0,0);
460             lcd_puts_P("POWER OFF!");
461             lcd_gotoxy(0,1);
462             lcd_puts_P("Reset to restart");
463             display_mode = 2;
464         }
465         else {
466             if (display_mode == 2) { // toggle LCD LED
467                 lcd_backlight(0); // show that uc is alive
468                 _delay_ms(250); // keep blinking rate low
469                 lcd_backlight(1);
470                 _delay_ms(240);
471             }
472             else { // Leaving this mode
473                 display0();
474                 display_mode = 0;
475                 lcd_backlight(0);
476             };
477         };
478     };
479
480     /* Acoustic Feedback */
481     if (acoustic_feedback == 1) { // BEEP mode
482         if (counts > rate_counts) {
483             beep(100); // simple version, only suitable for low limit
484         };
485     }
486     else if (acoustic_feedback == 2) { // ALIGN mode
487         beep(100); // NOT IMPLEMENTED YET
488     }
489     else { // quiet mode
490         PORTB |= (0 << PB3);
491     };
492
493     // Update Counts
494     rate_counts = counts;
495
496     /* Command Handling */
497
498     if (newcommand) {
499         counting = 0;
500         close_gate(); // assure that gate is closed while processing
501         cli(); // disable interrupts

```

```

502     lcd_backlight(1);
503
504     lcd_clrscr();
505     lcd_gotoxy(0,0);
506     lcd_puts_P("Handling Command:");
507     lcd_gotoxy(0,1);
508     lcd_puts(command);
509
510
511     if (strncasecmp_P(command, PSTR("IDN"), 4) == 0) { // identity
512         cmd_idn();
513     } else if (strncasecmp_P(command, PSTR("ACF"), 3) == 0) { // acoustic feedback
514         cmd_acf(command+3);
515     } else if (strncasecmp_P(command, PSTR("STAT"), 4) == 0) { // status
516         cmd_stat();
517     } else if (strncasecmp_P(command, PSTR("RESET"), 5) == 0) { // reset
518         cmd_reset();
519     } else {
520         uart_sendstr_P("ERROR: Unknown command:");
521         uart_sendstr(command);
522         uart_crlf();
523         uart_sendstr_P(" Available Commands: IDN, ACF, STAT, RESET");
524         uart_crlf();
525     };
526
527 /*
528     if (error) {
529         uart_sendstr_P("ERROR: ");
530         uart_sendlongint(error);
531         uart_crlf();
532     };*/
533
534     display0();
535     display_mode = 0;
536     lcd_backlight(0);
537
538     receive_commands();
539     counting = 1;
540
541     sei(); // enable interrupts
542 };
543 };

```

E.1.3 Board Layout and Circuit Diagram

The following pages contain the board layout and circuit diagram. The files are stored in kahuna: /data/eagle/Photon_Counter_Failsafe/.

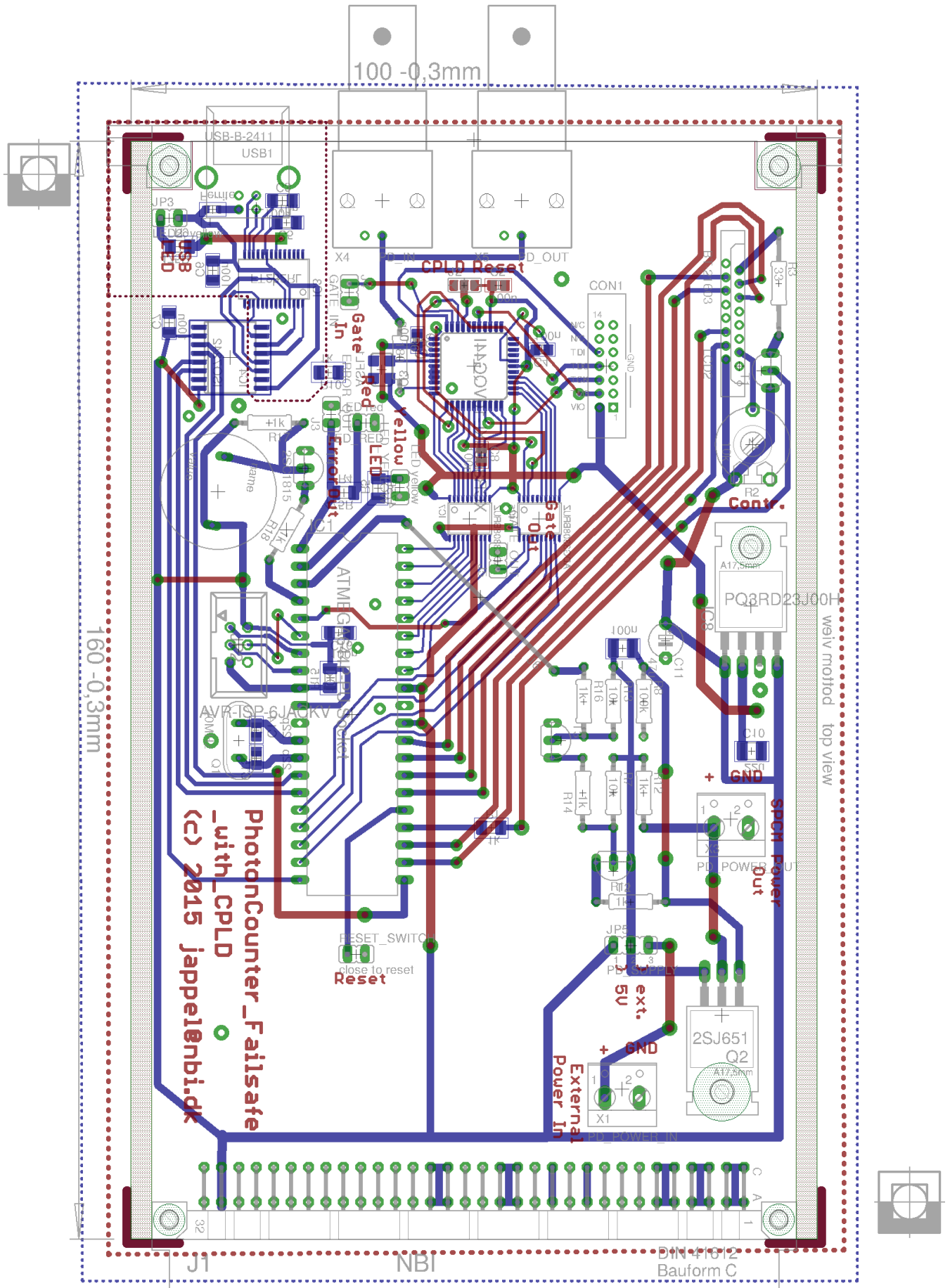


Figure E.1: Board layout of the SPCM Control Circuit.

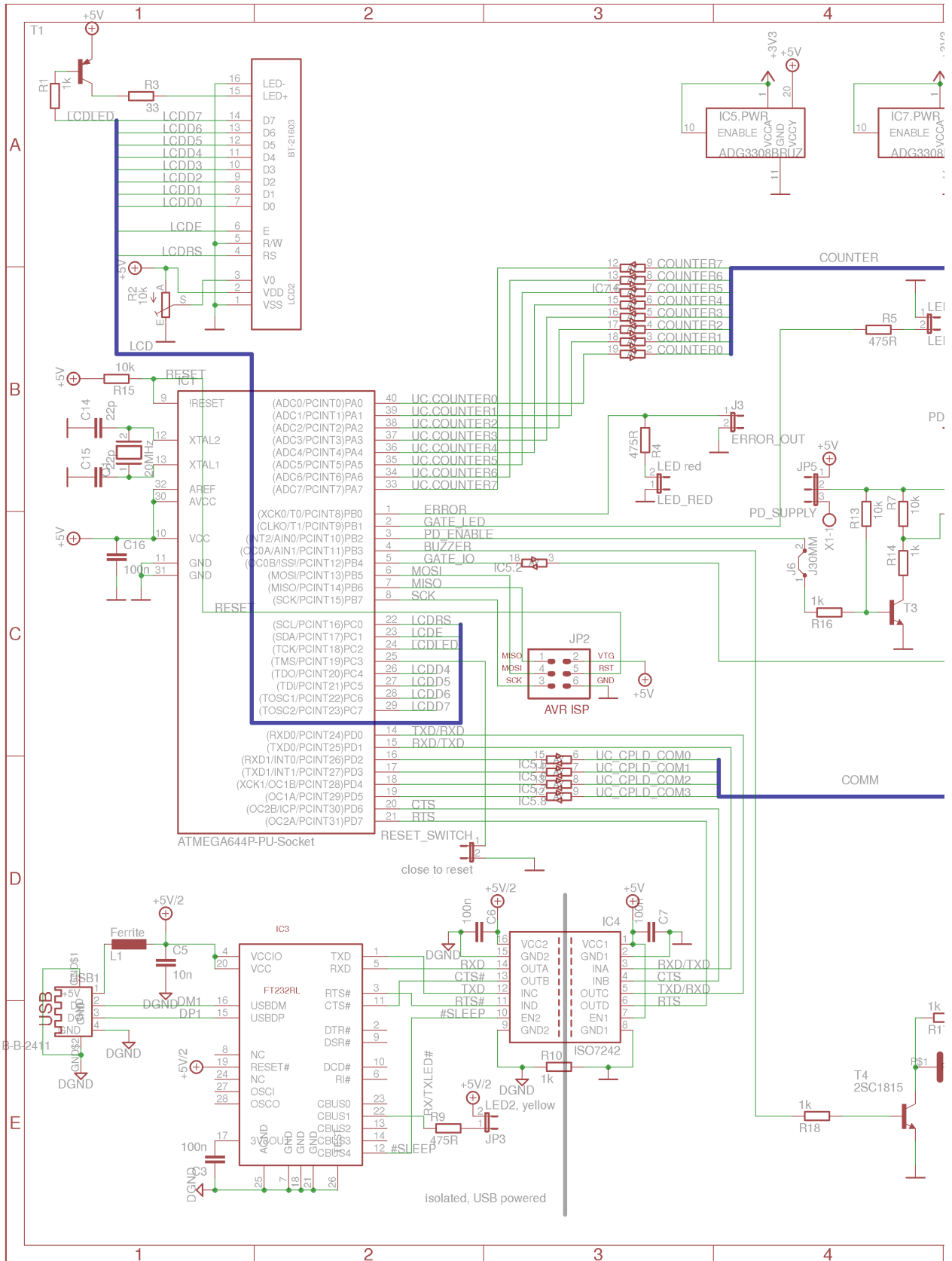
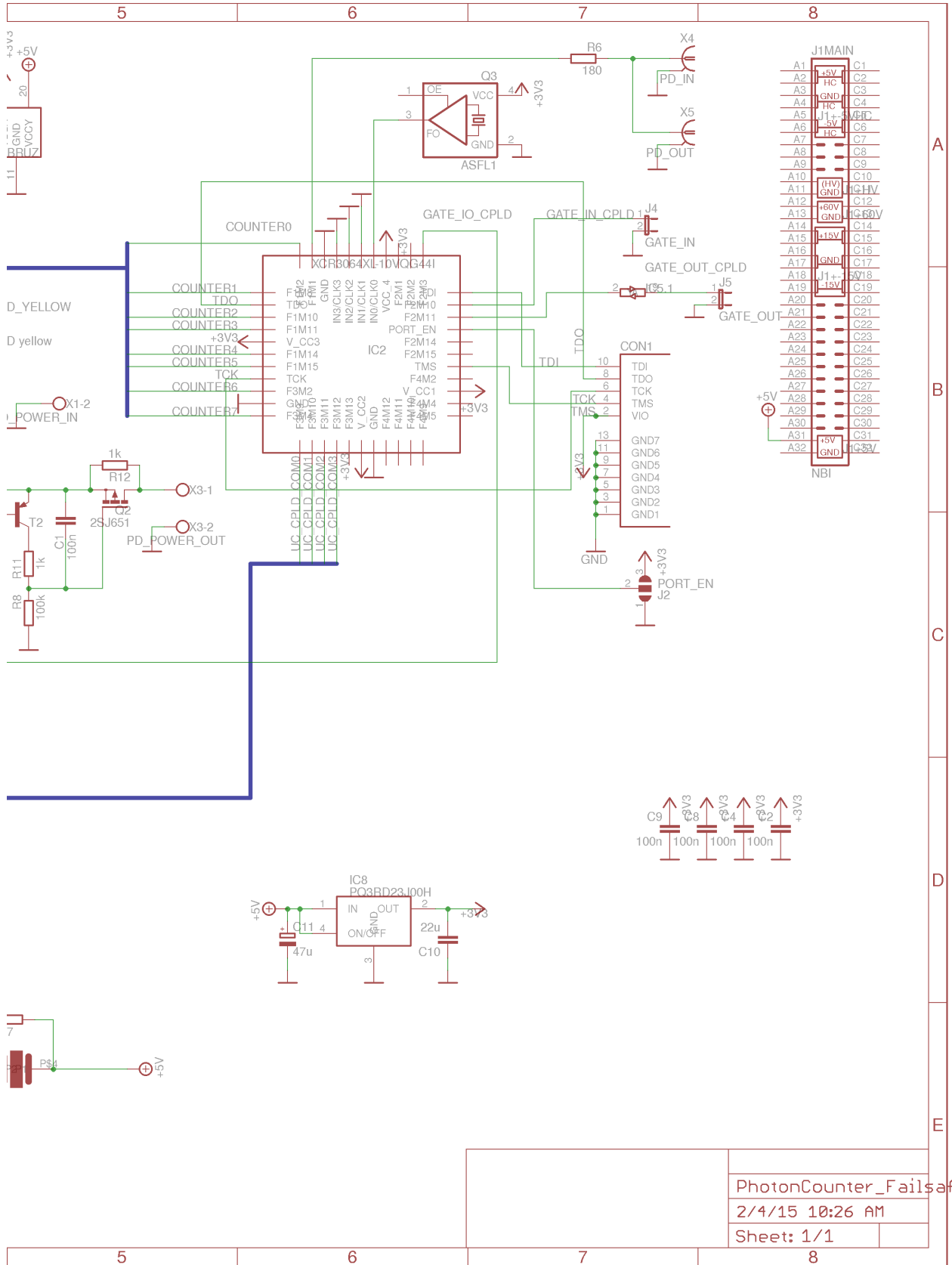


Figure E.2: Circuit diagram of the SPCM Control Circuit.



PhotonCounter_Failsaf
 2/4/15 10:26 AM
 Sheet: 1/1

E.2 LOCK CIRCUIT

The circuit used to lock both cavities and [ECDLs](#) is a versatile [PI](#) controller. In use at [QUANTOP](#) for many years in different hand-built incarnations, together with Michael Zugenmaier and Jürgen Appel, the circuit design was unified and prepared for external production. All locks described in this thesis utilize a similar circuit with some subset of the described features.

FUNCTIONALITY AND APPLICATION An error signal generated by a separate circuit (e. g. a dither-lock as is the case for the filter cavity described in section [10.1.3](#)) is fed into the lock circuit, which subsequently gives out a feedback signal.

DESIGN As this is a standard circuit in electronics, mostly consisting of a chain of operational amplifiers, we limit ourselves to a short description of the main features:

- *Lock freeze:* While this can also be accomplished by keeping the error signal constant, the input of the error signal into the integrator can be switched off via a [TTL](#) input.¹
- *Integrator reset:* The integrator (and thus the lock) can be turned off and thus reset by both a manual switch as well as a [TTL](#) input.
- *Lock offset:* Tunes the reference level for the error signal, which allows to adjust to different levels of error signals and to lock to offsets. Can be completely by setting a jumper.
- *Ramp generator:* The circuit provides a saw wave signal of variable amplitude and offset, which can both directly be accessed as well as added onto the feedback signal output. To aid lock monitoring, a trigger signal is generated as well.
- *Modulation input:* If necessary, a modulation signal can be added onto the output signal.
- *Integrator time constant:* The resistor and capacitor determining the time constant are mounted in a socket and can thus easily be changed.
- *Lock polarity:* To allow flexible application, the polarity of the lock can be changed by setting jumpers.

¹ Instructions by the author on how to calibrate the lock freeze can be found on the page `documentation:cavitylock` in the clock group's wiki.

BIBLIOGRAPHY

- Girish S. Agarwal. *Quantum Optics*. Cambridge University Press, 2013. (Cited on page 26.)
- Boris Albrecht, Pau Farrera, Georg Heinze, Matteo Cristiani, and Hugues de Riedmatte. Controlled rephasing of single collective spin excitations in a cold atomic quantum memory. *arXiv*, page 1501.07559, 2015. URL <http://arxiv.org/abs/1501.07559>. (Cited on page 165.)
- Jürgen Appel, Andrew MacRae, and A I Lvovsky. A versatile digital GHz phase lock for external cavity diode lasers. *Measurement Science and Technology*, 20(5):055302, 2009. URL <http://stacks.iop.org/0957-0233/20/i=5/a=055302>. (Cited on page 186.)
- Jürgen Appel, J.-B. Béguin, Heidi L. Sørensen, S. L. Christensen Christensen, E. Bookjans, k Kluge, I. Iakoupov, A. Sørensen, J. H. Müller, and E. S. Polzik. Probing Nanofiber-trapped Atomic Ensembles at the Quantum Level. In *Progress In Electromagnetics Research Symposium, Prague, Czech Republic*, 2015. Contributed Talk. (Cited on page 80.)
- Martin Appel. Readout Cavity Setup for a Deterministic Single Photon Source, 6 2015. Bachelor thesis, University of Copenhagen. (Cited on pages 148, 150, and 181.)
- Markus Aspelmeyer, Tobias J. Kippenberg, and Florian Marquardt. Cavity optomechanics. *Rev. Mod. Phys.*, 86:1391–1452, Dec 2014. doi: 10.1103/RevModPhys.86.1391. URL <http://link.aps.org/doi/10.1103/RevModPhys.86.1391>. (Cited on page 168.)
- M. Bajcsy, A. S. Zibrov, and M. D. Lukin. Stationary pulses of light in an atomic medium. *Nature*, 426:638–641, 12 2003. ISSN 0028-0836. doi: 10.1038/nature02176. URL <http://dx.doi.org/10.1038/nature02176>. (Cited on page 106.)
- J.-B. Béguin, M. Bookjans, E. L. Christensen, S. L. Sørensen, H. H. Müller, J. S. Polzik, E. and J. Appel. Generation and Detection of a Sub-Poissonian Atom Number Distribution in a One-Dimensional Optical Lattice. *Phys. Rev. Lett.*, 113:263603, Dec 2014a. doi: 10.1103/PhysRevLett.113.263603. URL <http://link.aps.org/doi/10.1103/PhysRevLett.113.263603>. (Cited on pages 3, 5, 44, 49, 74, and 76.)
- J.-B. Béguin, M. Bookjans, E. L. Christensen, S. L. Sørensen, H. H. Müller, J. S. Polzik, E. and J. Appel. Supplemental Material to Generation and Detection of a Sub-Poissonian Atom Number Distribution in a One-Dimensional Optical Lattice. *Phys. Rev. Lett.*, 113:263603, Dec 2014b.

- doi: 10.1103/PhysRevLett.113.263603. URL <http://link.aps.org/doi/10.1103/PhysRevLett.113.263603>. (Cited on page 43.)
- Jean-Baptiste S. Béguin. When light and atoms evanescently meet together. Master's thesis, University of Copenhagen, 6 2011. (Cited on pages 3 and 51.)
- Jean-Baptiste S. Béguin. *A one-dimensional quantum interface between a few atoms and weak light*. PhD thesis, University of Copenhagen, 04 2015. (Cited on pages 1, 3, 7, 29, 32, 36, 43, 44, 49, 52, 54, 55, 56, 63, 65, 67, 69, 70, 73, 74, 75, 80, 120, 167, and 186.)
- Erwan Bimbard, Rajiv Boddeda, Nicolas Vitrant, Andrey Grankin, Valentina Parigi, Jovica Stanojevic, Alexei Ourjoumtsev, and Philippe Grangier. Homodyne tomography of a single photon retrieved on demand from a cavity-enhanced cold atom memory. *Phys. Rev. Lett.*, 112:033601, Jan 2014. doi: 10.1103/PhysRevLett.112.033601. URL <http://link.aps.org/doi/10.1103/PhysRevLett.112.033601>. (Cited on page 165.)
- G. Birkl, M. Gatzke, I. H. Deutsch, S. L. Rolston, and W. D. Phillips. Bragg Scattering from Atoms in Optical Lattices. *Phys. Rev. Lett.*, 75:2823–2826, Oct 1995. doi: 10.1103/PhysRevLett.75.2823. URL <http://link.aps.org/doi/10.1103/PhysRevLett.75.2823>. (Cited on pages 4, 82, and 100.)
- Vladimir B. Braginsky and Farid Ya. Khalili. *Quantum Measurement*. Cambridge University Press, 1992. (Cited on page 118.)
- G Brambilla. Optical fibre nanowires and microwires: a review. *Journal of Optics*, 12(4):043001, 2010. URL <http://stacks.iop.org/2040-8986/12/i=4/a=043001>. (Cited on page 50.)
- Gilberto Brambilla. Nonlinear optics in optical micro- and nano-fibres. In *Optical Nanofiber Applications: From Quantum to Bio Technologies*, 5 2015. (Cited on page 61.)
- Andy W. Brown and Min Xiao. All-optical switching and routing based on an electromagnetically induced absorption grating. *Opt. Lett.*, 30(7):699–701, Apr 2005. doi: 10.1364/OL.30.000699. URL <http://ol.osa.org/abstract.cfm?URI=ol-30-7-699>. (Cited on pages 105 and 106.)
- Stephan Camerer, Maria Korppi, Andreas Jöckel, David Hunger, Theodor W. Hänsch, and Philipp Treutlein. Realization of an optomechanical interface between ultracold atoms and a membrane. *Phys. Rev. Lett.*, 107:223001, Nov 2011. doi: 10.1103/PhysRevLett.107.223001. URL <http://link.aps.org/doi/10.1103/PhysRevLett.107.223001>. (Cited on page 168.)
- D E Chang, L Jiang, A V Gorshkov, and H J Kimble. Cavity QED with atomic mirrors. *New Journal of Physics*, 14(6):063003, 2012. URL <http://stacks.iop.org/1367-2630/14/i=6/a=063003>. (Cited on pages 4 and 104.)

- D. E. Chang, J. I. Cirac, and H. J. Kimble. Self-organization of atoms along a nanophotonic waveguide. *Phys. Rev. Lett.*, 110:113606, Mar 2013. doi: 10.1103/PhysRevLett.110.113606. URL <http://link.aps.org/doi/10.1103/PhysRevLett.110.113606>. (Cited on page 106.)
- S L Christensen, J B Béguin, H. L. Sørensen, E Bookjans, D. Oblak, J. H. Müller, J. Appel, and E. S. Polzik. Toward quantum state tomography of a single polariton state of an atomic ensemble. *New Journal of Physics*, 15(1):015002, 2013. URL <http://stacks.iop.org/1367-2630/15/i=1/a=015002>. (Cited on pages v, vii, 5, 111, 114, 115, 118, and 119.)
- S. L. Christensen, J.-B. Béguin, E. Bookjans, H. L. Sørensen, J. H. Müller, J. Appel, and E. S. Polzik. Quantum interference of a single spin excitation with a macroscopic atomic ensemble. *Phys. Rev. A*, 89:033801, Mar 2014. doi: 10.1103/PhysRevA.89.033801. URL <http://link.aps.org/doi/10.1103/PhysRevA.89.033801>. (Cited on pages 1, 115, 119, 134, and 148.)
- Stephan L. Christensen. Generation of exotic quantum states in a cold ensemble of Caesium atoms. Master's thesis, University of Copenhagen, 8 2012. (Cited on pages 147 and 150.)
- Stephan L. Christensen. *Generation of exotic quantum states of a cold atomic ensemble*. PhD thesis, University of Copenhagen, 11 2014. (Cited on pages 1, 5, 27, 41, 43, 49, 111, 114, 115, 119, 125, 127, 129, 155, 157, 158, 159, 160, 163, 165, and 186.)
- Igor V. Ciapurin, Leonid B. Glebov, and Vadim I. Smirnov. Modeling of Gaussian beam diffraction on volume Bragg gratings in PTR glass. *Proc. SPIE*, 5742:183–194, 2005. doi: 10.1117/12.591215. URL <http://dx.doi.org/10.1117/12.591215>. (Cited on page 183.)
- A. A. Clerk, M. H. Devoret, S. M. Girvin, Florian Marquardt, and R. J. Schoelkopf. Introduction to quantum noise, measurement, and amplification. *Rev. Mod. Phys.*, 82:1155–1208, Apr 2010a. doi: 10.1103/RevModPhys.82.1155. URL <http://link.aps.org/doi/10.1103/RevModPhys.82.1155>. (Cited on pages 36, 37, 38, and 40.)
- A. A. Clerk, M. H. Devoret, S. M. Girvin, Florian Marquardt, and R. J. Schoelkopf. Introduction to Quantum Noise, Measurement, and Amplification: Online Appendices. *Rev. Mod. Phys.*, 82:1155–1208, Apr 2010b. doi: 10.1103/RevModPhys.82.1155. URL <http://link.aps.org/doi/10.1103/RevModPhys.82.1155>. (Cited on pages 15, 39, and 40.)
- Claude N. Cohen-Tannoudji. Nobel Lecture: Manipulating atoms with photons. *Rev. Mod. Phys.*, 70:707–719, Jul 1998. doi: 10.1103/RevModPhys.70.707. URL <http://link.aps.org/doi/10.1103/RevModPhys.70.707>. (Cited on page 32.)
- Yves Colombe. A nanofiber in an ion trap. In *Optical Nanofiber Applications: From Quantum to Bio Technologies*, 5 2015. (Cited on page 64.)

- G. Mauro D'Ariano, Matteo G.A. Paris, and Massimiliano F. Sacchi. Quantum Tomography. In Peter W. Hawkes, editor, **,* volume 128 of *Advances in Imaging and Electron Physics*, pages 205–308. Elsevier, 2003. doi: 10.1016/S1076-5670(03)80065-4. URL <http://www.sciencedirect.com/science/article/pii/S1076567003800654>. (Cited on page 118.)
- S. T. Dawkins, R. Mitsch, D. Reitz, E. Vetsch, and A. Rauschenbeutel. Dispersive Optical Interface Based on Nanofiber-Trapped Atoms. *Phys. Rev. Lett.*, 107:243601, Dec 2011. doi: 10.1103/PhysRevLett.107.243601. URL <http://link.aps.org/doi/10.1103/PhysRevLett.107.243601>. (Cited on page 74.)
- Luca Dellantonio. Entanglement criteria for Spin Squeezing. Master's thesis, University of Copenhagen, 9 2015. (Cited on page 163.)
- I. H. Deutsch, R. J. C. Spreeuw, S. L. Rolston, and W. D. Phillips. Photonic band gaps in optical lattices. *Phys. Rev. A*, 52:1394–1410, Aug 1995. doi: 10.1103/PhysRevA.52.1394. URL <http://link.aps.org/doi/10.1103/PhysRevA.52.1394>. (Cited on pages 80, 82, and 87.)
- Igor Dotsenko. Raman spectroscopy of single atoms. Master's thesis, Rheinische Friedrich-Wilhelms-Universität Bonn, 10 2002. (Cited on page 140.)
- J. S. Douglas, H. Habibian, C.-L. Hung, A. V. Gorshkov, H. J. Kimble, and D. E. Chang. Quantum many-body models with cold atoms coupled to photonic crystals. *Nature Photonics*, 9:236–331, 5 2015. ISSN 1749-4885. doi: 10.1038/nphoton.2015.57. URL <http://dx.doi.org/10.1038/nphoton.2015.57>. (Cited on pages 4 and 170.)
- M. Driscoll, H. Yilmaz, S. K. Ozdemir, L. Tian, S. Singamaneni, and L. Yang. Transient sensing of Au nanorods at plasmon frequency in aqueous solution using tapered optical fiber. In *Optical Nanofiber Applications: From Quantum to Bio Technologies*, 5 2015. (Cited on page 61.)
- L.-M. Duan, M. D. Lukin, J. I. Cirac, and P. Zoller. Long-distance quantum communication with atomic ensembles and linear optics. *Nature*, 414:413–418, Nov 2001a. doi: 10.1038/35106500. URL <http://www.nature.com/nature/journal/v414/n6862/abs/414413a0.html>. (Cited on pages 5, 111, 165, and 169.)
- L.-M. Duan, M. D. Lukin, J. I. Cirac, and P. Zoller. Supplemental Material to Long-distance quantum communication with atomic ensembles and linear optics. *Nature*, 414:413–418, Nov 2001b. doi: 10.1038/35106500. URL <http://www.nature.com/nature/journal/v414/n6862/abs/414413a0.html>. (Cited on page 27.)
- P.S. Edwards, C.T. Janisch, Bo Peng, Jiangang Zhu, S.K. Ozdemir, Lan Yang, and Zhiwen Liu. Label-free particle sensing by fiber taper-based raman spectroscopy. *Photonics Technology Letters, IEEE*, 26(20):2093–2096, Oct 2014. ISSN 1041-1135. doi: 10.1109/LPT.2014.2347970. (Cited on page 61.)

- Takeshi Egami and Simon J. L. Billinge. *Underneath the Bragg Peaks: Structural Analysis of Complex Materials*. Elsevier, 2003. (Cited on page 80.)
- Michael Esfeld. Das Messproblem der Quantenmechanik heute: Übersicht und Bewertung. In *Philosophie der Physik*. Suhrkamp, 2012. (Cited on page 35.)
- Jerome Esteve. Cold atoms: Trapped by nanostructures. *Nature Nanotechnology*, 8:317–318, 2013. ISSN 1748-3387. doi: 10.1038/nnano.2013.80. URL <http://dx.doi.org/10.1038/nnano.2013.80>. (Cited on page 29.)
- Christopher J. Foot. *Atomic Physics*. Oxford University Press, 2005. (Cited on pages 24, 28, 140, and 186.)
- Matthew R. Foreman, Jon D. Swaim, and Frank Vollmer. Whispering gallery mode sensors. *Adv. Opt. Photon.*, 7(2):168–240, Jun 2015. doi: 10.1364/AOP.7.000168. URL <http://aop.osa.org/abstract.cfm?URI=aop-7-2-168>. (Cited on pages 61 and 167.)
- Mark Fox. *Quantum Optics*. Oxford University Press, 2006. (Cited on page 15.)
- Mary C. Frawley, Alex Petcu-Colan, Viet Giang Truong, and Síle Nic Chormaic. Higher order mode propagation in an optical nanofiber. *Optics Communications*, 285(23):4648 – 4654, 2012. ISSN 0030-4018. doi: <http://dx.doi.org/10.1016/j.optcom.2012.05.016>. URL <http://www.sciencedirect.com/science/article/pii/S0030401812004294>. Special Issue: Optical micro/nanofibers: Challenges and Opportunities. (Cited on pages 167 and 168.)
- Steven French. Identity and Individuality in Quantum Theory. In Edward N. Zalta, editor, *The Stanford Encyclopedia of Philosophy*. The Metaphysics Research Lab, Center for the Study of Language and Information, Stanford University, fall 2015 edition, 2015. (Cited on page 64.)
- Cord Friebe. Messproblem, Minimal- und Kollapsinterpretationen. In *Philosophie der Quantenphysik*. Springer Spektrum, 2015. ISBN 978-3-642-37789-1. (Cited on page 35.)
- W. Friedrich, P. Knipping, and M. Laue. Interferenzercheinungen bei Röntgenstrahlen. *Annalen der Physik*, 346(10):971–988, 1913. ISSN 1521-3889. doi: 10.1002/andp.19133461004. URL <http://dx.doi.org/10.1002/andp.19133461004>. (Cited on pages 79 and 80.)
- Jian Fu, Xiang Yin, Ningyuan Li, and Limin Tong. Atom waveguide and 1D optical lattice using a two-color evanescent light field around an optical micro/nano-fiber. *Chinese Optics Letters*, 6(2):112–115, 2 2008. (Cited on page 167.)
- Bryan T. Gard, Keith R. Motes, Jonathan P. Olson, Peter P. Rohde, and Jonathan P. Dowling. *An Introduction to Boson-Sampling*, chapter 8, pages 167–192. World Scientific, 2015. doi: 10.1142/

- 9789814678704_0008. URL http://www.worldscientific.com/doi/abs/10.1142/9789814678704_0008. arXiv:1406.6767. (Cited on page 165.)
- Christopher C. Gerry and Peter L. Knight. *Introductory Quantum Optics*. Cambridge University Press, 2005. (Cited on pages 11, 15, 16, 19, 22, 24, and 25.)
- Alexei L. Glebov, Oleksiy Mokhun, Alexandra Rapaport, Sébastien Vergnole, Vadim Smirnov, and Leonid B. Glebov. Volume Bragg Gratings as Ultra-Narrow and Multiband Optical Filters. *Micro-Optics 2012*, 2012. doi: 10.1117/12.923575. (Cited on page 153.)
- A. Goban, K. S. Choi, D. J. Alton, D. Ding, C. Lacroute, M. Pototschnig, T. Thiele, N. P. Stern, and H. J. Kimble. Demonstration of a State-Insensitive, Compensated Nanofiber Trap. *Phys. Rev. Lett.*, 109:033603, Jul 2012. doi: 10.1103/PhysRevLett.109.033603. URL <http://link.aps.org/doi/10.1103/PhysRevLett.109.033603>. (Cited on pages 4, 67, 74, 80, and 167.)
- A. Goban, C.-L. Hung, J. D. Hood, S.-P. Yu, J. A. Muniz, O. Painter, and H. J. Kimble. Superradiance for atoms trapped along a photonic crystal waveguide. *Phys. Rev. Lett.*, 115:063601, Aug 2015. doi: 10.1103/PhysRevLett.115.063601. URL <http://link.aps.org/doi/10.1103/PhysRevLett.115.063601>. (Cited on pages 4 and 60.)
- A González-Tudela, V. Paulisch, D. E. Chang, H. J. Kimble, and J. I. Cirac. Deterministic generation of arbitrary photonic states assisted by dissipation. *arXiv*, page 1504.07600, 2015. URL <http://arxiv.org/abs/1504.07600>. (Cited on pages 4, 104, 105, and 165.)
- B. Gouraud, D. Maxein, A. Nicolas, O. Morin, and J. Laurat. Demonstration of a memory for tightly guided light in an optical nanofiber. *Phys. Rev. Lett.*, 114:180503, May 2015. doi: 10.1103/PhysRevLett.114.180503. URL <http://link.aps.org/doi/10.1103/PhysRevLett.114.180503>. (Cited on pages 4, 63, and 106.)
- Rudolf Grimm, Matthias Weidemüller, and Yurii B. Ovchinnikov. Optical Dipole Traps for Neutral Atoms. In Benjamin Bederson and Herbert Walther, editors, *, volume 42 of *Advances In Atomic, Molecular, and Optical Physics*, pages 95–170. Academic Press, 2000. doi: 10.1016/S1049-250X(08)60186-X. URL <http://www.sciencedirect.com/science/article/pii/S1049250X0860186X>. (Cited on pages 28 and 31.)
- M. Gross and S. Haroche. Superradiance: An essay on the theory of collective spontaneous emission. *Physics Reports*, 93(5):301 – 396, 1982. ISSN 0370-1573. doi: [http://dx.doi.org/10.1016/0370-1573\(82\)90102-8](http://dx.doi.org/10.1016/0370-1573(82)90102-8). URL <http://www.sciencedirect.com/science/article/pii/0370157382901028>. (Cited on page 60.)
- Rudolf Gross and Achim Marx. *Festkörperphysik*. Oldenbourg, 2012. (Cited on pages 79 and 100.)

- Florian Haas, Jürgen Volz, Roger Gehr, Jakob Reichel, and Jérôme Estève. Entangled States of More Than 40 Atoms in an Optical Fiber Cavity. *Science*, 344(6180):180–183, 2014. doi: 10.1126/science.1248905. URL <http://www.sciencemag.org/content/344/6180/180.abstract>. (Cited on pages 1 and 5.)
- K. Hammerer, M. Aspelmeyer, E. S. Polzik, and P. Zoller. Establishing Einstein-Poldosky-Rosen Channels between Nanomechanics and Atomic Ensembles. *Phys. Rev. Lett.*, 102:020501, Jan 2009. doi: 10.1103/PhysRevLett.102.020501. URL <http://link.aps.org/doi/10.1103/PhysRevLett.102.020501>. (Cited on page 168.)
- Klemens Hammerer, Anders S. Sørensen, and Eugene S. Polzik. Quantum interface between light and atomic ensembles. *Rev. Mod. Phys.*, 82:1041–1093, Apr 2010. doi: 10.1103/RevModPhys.82.1041. URL <http://link.aps.org/doi/10.1103/RevModPhys.82.1041>. (Cited on pages 3, 43, 49, and 65.)
- Serge Haroche and Jean-Michel Raimond. *Exploring the Quantum*. Oxford Graduate Texts, 2006. (Cited on pages 64, 65, and 136.)
- Patrick Hayden and Alex May. Summoning Information in Spacetime, or Where and When Can a Qubit Be? *arXiv*, page 1210.0913, 2013. URL <http://arxiv.org/abs/1210.0913>. (Cited on page 169.)
- Werner Heisenberg. *Der Teil und das Ganze*. Piper Taschenbuch, 2001. ISBN 978-3492222976. (Cited on page 229.)
- T. Hennessy and Th. Busch. Creating atom-number states around tapered optical fibers by loading from an optical lattice. *Phys. Rev. A*, 85:053418, May 2012. doi: 10.1103/PhysRevA.85.053418. URL <http://link.aps.org/doi/10.1103/PhysRevA.85.053418>. (Cited on page 168.)
- J. E. Hoffman, S. Ravets, J. A. Grover, P. Solano, P. R. Kordell, J. D. Wong-Campos, L. A. Orozco, and S. L. Rolston. Ultrahigh transmission optical nanofibers. *AIP Advances*, 4(6):067124, 2014. doi: 10.1063/1.4879799. URL <http://scitation.aip.org/content/aip/journal/adva/4/6/10.1063/1.4879799>. (Cited on page 51.)
- Jonathan E. Hoffman, Fredrik K. Fatemi, Guy Beadie, Steven L. Rolston, and Luis A. Orozco. Rayleigh scattering in an optical nanofiber as a probe of higher-order mode propagation. *Optica*, 2(5):416–423, May 2015. doi: 10.1364/OPTICA.2.000416. URL <http://www.osapublishing.org/optica/abstract.cfm?URI=optica-2-5-416>. (Cited on pages 51, 167, and 168.)
- T. Holstein and H. Primakoff. Field Dependence of the Intrinsic Domain Magnetization of a Ferromagnet. *Phys. Rev.*, 58:1098–1113, Dec 1940. doi: 10.1103/PhysRev.58.1098. URL <http://link.aps.org/doi/10.1103/PhysRev.58.1098>. (Cited on page 27.)

- Daniela Holzmann. Self-ordering and collective dynamics of transversely illuminated point-scatterers in a 1D trap. In *Optical Nanofiber Applications: From Quantum to Bio Technologies*, 5 2015. (Cited on page 106.)
- Daniela Holzmann and Helmut Ritsch. Collective scattering and oscillation modes of optically bound point particles trapped in a single mode waveguide field. *arXiv*, page 1509.01435, 9 2015. URL <http://arxiv.org/abs/1509.01435>. (Cited on page 106.)
- Daniela Holzmann, Matthias Sonnleitner, and Helmut Ritsch. Self-ordering and collective dynamics of transversely illuminated point-scatterers in a 1D trap. *The European Physical Journal D*, 68(11):352, 2014. ISSN 1434-6060. doi: 10.1140/epjd/e2014-50692-2. URL <http://dx.doi.org/10.1140/epjd/e2014-50692-2>. (Cited on page 106.)
- R.L. Hudson. When is the wigner quasi-probability density non-negative? *Reports on Mathematical Physics*, 6(2):249 – 252, 1974. ISSN 0034-4877. doi: [http://dx.doi.org/10.1016/0034-4877\(74\)90007-X](http://dx.doi.org/10.1016/0034-4877(74)90007-X). URL <http://www.sciencedirect.com/science/article/pii/003448777490007X>. (Cited on page 19.)
- Ivan Iakoupov. Open. 2015. (Cited on pages 82 and 86.)
- W. M. Itano, J. C. Bergquist, J. J. Bollinger, J. M. Gilligan, D. J. Heinzen, F. L. Moore, M. G. Raizen, and D. J. Wineland. Quantum projection noise: Population fluctuations in two-level systems. *Phys. Rev. A*, 47:3554–3570, May 1993. doi: 10.1103/PhysRevA.47.3554. URL <http://link.aps.org/doi/10.1103/PhysRevA.47.3554>. (Cited on page 41.)
- Tomi H. Johnson, Stephen R. Clark, and Dieter Jaksch. What is a quantum simulator? *EPJ Quantum Technology*, 1(1):1–12, 2014. ISSN 2196-0763. doi: 10.1140/epjqt10. URL <http://dx.doi.org/10.1140/epjqt10>. (Cited on page 170.)
- Maxime Joos and Quentin Glorieux. Hybrid devices with semiconductor nanocrystals. In *Optical Nanofiber Applications: From Quantum to Bio Technologies*, 5 2015. (Cited on page 55.)
- Shinya Kato and Takao Aoki. Strong coupling between a trapped single atom and an all-fiber cavity. *Phys. Rev. Lett.*, 115:093603, Aug 2015. doi: 10.1103/PhysRevLett.115.093603. URL <http://link.aps.org/doi/10.1103/PhysRevLett.115.093603>. (Cited on pages 104, 106, 166, and 167.)
- Thomas Kiesel. *Verification of nonclassicality in phase space*. PhD thesis, Universität Rostock, 6 2011. (Cited on page 16.)
- H. J. Kimble. The quantum internet. *Nature*, 453:1023–1030, 6 2008. ISSN 0028-0836. doi: 10.1038/nature07127. URL <http://dx.doi.org/10.1038/nature07127>. (Cited on page 169.)

- Kilian W. Kluge, Heidi L. Sørensen, Jean-Baptiste S. Béguin, Ivan Iakoupov, Anders S. Sørensen, Eva M. Bookjans, Jörg-Helge Müller, Eugene S. Polzik, and Jürgen Appel. Coherent Bragg-reflections from a one-dimensional atomic crystal. In *Optical Nanofiber Applications: From Quantum to Bio Technologies, Okinawa, Japan*, 5 2015a. Contributed Poster. (Cited on pages [iii](#) and [80](#).)
- Kilian W. Kluge, Heidi L. Sørensen, Jean-Baptiste S. Béguin, Ivan Iakoupov, Anders S. Sørensen, Jörg-Helge Müller, Eugene S. Polzik, and Jürgen Appel. Coherent Bragg-reflections from a one-dimensional atomic crystal. In *Vienna Summer School on Complex Quantum Systems, Vienna, Austria*, 9 2015b. Contributed Poster. (Cited on pages [iii](#) and [80](#).)
- Kilian W. Kluge, Heidi L. Sørensen, Jean-Baptiste S. Béguin, Ivan Iakoupov, Anders S. Sørensen, Jörg-Helge Müller, Eugene S. Polzik, and Jürgen Appel. Coherent Bragg scattering from a one-dimensional atomic crystal. In *QUANTOP Fuglsang Workshop, Fuglsang, Denmark*, 7 2015c. Invited Talk. (Cited on pages [iii](#) and [80](#).)
- Solvej Knudsen and Freja Thilde Pedersen. Producing adiabatic fiber tapers, 2014. Bachelor thesis, University of Copenhagen. (Cited on page [51](#).)
- H. Kogelnik and T. Li. Laser beams and resonators. *Appl. Opt.*, 5(10):1550–1567, Oct 1966. doi: 10.1364/AO.5.001550. URL <http://ao.osa.org/abstract.cfm?URI=ao-5-10-1550>. (Cited on page [148](#).)
- Herwig Kogelnik. Coupled Wave Theory for Thick Hologram Gratings. *Bell System Technical Journal*, 48(9):2909–2947, 1969. ISSN 1538-7305. doi: 10.1002/j.1538-7305.1969.tb01198.x. URL <http://dx.doi.org/10.1002/j.1538-7305.1969.tb01198.x>. (Cited on pages [154](#) and [183](#).)
- H. Krauter, D. Salart, C. A. Muschik, J. M. Petersen, H. Shen, T. Fernholz, and E. S. Polzik. Deterministic quantum teleportation between distant atomic objects. *Nature Physics*, 9:400–404, 7 2013. ISSN 1745-2473. doi: 10.1038/nphys2631. URL <http://dx.doi.org/10.1038/nphys2631>. (Cited on pages [165](#) and [170](#).)
- Ravi Kumar, Vandna Gokhroo, Kieran Deasy, Aili Maimaiti, Mary C Frawley, Ciarán Phelan, and Síle Nic Chormaic. Interaction of laser-cooled 87 Rb atoms with higher order modes of an optical nanofibre. *New Journal of Physics*, 17(1):013026, 2015a. URL <http://stacks.iop.org/1367-2630/17/i=1/a=013026>. (Cited on page [167](#).)
- Ravi Kumar, Vandna Gokhroo, and Síle Nic Chormaic. Multi-level cascaded electromagnetically induced transparency in cold atoms using an optical nanofibre interface. *arXiv*, page 1507.06451, 7 2015b. URL <http://arxiv.org/abs/1507.06451>. (Cited on page [106](#).)
- Soo Choi Kyung. Testing the Volume Bragg Grating. Technical report, California Institute of Technology, Dec 2010. Unpublished. (Cited on page [184](#).)

- Rolf Landauer. The physical nature of information. *Physics Letters A*, 217, 1996. (Cited on page 63.)
- Fam Le Kien and A. Rauschenbeutel. Anisotropy in scattering of light from an atom into the guided modes of a nanofiber. *Phys. Rev. A*, 90:023805, Aug 2014a. doi: 10.1103/PhysRevA.90.023805. URL <http://link.aps.org/doi/10.1103/PhysRevA.90.023805>. (Cited on pages 49, 54, 55, 56, and 59.)
- Fam Le Kien and A. Rauschenbeutel. Propagation of nanofiber-guided light through an array of atoms. *Phys. Rev. A*, 90:063816, Dec 2014b. doi: 10.1103/PhysRevA.90.063816. URL <http://link.aps.org/doi/10.1103/PhysRevA.90.063816>. (Cited on page 60.)
- Fam Le Kien, V. I. Balykin, and K. Hakuta. Atom trap and waveguide using a two-color evanescent light field around a subwavelength-diameter optical fiber. *Phys. Rev. A*, 70:063403, Dec 2004. doi: 10.1103/PhysRevA.70.063403. URL <http://link.aps.org/doi/10.1103/PhysRevA.70.063403>. (Cited on pages 3 and 63.)
- Fam Le Kien, S. Dutta Gupta, V. I. Balykin, and K. Hakuta. Spontaneous emission of a cesium atom near a nanofiber: Efficient coupling of light to guided modes. *Phys. Rev. A*, 72:032509, Sep 2005. doi: 10.1103/PhysRevA.72.032509. URL <http://link.aps.org/doi/10.1103/PhysRevA.72.032509>. (Cited on page 56.)
- J Lee, J A Grover, J E Hoffman, L A Orozco, and S L Rolston. Inhomogeneous broadening of optical transitions of 87 rb atoms in an optical nanofiber trap. *Journal of Physics B: Atomic, Molecular and Optical Physics*, 48 (16):165004, 2015. URL <http://stacks.iop.org/0953-4075/48/i=16/a=165004>. (Cited on pages 67, 74, 153, and 167.)
- Timothy Lee, Yongmin Jung, Christophe A. Codemard, Ming Ding, Neil G. R. Broderick, and Gilberto Brambilla. Broadband third harmonic generation in tapered silica fibres. *Opt. Express*, 20(8):8503–8511, Apr 2012. doi: 10.1364/OE.20.008503. URL <http://www.opticsexpress.org/abstract.cfm?URI=oe-20-8-8503>. (Cited on page 61.)
- Ulf Leonhardt. *Measuring the Quantum State of Light*. Cambridge University Press, 1997. (Cited on pages 11, 13, 14, 16, 36, and 118.)
- Ying Lia Li, James Millen, and P. F. Barker. Macroscopic Center-of-mass Cooling using Whispering Gallery Mode Resonances. *arXiv*, page 1508.06217, 8 2015. URL <http://arxiv.org/abs/1508.06217>. (Cited on page 61.)
- Lars Liebermeister, Fabian Petersen, Asmus v. Münchow, Daniel Burchardt, Juliane Hermelbracht, Toshiyuki Tashima, Andreas W. Schell, Oliver Benson, Thomas Meinhardt, Anke Krueger, Ariane Stiebeiner, Arno Rauschenbeutel, Harald Weinfurter, and Markus Weber. Tapered fiber coupling of single photons emitted by a deterministically positioned single nitrogen vacancy center. *Applied Physics Letters*, 104(3):031101, 2014. doi:

- <http://dx.doi.org/10.1063/1.4862207>. URL <http://scitation.aip.org/content/aip/journal/apl/104/3/10.1063/1.4862207>. (Cited on page 55.)
- Anne Louchet-Chauvet, Jürgen Appel, Jelmer J Renema, Daniel Oblak, Niels Kjaergaard, and Eugene S Polzik. Entanglement-assisted atomic clock beyond the projection noise limit. *New Journal of Physics*, 12(6):065032, 2010. URL <http://stacks.iop.org/1367-2630/12/i=6/a=065032>. (Cited on pages 5 and 163.)
- A. I. Lvovsky and M. G. Raymer. Continuous-variable optical quantum-state tomography. *Rev. Mod. Phys.*, 81:299–332, Mar 2009. doi: 10.1103/RevModPhys.81.299. URL <http://link.aps.org/doi/10.1103/RevModPhys.81.299>. (Cited on page 118.)
- A V Masalov and V G Minogin. Pumping of higher-order modes of an optical nanofiber by laser excited atoms. *Laser Physics Letters*, 10(7):075203, 2013. URL <http://stacks.iop.org/1612-202X/10/i=7/a=075203>. (Cited on page 167.)
- Robert McConnell, Hao Zhang, Jiazhong Hu, Senka Cuk, and Vladan Vuletic. Entanglement with negative Wigner function of almost 3,000 atoms heralded by one photon. *Nature*, 519:439–442, 2015. ISSN 0028-0836. doi: 10.1038/nature14293. URL <http://dx.doi.org/10.1038/nature14293>. (Cited on pages 1, 5, and 120.)
- Donald A. McQuarrie. The Kronig-Penney Model: A Single Lecture Illustrating the Band Structure of Solids. *The Chemical Educator*, 1(1):1–10, 1996. doi: 10.1007/s00897960003a. URL <http://dx.doi.org/10.1007/s00897960003a>. (Cited on page 80.)
- Harold J. Metcalf and Peter van der Straten. *Laser Cooling and Trapping*. Springer, New York, 1999. (Cited on pages 28, 29, and 32.)
- R. Mitsch, C. Sayrin, B. Albrecht, P. Schneeweiss, and A. Rauschenbeutel. Exploiting the local polarization of strongly confined light for submicrometer-resolution internal state preparation and manipulation of cold atoms. *Phys. Rev. A*, 89:063829, Jun 2014a. doi: 10.1103/PhysRevA.89.063829. URL <http://link.aps.org/doi/10.1103/PhysRevA.89.063829>. (Cited on pages 72, 105, 114, 123, 127, 165, and 167.)
- R. Mitsch, C. Sayrin, B. Albrecht, P. Schneeweiss, and A. Rauschenbeutel. Quantum state-controlled directional spontaneous emission of photons into a nanophotonic waveguide. *Nat. Commun.*, 5, Dec 2014b. doi: 10.1038/ncomms6713. URL <http://dx.doi.org/10.1038/ncomms6713>. (Cited on pages 49, 58, and 127.)
- Ryutaro Nagai and Takao Aoki. Ultra-low-loss tapered optical fibers with minimal lengths. *Opt. Express*, 22(23):28427–28436, Nov 2014. doi: 10.1364/OE.22.028427. URL <http://www.opticsexpress.org/abstract.cfm?URI=oe-22-23-28427>. (Cited on page 51.)

- Michael A. Nielsen and Isaac L. Chuang. *Quantum Computation and Quantum Information*. Cambridge University Press, 2000. ISBN 978-0521635035. (Cited on pages 35, 65, 118, 163, and 169.)
- Daniel Oblak. *Quantum State Engineering in Cold Caesium Atoms*. PhD thesis, University of Copenhagen, 7 2010. (Cited on pages 1, 5, 43, 71, 72, 128, and 186.)
- Luis A. Orozco. Nanofibers for coupling atoms to superconducting qubits, a progress report. In *Optical Nanofiber Applications: From Quantum to Bio Technologies*, 5 2015. (Cited on page 168.)
- Christine P. Pedersen. Characterizing thermal properties of tapered nanofibers. Master's thesis, University of Copenhagen, 6 2015. (Cited on pages 50 and 51.)
- B. Peng, Ş. K. Özdemir, S. Rotter, H. Yilmaz, M. Liertzer, F. Monifi, C. M. Bender, F. Nori, and L. Yang. Loss-induced suppression and revival of lasing. *Science*, 346(6207):328–332, 2014. doi: 10.1126/science.1258004. URL <http://www.sciencemag.org/content/346/6207/328.abstract>. (Cited on page 61.)
- Plamen Petrov. *Quantum noise limited light interferometry with cold trapped atoms*. PhD thesis, University of Copenhagen, 2006. (Cited on pages 5 and 185.)
- C.F. Phelan, T. Hennessy, and Th. Busch. Shaping the evanescent field of optical nanofibers for cold atom trapping. *Opt. Express*, 21(22):27093–27101, Nov 2013. doi: 10.1364/OE.21.027093. URL <http://www.opticsexpress.org/abstract.cfm?URI=oe-21-22-27093>. (Cited on page 168.)
- Max Planck. *Das Wesen des Lichts*. Verlag von Julius Springer, 1920. (Cited on page 11.)
- G. Raithel, G. Birkl, A. Kastberg, W. D. Phillips, and S. L. Rolston. Cooling and Localization Dynamics in Optical Lattices. *Phys. Rev. Lett.*, 78:630–633, Jan 1997. doi: 10.1103/PhysRevLett.78.630. URL <http://link.aps.org/doi/10.1103/PhysRevLett.78.630>. (Cited on page 83.)
- D. Reitz, C. Sayrin, R. Mitsch, P. Schneeweiss, and A. Rauschenbeutel. Coherence Properties of Nanofiber-Trapped Cesium Atoms. *Phys. Rev. Lett.*, 110:243603, Jun 2013. doi: 10.1103/PhysRevLett.110.243603. URL <http://link.aps.org/doi/10.1103/PhysRevLett.110.243603>. (Cited on pages 123, 129, 134, and 137.)
- D. Reitz, C. Sayrin, B. Albrecht, I. Mazets, R. Mitsch, P. Schneeweiss, and A. Rauschenbeutel. Backscattering properties of a waveguide-coupled array of atoms in the strongly nonparaxial regime. *Phys. Rev. A*, 89:031804, Mar 2014. doi: 10.1103/PhysRevA.89.031804. URL <http://link.aps.org/doi/10.1103/PhysRevA.89.031804>. (Cited on pages 4, 80, and 89.)

- Daniel Reitz and Arno Rauschenbeutel. Nanofiber-based double-helix dipole trap for cold neutral atoms. *Optics Communications*, 285(23): 4705 – 4708, 2012. ISSN 0030-4018. doi: <http://dx.doi.org/10.1016/j.optcom.2012.06.034>. URL <http://www.sciencedirect.com/science/article/pii/S0030401812005780>. Special Issue: Optical micro/nanofibers: Challenges and Opportunities. (Cited on page 168.)
- L. Ricci, M. Weidemüller, T. Esslinger, A. Hemmerich, C. Zimmermann, V. Vuletic, W. König, and T.W. Hänsch. A compact grating-stabilized diode laser system for atomic physics. *Optics Communications*, 117(5–6):541–549, 1995. ISSN 0030-4018. doi: 10.1016/0030-4018(95)00146-Y. URL <http://www.sciencedirect.com/science/article/pii/003040189500146Y>. (Cited on page 185.)
- M. Saffman, D. Oblak, J. Appel, and E. S. Polzik. Spin squeezing of atomic ensembles by multicolor quantum nondemolition measurements. *Phys. Rev. A*, 79:023831, Feb 2009. doi: 10.1103/PhysRevA.79.023831. URL <http://link.aps.org/doi/10.1103/PhysRevA.79.023831>. (Cited on pages 5 and 163.)
- Guillem Sagué Cassany. *Cold atom physics using ultra-thin optical fibres*. PhD thesis, Rheinische Friedrich-Wilhelms-Universität Bonn, 12 2008. (Cited on pages 51, 52, 53, 54, 63, and 167.)
- G Sagué, A Baade, and A Rauschenbeutel. Blue-detuned evanescent field surface traps for neutral atoms based on mode interference in ultrathin optical fibres. *New Journal of Physics*, 10(11):113008, 2008. URL <http://stacks.iop.org/1367-2630/10/i=11/a=113008>. (Cited on page 167.)
- Jun John Sakurai and Jim Napolitano. *Modern quantum mechanics*. Addison-Wesley, 2nd edition, 2011. (Cited on pages 35 and 36.)
- Bahaa E. A. Saleh and Malvin Carl Teich. *Fundamentals of Photonics*. John Wiley & Sons, 2007. (Cited on pages 52 and 141.)
- C. Sayrin, C. Clausen, B. Albrecht, P. Schneeweiss, and A. Rauschenbeutel. Storage of fiber-guided light in a nanofiber-trapped ensemble of cold atoms. *Optica*, 2(4):353–356, Apr 2015. doi: 10.1364/OPTICA.2.000353. URL <http://www.osapublishing.org/optica/abstract.cfm?URI=optica-2-4-353>. (Cited on pages 4, 63, and 106.)
- Andreas W. Schell, Hideaki Takashima, Shunya Kamioka, Yasuko Oe, Masazumi Fujiwara, Oliver Benson, and Shigeki Takeuchi. Highly Efficient Coupling of Nanolight Emitters to a Ultra-Wide Tunable Nanofibre Cavity. *Scientific Reports*, 5, 2015. doi: 10.1038/srep09619. URL <http://dx.doi.org/10.1038/srep09619>. (Cited on page 50.)
- Alexander Schilke, Claus Zimmermann, Philippe W. Courteille, and William Guerin. Photonic Band Gaps in One-Dimensionally Ordered Cold Atomic Vapors. *Phys. Rev. Lett.*, 106:223903, Jun 2011. doi: 10.1103/PhysRevLett.106.223903. URL <http://link.aps.org/doi/10.1103/PhysRevLett.106.223903>. (Cited on pages 4 and 84.)

- Alexander Schilke, Claus Zimmermann, and William Guerin. Photonic properties of one-dimensionally-ordered cold atomic vapors under conditions of electromagnetically induced transparency. *Phys. Rev. A*, 86:023809, Aug 2012. doi: 10.1103/PhysRevA.86.023809. URL <http://link.aps.org/doi/10.1103/PhysRevA.86.023809>. (Cited on page 106.)
- Wolfgang P. Schleich. *Quantum Optic in Phase Space*. Wiley-VCH, Berlin, 2001. (Cited on pages 16, 17, and 18.)
- N. Schlosser, G. Reymond, and P. Grangier. Collisional blockade in microscopic optical dipole traps. *Phys. Rev. Lett.*, 89:023005, Jun 2002. doi: 10.1103/PhysRevLett.89.023005. URL <http://link.aps.org/doi/10.1103/PhysRevLett.89.023005>. (Cited on page 70.)
- S. Slama, C. von Cube, B. Deh, A. Ludewig, C. Zimmermann, and Ph. W. Courteille. Phase-Sensitive Detection of Bragg Scattering at 1D Optical Lattices. *Phys. Rev. Lett.*, 94:193901, May 2005a. doi: 10.1103/PhysRevLett.94.193901. URL <http://link.aps.org/doi/10.1103/PhysRevLett.94.193901>. (Cited on pages 4 and 83.)
- S. Slama, C. von Cube, A. Ludewig, M. Kohler, C. Zimmermann, and Ph. W. Courteille. Dimensional crossover in bragg scattering from an optical lattice. *Phys. Rev. A*, 72:031402, Sep 2005b. doi: 10.1103/PhysRevA.72.031402. URL <http://link.aps.org/doi/10.1103/PhysRevA.72.031402>. (Cited on pages 83 and 107.)
- S. Slama, C. von Cube, M. Kohler, C. Zimmermann, and Ph. W. Courteille. Multiple reflections and diffuse scattering in Bragg scattering at optical lattices. *Phys. Rev. A*, 73:023424, Feb 2006. doi: 10.1103/PhysRevA.73.023424. URL <http://link.aps.org/doi/10.1103/PhysRevA.73.023424>. (Cited on pages 83, 84, and 94.)
- Anders S. Sørensen and Klaus Mølmer. Entanglement and extreme spin squeezing. *Phys. Rev. Lett.*, 86:4431–4434, May 2001. doi: 10.1103/PhysRevLett.86.4431. URL <http://link.aps.org/doi/10.1103/PhysRevLett.86.4431>. (Cited on page 163.)
- H. L. Sørensen, E. S. Polzik, and J. Appel. Heater Self-Calibration Technique for Shape Prediction of Fiber Tapers. *J. Lightwave Technol.*, 32(10):1886–1891, May 2014. URL <http://jlt.osa.org/abstract.cfm?URI=jlt-32-10-1886>. (Cited on page 50.)
- H. L. Sørensen, J.-B. Béguin, K. W. Kluge, I. Iakoupov, A. S. Sørensen, E. S. Polzik, and J. Appel. Coherent back-scattering off one-dimensional atomic strings. 2015a. (Cited on pages iii, 2, 4, 80, 82, 86, 91, 97, and 101.)
- Heidi L. Sørensen. Controlling the shape of subwavelength-diameter tapered optical fibers. Master's thesis, University of Copenhagen, 8 2013. (Cited on pages 49, 50, 51, and 54.)

- Heidi L. Sørensen. *Open*. PhD thesis, University of Copenhagen, 12 2015. (Cited on pages 1, 7, 80, 82, 85, 89, 90, 91, 97, 101, and 140.)
- Heidi L. Sørensen, Kilian Kluge, , Jean-Baptiste. Béguin, Ivan Iakoupov, Anders S. Sørensen, Jörg-Helge Müller, Eugene S. Polzik, and Jürgen Appel. One-dimensional atomic crystal mirror. In *Quantum Simulation and Computation: From fundamentals to applications and implementations*, Gothenborg, Sweden, 6 2015b. Contributed Poster. (Cited on page 80.)
- Francisco Soto and Pierre Claverie. When is the Wigner function of multidimensional systems nonnegative? *Journal of Mathematical Physics*, 24(1):97–100, 1983. doi: <http://dx.doi.org/10.1063/1.525607>. URL <http://scitation.aip.org/content/aip/journal/jmp/24/1/10.1063/1.525607>. (Cited on page 19.)
- Daniel A. Steck. Cesium d line data, 12 2010. Version 1.6. (Cited on pages 21, 22, 23, 28, 33, 115, 129, 130, and 131.)
- M. Sumetsky, Y. Dulashko, J. M. Fini, and A. Hale. Optical microfiber loop resonator. *Applied Physics Letters*, 86(16):161108, 2005. doi: <http://dx.doi.org/10.1063/1.1906317>. URL <http://scitation.aip.org/content/aip/journal/apl/86/16/10.1063/1.1906317>. (Cited on page 167.)
- M. Sumetsky, Y. Dulashko, J.M. Fini, A. Hale, and D.J. DiGiovanni. The microfiber loop resonator: theory, experiment, and application. *Journal of Lightwave Technology*, 24:242–250, 1 2006. ISSN 0733-8724. doi: 10.1109/JLT.2005.861127. (Cited on pages 50 and 167.)
- M. Sumetsky, D. J. DiGiovanni, Y. Dulashko, J. M. Fini, X. Liu, E. M. Monberg, and T. F. Taunay. Surface nanoscale axial photonics: robust fabrication of high-quality-factor microresonators. *Opt. Lett.*, 36(24):4824–4826, Dec 2011. doi: 10.1364/OL.36.004824. URL <http://ol.osa.org/abstract.cfm?URI=ol-36-24-4824>. (Cited on page 50.)
- Limin Tong, Fei Zi, Xin Guo, and Jingyi Lou. Optical microfibers and nanofibers: A tutorial. *Optics Communications*, 285(23):4641–4647, 2012. ISSN 0030-4018. doi: 10.1016/j.optcom.2012.07.068. URL <http://www.sciencedirect.com/science/article/pii/S0030401812007389>. Special Issue: Optical micro/nanofibers: Challenges and Opportunities. (Cited on page 49.)
- E. Vetsch, D. Reitz, G. Sagué, R. Schmidt, S. T. Dawkins, and A. Rauschenbeutel. Optical Interface Created by Laser-Cooled Atoms Trapped in the Evanescent Field Surrounding an Optical Nanofiber. *Phys. Rev. Lett.*, 104:203603, May 2010. doi: 10.1103/PhysRevLett.104.203603. URL <http://link.aps.org/doi/10.1103/PhysRevLett.104.203603>. (Cited on pages 3, 49, 63, 67, and 74.)
- E. Vetsch, S.T. Dawkins, R. Mitsch, D. Reitz, P. Schneeweiss, and A. Rauschenbeutel. Nanofiber-Based Optical Trapping of Cold Neutral Atoms. *IEEE*

- Journal of Selected Topics in Quantum Electronics*, 18:1763–1770, November/December 2012. (Cited on pages 72 and 73.)
- B Vogell, T Kampschulte, M T Rakher, A Faber, P Treutlein, K Hammerer, and P Zoller. Long distance coupling of a quantum mechanical oscillator to the internal states of an atomic ensemble. *New Journal of Physics*, 17(4):043044, 2015. URL <http://stacks.iop.org/1367-2630/17/i=4/a=043044>. (Cited on page 168.)
- S Vorrath, S A Möller, P Windpassinger, K Bongs, and K Sengstock. Efficient guiding of cold atoms through a photonic band gap fiber. *New Journal of Physics*, 12(12):123015, 2010. URL <http://stacks.iop.org/1367-2630/12/i=12/a=123015>. (Cited on page 65.)
- D. F. Walls and G. J. Milburn. *Quantum Optics*. Springer, 2007. (Cited on pages 11, 14, and 39.)
- Matthias Weidemüller, Andreas Hemmerich, Axel Görlitz, Tilman Esslinger, and Theodor W. Hänsch. Bragg Diffraction in an Atomic Lattice Bound by Light. *Phys. Rev. Lett.*, 75:4583–4586, Dec 1995. doi: 10.1103/PhysRevLett.75.4583. URL <http://link.aps.org/doi/10.1103/PhysRevLett.75.4583>. (Cited on pages 4, 82, 83, and 87.)
- Matthias Weidemüller, Axel Görlitz, Theodor W. Hänsch, and Andreas Hemmerich. Local and global properties of light-bound atomic lattices investigated by Bragg diffraction. *Phys. Rev. A*, 58:4647–4661, Dec 1998. doi: 10.1103/PhysRevA.58.4647. URL <http://link.aps.org/doi/10.1103/PhysRevA.58.4647>. (Cited on page 83.)
- Eric W. Weisstein. Bessel Differential Equation, a. URL <http://mathworld.wolfram.com/BesselDifferentialEquation.html>. (Cited on page 53.)
- Eric W. Weisstein. Modified Bessel Differential Equation, b. URL <http://mathworld.wolfram.com/ModifiedBesselDifferentialEquation.html>. (Cited on page 53.)
- Eric W. Weisstein. Jacobi-Anger Expansion, c. URL <http://mathworld.wolfram.com/Jacobi-AngerExpansion.html>. (Cited on page 141.)
- C. Wieman and T. W. Hänsch. Doppler-free laser polarization spectroscopy. *Phys. Rev. Lett.*, 36:1170–1173, May 1976. doi: 10.1103/PhysRevLett.36.1170. URL <http://link.aps.org/doi/10.1103/PhysRevLett.36.1170>. (Cited on page 186.)
- E. Wigner. On the Quantum Correction For Thermodynamic Equilibrium. *Phys. Rev.*, 40:749–759, Jun 1932. doi: 10.1103/PhysRev.40.749. URL <http://link.aps.org/doi/10.1103/PhysRev.40.749>. (Cited on page 16.)
- P. J. Windpassinger, D. Oblak, P. G. Petrov, M. Kubasik, M. Saffman, C. L. Garrido Alzar, J. Appel, J. H. Müller, N. Kjærgaard, and E. S. Polzik. Non-destructive Probing of Rabi Oscillations on the Cesium Clock Transition

- near the Standard Quantum Limit. *Phys. Rev. Lett.*, 100:103601, Mar 2008. doi: 10.1103/PhysRevLett.100.103601. URL <http://link.aps.org/doi/10.1103/PhysRevLett.100.103601>. (Cited on pages 41, 43, and 134.)
- Patrick J. Windpassinger. *Non-destructive quantum state measurements and Quantum noise squeezing*. PhD thesis, University of Copenhagen, 12 2008. (Cited on pages 5 and 136.)
- Ramachandrarao Yalla, K. P. Nayak, and K. Hakuta. Fluorescence photon measurements from single quantum dots on an optical nanofiber. *Opt. Express*, 20(3):2932–2941, Jan 2012. doi: 10.1364/OE.20.002932. URL <http://www.opticsexpress.org/abstract.cfm?URI=oe-20-3-2932>. (Cited on page 55.)
- S.-P. Yu, J. D. Hood, J. A. Muniz, M. J. Martin, Richard Norte, C.-L. Hung, Seán M. Meenehan, Justin D. Cohen, Oskar Painter, and H. J. Kimble. Nanowire photonic crystal waveguides for single-atom trapping and strong light-matter interactions. *Applied Physics Letters*, 104(11):111103, 2014. doi: 10.1063/1.4868975. URL <http://scitation.aip.org/content/aip/journal/apl/104/11/10.1063/1.4868975>. (Cited on page 65.)

LIST OF FIGURES

Figure 1.1	Coherent states in phase space	14
Figure 1.2	Schleich's motivation of the Wigner function	16
Figure 1.3	Coherent state Wigner function	17
Figure 1.4	Fock state Wigner function	18
Figure 2.1	Full level structure of cesium	22
Figure 2.2	Two-level atom	23
Figure 2.3	Rabi oscillations	25
Figure 2.4	Bloch sphere	26
Figure 2.5	Principle operation of a MOT	29
Figure 2.6		30
Figure 2.7	MOT setup	30
Figure 3.1	Homodyne detection	37
Figure 3.2	A single spin in a one-sided cavity	39
Figure 3.3	Two-Color Setup	45
Figure 4.1	Microscope image of a nanofiber	49
Figure 4.2	Nanofiber Fabrication	50
Figure 4.3	Adiabatic Taper	51
Figure 4.4	Quasilinear polarization	55
Figure 4.5	Coordinate system	56
Figure 4.6	Directionality coefficient	59
Figure 5.1	Caterpillar trap configuration	66
Figure 5.2	Caterpillar trap potential	66
Figure 5.3	Trap setup	68
Figure 5.4	Trapping sequence	69
Figure 5.5	Trap lifetime and OD	71
Figure 5.6	Radial trap frequency	72
Figure 5.7	Nanofiber polarization alignment	73
Figure 5.8	Atom counting	75
Figure 6.1	Bragg Condition	79
Figure 6.2	Regularly spaced scatterers	80
Figure 6.3	Coherent enhancement of emission by an optically thin ensemble of atoms	81
Figure 6.4	Dependence of back-reflection on scatterer localization	81
Figure 6.5	Bragg scattering setup by Slama et al.	83
Figure 6.6	Bragg superstructure	85
Figure 6.8	Dark lattice scheme	86
Figure 6.9	Atomic mirror setup	87
Figure 6.10	Preparation sequence for an atomic mirror	88
Figure 6.11	Atomic mirror example measurement	89
Figure 6.12	Power calibration for atomic mirror	89

Figure 6.13	Estimating the number of atoms from the optical depth	90
Figure 7.1	Reflection coefficients for varying E_{struct}	92
Figure 7.2	Reflection coefficients for varying Δ_{probe}	93
Figure 7.3	Reflection for varying P_{probe}	95
Figure 7.4	Reflection coefficients for varying λ_{struct}	96
Figure 7.5	Repeated structuring pulse	98
Figure 7.6	Effect of probe light on Bragg reflection	99
Figure 7.7	Trap temperature measurement using the Debye-Waller factor	100
Figure 7.8	Repeated preparation sequence	101
Figure 7.9	Investigating the failure of repeated preparation	103
Figure 7.10	Atomic Fabry-Perót type cavity	104
Figure 7.11	Deterministic quantum state preparation using atomic crystals	105
Figure 7.12	Atomic Mirror with EIT	106
Figure 8.1	DLCZ scheme	111
Figure 8.2	Comparison of level sets	113
Figure 8.3	State tomography by population difference measurement	120
Figure 9.1	Optical pumping setup	124
Figure 9.2	Optical pumping sequence	125
Figure 9.3	Optical pumping results	126
Figure 9.4	Microwave Setup	128
Figure 9.5	Landau-Zener sweep	130
Figure 9.6	Landau-Zener sweep (detail)	130
Figure 9.7	Magnetic bias field calibration	131
Figure 9.8	Sequence for clock frequency estimation	132
Figure 9.9	Clock frequency estimation	132
Figure 9.10	Rabi sequence	133
Figure 9.11	Relationship of effective Rabi frequency and amplitude	134
Figure 9.12	Estimating τ_1	135
Figure 9.14	Continuous observation of Rabi oscillations	136
Figure 9.15	Ramsey sequence	137
Figure 9.16	Ramsey fringes	138
Figure 9.17	Ramsey fringe contrast	138
Figure 9.18	Finetuning the probe laser	139
Figure 9.19	QND measurement	139
Figure 9.20	Raman process	140
Figure 9.21	EOM sideband intensities	142
Figure 9.22	Raman setup	143
Figure 9.23	EOM carrier depletion measurement	144
Figure 9.24	Suggested final experimental sequence	145
Figure 10.1	Detection setup	147
Figure 10.2	Filter cavity design	148

Figure 10.3	Principle function of the filter cavity	149
Figure 10.4	FSR	150
Figure 10.5	Filter cavity FSR	151
Figure 10.6	Thermal stability of the filter cavity	152
Figure 10.7	Filter cavity linewidth and rejection	153
Figure 10.8	Spectral dependence of VBG reflection	154
Figure 10.9	SPCM detection efficiency	155
Figure 10.10	SPCM setup	155
Figure 11.1	Squeezed state	164
Figure A.1	Duration of Structuring Pulse	173
Figure A.2	Power of Structuring Pulse	174
Figure A.3	Effect of probe light on Bragg reflection II	175
Figure A.4	Effect of probe light on Bragg reflection III	176
Figure A.5	Transmission signal for repeated structuring pulse	177
Figure A.6	Atoms do not heat without structuring	178
Figure A.7	Detection of Bragg reflections in a few shots	179
Figure C.1	Angular dependence of VBG reflection	184
Figure E.1	SPCM Control Circuit board layout	201
Figure E.2	SPCM Control Circuit circuit diagram	202

LIST OF TABLES

Table 7.1	Optimum atomic mirror preparation parameters	97
Table C.1	Parameters for OptiGrate RBG-852-99	183

LISTINGS

Listing E.1	main.ucf	191
Listing E.2	main.vhd	191
Listing E.3	sampling_gray_counter.vhd	192
Listing E.4	gate_control.vhd	193
Listing E.5	Photoncounter_Failsafe.c	193

LIST OF ACRONYMS

AFS atomic Fock state

AOM	acousto-optical modulator
APD	avalanche photo diode
BEC	Bose-Einstein condensate
CCD	charge coupled device
CPLD	complex programmable logic device
CSS	collective spin state
DAC	digital-to-analog converter
DC	direct current
DDS	direct digital synthesizer
DRO	dielectric resonance oscillator
DLCZ	Duan, Lukin, Cirac, Zoller
ECDL	external cavity diode laser
EIT	electromagnetically induced transparency
EOM	electro-optical modulator
FET	field-effect transistor
FPGA	field programmable gate array
FSR	free spectral range
GPS	Global Positioning System
LCD	liquid crystal display
LED	light-emitting diode
LO	local oscillator
MOT	magneto-optical trap
NBI	Niels Bohr Institute
OCCO	oven controlled crystal oscillator
OD	optical depth
PBS	polarizing beamsplitter
PCB	printed circuit board
PI	proportional-integral
PLL	phase-lock loops
PMT	photo-multiplier
PTR	photo-thermo-reflective
QED	quantum electrodynamics
QND	quantum non-demolition
QUANTOP	Danish Center for Quantum Optics
QPD	quasi-probability distribution
RF	radio-frequency
RWA	rotating-wave approximation
SES	single excitation state
SI	Système international d'unités
SNR	signal to noise ratio
SPCM	single photon counting module
SSS	spin squeezed state
SVN	Apache Subversion
Ti:Sa	titanium sapphire laser
TMS	transversal mode spacing
TTL	transistor-transistor logic

USB Universal Serial Bus
UV ultraviolet
VBG Volume Bragg Grating
VI virtual instrument
WGM whispering gallery mode

ACKNOWLEDGMENTS

At the very end of my thesis, it is my pleasure to acknowledge and thank all the people who in various ways contributed to it.

First and foremost, my thanks go to Eugene Polzik, Jörg-Helge Müller, and Jürgen Appel for welcoming me into their group at the Niels Bohr Institute. Special thanks go to Stefan Christensen, who during my first months at [QUANTOP](#) was my mentor, introducing me to the experimental and theoretical basics, and subsequently became a source of encouragement and outside perspective.

Heidi Lundgaard Sørensen took it upon her to teach me the operation of the nanofiber experiment. I enjoyed and learned a lot from our collaboration on the “atomic mirror”, not only about physics, but how to approach an exploration into unknown terrain. Jean-Baptiste Béguin introduced me to the wonders of quantum states and was incredibly helpful in shaping my understanding of experimental quantum physics. Without his guidance, this thesis would look much worse and I would have achieved much less. Michael Zugenmaier was more than once a helpful supporter when it came to filter cavities and electronics. All of you were excellent colleagues and collaborators – it was a pleasure to share a lab and learn from you.

Jürgen Appel gave me a lot of freedom to explore and take charge of things, always willing to share a piece of his infinite knowledge. Jörg-Helge Müller did not only agree to serve as the co-supervisor of this thesis, but also supervised my “Master Research Project for Exchange Students” which made my stay in Copenhagen possible. His always cheerful evening visits to the lab were not only tremendously valuable for experimental progress, but helped to keep the spirits high. Eugene Polzik was a tireless and encouraging supporter, who despite frequent travels and his duties as the head of [QUANTOP](#) was always interested to hear about the mundane details of my work in the lab.

A big “thank you” goes to Stephan Reitzenstein, who despite his ever growing group immediately agreed to serve as the advisor for this thesis at TU Berlin, even though the project did not fall into his line of research. I could not have wished for a more smooth and encouraging cooperation.

I am much obliged to Patrick Windpassinger, who in the spring of 2014 together with his group welcomed me at the University of Mainz and subsequently paved my way to Copenhagen. I am especially indebted to Maria Langbecker and Noaman Moamad who introduced me to “real” laser physics, atom trapping, optical fibers, and the work in a quantum optics lab.

This thesis concludes my undergraduate studies of physics. I will therefore use this opportunity to thank Jan-Philipp Schröder for being a friend

and colleague, enduring four semesters of lab courses with me. Also, thank you for dragging me to Prof. Dreismann's lecture on quantum information two years ago – that day was the very beginning of this thesis. Huge thanks to Farsane Tabataba-Vakili, who from day one was a friend and comrade-in-arms, especially during numerous exam preparations. I can only admire your persistence and dedication to seemingly everything you undertake, which has saved me more than once. On the same note, thanks to Kilian Kuhla for pushing and pulling me through years of theoretical physics; and to Janina and you for providing me shelter during the last days of my work on this thesis. Thank you Conny, Felix, Alex, Wassilij, Elli, Clemens, and all the others who shared parts of my four years at TU Berlin with me.

I certainly would not have been able to even dream of beginning this thesis if not for my four years in the Projektlabor. I thank Maxmilian Bucher for guiding and encouraging me during my first three semesters and being a mentor beyond that time. I thank Thomas Möller and the whole team for the opportunity to join as a teaching assistant early on in my studies – it certainly was not an easy decision to move on so quickly. I am especially grateful to Andrea Merli and Daniela Rupp for their support.

Although at times one can feel otherwise, there is a life outside of the lab. I thank all my friends, old and new, who explored Copenhagen with me. And thank you, Anna – 2015 was a much better year because of you.

Finally, and most importantly, I thank my family. Nothing would have been possible without the everlasting support and encouragement of my parents.

*And all at once
a step outside
into the wind and rain.*

— Villagers

COLOPHON

This thesis was typeset in \LaTeX (*pdflatex*) using the typographical look-and-feel *classicthesis* developed by André Miede.

Analysis and modeling were done in *Python*, using the *scipy* and *qutip* packages, as well as in *Mathematica*.

All plots were rendered using the *matplotlib* package. Graphics were created with *Inkscape*.

Final Version as of October 23, 2015 (`masterthesis` Version 1.0).